TECHNISCHE UNIVERSITÄT WIEN
Vienna | Austria

DISSERTATION

Micropolar continuum modeling of lattice materials

carried out for the purpose of obtaining the degree of Doctor technicae (Dr. techn.),
submitted at TU Wien, Faculty of Mechanical and Industrial Engineering, by

Dipl.-Ing. Marius M. Schasching

[redacted]

under the supervision of

Assoc. Prof. Dipl.-Ing.in Dr.in techn. Melanie Todt

Institute of Lightweight Design and Structural Biomechanics, E317

reviewed by

Assoc. Prof. Boyang Chen, PhD
Faculty of Aerospace Engineering
Delft University of Technology, Netherlands

Univ.-Prof. Dipl.-Ing. Dr. mont. Thomas Antretter
Chair of Mechanics
Montanuniversität Leoben, Austria

Affidavit

I declare in lieu of oath, that I wrote this thesis and carried out the associated research myself, using only the literature cited in this volume. If text passages from sources are used literally, they are marked as such.

I confirm that this work is original and has not been submitted for examination elsewhere, nor is it currently under consideration for a thesis elsewhere. I acknowledge that the submitted work will be checked electronically-technically using suitable and state-of-the-art means (plagiarism detection software). On the one hand, this ensures that the submitted work was prepared according to the high-quality standards within the applicable rules to ensure good scientific practice "Code of Conduct" at the TU Wien. On the other hand, a comparison with other student theses avoids violations of my personal copyright.

Vienna, December 2023

Marius M. Schasching

Abstract

Lattice materials are becoming increasingly important in lightweight design as they can now be manufactured to meet desired properties using advancing additive manufacturing techniques. Reliable predictions of their mechanical response are required to use them in engineering applications in an efficient way. Among the numerous failure mechanisms that may occur in lattice materials, this thesis focuses on the buckling of lattice beams caused by global compressive loading. For the sake of efficiency, a continuum modeling approach is aimed for, which is addressed by using micropolar continuum theory. It is a promising approach to describe the required deformation mechanisms based on the internal length scale of the micropolar continuum. However, investigating buckling of lattice beams based on micropolar modeling is not common in the literature. In a first step, the micropolar elastic constants for the constitutive relations are determined, since these are generally not available in the literature. Additionally, a geometrically nonlinear model is required to study buckling. Such a model is not yet available out of the box and, therefore, must be implemented in the Finite Element Method framework of interest.

An energy-based homogenization approach commonly used in the literature is employed to derive the micropolar elastic constants of 2D and 3D lattices. The method provides two sets of constants for the very same lattice depending on assumptions made during the derivation. Comparing these sets, some of the constants associated with the rotation field differ from each other in both sign and magnitude. Both sets have caused some controversy in the literature about the validity of the method in general. To contribute to the discussion a numerical study is carried out based on 2D lattices. This study is also used as basis for the derivation of the constants of the 3D lattices aimed for in the present thesis. For the set with constants showing negative signs, the internal length of the lattices and the meshing parameters are found to be competing length scales. Conditions are proposed to circumvent such interference. In contrast, the set with constants showing only positive signs can be used without constraints as long as a proper discretization is ensured such that the gradients of the kinematic fields are captured properly. Based on the findings, micropolar elastic constants of various types of 3D lattices are derived. To evaluate the validity of these constants, continuum models are compared to discrete models in terms of strain energies and rotation fields.

To study buckling, a geometrically nonlinear model proposed in the literature is implemented in ABAQUS as a user element. For verification of the implementation, benchmark problems are used. It is investigated to what extent the model is capable of estimating critical loads and predicting the postbuckling behavior of lattice beams when remaining within the linear strain regime. Discrete models serve as reference. The postbuckling regime is accessed by imposing eigenmode-affine imperfections based on linear eigenvalue analysis of the discrete models and random-based imperfections inspired by imperfections commonly occurring in additive manufacturing. The comparison with discrete models shows that the overall behavior can be qualitatively captured by the models and that even localizations of deformation are captured as long as the localized deformations remain small. While further studies are necessary to identify the limits of the model to provide the reliability required for any engineering application, the present contribution provides evidence

that the micropolar continuum offers the capability of replacing discrete models for buckling and postbuckling predictions of lattice materials.

Kurzfassung

Gittermaterialien gewinnen im Leichtbau zunehmend an Bedeutung, da sie heute mithilfe additiver Fertigungsverfahren mit den gewünschten Eigenschaften hergestellt werden können. Zuverlässige Vorhersagen des mechanischen Verhaltens sind erforderlich, um sie in technischen Anwendungen in effizienter Weise einsetzen zu können. Unter den zahlreichen Versagensmechanismen, die in Gittermaterialen auftreten können, konzentriert sich diese Arbeit auf das Knicken von Gitterbalken, das durch globale Drucklasten verursacht werden kann. Aus Gründen der Effizienz wird dabei ein kontinuumsmechanischer Ansatz auf Basis der mikropolaren Theorie verfolgt. Diese Theorie stellt einen vielversprechenden Ansatz dar, um die benötigten Verformungsmechanismen mithilfe einer internen Länge, welche dieser Theorie zugrunde liegt, zu beschreiben. Allerdings, sind Beulanalysen von Gitterbalken mithilfe mikropolarer Modelle in der Literature nicht üblich. In einem ersten Schritt werden die mikropolar elastischen Konstanten für das zugrundeliegende Konstitutivgesetz bestimmt, da diese im Allgemeinen nicht in der Literatur verfügbar sind. Zusätzlich wird ein geometrisch nichtlineares Modell benötigt, um Beulen untersuchen zu können. Solche Modelle sind nicht als Standardmodelle verfügbar und sind daher erst in ein Finite Elemente Programm zu implementieren.

Eine in der Literatur übliche energiebasierte Homogenisierungsmethode wird angewendet, um die mikropolar elastischen Konstanten von 2D und 3D Gittermaterialien zu bestimmen. In Abhängigkeit der getroffenen Annahmen, liefert diese Methode zwei Sätze von Konstanten für ein und dasselbe Gitter. Vergleicht man diese beiden Sätze, so unterscheiden sich einige der Konstanten, die mit dem Rotationsfeld verknüpft sind, sowohl im Vorzeichen als auch in der Größe. Beide Sätze haben in der Literatur zu einer gewissen Kontroverse über die Gültigkeit der Methode im allgemeinen geführt. Daher wird eine numerische Studie auf Basis von 2D Gittern durchgeführt, um einerseits zur Diskussion beizutragen und andererseits eine Grundlage für die Bestimmung der Konstanten für die 3D Gitter zu erhalten, die in dieser Arbeit bestimmt werden sollen. Für den Satz von Konstanten mit negativen Vorzeichen werden dabei die interne Länge des Gitters und die Vernetzungsparameter als zwei konkurrierende Längenskalen identifiziert. Es werden Bedingungen formuliert, um Interferenzen zu vermeiden. Hingegen kann der Satz von Konstanten mit positiven Vorzeichen ohne Einschränkungen verwendet werden, sofern die Diskretisierung ausreichend fein ist, um Gradienten in den kinematischen Feldern abbilden zu können. Basierend auf diesen Ergebnissen werden mikropolare elastische Konstanten für verschiedene 3D Gittertypen ermittelt. Die Validität der Konstanten wird durch den Vergleich von Kontinuumsmodellen mit diskreten Modellen evaluiert.

Um Beulen zu untersuchen, wird ein in der Literatur vorgeschlagenes, geometrisch nichtlineares Modell in ABAQUS als Benutzerelement implementiert. Die Implementierung wird anhand von Benchmark-Problemen verifiziert. Es wird untersucht bis zu welchem Grad das Modell, unter der Annahme kleiner Verzerrungen, in der Lage ist, kritische Lasten abschätzen und das Nachbeulverhalten von Gitterbalken abbilden zu können. Diskrete Modelle dienen dabei als Referenz. Das Nachbeulverhalten wird einerseits durch Eigenform affine Imperfektionen, basierend auf linearen Eigenwertanalysen der diskreten Modelle zugänglich gemacht. Andererseits werden zufallsbasierte Imperfektionen verwendet, welche durch gewöhnlich in der additiven Fertigung

auftretende Imperfektionen inspiriert sind. Der Vergleich mit diskreten Modellen zeigt, dass die Kontinuumsmodelle sowohl das globale Verhalten qualitativ erfassen als auch Deformationslokalisierungen, solange diese klein sind, abbilden können. Während weitere Studien notwendig sind, um die Grenzen der mikropolaren Modelle bestimmen zu können, die in technischen Anwendungen zwingend erforderlich sind, zeigt diese Arbeit auf, dass mikropolare Kontinuumsmodelle, grundsätzlich die Möglichkeit bieten diskrete Modelle für Beul- und Nachbeulanalysen zu ersetzen.

Acknowledgement

Isn't the nice thing about the acknowledgement that one can be personal, leaving that little space of freedom that is not welcome in the scientific sections? The answer may be personal as well.

First of all, I would like to express my deepest gratitude to Assoc. Prof. Dr. Melanie Todt for her support and guidance during my doctoral studies. Thank you for always asking the right questions to consolidate my ideas and for giving heretical thinking a chance, which often enabled fruitful discussions and paved the way for further ideas. I would also like to thank Assoc. Prof. Dr. Heinz Pettermann and Ao.Univ.-Prof.i.R. Dr. Helmut Böhm for sharing their experience with me.

Paul, I don't know whether to thank you for having pushed me to convince myself to take on the challenge of a PhD or not, but what I do know for sure is that I would like to thank you for the time spent together at the Institute and for the inspiring discussions well beyond every work related topic. I would like to be honest at this point, it didn't take much convincing. I also would like to thank my colleague Fabian for keeping this discussions alive and for helping me fight with Heisenbugs in Fortran and much more. Thank you that I could not count those hours that would otherwise have been lost. Furthermore, I would also like to thank my colleagues Anam and Pavan for the valuable discussions during the coffee breaks.

In general, I would like to thank all the members of the ILSB for creating such a friendly and supportive atmosphere.

I am also very grateful to my family and friends for their support during this time.

The above acknowledgements would be redundant if there were not one more person to thank. Without the help of my partner Anna, who looked after Matilda and Xaver throughout the time I worked on the thesis, and who supported me through all the challenges that scientific working in combination with family life entails, I would not have been able to write a single page of this thesis. Thank you Anna, the whole work is dedicated to you.

Contents

Notation

Throughout this thesis italic letters refer to *scalars* and boldface letters designate tensorial quantities. Underlined letters indicate *first order tensors* or *vectors*, letters with a single tilde placed below refer to *second order tensors*, underlined letters with a single tilde placed below designate *third order tensors*, and blackboard letters with a double tilde placed below indicate *fourth order tensors*. All components of tensors are given with respect to a Cartesian basis.

Square brackets indicate that either vectors and matrices in general or a vector-matrix notation of second or fourth order tensors is used. Unless stated otherwise, the components for the vector-matrix notation are arranged as given in Eq. (2.62). Ambiguity remains for second order tensors in vector-matrix notation and for matrices in general. Thus, if a tensor is used, this is explicitly stated.

Tensor notation

a, b	...	scalars
$\underline{\mathbf{a}}$, $\underline{\mathbf{b}}$	...	tensors of the first order (or first order tensors) or vectors
$\underset{\sim}{\mathbf{A}}$, $\underset{\sim}{\mathbf{a}}$	...	tensors of the second order (or second order tensors)
$\underline{\underset{\sim}{\mathbf{A}}}$, $\underline{\underset{\sim}{\mathbf{a}}}$	...	tensors of the third order (or third order tensors)
$\underset{\approx}{\mathbb{A}}$, $\underline{\underset{\approx}{\mathbf{a}}}$	...	tensors of the fourth order (or fourth order tensors)

Index notation

a, b	...	scalars
a_i, b_i	...	vectors
A_{ij}, a_{ij}	...	second order tensors
A_{ijk}, a_{ijk}	...	third order tensors
$\mathbb{A}_{ijkl}$, a_{ijkl}	...	fourth orders tensor

Vector-matrix notation

$[\underset{\sim}{\mathbf{A}}]$, $[\underset{\sim}{\mathbf{a}}]$	...	second order tensors
$[\underset{\approx}{\mathbb{A}}]$, $[\underline{\underset{\approx}{\mathbf{a}}}]$	...	fourth order tensors

Vectors and matrices in general

$[\underline{\mathbf{A}}]$, $[\underline{\mathbf{a}}]$	...	vector
$[\underset{\sim}{\mathbf{A}}]$, $[\underset{\sim}{\mathbf{a}}]$	...	matrix

List of Symbols

The symbols are grouped by scalars, first, second, third and fourth order tensors, and FEM related variables, respectively. Within each group, Latin symbols in alphabetic order are placed before Greek symbols in alphabetic order.

Scalars

A	cross section of 3D lattice member	mm^2
A_{bc}	area of base cell	mm^2
A_{int}, A_{ext} ...	internal and external energies	N mm
$\mathcal{B}$	micropolar body	
E_{s}	Young's modulus of parent material	$\mathrm{N/mm}^2$
E_{se}, ΔE_{se} ...	total and incremental strain energies	N mm
G_{s}	shear modulus of parent material	$\mathrm{N/mm}^2$
h	out-of-plane thickness associated with plane strain assumption	mm
$H(\cdot)$	Heavyside function	
$I_{\mathrm{m}}, I_{\mathrm{n}}, I_{\mathrm{t}}$	geometrical moments of inertia of m-, n-, and t-axis of 3D lattice member	mm^4
J	determinant of the deformation gradient tensor	
L, l	lengths at macroscale and microscale	mm
n_{bc}	number of lattice members comprising a base cell	
N_1xN_2(xN_3)	number of base cells in 1, 2, (and 3)-direction comprising the lattice	
$\mathcal{P}$	material point or particle	
r	radius of 3D lattice member	mm
S, s	surfaces in reference and current configurations	mm^2
$\partial\mathcal{R}_0$, $\partial\mathcal{R}_t$ ...	surface boundaries in reference and current configurations	mm^2
t	thickness of 2D lattice member	mm
t	time	s
V, v	volumes of micropolar body in reference and current configurations	mm^3
V_{bc}, V_s	volumes of basce cell and parent material	mm^3
W_{IJ}	strain energy of lattice member IJ	mm^2
η_i, $\underline{\boldsymbol{H}}_i$	i^{th} eigenvalue and eigenmode	
$\lambda, \mu, \nu; \alpha, \beta, \gamma$	micropolar elastic constants of isotropic material	$\mathrm{N/m}^2\mathrm{m}$; N
ν_{s}	Poisson's ratio of parent material	
ξ_i, ξ	scaling factor for the i^{th} eigenmode and for deviation of radii	
ρ_0, ρ_t	densities in reference and current configurations	$\mathrm{kg/mm}^3$
ρ_{r}	relative density	
χ_y	averaged relative error of DOF y	
ψ	strain energy density	$\mathrm{N/mm}^2$

First order tensors and general vectors

$\underline{\mathbf{E}}_i$, $\underline{\mathbf{e}}_i$	basis vectors in 1, 2, and 3-direction in reference and current configurations	
$\underline{\mathbf{D}}_i$, $\underline{\mathbf{d}}_i$	directors $i = 1, 2, 3$ of trihedral of $\mathcal{P}$ in reference and current configurations	
$\underline{\mathbf{f}}$	body force density vector	N/kg
$\underline{\mathbf{m}}$	body moment density vector	Nmm/kg
$\underline{\mathbf{t}}$, $\underline{\tilde{\mathbf{t}}}$, $\underline{\breve{\mathbf{t}}}$	stress vectors related to Cauchy-, PK1-, and PK2-like stress tensors	N/mm^2
${}^{\kappa}\underline{\mathbf{t}}$, ${}^{\kappa}\underline{\tilde{\mathbf{t}}}$, ${}^{\kappa}\underline{\breve{\mathbf{t}}}$	couple stress vectors related to Cauchy-, PK1-, and PK2-like couple stress tensors	N/mm
${}^{\chi}\underline{\mathbf{t}}$, ${}^{\chi}\underline{\tilde{\mathbf{t}}}$, ${}^{\chi}\underline{\breve{\mathbf{t}}}$ ...	axial vectors of Cauchy-, PK1-, and PK2-like stress tensor	N/mm^2
$\underline{\mathbf{u}}$	displacement vector	mm
$\underline{\mathbf{U}}_I$	nodal displacement vector at node I	mm
$\underline{\mathbf{X}}$, $\underline{\mathbf{x}}$	position vectors of particle in the reference and current configurations	mm
$[\underline{\boldsymbol{\varepsilon}}]$	linear micropolar generalized vector of strain and curvature components	-,1/mm
$[\underline{\boldsymbol{\sigma}}]$	linear micropolar generalized vector of stress and couple stress components	N/mm^2, N/mm
$\underline{\boldsymbol{\phi}}$	microrotation vector	rad
$\underline{\boldsymbol{\Phi}}_I$	nodal rotation vector at node I	rad

Second order tensors and general matrices

$[\underset{\approx}{\mathbb{D}}]$	generalized fourth order elasticity tensor in vector-matrix notation or micropolar elasticity matrix	N/mm^2, N
$\underset{\sim}{\mathbf{E}}$, $\underset{\sim}{\mathbf{e}}$	micropolar relative Lagrangian and Eulerian stretch tensors	
$\underset{\sim}{\mathbf{F}}$	deformation gradient tensor	
$\underset{\sim}{\mathbf{I}}$	identity tensor	
$\underset{\sim}{\boldsymbol{\mathscr{K}}}$, $\underset{\sim}{\boldsymbol{\mathscr{k}}}$	micropolar relative Lagrangian and Eulerian wryness tensors	1/mm
$\underset{\sim}{\mathbf{T}}$, $\underset{\sim}{\tilde{\mathbf{T}}}$, $\underset{\sim}{\breve{\mathbf{T}}}$	Cauchy-, PK1-, and PK2-like stress tensors	N/mm^2
${}^{\kappa}\underset{\sim}{\mathbf{T}}$,${}^{\kappa}\underset{\sim}{\tilde{\mathbf{T}}}$,${}^{\kappa}\underset{\sim}{\breve{\mathbf{T}}}$ ...	Cauchy-, PK1-, and PK2-like couple stress tensors	N/mm
$[\underset{\sim}{\mathbf{T}}_{\mathrm{r}}^{(e)}]$	transformation matrix	
$\underset{\sim}{\mathbf{R}}$,$\underset{\sim}{\mathbf{R}}^{\mathrm{mac}}$,$\underset{\sim}{\mathbf{R}}^{\mathrm{eff}}$.	microrotation, macrorotation, and effective rotation tensors	
$\underset{\sim}{\boldsymbol{\varepsilon}}$, $\underset{\sim}{\boldsymbol{\kappa}}$	linearized micropolar strain and curvature tensors	-, 1/mm
$\underset{\sim}{\boldsymbol{\sigma}}$, ${}^{\kappa}\underset{\sim}{\boldsymbol{\sigma}}$	linear stress and couple stress tensors	N/mm^2, N/mm

Third order tensors

$\underset{\approx}{\boldsymbol{\epsilon}}$	Levi-Civita symbol or permutation tensor	

Fourth order tensors

$\underset{\approx}{\mathbb{A}}$	elasticity tensor relating strains and stresses	N/mm^2
$\underset{\approx}{\mathbb{B}}$	elasticity tensor relating curvatures and couple stresses	N
$\underset{\approx}{\mathbb{C}}$	elasticity tensor coupling strains-curvatures and stresses-couple stresses	N/mm^2, N
$\underset{\approx}{\mathbb{O}}$	zero fourth order tensor	
$\underset{\approx}{\mathbb{T}}$	transformation tensor	

FEM related

$[\underset{\sim}{\mathbf{B}}_{\mathrm{N}}^{(e)}]$	matrix of derivatives of element shape functions	
$[\underset{\sim}{\mathbf{d}}]$	differential operator matrix	
h_e	element size	mm
$\underset{\sim}{\breve{\mathbf{J}}}_{\xi}$, $\underset{\sim}{\mathbf{J}}_{\xi}$	Jacobian matrices to map reference and current configurations to parent element space	
$\breve{J}_{\xi}$, J_{ξ}	determinants of Jacobian matrices	

$[\underset{\sim}{\mathbf{k}}^{(e)}_{\text{local}}]$, $[\underset{\sim}{\mathbf{k}}^{(e)}_{\text{global}}]$	element stiffness matrices in local and global coordinate system	N/mm, Nmm/rad
$[\underset{\sim}{\mathbf{K}}_0]$, $[\underset{\sim}{\mathbf{K}}_{\text{T}}]$ ...	initial and tangent stiffness matrices	N/mm, Nmm/rad
M_1xM_2(xM_3)	number of continuum elements in 1, 2, (and 3)-direction	
$\mathcal{M}$	ratio of internal length over element size	
N^u, N^ϕ	interpolation functions for displacement and microrotation vectors	
$n^{(e)}$	number of nodes per element	
n_{el}	number of elements	
n_{int}	number of integration points per element	
$[\underset{\sim}{\mathbf{N}}^{(e)}]$	vector of element shape functions	
p_e	order of interpolation function	
$[\underset{\sim}{\mathbf{q}}]$, ${}^u\underset{\sim}{\mathbf{q}}$, ${}^\phi\underset{\sim}{\mathbf{q}}$ ..	generalized force and moment, force, moment vectors	N, N mm
$[\underset{\sim}{\mathbf{r}}]$, ${}^u\underset{\sim}{\mathbf{r}}$, ${}^\phi\underset{\sim}{\mathbf{r}}$ ...	residual generalized force and moment, force, moment vectors	N, N mm
$[\underset{\sim}{\mathbf{U}}^{(e)}_{\text{global}}]$,	generalized nodal displacement and rotation vector	
$[\underset{\sim}{\mathbf{U}}^{(e)}_{\text{local}}]$	in global and local coordinate system of element (e)	mm, rad
w_p	weighting factor of integration point p	
$[\underset{\sim}{\mathbf{y}}]$	generalized displacement and microrotation vector or solution vector	mm, rad
ϑ	perturbation factor for perturbing the solution vector	
$\underset{\sim}{\boldsymbol{\xi}}$	coordinate vector of element parent domain	
Ω, $\Omega^{(e)}_\xi$	computation and element parent domains	

Acronyms

2D	two-dimensional (or two dimensions)
3D	three-dimensional (or three dimensions)
AM	additive manufacturing
BCC	body centered cubic
BCCCP	body centered cubic reinforced by primitive cubic
BVP	boundary-value problem
CC	continuum based on classical elasticity theory
CET	classical elasticity theory
CST	couple stress theory
DOF	degree of freedom
FEM	Finite Element Method
LSD	left hand-side definition of stress components
MC	micropolar continuum
MEC	micropolar elastic constant
MPBC	midpoint or origin of base cell
PC	primitive cubic
PK	Piola-Kirchhoff
PO	primitive orthorhombic
RSD	right hand-side definition of stress components
SDV	user-defined solution-dependent state variable
UEL	ABAQUS user element
UMAT	ABAQUS user material

Chapter 1

Introduction

1.1 Motivation

The ongoing process of weight reduction for improving the performance of structures in various engineering applications is a constant challenge for lightweight design encompassing designs, materials, and manufacturing processes. Over the past decades, advances in all three disciplines have significantly contributed to the development of so-called lattice materials. Lattice materials consist of a combination of one or more materials arranged in a predefined arrangement on a much smaller scale, namely, the microscopic scale. Hence, their mechanical properties depend not only on the combination of the materials used, but also on the structural configuration at the microscale, i.e., the microstructure. For periodic arrangements of base cells, which are the smallest geometric unit on the microscale that can be used to represent the lattice by periodic arrangement in all spatial directions, the microstructure acts as a main contributor to the mechanical properties on the macroscopic scale [38]. On the basis of this knowledge and progressing additive manufacturing (AM) techniques, e.g., [60, 70], the chance of designing man-tailored structures comes up to meet desired properties. Superior mechanical properties can be achieved in terms of stiffness-to-density ratios [91], strength-to-density ratios, auxeticity [11], energy-absorbing capabilities [87], and much more, see, e.g., [31]. Hence, lattice materials are becoming increasingly important in a wide range of advanced biomedical and aerospace applications, such as patient-specific medical implants [84] and multifunctional sandwich panels [12], respectively. Applications based on lattice materials cover various length scales, ranging from dimensions of micrometers to meters, such as microlattice materials [45, 81, 87] and composite lattice materials [50], respectively. Lattice materials have already been manufactured on the nanoscale, e.g., [94]. Based on the differences in length scale between the macroscopic deformations and the microstructure one distinguishes sometimes between *lattice materials* and *lattice structures*, see, e.g., [85]. No differentiation is made in this work and the terms are used synonymously.

The high strength-to-density ratio of lattice structures is of special interest in lightweight design applications. To further exploit their weight-saving potential, slender lattice structures can be used. However, slender lattice structures are prone to structural instabilities when exposed to compressive stress states, which may be caused by both tensile and compressive overall loading conditions. The compressive strength of these materials is governed by the buckling load rather than the strength of the parent material [67]. The resistance to buckling is determined by various parameters, such as macroscopic dimensions, microstructure, boundary conditions, free edges, and deviations from the originally intended perfect design known as imperfections. Additionally, these parameters influence the resulting deformations on both the microscopic and the macro-

scopic scale once the critical buckling load is exceeded. The resulting buckling modes with wavelengths as small as the microstructure are referred to as local instabilities while those close to the overall dimension of the lattice structure are designated as global instabilities. For lattice structures manufactured by AM, imperfections based on the manufacturing process are likely to occur. Common manufacturing imperfections are deviations from the originally intended geometry and a poor distribution of material, e.g., [99]. Even small deviations can change the overall structural behavior of the lattice structure, making buckling more likely and undermining its functionality in service. Independent of whether buckling is intended to be avoided in engineering applications, e.g., [51], or to be exploited, e.g., [52], appropriate descriptive models are necessary to properly predict the structural behavior of lattice structures. To achieve safety-related reliability for their utilization, detailed information about local mechanisms, such as local nonlinear deformations is necessary. For this purpose, numerical modeling by means of the Finite Element Method (FEM) is often employed. This can save both time and cost in the development process of such materials and components made out of them.

Discrete FEM models of lattice materials, i.e., models explicitly resolving each lattice member by finite elements, may be the first choice to predict the mechanical response of such materials. The lattice members can be discretized by either using solid elements, e.g., [57], or using structural elements, such as beam elements, e.g., [59]. However, for finite-sized lattice structures comprised of a large number of base cells, FEM simulations of such models may show high computational effort, especially when considering the aforementioned buckling nonlinearities. Furthermore, as pre-processing is one of the most time-consuming steps for structural engineers conducting FEM simulations [14], discrete modeling approaches are disadvantageous compared to other modeling strategies such as continuum modeling.

To address the drawbacks of discrete models, one may prefer to treat the internal architecture as an effective, or homogenized, material. For this purpose, an appropriate constitutive law is required that shows the same effective mechanical response as the discrete structure. As long as the base cell is far smaller than the macroscopic dimensions of the lattice, i.e., the separation of scales is satisfied, the classical elasticity theory (CET), or Cauchy continuum theory, is applicable for describing the effective response of the lattice structure. Various first-order homogenization approaches are available to determine the corresponding effective material moduli for the CET continuum, see [3] for an overview. Once the macroscopic dimensions of the lattice structure and the size of its microstructure are of the same order of magnitude, i.e., the separation of scales is not satisfied, the CET continuum is no longer able to capture the effective response properly. Size effects start to play an important role, e.g., [54, 97], which are directly related to the size of the microstructure with respect to the macroscopic dimensions of the sample. This also holds true for cases where local instabilities occur as observed, e.g., in the formation of crush bands [74, 77]. To account for these phenomena, generalized continuum models can be used to introduce an additional length scale into the constitutive laws. Various generalized continuum theories are available in the literature, see, e.g., [32, 33, 73] for an overview.

Which of these theories is best suited for serving as an appropriate descriptive model depends mainly on the deformation mechanisms of the microstructure. To decide which deformation mechanism dominates the mechanical response, it is of interest whether the response is governed by stretching or bending of the lattice members, i.e., stretching-dominated and bending-dominated lattice materials are distinguished, e.g. [5, 20]. The deformation of the lattice members of slender rigid-jointed lattice materials can either be stretching- or bending-dominated depending various parameters, such as the geometry of the base cell. However, due to their slenderness their deformation behavior is characterized by both displacements and rotations as independent fields. Consequently, the modeling of such lattice materials in terms of continuum theory asks for generalized theories capable of accounting for both fields independently. The micropolar field theory is

such a theory and may serve as the basis for an appropriate descriptive model [73]. This theory is used in the present work.

The capability of micropolar continuum modeling for reasonably predicting the buckling and postbuckling behavior of finite-sized slender lattice structures by means of the FEM is investigated in the present work. For lattice structures, the challenge is to account for both global and local structural instabilities caused by certain loading conditions. For micropolar continuum modeling, this means that both large displacements and finite rotations as well as finite strains on the macroscale need to be considered, respectively. The macroscopic finite strains are governed by large displacements or finite rotations within the microstructure rather than by material nonlinearities of the parent material, such as plasticity and damage. To deal with the complexity of the nonlinearities present in micropolar continuum modeling of lattice structures, a descriptive model capable of handling the mechanical response in the linear regime is sought for and investigated in a first step. Based on these insights, the micropolar continuum model is extended to account for large displacements and finite rotations while remaining within the small strain regime. Therefore, the model shall allow to capture global instabilities. Once the critical global load is reached, the postbuckling behavior can be studied. The capability of the model to capture local instabilities without explicitly considering finite strains is of further interest in the present work.

1.2 State of the art

The approaches in the literature for modeling lattice structures using the FEM are quite extensive. For the sake of brevity, the focus is set on continuum modeling approaches and, in particular, on micropolar continuum modeling, which is the approach aimed for in the present thesis. Various other continuum approaches can be found in the literature, see, e.g., [95], and some of them are briefly outlined to provide a brief overview of the various types of models.

The constitutive laws necessary for describing the effective mechanical response of lattice materials are often based on a strain energy functional derived via various homogenization techniques exploiting different continuum theories. Which approach is well-suited for a particular lattice is mainly determined by the local deformation mechanisms, which can be roughly divided into stretching- and bending-dominated ones [5, 20].

Models accounting for stretching-dominated, or pin-jointed, periodic networks is addressed, e.g., in [76] using CET and in [19, 21] using second gradient theory. These models have in common that the strain energy contribution of angle changes between lattice members is described via the displacement field rather than introducing independent rotational degrees of freedom (DOFs) as is the case for micropolar continua. In [76], the effective constitutive response of a pin-jointed honeycomb is derived based on the potential energy functional of a base cell accounting for the local snap-through mechanism. Stretching-dominated diamond, and triangular lattices are used to study the capability of the model presented in [21], which accounts for localized deformation, such as plasticized lattice members. Pantographic lattices, which consist of two families of beams connected by pin joints that allow relative motion at the expense of some deformation energy, are the basis for the model presented in [19] to describe the deformations of such lattices. In [39], the buckling modes of pantographic lattices are further investigated using a similar model.

Continuum modeling of bending-dominated, or rigid-jointed, lattice materials are addressed, e.g., in [63, 64] employing CET, in [16, 42, 53, 86] using micropolar continuum theory, in [40, 41] making use of second gradient theory, and in [13] using a micromorphic continuum model. Beam-like lattice structures subjected to large deformations are the basis for evaluating the model presented in [63]. This model accounts for the underlying small-scale deformation mechanisms based on a strain energy functional that is set up by a finite

set of assumed local deformation modes of the corresponding discrete lattice without resorting to micropolar elasticity. The investigations are based on large planar structures consisting of only a small number of base cells. In [64], the model is extended to account for elasto-plastic material behavior. The multiscale modeling technique presented in [40] is a second gradient model accounting for both translational and rotational DOFs at the macroscale and allows numerically efficient modeling of inhomogeneous deformation states on the macroscale. It is a compromise between computational homogenization methods (FE2), where the deformation state of a representative volume element is solved numerically, and analytical methods. In [41], the model was extended to three dimensions (3D) to study, e.g., the bending-dominated bitruncated octahedron lattice.

Other concepts of continuum modeling include multiscale approaches, e.g., in [92, 93], quasicontinuum methods, e.g., in [78], and substructuring approaches, e.g., in [49]. In [93], local buckling modes of bending-dominated lattices are accounted for via a FE2 approach, which allows for a nonlinear constitutive model at the macroscale. The quasicontinuum model in [78] with the focus set on computational efficiency accounts for geometrically nonlinear deformations at the microscale and is well-suited for stretching-dominated lattices. Substructuring is used in [49] to investigate the buckling of large structures. The micromorphic model presented in [90] is able to capture local and global buckling of a pattern-transforming metamaterial.

The majority of the more sophisticated models mentioned, such as [40, 41, 78, 90], are considered to be too complex for a straightforward implementation, either in terms of the homogenization approach or the technical realization. Therefore, this work focuses on micropolar continuum modeling for the following reasons. On the one hand, it has already been shown in the literature that micropolar continuum models are able to capture local deformation mechanisms related to the microscale. They allow, e.g., modeling shear localization in two-dimensional (2D) granular media [74]. On the other hand, it is well-suited also for lattice materials showing bending-dominated behavior at the microscale [73]. Furthermore, micropolar modeling of lattice materials is widely used in the literature, e.g., in [15, 16, 53, 86, 97] for 2D and in [18, 23] for 3D lattices.

To study lattice materials with micropolar continuum models, a suitable homogenization method is required to obtain the effective material, i.e., the corresponding micropolar elastic constants (MECs) required for the constitutive relations. Various methods are available in the literature, such as energy-based methods, e.g., in [15, 36, 53], methods based on structural analysis of the base cell, e.g., in [96], and asymptotic homogenization methods, e.g., in [22, 42] for linear and in [24, 25] for nonlinear deformations, respectively. With the exception of [24, 25], these methods are only suitable to account for the linear elastic response and have been employed mainly to study 2D lattices. For studying 3D lattices with micropolar models, there are only a few contributions in the literature. Linear modeling has been used, e.g., in [23] to study a 3D chiral lattice and in [18] to give insight into the mechanical couplings in the constitutive relations predicted by the so-called decoupled micropolar elasticity theory presented therein. Models must be able to account for large deformations to study buckling, i.e., geometrically nonlinear models are required.

Geometrically nonlinear models based on continuum elements have been presented in [8, 9, 44, 69, 74] considering isotropic materials and in [69] even for transversally isotropic materials. All these models account for 3D, except the model in [74], which investigates shear localization in 2D granular media considering a hypoplastic constitutive law. Models based on micropolar beam theory can be found in [56, 75], where size-dependence in isotropic materials is considered in [75], and buckling of 3D chiral column lattices is studied in [56]. However, the beam element based models are inferior to the continuum element based models in terms of a broader range of applications, which is why the latter are of interest in this work. Continuum element based models must be considered mathematically intricate for deriving the tangent stiffness matrix. Therefore, a central finite difference scheme to numerically evaluate the tangent stiffness matrix [8] is used in the present thesis.

To properly capture the deformation mechanisms for large deformations even at the microscale, a suitable homogenization method is required, such as the nonlinear asymptotic homogenization method presented in [24]. However, the nonlinear behavior at the microscale in conjunction with a geometrically nonlinear model must be considered as very complex for the implementation in a FEM framework. Therefore, linear elastic material behavior is considered in the first place. The energy-based homogenization methods, such as the ones presented in [10, 36, 53], are considered to be suitable for determining the corresponding MECs. For the sake of simplicity, the homogenization approach presented for 2D models in [10, 53] is used and extended to 3D accordingly. To the best of the author's knowledge, micropolar modeling of lattice materials using a continuum element based formulation in 3D undergoing large deformations but staying within the linear strain regime has not been presented in the literature before.

1.3 Scope of present work

The overall aim of the present thesis is to set up a framework by means of the FEM for studying 3D beams made out of lattice materials, in the following denoted as lattice beams, under global compressive loading within the context of continuum modeling. For this purpose, the micropolar continuum theory is employed, which is well-suited for bending-dominated slender lattices and allows for a more relaxed separation of scales compared to the CET continuum. To study 3D lattices in the context of micropolar continuum modeling, the corresponding MECs need to be determined. These constants are in general not available in the literature and are derived for various lattice types based on the homogenization method presented in [10, 53]. This method yields two different sets of MECs for the same lattice type, based on the assumptions made during the derivation. This has caused an ongoing debate in the literature. To decide which set is to be used for the 3D lattices, a numerical study is carried out on the basis of 2D lattices. To verify the MECs obtained for the 3D lattices, a comparison is made between continuum and discrete lattice models. Slender lattice beams undergoing large displacements and rotations under global compressive loading, require geometrically nonlinear micropolar continuum models. Therefore, the geometrically nonlinear micropolar model presented in [8] is implemented in ABAQUS with some modifications based on [44]. The geometrically nonlinear micropolar continuum is verified against benchmark examples taken from literature. Within the scope of the present thesis, only the linear strain regime is considered. Otherwise, nonlinear homogenization methods are needed.

1.4 Outline of the thesis

In Chapter 2 the micropolar continuum theory necessary to set up a boundary-value problem (BVP) is presented. The stress and strain measures as well as the constitutive laws used for the FEM implementation presented in Chapter 4 are introduced.

Chapter 3 focuses on the homogenization method used to derive the MECs of lattice structures for an equivalent micropolar continuum. These constants are derived for the primitive orthorhombic (PO), the body centered cubic (BCC), and the body centered cubic reinforced by primitive cubic (BCCCP) lattices. Additionally, the controversy that the method has caused in the literature is addressed, and a numerical study based on 2D lattices is proposed to contribute to the discussion.

In Chapter 4 the FEM implementations are outlined, where two different FEM frameworks are used, namely, ABAQUS and NGSolve. Implementations in two and three dimensions are presented for the linear micropolar

continuum using both frameworks. Additionally, the implementation of the 3D geometrically nonlinear micropolar continuum in ABAQUS is outlined.

Chapters 5, 6, and 7 cover the numerical applications. Chapter 5 outlines the numerical study proposed in Chapter 3 to contribute to the discussion on the controversially disputed homogenization method. To verify the MECs derived for the 3D lattices presented in Chapter 3, a comparison is made between continuum and discrete lattice models for various load cases presented in Chapter 6. In Chapter 7, the geometrically nonlinear micropolar continuum is verified against benchmark examples taken from literature and the chapter is closed by studying the capabilities of the geometrically nonlinear micropolar continuum to account for slender lattice beams under global compressive loadings.

Finally, Chapter 8 summarizes the results and gives a brief outlook on future work.

Chapter 2

Micropolar theory

In the following, the micropolar continuum is introduced within the generalized mechanical continuum theory. The kinematics and kinetics resulting from the additional DOFs compared to CET are presented. The equations of motion and boundary conditions to set up a BVP as well as constitutive laws for micropolar continua are introduced. From the defined nonlinear strain measures, the corresponding measures of the linear micropolar continuum are derived. The presented micropolar theory mainly follows [28]. This also applies to the notation used to represent the physical quantities. No proofs or derivations are provided for the various equations given, which have already been outlined in [28] as well as in various other works. Only the equations necessary for the implementation in Chapter 4 are presented.

2.1 Classification of micropolar continua

Following the classification of generalized mechanical continuum theories proposed in [32], the micropolar continuum is introduced. The classification is shown in Figure 2.1. For any continuous media $\mathcal{B}$, it distinguishes between continua that do or do not satisfy the principle of local action. The principle of local action states that the mechanical state at each material point or particle, $\mathcal{P}$, of $\mathcal{B}$ is uniquely determined by an arbitrary small neighborhood of $\mathcal{P}$ [89]. Media that do not satisfy this principle are called nonlocal and are using an integral formulation for the constitutive equations, e.g., [29]. In [62], models describing this type of media are summarized as *strongly nonlocal*. Media satisfying the principle of local action, are further classified into simple and non-simple media. According to [32], for simple media, the response at $\mathcal{P}$ of $\mathcal{B}$ to deformations homogeneous in a neighborhood of $\mathcal{P}$ uniquely determines its response to every deformation at $\mathcal{P}$. The continuum based on the CET belongs to this kind of media. The non-simple media are subdivided into the classes of higher grade and higher order media. The material behaviour of higher grade media is sensitive to higher gradients of the displacement field, such as second or third order [65], or, even more generally, to higher gradients of some internal variables [61], e.g., variables describing the localization of damage. The material behaviour of higher order media is characterized by additional DOFs at each material point $\mathcal{P}$, which introduces internal length scales into the field theory [30]. The response of this kind of media depends on the ratio of the external characteristic length L to the internal or intrinsic characteristic length l, which is directly related to the microstructure of the media. The media shows size-dependent material behaviour. For this reason, the separation of length scales that applies to these media is more relaxed than within the CET, for which $L/l \gg 1$ must apply, otherwise the principle of local action is not satisfied [30]. Higher order media are sometimes called continua with microstructure.

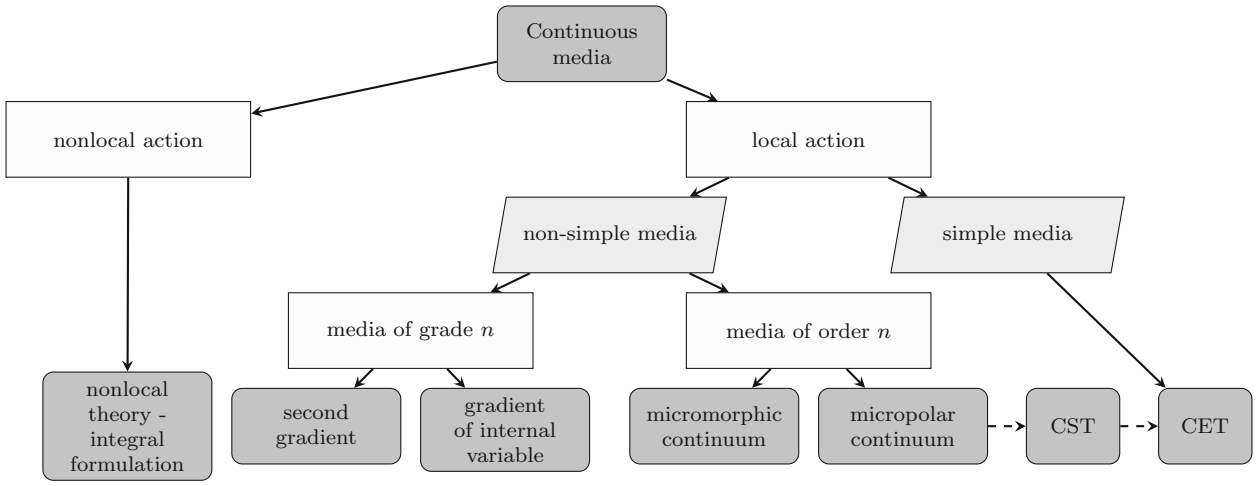

Figure 2.1: Flowchart showing the classification of generalized continua. Taken and modified from [32].

The simplest continuum belonging to this class is the *micropolar continuum* or COSSERAT continuum, which is characterized by three additional rotational DOFs in the form of a rigid triad attached to every $\mathcal{P}$. The mechanical foundation of this type of continuum has been mainly developed by ERINGEN and his co-workers based on the ideas of the COSSERAT brothers [17] and is summarized within the book of ERINGEN [30], including an overview of the historical background. If the rigid directors of the triad are replaced by stretchable ones without accounting for shear deformations, i.e., being constrained to have breathing-type microdeformations [30], the *microstretch media* is obtained showing four additional DOFs at each material point $\mathcal{P}$ compared to CET. If the directors additionally account for shear deformations, i.e., are fully deformable, the *micromorphic continuum* is obtained which is characterized by nine additional DOFs at $\mathcal{P}$ compared to CET. As a special case, the couple stress theory (CST) can be considered, e.g., [66], which exists somewhere between the micropolar continuum and the CET continuum. Its rotation field depends only on the displacement field, i.e., no additional DOFs are added. The classification proposed by [32] cannot be considered a complete picture, as there is a number of different other approaches and variations of the aforementioned approaches, e.g., the *relaxed linear micromorphic continuum* presented in [71]. However, it provides a good basis for classifying the micropolar continua. For the studies on continuum modeling of rigid-jointed lattice structures intended in this work, the micropolar continuum is considered to be an appropriate descriptive model [73]. Its theory is outlined in Sections 2.2 - 2.4.

2.2 Kinematics

Introduction. The micropolar theory belongs to the class of higher order theories. Compared to the CET, the translational or displacement DOFs are supplemented by independent rotational or orientational DOFs to describe the motion of its particles $\mathcal{P}$. Each particle's motion is defined by a position vector associated with the displacement DOFs and an attached rigid orthonormal trihedral associated with the rotational DOFs, see Figure 2.2.

Measures of deformation. The relative deformation of the continuum, which combines rigid body motions and changes in size and shape, is measured by introducing two configurations of $\mathcal{B}$ at two points in time, t_1 and t_2. At $t_1 = 0$ or another fixed point in time, the configuration is called *reference* or *material configuration*,

$\mathcal{R}_0$, while at time $t_2 = t$ it is called *current* or *spatial configuration*, $\mathcal{R}_t$. In general, it is distinguished between a *reference* and a *spatial frame of reference* given by the base vectors $\underline{\mathbf{E}}_I$ and $\underline{\mathbf{e}}_i$, respectively, where I and i denote the three spatial directions corresponding to the material and spatial frame of reference, respectively. For the sake of simplicity, both frames are assumed to remain equal during deformation as shown in Figure 2.2 and, thus, for tensorial quantities, no distinction is made between lower and upper case letters in the indices. In Figure 2.2, the position vectors are denoted by $\underline{\mathbf{X}}$ and $\underline{\mathbf{x}}$, while the directors or base vectors of the trihedral are denoted by $\underline{\mathbf{D}}_i$ and $\underline{\mathbf{d}}_i$, for the reference and current configurations, respectively. The vector fields describing the motion of $\mathcal{B}$ read

$$\underline{\mathbf{x}} = \underline{\mathbf{x}}(\underline{\mathbf{X}}, t) \quad , \quad \underline{\mathbf{d}}_i = \underline{\mathbf{d}}_i(\underline{\mathbf{X}}, t) \quad . \tag{2.1}$$

Since the directors $\underline{\mathbf{d}}_i$ of the trihedral remain orthonormal during the deformation process, the change of the directors from the reference to the current configuration can be described by a *proper orthogonal second order tensor*

$$\underset{\sim}{\mathbf{R}} = \underline{\mathbf{d}}_i \otimes \underline{\mathbf{D}}_i \quad , \quad R_{ij} = R_{ij}\underline{\mathbf{e}}_i \otimes \underline{\mathbf{E}}_j \quad , \tag{2.2}$$

$$\underline{\mathbf{d}}_i = \underset{\sim}{\mathbf{R}}\underline{\mathbf{D}}_i \tag{2.3}$$

which is called the *microrotation tensor*. The microrotation tensor as a *proper orthogonal second order tensor* shows the following properties

$$\underset{\sim}{\mathbf{R}}^{\mathrm{T}}\underset{\sim}{\mathbf{R}} = \underset{\sim}{\mathbf{I}} \quad , \quad \det(\underset{\sim}{\mathbf{R}}) = 1 \quad , \quad \underset{\sim}{\mathbf{R}}^{-1} = \underset{\sim}{\mathbf{R}}^{\mathrm{T}} \quad , \tag{2.4}$$

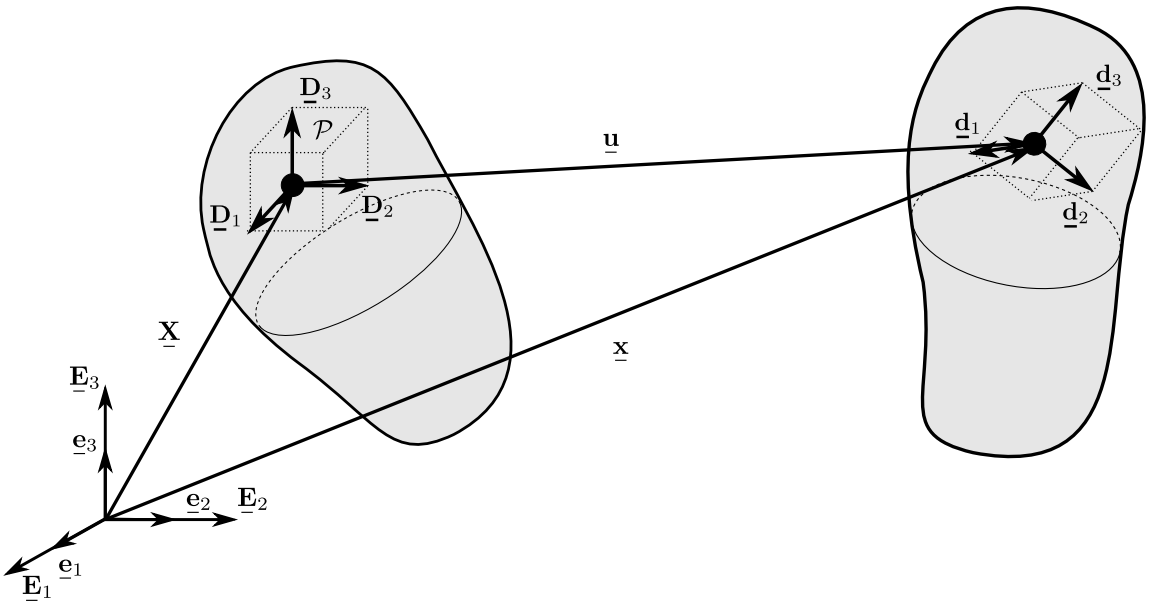

Figure 2.2: Deformation of a micropolar body $\mathcal{B}$ and particle $\mathcal{P}$ with displacement DOFs and attached rigid orthonormal trihedral associated with rotational DOFs.

and belongs to the so-called special orthogonal group or rotation group SO(3), i.e., $\underset{\sim}{\mathbf{R}} \in \mathrm{SO}(3)$. Any orthogonal second order tensor with property $\det(\underset{\sim}{\mathbf{R}}) = -1$ represents a pure reflection of the basis and does not belong to this group. It follows that Eq. (2.1) can be alternatively described by the relation

$$\begin{aligned} \underline{\mathbf{u}} = \underline{\mathbf{u}}(\underline{\mathbf{X}}, t) = \underline{\mathbf{x}}(\underline{\mathbf{X}}, t) - \underline{\mathbf{X}} \quad , \quad \underset{\sim}{\mathbf{R}} = \underset{\sim}{\mathbf{R}}(\underline{\mathbf{X}}, t) \quad , \\ u_i(X_j, t) = x_i(X_j, t) - X_i \quad , \end{aligned} \tag{2.5}$$

where the displacement vector, $\underline{\mathbf{u}}$, is used as an alternative to the position vector to describe the translational DOFs and the microrotation tensor, $\underset{\sim}{\mathbf{R}}$, is used to describe the rotational DOFs. The three components of the displacement vector $\underline{\mathbf{u}}$ are independent. In contrast, among the nine components of $\underset{\sim}{\mathbf{R}}$ only three are independent. The other six are constrained by the orthogonality conditions given in Eq. (2.4). This gives rise to the use of a parametrization of the rotation. There are many different ways to parameterize the rotation, which can roughly be divided into two classes, namely, *vectorial* and *non-vectorial parametrizations* [80], respectively. The vectorial parametrization uses three independent scalar parameters as Cartesian components of a generalized vector, such as various finite rotation vectors or exponential map parameters. The non-vectorial parametrization can either be composed of three scalar parameters, which cannot be treated as vector components, such as Euler angles, or expressed in terms of even more scalar parameters with additional constraints, such as quaternions or direction cosines.

In this work, a vectorial parametrization is employed that uses a finite rotation vector. Following [4], there exists a skew-symmetric second order tensor $\underset{\sim}{\mathbf{W}} = -\underset{\sim}{\mathbf{W}}^{\mathrm{T}}$ for every rotation allowing to express the rotation tensor as

$$\underset{\sim}{\mathbf{R}} = \exp(\underset{\sim}{\mathbf{W}}) = \sum_{n=0}^{\infty} \frac{\underset{\sim}{\mathbf{W}}^n}{n!} = \underset{\sim}{\mathbf{I}} + \underset{\sim}{\mathbf{W}} + \frac{\underset{\sim}{\mathbf{W}}^2}{2!} + \frac{\underset{\sim}{\mathbf{W}}^3}{3!} + \ldots \quad . \tag{2.6}$$

The skew-symmetric second order tensor, $\underset{\sim}{\mathbf{W}}$, allows the following relation for any arbitrary non-zero vector $\underline{\mathbf{c}}$ to be described by

$$\underset{\sim}{\mathbf{W}}\underline{\mathbf{c}} = \underline{\boldsymbol{\phi}} \times \underline{\mathbf{c}} \tag{2.7}$$

with $\underline{\boldsymbol{\phi}}$ being the axial vector of $\underset{\sim}{\mathbf{W}}$, namely,

$$\underline{\boldsymbol{\phi}} = \mathrm{axl}(\underset{\sim}{\mathbf{W}}) \tag{2.8}$$

The definition of $\mathrm{axl}(\cdot)$ is given in Eq. (A.20). The axial vector, $\underline{\boldsymbol{\phi}}$, is called the *microrotation vector*, if its corresponding skew-symmetric second order tensor $\underset{\sim}{\mathbf{W}}$ is related to the microrotation tensor $\underset{\sim}{\mathbf{R}}$. The microrotation vector is composed of a rotation axis $\underline{\boldsymbol{\phi}}/\|\underline{\boldsymbol{\phi}}\|$ and its rotation angle, $\|\underline{\boldsymbol{\phi}}\| = \sqrt{\underline{\boldsymbol{\phi}} \cdot \underline{\boldsymbol{\phi}}} = \Phi$. In [80], a closed-form expression of Eq. (2.6) is given as

$$\begin{aligned} \underset{\sim}{\mathbf{R}} = \cos(\|\underline{\boldsymbol{\phi}}\|)\underset{\sim}{\mathbf{I}} + \frac{1 - \cos(\|\underline{\boldsymbol{\phi}}\|)}{\|\underline{\boldsymbol{\phi}}\|^2}(\underline{\boldsymbol{\phi}} \otimes \underline{\boldsymbol{\phi}}) + \frac{\sin(\|\underline{\boldsymbol{\phi}}\|)}{\|\underline{\boldsymbol{\phi}}\|}\underline{\boldsymbol{\phi}} \times \underset{\sim}{\mathbf{I}} \quad , \\ R_{ij} = \cos(\Phi)\delta_{ij} + \frac{(1 - \cos(\Phi))}{\Phi^2}\phi_i\phi_j + \frac{\sin(\Phi)}{\Phi}\epsilon_{ikj}\phi_k \quad , \end{aligned} \tag{2.9}$$

where $\underline{\boldsymbol{\phi}} \times \underset{\sim}{\mathbf{I}}$ is equal to the skew-symmetric tensor of $\underline{\boldsymbol{\phi}}$, i.e., $\underset{\sim}{\mathbf{W}} = \underline{\boldsymbol{\phi}} \times \underset{\sim}{\mathbf{I}}$, see Appendix A for further information on skew-symmetric matrices.

Since the microrotation tensor, $\underset{\sim}{\mathbf{R}}$, can be expressed in terms of the microrotation vector, $\underline{\boldsymbol{\phi}}$, using Eq. (2.9), Eq. (2.5) can also be given as

$$\underline{\mathbf{x}} = \underline{\mathbf{x}}(\underline{\mathbf{X}}, t) \quad , \quad \underline{\boldsymbol{\phi}} = \underline{\boldsymbol{\phi}}(\underline{\mathbf{X}}, t) \quad . \tag{2.10}$$

For finite rotations, the non-commutativity and non-additivity of members of the SO(3) group need to be considered. In general, for a compound rotation of two rotations $\underset{\sim}{\mathbf{R}}_1$ and $\underset{\sim}{\mathbf{R}}_2$ the non-commutativity is expressed by

$$\underset{\sim}{\mathbf{R}}_1\underset{\sim}{\mathbf{R}}_2 \neq \underset{\sim}{\mathbf{R}}_2\underset{\sim}{\mathbf{R}}_1 \quad , \tag{2.11}$$

which means that a different order of consecutive rotations gives different results. This is true, unless the axes of rotation are parallel. The non-additivity of two consecutive rotations reads

$$\underset{\sim}{\mathbf{R}}_1 + \underset{\sim}{\mathbf{R}}_2 \neq \underset{\sim}{\mathbf{R}}_3 \quad , \qquad \underset{\sim}{\mathbf{R}}_1\underset{\sim}{\mathbf{R}}_2 = \underset{\sim}{\mathbf{R}}_3 \quad , \tag{2.12}$$

Deformation gradient tensor. For describing the deformation of a continuum, the relation between an infinitesimal *material line element* or *material tangent vector* $\mathrm{d}\underline{\mathbf{X}}$ in the reference configuration and an infinitesimal *spatial line element* or *spatial tangent vector* $\mathrm{d}\underline{\mathbf{x}}$ in the current configuration is associated with the two-point *deformation gradient tensor* defined as

$$\underset{\sim}{\mathbf{F}} = \mathrm{Grad}_{\mathrm{R}}(\underline{\mathbf{x}}) = \underline{\mathbf{x}} \otimes \underline{\boldsymbol{\nabla}}_X = \frac{\partial x_i}{\partial X_j}\underline{\mathbf{e}}_i \otimes \underline{\mathbf{E}}_j = F_{ij}\underline{\mathbf{e}}_i \otimes \underline{\mathbf{E}}_j = \begin{bmatrix} \frac{\partial x_1}{\partial X_1} & \frac{\partial x_1}{\partial X_2} & \frac{\partial x_1}{\partial X_3} \\ \frac{\partial x_2}{\partial X_1} & \frac{\partial x_2}{\partial X_2} & \frac{\partial x_2}{\partial X_3} \\ \frac{\partial x_3}{\partial X_1} & \frac{\partial x_3}{\partial X_2} & \frac{\partial x_3}{\partial X_3} \end{bmatrix} \quad , \tag{2.13}$$

$$F_{ij} = u_i\nabla_j + \delta_{ij} \quad ,$$

which allows for the map $\mathrm{d}\underline{\mathbf{x}} = \underset{\sim}{\mathbf{F}}(\underline{\mathbf{X}}, t)\mathrm{d}\underline{\mathbf{X}}$. The deformation process is assumed to be invertible such that $\mathrm{d}\underline{\mathbf{X}} = \underset{\sim}{\mathbf{F}}^{-1}(\underline{\mathbf{x}}, t)\mathrm{d}\underline{\mathbf{x}}$ holds true, where $\underset{\sim}{\mathbf{F}}^{-1}$ is the inverse of the deformation gradient tensor. This implies $J = \det(\underset{\sim}{\mathbf{F}}) \neq 0$.

The deformation gradient tensor can further be used to transform any infinitesimal material surface element $\mathrm{d}\underline{\mathbf{S}} = \underline{\mathbf{N}}\mathrm{d}S$ and material volume element $\mathrm{d}V$ from the reference to the current configuration via

$$\mathrm{d}\underline{\mathbf{s}} = J(\underline{\mathbf{X}}, t)\underset{\sim}{\mathbf{F}}(\underline{\mathbf{X}}, t)^{-\mathrm{T}}\mathrm{d}\underline{\mathbf{S}} \quad , \tag{2.14}$$

$$\mathrm{d}v = J(\underline{\mathbf{X}}, t)\mathrm{d}V \quad , \tag{2.15}$$

where $\mathrm{d}\underline{\mathbf{s}} = \underline{\mathbf{n}}\mathrm{d}s$ denotes the spatial surface element and $\mathrm{d}v$ is the spatial volume element. The surface normals $\underline{\mathbf{N}}$ and $\underline{\mathbf{n}}$ are defined with respect to the reference and current configuration, respectively. From Eq. (2.15), it follows that $J > 0$ for physical reasons, i.e., the impenetrability of matter. From the conservation of mass follows $J = \rho_0/\rho_t$, where ρ_0 and ρ_t are the densities corresponding to the reference and current configuration, respectively.

Macrorotation tensor. For the micropolar continuum, the polar decomposition of the deformation gradient tensor into stretch and rigid body rotation tensors, as known for the CET, can be extended. A diagram considering all the splits possible for this continuum is presented in [69]. Based on the fact that the microrotation tensor defines the orientation of the particles, cf. Eq. (2.2), it is shown in [69], that the microrotation tensor is the reason for the micropolar nature of the problem but does not describe the micropolar mechanical response. This is based on the fact that the microrotation tensor is composed of the macrorotation field described by $\underset{\sim}{\mathbf{R}}^{\mathrm{mac}}$ and an additional field denoted by $\underset{\sim}{\mathbf{R}}^{\mathrm{eff}}$ given as

$$\underset{\sim}{\mathbf{R}} = \underset{\sim}{\mathbf{R}}^{\mathrm{mac}}\left(\underset{\sim}{\mathbf{R}}^{\mathrm{eff}}\right)^{\mathrm{T}} \quad . \tag{2.16}$$

Due to the nature of the macrorotation tensor representing a rigid body rotation, the effect is solely based on the additional field, $\underset{\sim}{\mathbf{R}}^{\mathrm{eff}}$, which will further be called *effective rotation field*. The macrorotation tensor can be derived from the polar decomposition of the deformation gradient tensor into a (macro)rotation tensor and a stretch tensor based on the CET continuum, see, e.g., [48]. With the macrorotation at hand, the effective rotation field is obtained via rearranging Eq. (2.16) as

$$\underset{\sim}{\mathbf{R}}^{\mathrm{eff}} = \underset{\sim}{\mathbf{R}}^{\mathrm{T}} \underset{\sim}{\mathbf{R}}^{\mathrm{mac}} \quad . \tag{2.17}$$

Strain measures. The deformation gradient tensor, $\underset{\sim}{\mathbf{F}}$, is not appropriate for describing the local changes in size and shape as it additionally contains local rigid body rotations. This also holds true for the microrotation tensor, $\underset{\sim}{\mathbf{R}}$, describing the changes in orientation. Therefore, it is necessary to define proper measures to describe the deformations due to stretching and curvature changes in the form of second order tensors, which are further referred to as strain measures. For the nonlinear micropolar continuum, the strain measures for stretches and changes of orientations can be defined on the basis of different methods. In [79], the strain measures are introduced via three methods, namely, via a geometrical approach, as work-conjugates of the corresponding stress measures based on the local equilibrium equations, and via the principle of material frame-indifference of the strain energy potential. It is shown that the same strain measures can be obtained with all three methods. The introduced strain measures account for unrestricted translations, stretches, and changes of orientations of the micropolar body $\mathcal{B}$. These measures are used in this work. In the literature, various other measures have been proposed. For an overview see [79].

In [79], the strain measures for stretches and changes of orientations of $\mathcal{B}$ with respect to the reference configuration are called the *relative Lagrangian stretch tensor*, $\underset{\sim}{\mathbf{E}}$, and *relative Lagrangian wryness tensors*, $\underset{\sim}{\boldsymbol{\mathscr{K}}}$, and are defined as

$$\begin{aligned}
\underset{\sim}{\mathbf{E}} &= \underset{\sim}{\mathbf{R}}^{\mathrm{T}} \underset{\sim}{\mathbf{F}} - \underset{\sim}{\mathbf{I}} \quad , && (2.18)\\
E_{ij} &= R_{ki} F_{kj} - \delta_{ij} \quad ,\\
\underset{\sim}{\boldsymbol{\mathscr{K}}} &= \operatorname{axl}(\underset{\sim}{\mathbf{R}}^{\mathrm{T}} \frac{\partial \underset{\sim}{\mathbf{R}}}{\partial X_k}) \otimes \underline{\mathbf{E}}_k = -\frac{1}{2} \underset{\cong}{\boldsymbol{\epsilon}} : (\underset{\sim}{\mathbf{R}}^{\mathrm{T}} \cdot \operatorname{Grad}_{\mathrm{R}}(\underset{\sim}{\mathbf{R}})) = -\frac{1}{2} \underset{\cong}{\boldsymbol{\epsilon}} : \underset{\sim}{\boldsymbol{\Gamma}} \quad , && (2.19)\\
\mathscr{K}_{ij} &= -\frac{1}{2} \epsilon_{ikl} \Gamma_{klj} \quad \text{with} \quad \Gamma_{klj} = R_{mk} R_{ml} \nabla_j\\
&= \frac{1}{2} \epsilon_{ikm} R_{lm} R_{lk,j} \quad \text{with} \quad R_{lk,j} = R_{lk} \nabla_j \quad ,
\end{aligned}$$

respectively, where $\underset{\sim}{\mathbf{R}}$ is the microrotation tensor given in Eq. (2.9), $\underset{\sim}{\mathbf{F}}$ denotes the deformation gradient tensor given in Eq. (2.13), and $\underset{\cong}{\boldsymbol{\epsilon}}$ is the Levi-Civita tensor of third order, cf. Eq. (A.1). The corresponding strain measures with respect to the current configuration are called *relative Eulerian stretch tensor* and *relative Eulerian wryness tensor* and are defined as [79]

$$\begin{aligned}
\underset{\sim}{\mathbf{e}} &= \underset{\sim}{\mathbf{I}} - \underset{\sim}{\mathbf{R}} \underset{\sim}{\mathbf{F}}^{-1} \quad , && (2.20)\\
e_{ij} &= \delta_{ij} - R_{ik} F^{-1}_{kj} \quad ,\\
\underset{\sim}{\boldsymbol{\mathscr{k}}} &= -\frac{1}{2} \underset{\sim}{\mathbf{R}} \underset{\cong}{\boldsymbol{\epsilon}} : (\underset{\sim}{\mathbf{R}}^{\mathrm{T}} \cdot \operatorname{grad}_{\mathrm{R}}(\underset{\sim}{\mathbf{R}})) \quad , && (2.21)\\
\mathscr{k}_{ij} &= -\frac{1}{2} R_{ik} \gamma_{kj} \quad \text{with} \quad \gamma_{kj} = \epsilon_{klm} \Gamma_{lmj}\\
&= -\frac{1}{2} R_{ik} \epsilon_{knm} R_{lm} R_{ln,j} \quad ,
\end{aligned}$$

respectively. In [79], the relations between the Lagrangian and Eulerian strain measures are given as

$$\underset{\sim}{\mathbf{e}} = \underset{\sim}{\mathbf{R}}\underset{\sim}{\mathbf{E}}\underset{\sim}{\mathbf{F}}^{-1} \quad , \quad \underset{\sim}{\boldsymbol{\mathcal{k}}} = \underset{\sim}{\mathbf{R}}\underset{\sim}{\boldsymbol{\mathcal{K}}}\underset{\sim}{\mathbf{F}}^{-1} \quad , \tag{2.22}$$

$$\underset{\sim}{\mathbf{E}} = \underset{\sim}{\mathbf{R}}^{\mathrm{T}}\underset{\sim}{\mathbf{e}}\underset{\sim}{\mathbf{F}} \quad , \quad \underset{\sim}{\boldsymbol{\mathcal{K}}} = \underset{\sim}{\mathbf{R}}^{\mathrm{T}}\underset{\sim}{\boldsymbol{\mathcal{k}}}\underset{\sim}{\mathbf{F}} \quad . \tag{2.23}$$

The most important properties of these strain measures are [79],

- For the absence of any deformation or mere rigid body translations, i.e., $\underset{\sim}{\mathbf{F}} = \underset{\sim}{\mathbf{R}} = \underset{\sim}{\mathbf{I}}$, the measures vanish. Therefore, these measures are also called *natural* or being of *relative type*.
- For any rigid body deformations of $\mathcal{B}$, i.e., $\underline{\mathbf{x}} = \underset{\sim}{\mathbf{R}}\underline{\mathbf{X}} + \underline{\mathbf{a}}$ and $\underline{\mathbf{d}}_i = \underset{\sim}{\mathbf{R}}\underline{\mathbf{D}}_i$, where $\underline{\mathbf{a}}$ denotes a constant displacement and $\underset{\sim}{\mathbf{R}}$ represents a proper orthogonal tensor, the measures vanish as well.
- In general, the measures are non-symmetric, i.e., $\underset{\sim}{\mathbf{E}} \neq \underset{\sim}{\mathbf{E}}^{\mathrm{T}}$ and $\underset{\sim}{\boldsymbol{\mathcal{K}}} \neq \underset{\sim}{\boldsymbol{\mathcal{K}}}^{\mathrm{T}}$ as well as $\underset{\sim}{\mathbf{e}} \neq \underset{\sim}{\mathbf{e}}^{\mathrm{T}}$ and $\underset{\sim}{\boldsymbol{\mathcal{k}}} \neq \underset{\sim}{\boldsymbol{\mathcal{k}}}^{\mathrm{T}}$.

For further details see [79]. For infinitesimal or small displacements and rotations, i.e.,

$$\|\underline{\mathbf{u}}\| \ll 1 \quad , \quad \|\mathrm{Grad}_{\mathrm{R}}(\underline{\mathbf{u}})\| \ll 1 \quad , \quad \|\underline{\boldsymbol{\phi}}\| \ll 1 \quad , \quad \text{and} \quad \|\mathrm{Grad}_{\mathrm{R}}(\underline{\boldsymbol{\phi}})\| \ll 1 \quad , \tag{2.24}$$

the strain measures associated with the linear micropolar continuum theory are obtained. The microrotation tensor given in Eq.(2.9) takes the form

$$\underset{\sim}{\mathbf{R}} \approx \underset{\sim}{\mathbf{I}} + \underline{\boldsymbol{\phi}} \times \underset{\sim}{\mathbf{I}} \quad , \tag{2.25}$$

with the geometrically linearized trigonometric functions $\sin\|\underline{\boldsymbol{\phi}}\| \approx \|\underline{\boldsymbol{\phi}}\|$ and $\cos\|\underline{\boldsymbol{\phi}}\| \approx 1$, see, e.g., [80]. The linear strain measures are then obtained from Eqs. (2.18) and (2.19) or Eqs. (2.20) and (2.21) using Eq. (2.25) as

$$\underset{\sim}{\boldsymbol{\varepsilon}} = \mathrm{Grad}_{\mathrm{R}}(\underline{\mathbf{u}}) - \underline{\boldsymbol{\phi}} \times \underset{\sim}{\mathbf{I}} = \underline{\mathbf{u}} \otimes \underline{\boldsymbol{\nabla}} - \underline{\boldsymbol{\phi}} \times \underset{\sim}{\mathbf{I}} \quad , \quad \varepsilon_{ij} = u_{i,j} + \epsilon_{ijk}\phi_k \quad , \tag{2.26}$$

$$\underset{\sim}{\boldsymbol{\kappa}} = \mathrm{Grad}_{\mathrm{R}}(\underline{\boldsymbol{\phi}}) = \underline{\boldsymbol{\phi}} \otimes \underline{\boldsymbol{\nabla}} \quad , \quad \kappa_{ij} = \phi_{i,j} \quad , \tag{2.27}$$

where $\underset{\sim}{\boldsymbol{\varepsilon}}$ and $\underset{\sim}{\boldsymbol{\kappa}}$ will further be called *strain tensor* and *curvature tensor*, respectively. These measures can also be found, e.g., in [44], but can also be defined by applying the gradient from the left to the kinematic fields with appropriate consideration of the microrotations, see, e.g., [47, 53]. This leads to

$$\hat{\underset{\sim}{\boldsymbol{\varepsilon}}} = \mathrm{Grad}_{\mathrm{L}}(\underline{\mathbf{u}}) + \underline{\boldsymbol{\phi}} \times \underset{\sim}{\mathbf{I}} = \underline{\boldsymbol{\nabla}} \otimes \underline{\mathbf{u}} + \underline{\boldsymbol{\phi}} \times \underset{\sim}{\mathbf{I}} \quad , \quad \hat{\varepsilon}_{ij} = u_{j,i} - \epsilon_{ijk}\phi_k \quad , \tag{2.28}$$

$$\hat{\underset{\sim}{\boldsymbol{\kappa}}} = \mathrm{Grad}_{\mathrm{L}}(\underline{\boldsymbol{\phi}}) = \underline{\boldsymbol{\nabla}} \otimes \underline{\boldsymbol{\phi}} \quad , \quad \hat{\kappa}_{ij} = \phi_{j,i} \quad . \tag{2.29}$$

Note that the relation $\underset{\sim}{\boldsymbol{\varepsilon}} = \hat{\underset{\sim}{\boldsymbol{\varepsilon}}}^{\mathrm{T}}$ and $\underset{\sim}{\boldsymbol{\kappa}} = \hat{\underset{\sim}{\boldsymbol{\kappa}}}^{\mathrm{T}}$ hold true. There are also mixed definitions, e.g., in [30], where the gradient is applied to the displacement field from the left and to the rotation field from the right. For infinitesimal displacements and rotations, it further follows that $\underline{\mathbf{X}} \approx \underline{\mathbf{x}}$ and $\mathrm{Grad}_{\mathrm{R}}(\underline{\mathbf{u}}) \approx \mathrm{grad}_{\mathrm{R}}(\underline{\mathbf{u}})$, see, e.g., [28], which leads to the following relation

$$\underset{\sim}{\boldsymbol{\varepsilon}} \approx \underset{\sim}{\mathbf{E}} \approx \underset{\sim}{\mathbf{e}} \quad , \quad \underset{\sim}{\boldsymbol{\kappa}} \approx \underset{\sim}{\boldsymbol{\mathcal{K}}} \approx \underset{\sim}{\boldsymbol{\mathcal{k}}} \quad . \tag{2.30}$$

Which definitions of the strain measures given in Eqs. (2.18)-(2.21) and Eqs. (2.26)-(2.29) are used for the implementations will be stated in the corresponding sections.

2.3 Kinetics

In the following, the stress measures of the micropolar continuum are introduced and the equations of motion for static problems are outlined. Boundary conditions are introduced to set up a BVP. The equations are given with respect to the reference and spatial configuration.

Following [28], the Cauchy theorem for the micropolar continuum states that for any point $\mathcal{P}$ of $\mathcal{B}$ there exist second order tensors $\underset{\sim}{\mathbf{T}}$ and ${}^{\kappa}\underset{\sim}{\mathbf{T}}$ such that the stress vector, $\underline{\mathbf{t}}$, and the couple stress vector, ${}^{\kappa}\underline{\mathbf{t}}$, acting at a point of a surface with normal, $\underline{\mathbf{n}}$, can be expressed through

$$\underline{\mathbf{t}}(\underline{\mathbf{x}}, \underline{\phi}, \underline{\mathbf{n}}) = \underset{\sim}{\mathbf{T}}(\underline{\mathbf{x}}, \underline{\phi}, t)\underline{\mathbf{n}} \quad , \quad t_i = T_{ij} n_j \quad , \tag{2.31}$$

$${}^{\kappa}\underline{\mathbf{t}}(\underline{\mathbf{x}}, \underline{\phi}, \underline{\mathbf{n}}) = {}^{\kappa}\underset{\sim}{\mathbf{T}}(\underline{\mathbf{x}}, \underline{\phi}, t)\underline{\mathbf{n}} \quad , \quad {}^{\kappa}t_i = {}^{\kappa}T_{ij} n_j \quad . \tag{2.32}$$

In [28], the existence of the stress and couple stress tensors is proven by using the first and second Euler's law of motion or *balance of momentum* and *balance of moment of momentum*, respectively. First the balance equations are applied to an arbitrary parallelepiped and then to an arbitrary tetrahedron. This proof is possible only with the help of Cauchy's lemma, which represents Newton's third axiom of reciprocal actions for micropolar bodies [28]. It postulates that stress and couple stress vectors are odd functions with respect to the surface normal, $\underline{\mathbf{n}}$, reading

$$\underline{\mathbf{t}}(\underline{\mathbf{x}}, \underline{\mathbf{n}}) = -\underline{\mathbf{t}}(\underline{\mathbf{x}}, -\underline{\mathbf{n}}) \quad , \tag{2.33}$$

$${}^{\kappa}\underline{\mathbf{t}}(\underline{\mathbf{x}}, \underline{\mathbf{n}}) = -{}^{\kappa}\underline{\mathbf{t}}(\underline{\mathbf{x}}, -\underline{\mathbf{n}}) \quad . \tag{2.34}$$

A proof of this lemma can be found in [28], which is based on dividing $\mathcal{B}$ into two parts by an arbitrary surface and then applying the balance equations to both parts. The stress tensor in Eq. (2.31) and the couple stress tensor in Eq. (2.32) are referred to as being Cauchy-like, meaning that the measures are defined with respect to the current configuration. The components of the stress and couple stress tensors with respect to a Cartesian basis $\underline{\mathbf{e}}_i$ are defined as

$$\underset{\sim}{\mathbf{T}} = T_{ij}\underline{\mathbf{e}}_i \otimes \underline{\mathbf{e}}_j \quad , \quad {}^{\kappa}\underset{\sim}{\mathbf{T}} = {}^{\kappa}T_{ij}\underline{\mathbf{e}}_i \otimes \underline{\mathbf{e}}_j \quad , \tag{2.35}$$

where the first subscript, i, denotes the direction of the coordinate base and the second subscript, j, represents the direction of the surface normal. This is schematically depicted in Figure 2.3, where also the rule of signs for the components can be found. This notation of subscripts will further be called the right hand-side definition of stress components (RSD). There exists a different notation, where first and second subscript interchange, which will further be called left hand-side definition of stress components (LSD). In the literature, both notations can be found. In general, the stress as well as the couple stress tensor are not symmetric, i.e., $\underset{\sim}{\mathbf{T}} \neq \underset{\sim}{\mathbf{T}}^{\mathrm{T}}$ and ${}^{\kappa}\underset{\sim}{\mathbf{T}} \neq {}^{\kappa}\underset{\sim}{\mathbf{T}}^{\mathrm{T}}$. Consequently, attention must be paid to the definition of the indices. Furthermore, the non-symmetry of the tensors prevents the use of the spectral decomposition to determine principal stresses, for alternative methods see [28].

The equations of motion of a micropolar body $\mathcal{B}$ in the local form can be derived through Euler's first and second law [28]. For a static problem, the equations read

$$\mathrm{div}_{\mathrm{R}}(\underset{\sim}{\mathbf{T}}) + \rho_t \underline{\mathbf{f}} = \underline{\mathbf{0}} \quad , \tag{2.36}$$

$$\mathrm{div}_{\mathrm{R}}({}^{\kappa}\underset{\sim}{\mathbf{T}}) - {}^{\chi}\underline{\mathbf{t}} + \rho_t \underline{\mathbf{m}} = \underline{\mathbf{0}} \quad , \tag{2.37}$$

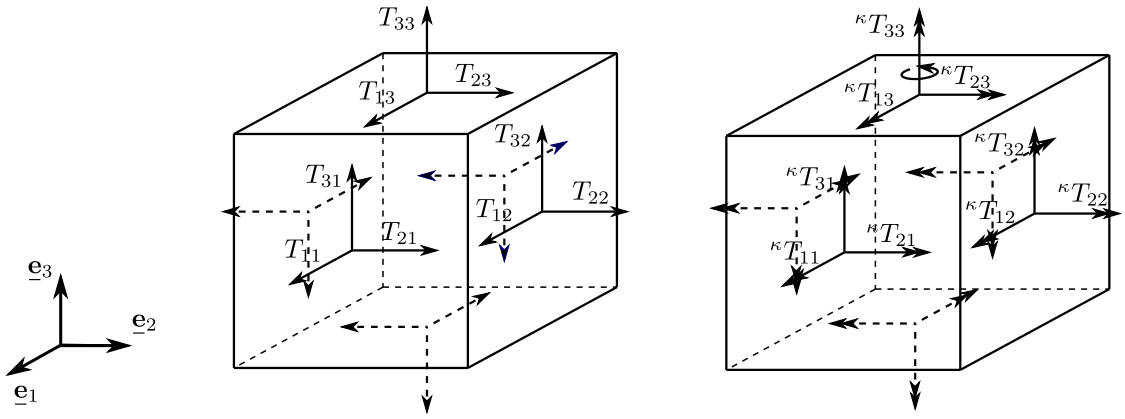

Figure 2.3: Stress and couple stress components acting on a cuboid based on the right hand-side definition of stress components, where the solid arrows indicate positive values and dashed arrows represent negative values.

where $\underline{\mathbf{f}}$ and $\underline{\mathbf{m}}$ denote the body forces and moments per unit mass, respectively, ρ_t describes the density in the current configuration, and ${}^{\chi}\underline{\mathbf{t}} = (\underset{\sim}{\mathbf{T}})_{\times}$ is the axial stress vector defined according to Eq. (A.21) in Appendix A. All quantities are given with respect to the current configuration, hence, the equations are referred to as *Eulerian equations of motion*. In the literature, various representations of the axial stress vector ${}^{\chi}\underline{\mathbf{t}}$ can be found. Note that if Eq. (A.20) is used to define the axial stress vector ${}^{\chi}\underline{\mathbf{t}}$ as ${}^{\chi}\underline{\mathbf{t}} = \mathrm{axl}(\underset{\sim}{\mathbf{T}} - \underset{\sim}{\mathbf{T}}^{\mathrm{T}}) = -\underline{\underline{\boldsymbol{\epsilon}}} : \underset{\sim}{\mathbf{T}} (= -(\underset{\sim}{\mathbf{T}})_{\times})$, Eq. (2.37) reads $\mathrm{div}_{\mathrm{R}}({}^{\kappa}\underset{\sim}{\mathbf{T}}) + {}^{\chi}\underline{\mathbf{t}} + \rho_t \underline{\mathbf{m}} = \underline{\mathbf{0}}$, see, e.g., [8] and [26]. Consequently, the definition of ${}^{\chi}\underline{\mathbf{t}}$ has an impact on the formulation of the balance equations.

In [28], *Piola's identity*,

$$\mathrm{Div}_{\mathrm{R}}(J\underset{\sim}{\mathbf{F}}^{-\mathrm{T}}) = \underline{\mathbf{0}}, \tag{2.38}$$

is used to obtain the corresponding *Lagrangian equations of motion*, which reads

$$\mathrm{Div}_{\mathrm{R}}(\tilde{\underset{\sim}{\mathbf{T}}}) + \rho_0 \underline{\mathbf{f}} = \underline{\mathbf{0}} \quad , \tag{2.39}$$

$$\mathrm{Div}_{\mathrm{R}}({}^{\kappa}\tilde{\underset{\sim}{\mathbf{T}}}) - {}^{\chi}\tilde{\underline{\mathbf{t}}} + \rho_0 \underline{\mathbf{m}} = \underline{\mathbf{0}} \quad , \tag{2.40}$$

where $\tilde{\underset{\sim}{\mathbf{T}}}$ is the first Piola-Kirchhoff (PK1)-like stress tensor, ${}^{\kappa}\tilde{\underset{\sim}{\mathbf{T}}}$ denotes the PK1-like couple stress tensor, ${}^{\chi}\tilde{\underline{\mathbf{t}}} = (\tilde{\underset{\sim}{\mathbf{T}}}\underset{\sim}{\mathbf{F}}^{\mathrm{T}})_{\times}$ is the PK1-like axial stress vector, and ρ_0 is the density in the reference configuration. The PK1-like stress tensors are two-point tensors with the left and right legs associated with the current and reference configurations, respectively. To entirely refer to the reference configuration, the second Piola-Kirchhoff (PK2)-like tensors can be introduced by

$$\breve{\underset{\sim}{\mathbf{T}}} = \underset{\sim}{\mathbf{R}}^{\mathrm{T}} \tilde{\underset{\sim}{\mathbf{T}}} \quad , \quad {}^{\kappa}\breve{\underset{\sim}{\mathbf{T}}} = \underset{\sim}{\mathbf{R}}^{\mathrm{T}} {}^{\kappa}\tilde{\underset{\sim}{\mathbf{T}}} \quad , \tag{2.41}$$

where $\breve{\underset{\sim}{\mathbf{T}}}$ is the PK2-like stress tensor and ${}^{\kappa}\breve{\underset{\sim}{\mathbf{T}}}$ denotes the PK2-like couple stress tensor [28]. This relation can be used together with Eqs. (2.39) and (2.40) to obtain the Lagrangian equations of motion based on the PK2-like stress tensors as

$$\mathrm{Div}_{\mathrm{R}}(\underset{\sim}{\mathbf{R}}\breve{\underset{\sim}{\mathbf{T}}}) + \rho_0 \underline{\mathbf{f}} = \underline{\mathbf{0}} \quad , \tag{2.42}$$

$$\mathrm{Div}_{\mathrm{R}}(\underset{\sim}{\mathbf{R}}{}^{\kappa}\breve{\underset{\sim}{\mathbf{T}}}) - {}^{\chi}\breve{\underline{\mathbf{t}}} + \rho_0 \underline{\mathbf{m}} = \underline{\mathbf{0}} \quad , \tag{2.43}$$

respectively, where ${}^{\chi}\underset{\sim}{\underline{\breve{t}}} = (\underset{\sim}{\mathbf{R}}\underset{\sim}{\breve{\mathbf{T}}}\underset{\sim}{\mathbf{F}}^{\mathrm{T}})_{\times}$ is the PK2-like axial stress vector. Complementing the equations of motion with the corresponding boundary conditions, the BVP in Lagrangian and Eulerian description is obtained, respectively. Static boundary conditions consist of external forces and couples as well as kinematic conditions, also known as Neumann-type and Dirichlet-type boundary conditions, respectively. Whether the boundary conditions should be applied on the boundary surface $\partial\mathcal{R}_0$ corresponding to the reference configuration or applied on the $\partial\mathcal{R}_t$ of current configuration, depends on the equations of motion chosen for the BVP. For the external forces and couples, it follows

$$
\begin{aligned}
\underline{\mathbf{t}}^* &= \underset{\sim}{\mathbf{T}}\underline{\mathbf{n}} && \text{on } \partial\mathcal{R}_t^f \quad , \quad t_i^* = T_{ij}n_j && \text{on } \partial\mathcal{R}_t^{f_i} \quad , \\
{}^{\kappa}\underline{\mathbf{t}}^* &= {}^{\kappa}\underset{\sim}{\mathbf{T}}\underline{\mathbf{n}} && \text{on } \partial\mathcal{R}_t^m \quad , \quad {}^{\kappa}t_i^* = {}^{\kappa}T_{ij}n_j && \text{on } \partial\mathcal{R}_t^{m_i} \quad , \\
\underline{\tilde{\mathbf{t}}}^* &= \underset{\sim}{\tilde{\mathbf{T}}}\underline{\mathbf{N}} && \text{on } \partial\mathcal{R}_0^f \quad , \quad \tilde{t}_i^* = \tilde{T}_{ij}N_j && \text{on } \partial\mathcal{R}_0^{f_i} \quad , \\
{}^{\kappa}\underline{\tilde{\mathbf{t}}}^* &= {}^{\kappa}\underset{\sim}{\tilde{\mathbf{T}}}\underline{\mathbf{N}} && \text{on } \partial\mathcal{R}_0^m \quad , \quad {}^{\kappa}\tilde{t}_i^* = {}^{\kappa}\tilde{T}_{ij}N_j && \text{on } \partial\mathcal{R}_0^{m_i} \quad , \\
\underline{\breve{\mathbf{t}}}^* &= (\underset{\sim}{\mathbf{R}}\underset{\sim}{\breve{\mathbf{T}}})\underline{\mathbf{N}} && \text{on } \partial\mathcal{R}_0^f \quad , \quad \breve{t}_i^* = R_{ik}\breve{T}_{kj}N_j && \text{on } \partial\mathcal{R}_0^{f_i} \quad , \\
{}^{\kappa}\underline{\breve{\mathbf{t}}}^* &= (\underset{\sim}{\mathbf{R}}{}^{\kappa}\underset{\sim}{\breve{\mathbf{T}}})\underline{\mathbf{N}} && \text{on } \partial\mathcal{R}_0^m \quad , \quad {}^{\kappa}\breve{t}_i^* = R_{ik}{}^{\kappa}\breve{T}_{kj}N_j && \text{on } \partial\mathcal{R}_0^{m_i} \quad ,
\end{aligned}
\tag{2.44}
$$

where the superscript $*$ indicates prescribed values and the relations $\partial\mathcal{R}_0^f \cup \partial\mathcal{R}_0^m = \partial\mathcal{R}_0^{\sigma_f}$ and $\partial\mathcal{R}_t^f \cup \partial\mathcal{R}_t^m = \partial\mathcal{R}_t^{\sigma_f}$ hold. The kinematic boundary conditions can be given as

$$
\underline{\mathbf{u}} = \underline{\mathbf{u}}^* \quad \text{on } \partial\mathcal{R}_t^u \text{ (or } \partial\mathcal{R}_0^u) \quad , \quad u_i = u_i^* \quad \text{on } \partial\mathcal{R}_t^{u_i} \text{ (or } \partial\mathcal{R}_0^{u_i}) \quad , \tag{2.45}
$$

$$
\underline{\boldsymbol{\phi}} = \underline{\boldsymbol{\phi}}^* \text{ (or } \underset{\sim}{\mathbf{R}} = \underset{\sim}{\mathbf{R}}^*) \quad \text{on } \partial\mathcal{R}_t^{\phi} \text{ (or } \partial\mathcal{R}_0^{\phi}) \quad , \quad \phi_i = \phi_i^* \text{ (or } R_{ij} = R_{ij}^*) \quad \text{on } \partial\mathcal{R}_t^{\phi_i} \text{ (or } \partial\mathcal{R}_0^{\phi_i}) \quad , \tag{2.46}
$$

where either the finite rotation vector or the microrotation tensor can be used for prescribing rotational DOFs. For the kinematic conditions, the relations $\partial\mathcal{R}_0^u \cup \partial\mathcal{R}_0^{\phi} = \partial\mathcal{R}_0^{\sigma_u}$ and $\partial\mathcal{R}_t^u \cup \partial\mathcal{R}_t^{\phi} = \partial\mathcal{R}_t^{\sigma_u}$ hold. For the particular case of a fixed micropolar body, it follows that

$$
\underline{\mathbf{u}} = \underline{\mathbf{0}} \quad \text{on } \partial\mathcal{R}_t^u \text{ (or } \partial\mathcal{R}_0^u) \quad , \tag{2.47}
$$

$$
\underline{\boldsymbol{\phi}} = \underline{\mathbf{0}} \text{ (or } \underset{\sim}{\mathbf{R}} = \underset{\sim}{\mathbf{I}}) \quad \text{on } \partial\mathcal{R}_t^{\phi} \text{ (or } \partial\mathcal{R}_0^{\phi}) \quad . \tag{2.48}
$$

The relation $\partial\mathcal{R}_t^{\sigma} \cap \partial\mathcal{R}_t^u = \emptyset$ is necessary to exclude Robin boundary conditions, i.e., mixed boundary conditions as a combination of Neumann- and Dirichlet-type boundary conditions.

As already indicated by Piola's identity Eq. (2.38) and Eq. (2.41), the stress and couple stress tensors of the micropolar body show certain relations with respect to the reference and current configuration. These relations can be summarized as *Piola transformations*, i.e., push-forward and pull-back operations for stress and couple stress tensors. In [28], the following relations are given

$$
\begin{aligned}
\underset{\sim}{\mathbf{T}} &= \frac{1}{J}\underset{\sim}{\mathbf{R}}\underset{\sim}{\breve{\mathbf{T}}}\underset{\sim}{\mathbf{F}}^{\mathrm{T}} \quad , \quad \underset{\sim}{\mathbf{T}} = \frac{1}{J}\underset{\sim}{\tilde{\mathbf{T}}}\underset{\sim}{\mathbf{F}}^{\mathrm{T}} \quad , \quad {}^{\kappa}\underset{\sim}{\mathbf{T}} = \frac{1}{J}\underset{\sim}{\mathbf{R}}{}^{\kappa}\underset{\sim}{\breve{\mathbf{T}}}\underset{\sim}{\mathbf{F}}^{\mathrm{T}} \quad , \quad {}^{\kappa}\underset{\sim}{\mathbf{T}} = \frac{1}{J}{}^{\kappa}\underset{\sim}{\tilde{\mathbf{T}}}\underset{\sim}{\mathbf{F}}^{\mathrm{T}} \quad , \\
\underset{\sim}{\tilde{\mathbf{T}}} &= J\underset{\sim}{\mathbf{T}}\underset{\sim}{\mathbf{F}}^{-\mathrm{T}} \quad , \quad \underset{\sim}{\tilde{\mathbf{T}}} = \underset{\sim}{\mathbf{R}}\underset{\sim}{\breve{\mathbf{T}}} \quad , \quad {}^{\kappa}\underset{\sim}{\tilde{\mathbf{T}}} = J{}^{\kappa}\underset{\sim}{\mathbf{T}}\underset{\sim}{\mathbf{F}}^{-\mathrm{T}} \quad , \quad {}^{\kappa}\underset{\sim}{\tilde{\mathbf{T}}} = \underset{\sim}{\mathbf{R}}{}^{\kappa}\underset{\sim}{\breve{\mathbf{T}}} \quad , \\
\underset{\sim}{\breve{\mathbf{T}}} &= J\underset{\sim}{\mathbf{R}}^{\mathrm{T}}\underset{\sim}{\mathbf{T}}\underset{\sim}{\mathbf{F}}^{-\mathrm{T}} \quad , \quad \underset{\sim}{\breve{\mathbf{T}}} = \underset{\sim}{\mathbf{R}}^{\mathrm{T}}\underset{\sim}{\tilde{\mathbf{T}}} \quad , \quad {}^{\kappa}\underset{\sim}{\breve{\mathbf{T}}} = J\underset{\sim}{\mathbf{R}}^{\mathrm{T}}{}^{\kappa}\underset{\sim}{\mathbf{T}}\underset{\sim}{\mathbf{F}}^{-\mathrm{T}} \quad , \quad {}^{\kappa}\underset{\sim}{\breve{\mathbf{T}}} = \underset{\sim}{\mathbf{R}}^{\mathrm{T}}{}^{\kappa}\underset{\sim}{\tilde{\mathbf{T}}} \quad .
\end{aligned}
\tag{2.49}
$$

The stress and strain measures defined must be work-conjugate in order to give reasonable physical results. In [28], it is shown that the Cauchy-like stress and couple stress tensors are the work-conjugates to the relative Eulerian stretch and wryness tensors, respectively, and the PK2-like stress and couple stress tensors are the

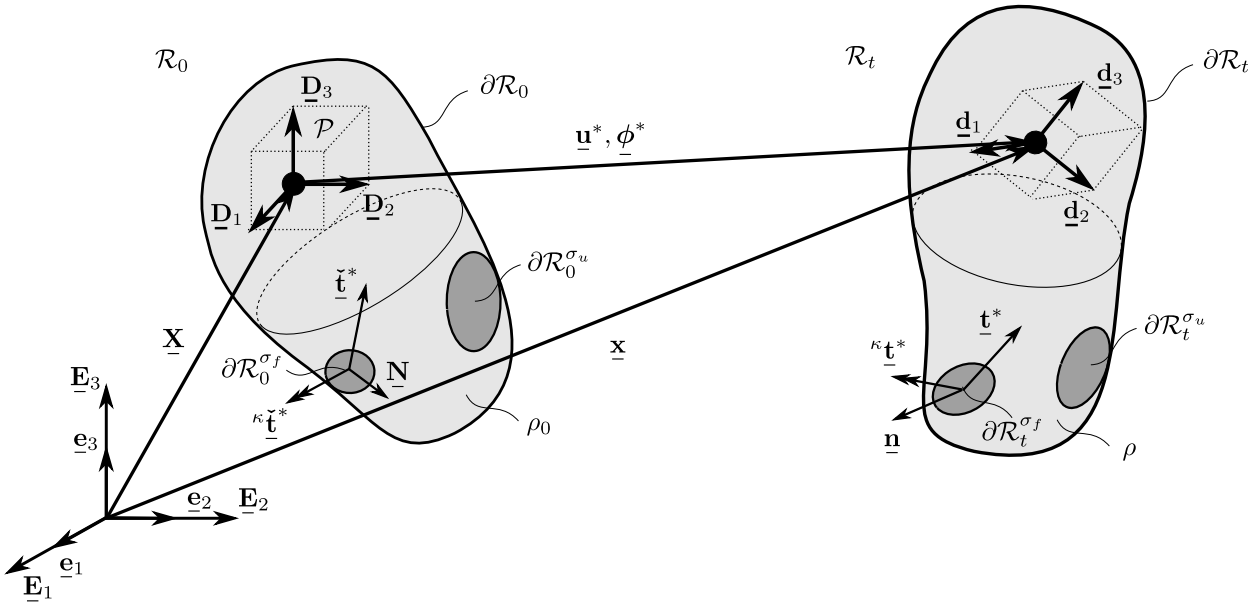

Figure 2.4: Boundary conditions for the BVP.

work-conjugates to the relative Lagrangian stretch and wryness tensors, respectively. This is summarized as follows

$$\begin{aligned} \underset{\sim}{\mathbf{T}} &\leftrightarrow \underset{\sim}{\mathbf{e}} \quad , \quad {}^{\kappa}\underset{\sim}{\mathbf{T}} \leftrightarrow \underset{\sim}{\boldsymbol{\hbar}} \quad , \\ \tilde{\underset{\sim}{\mathbf{T}}} &\leftrightarrow \underset{\sim}{\mathbf{R}}\underset{\sim}{\mathbf{E}} \quad , \quad {}^{\kappa}\tilde{\underset{\sim}{\mathbf{T}}} \leftrightarrow \underset{\sim}{\mathbf{R}}\underset{\sim}{\boldsymbol{\mathscr{K}}} \quad , \\ \check{\underset{\sim}{\mathbf{T}}} &\leftrightarrow \underset{\sim}{\mathbf{E}} \quad , \quad {}^{\kappa}\check{\underset{\sim}{\mathbf{T}}} \leftrightarrow \underset{\sim}{\boldsymbol{\mathscr{K}}} \quad . \end{aligned} \tag{2.50}$$

It is worth noting that the CET continuum is obtained by setting ${}^{\kappa}\underset{\sim}{\mathbf{T}} = \underset{\sim}{\mathbf{0}}$ and not considering any body moments $\underline{\mathbf{m}} = \underline{\mathbf{0}}$, which leads to ${}^{\chi}\underline{\mathbf{t}} = (\underset{\sim}{\mathbf{T}})_{\times} = \underline{\mathbf{0}}$ and further to $\underset{\sim}{\mathbf{T}} = \underset{\sim}{\mathbf{T}}^{\mathrm{T}}$.

2.4 Constitutive law

The dependence of the stress measures on the deformations are described by constitutive laws. For conservative systems, the strain energy density or strain energy potential of isothermal *physically linear micropolar solids*, is given as a quadratic function of strain measures as

$$\begin{aligned} \psi(\underset{\sim}{\mathbf{E}}, \underset{\sim}{\boldsymbol{\mathscr{K}}}) &= \frac{1}{2}(\underset{\sim}{\mathbf{E}} : \underset{\approx}{\mathbb{A}}^0 : \underset{\sim}{\mathbf{E}} + 2\underset{\sim}{\mathbf{E}} : \underset{\approx}{\mathbb{C}}^0 : \underset{\sim}{\boldsymbol{\mathscr{K}}} + \underset{\sim}{\boldsymbol{\mathscr{K}}} : \underset{\approx}{\mathbb{B}}^0 : \underset{\sim}{\boldsymbol{\mathscr{K}}}) \quad , \\ \psi(E_{ij}, \mathscr{K}_{ij}) &= \frac{1}{2}(\mathbb{A}^0_{klmn}E_{kl}E_{mn} + 2\mathbb{C}^0_{klmn}E_{kl}\mathscr{K}_{mn} + \mathbb{B}^0_{klmn}\mathscr{K}_{kl}\mathscr{K}_{mn}) \quad , \end{aligned} \tag{2.51}$$

where $\underset{\approx}{\mathbb{A}}^0$, $\underset{\approx}{\mathbb{B}}^0$, $\underset{\approx}{\mathbb{C}}^0$ are fourth order elasticity tensors in the material description, i.e., $(\cdot)^0$ indicates that the tensors are given with respect to the reference configuration. The elasticity tensor $\underset{\approx}{\mathbb{A}}^0$ is related to the stretch and stress measures, while $\underset{\approx}{\mathbb{B}}^0$ is related to the wryness and couple stress measures. The elasticity tensor $\underset{\approx}{\mathbb{C}}^0$ couples the stretch tensor and the wryness tensor.

Considering only infinitesimal displacements and rotations as given in Eq. (2.24), the *linear micropolar solid* is obtained, for which the strain energy density takes the form

$$\psi(\underset{\sim}{\boldsymbol{\varepsilon}}, \underset{\sim}{\boldsymbol{\kappa}}) = \frac{1}{2}(\underset{\sim}{\boldsymbol{\varepsilon}} : \underset{\approx}{\mathbb{A}} : \underset{\sim}{\boldsymbol{\varepsilon}} + 2\underset{\sim}{\boldsymbol{\varepsilon}} : \underset{\approx}{\mathbb{C}} : \underset{\sim}{\boldsymbol{\kappa}} + \underset{\sim}{\boldsymbol{\kappa}} : \underset{\approx}{\mathbb{B}} : \underset{\sim}{\boldsymbol{\kappa}}) \quad , \tag{2.52}$$
$$\psi(\varepsilon_{ij}, \kappa_{ij}) = \frac{1}{2}(\mathbb{A}_{klmn}\varepsilon_{kl}\varepsilon_{mn} + 2\mathbb{C}_{klmn}\varepsilon_{kl}\kappa_{mn} + \mathbb{B}_{klmn}\kappa_{kl}\kappa_{mn}) \quad ,$$

where no superscript is attached to the elasticity tensors indicating the linear character. As all further considerations are restricted to conservative systems, stresses and couple stresses of the linear micropolar continuum can be derived directly from the strain energy potential by

$$\begin{aligned} \underset{\sim}{\boldsymbol{\sigma}} &= \frac{\partial \psi}{\partial \underset{\sim}{\boldsymbol{\varepsilon}}} \quad , \quad \sigma_{ij} = \frac{\partial \psi}{\partial \varepsilon_{ij}} \quad , \\ {}^{\kappa}\underset{\sim}{\boldsymbol{\sigma}} &= \frac{\partial \psi}{\partial \underset{\sim}{\boldsymbol{\kappa}}} \quad , \quad {}^{\kappa}\sigma_{ij} = \frac{\partial \psi}{\partial \kappa_{ij}} \quad . \end{aligned} \tag{2.53}$$

and the elasticity tensors can be given as

$$\begin{aligned} \underset{\approx}{\mathbb{A}} &= \frac{\partial^2 \psi}{\partial \underset{\sim}{\boldsymbol{\varepsilon}} \partial \underset{\sim}{\boldsymbol{\varepsilon}}} \quad , \quad \mathbb{A}_{ijkl} = \frac{\partial^2 \psi}{\partial \varepsilon_{ij} \partial \varepsilon_{kl}} \quad , \\ \underset{\approx}{\mathbb{B}} &= \frac{\partial^2 \psi}{\partial \underset{\sim}{\boldsymbol{\kappa}} \partial \underset{\sim}{\boldsymbol{\kappa}}} \quad , \quad \mathbb{B}_{ijkl} = \frac{\partial^2 \psi}{\partial \kappa_{ij} \partial \kappa_{kl}} \quad , \\ \underset{\approx}{\mathbb{C}} &= \frac{\partial^2 \psi}{\partial \underset{\sim}{\boldsymbol{\varepsilon}} \partial \underset{\sim}{\boldsymbol{\kappa}}} \quad , \quad \mathbb{C}_{ijkl} = \frac{\partial^2 \psi}{\partial \varepsilon_{ij} \partial \kappa_{kl}} \quad . \end{aligned} \tag{2.54}$$

With Eqs. (2.52) and (2.53), the constitutive laws can be given as

$$\begin{aligned} \underset{\sim}{\boldsymbol{\sigma}} &= \underset{\approx}{\mathbb{A}} : \underset{\sim}{\boldsymbol{\varepsilon}} + \underset{\approx}{\mathbb{C}} : \underset{\sim}{\boldsymbol{\kappa}} \quad , \quad \sigma_{ij} = \mathbb{A}_{ijkl}\varepsilon_{kl} + \mathbb{C}_{ijkl}\kappa_{kl} \quad , \\ {}^{\kappa}\underset{\sim}{\boldsymbol{\sigma}} &= \underset{\approx}{\mathbb{C}}^{\mathrm{T}} : \underset{\sim}{\boldsymbol{\varepsilon}} + \underset{\approx}{\mathbb{B}} : \underset{\sim}{\boldsymbol{\kappa}} \quad , \quad {}^{\kappa}\sigma_{ij} = \mathbb{C}_{klij}\varepsilon_{kl} + \mathbb{B}_{ijkl}\kappa_{kl} \quad . \end{aligned} \tag{2.55}$$

Equation (2.54) already reveals that the elasticity tensors $\underset{\approx}{\mathbb{A}}$ and $\underset{\approx}{\mathbb{B}}$ show major symmetry, i.e.,

$$\underset{\approx}{\mathbb{A}} = \underset{\approx}{\mathbb{A}}^{\mathrm{T}} \quad , \quad \mathbb{A}_{ijkl} = \mathbb{A}_{klij} \quad , \tag{2.56}$$
$$\underset{\approx}{\mathbb{B}} = \underset{\approx}{\mathbb{B}}^{\mathrm{T}} \quad , \quad \mathbb{B}_{ijkl} = \mathbb{B}_{klij} \quad . \tag{2.57}$$

For the most general case, this leads to 45 independent components for each of the elasticity tensors $\underset{\approx}{\mathbb{A}}$ and $\underset{\approx}{\mathbb{B}}$, which is a consequence of the non-symmetry of the strain and curvature measures, see Eqs. (2.26) and (2.27). The components of the elasticity tensors are further referred to as micropolar elastic constants MECs. The coupling tensor $\underset{\approx}{\mathbb{C}}$ does not show any symmetry, hence, it is composed of 81 independent MECs. In total, the linear micropolar continuum shows 171 independent MECs for the general anisotropic case, e.g., [98]. The number of independent constants can be significantly reduced by taking material symmetries into account. In [27], the strain energy density is proposed to additionally depend on the so-called microstructure curvature tensor defined therein, resulting in even more MECs to be required. In this work, it is assumed that the elasticity tensors depend only on the strain measures as given in Eq. (2.51) or Eq. (2.52).

For the case of *centrosymmetric materials* exclusively studied in this work, it follows that $\underset{\approx}{\mathbb{C}} = \underset{\approx}{\mathbb{O}}$. This reduces the number of independent MECs to 90. For such materials, the strain energy density according to Eq. (2.52) and the constitutive law given in Eq. (2.55) take the form

$$\psi = \frac{1}{2}(\underset{\sim}{\boldsymbol{\varepsilon}} : \underset{\approx}{\mathbb{A}} : \underset{\sim}{\boldsymbol{\varepsilon}} + \underset{\sim}{\boldsymbol{\kappa}} : \underset{\approx}{\mathbb{B}} : \underset{\sim}{\boldsymbol{\kappa}}) \quad , \tag{2.58}$$

$$\underset{\sim}{\boldsymbol{\sigma}} = \underset{\approx}{\mathbb{A}} : \underset{\sim}{\boldsymbol{\varepsilon}} \quad , \tag{2.59}$$

$${}^{\kappa}\underset{\sim}{\boldsymbol{\sigma}} = \underset{\approx}{\mathbb{B}} : \underset{\sim}{\boldsymbol{\kappa}} \quad . \tag{2.60}$$

In vector-matrix notation, the constitutive law for the linear micropolar continuum follows as

$$\underbrace{\begin{bmatrix} [\underset{\sim}{\boldsymbol{\sigma}}] \\ [{}^{\kappa}\underset{\sim}{\boldsymbol{\sigma}}] \end{bmatrix}}_{[\underset{\sim}{\boldsymbol{\sigma}}]} = \underbrace{\begin{bmatrix} [\underset{\approx}{\mathbb{A}}] & [\underset{\approx}{\mathbb{C}}] \\ [\underset{\approx}{\mathbb{C}}]^{\mathrm{T}} & [\underset{\approx}{\mathbb{B}}] \end{bmatrix}}_{[\underset{\approx}{\mathbb{D}}]} \underbrace{\begin{bmatrix} [\underset{\sim}{\boldsymbol{\varepsilon}}] \\ [\underset{\sim}{\boldsymbol{\kappa}}] \end{bmatrix}}_{[\underset{\sim}{\boldsymbol{\varepsilon}}]} \quad , \tag{2.61}$$

where $[\underset{\approx}{\mathbb{D}}]$ is the corresponding micropolar elasticity matrix, $[\underset{\sim}{\boldsymbol{\sigma}}]$ and $[\underset{\sim}{\boldsymbol{\varepsilon}}]$ denote the generalized vectors of strain and stress measure components, respectively. For the vector-matrix notation, any sequence of tensor components can be chosen. In this work, the components are arranged in the following order

$$(\cdot)_{ij} \quad \text{with} \quad ij = \{11, 22, 33, 23, 31, 12, 32, 13, 21\} \quad , \tag{2.62}$$

which corresponds to the arrangement used in [27], see Appendix B. For 3D problems, the vector-matrix notation does not offer much advantage over the tensorial representation, which is in contrast to the CET when using, e.g., Voigt-Nye notation. This is a consequence of the non-symmetry of the strain and stress measures of the micropolar continuum, which does not allow to reduce the size of the matrices. Nevertheless, for in-plane or 2D considerations, the vector-matrix notation leads to a more compact form.

For in-plane considerations, either a state of plane strain or plane stress can be used. For all 2D problems considered in this work, the dimension of the out-of-plane direction $\underline{\mathbf{e}}_3$ is much larger than those of the two remaining in-plane directions $\underline{\mathbf{e}}_1$ and $\underline{\mathbf{e}}_2$. Therefore, non-generalized plane strain is assumed to be an acceptable approximation. All physical quantities are independent of x_3 and, hence, just depend on x_1, x_2, and t. For stress measures based on LSD as well as strain measures based on gradients applied from the left hand-side, the constitutive law for the linear micropolar continuum in matrix-vector notation considering centrosymmetric materials in 2D then leads to

$$\begin{bmatrix} \sigma_{11} \\ \sigma_{22} \\ \sigma_{12} \\ \sigma_{21} \\ {}^{\kappa}\sigma_{13} \\ {}^{\kappa}\sigma_{23} \end{bmatrix} = \begin{bmatrix} D_{11} & D_{12} & & & & \\ D_{12} & D_{22} & & & & \\ & & D_{33} & D_{34} & & \\ & & D_{34} & D_{44} & & \\ & & & & D_{55} & \\ & & & & & D_{66} \end{bmatrix} \begin{bmatrix} \varepsilon_{11} \\ \varepsilon_{22} \\ \varepsilon_{12} \\ \varepsilon_{21} \\ \kappa_{13} \\ \kappa_{23} \end{bmatrix} \quad , \tag{2.63}$$

where the components of the kinematic fields that are not associated with the plane strain assumption are considered to be zero, i.e., $u_3 = \phi_1 = \phi_2 = 0$. The out-of-plane stress and couple stress follow as $\sigma_{33} = \mathbb{A}_{33kl}\varepsilon_{kl}$ and ${}^{\kappa}\sigma_{33} = \mathbb{B}_{33kl}\kappa_{kl}$, respectively. Both are not of interest in the present work. In index notation, the strain

measures based on applying right gradients, cf. Eqs. (2.26) and (2.27), as well as applying left gradients, cf. Eqs. (2.28) and (2.29), then take the form

$$\varepsilon_{ij} = u_{i,j} + \epsilon_{ij3}\phi_3 \quad , \quad \kappa_{3j} = \phi_{3,j} \quad , \tag{2.64}$$

$$\hat{\varepsilon}_{ij} = u_{j,i} - \epsilon_{ij3}\phi_3 \quad , \quad \hat{\kappa}_{j3} = \phi_{3,j} \quad , \tag{2.65}$$

respectively, with $i, j \in \{1, 2\}$.

2.5 Material symmetries

If symmetries exist for a particular material, the number of independent MECs can be significantly reduced. The symmetries are obtained by mirror reflections and rotations about different axes in space. Following [27], the most important symmetries for the present thesis can be obtained by

- mirror reflection and rotations of 180° about a single unit vector $\underline{\mathbf{e}}$ resulting in *monoclinic* symmetry.
- mirror reflection and rotations of 180° about three orthonormal unit vectors $\underline{\mathbf{e}}_i$ resulting in *orthotropic* symmetry.
- mirror reflection and rotations of 90° about three orthonormal unit vectors $\underline{\mathbf{e}}_i$ resulting in *cubic* symmetry.
- mirror reflection and arbitrary rotations about a unit vector $\underline{\mathbf{e}}$ resulting in *transversely isotropic* symmetry.
- arbitrary mirror reflections and rotations about three orthonormal unit vectors $\underline{\mathbf{e}}_i$ resulting in *isotropy*, which is considered to show full symmetry.

The corresponding elasticity tensors for these symmetries with respect to the material principle axes can be found in vector-matrix notation based on Eq. (2.62) in Appendix B.

Isotropic material. Following the notation used in [26, 44], the constitutive law for a linear micropolar isotropic material reads

$$\underset{\sim}{\mathbf{T}} = \lambda \mathrm{tr}(\underset{\sim}{\mathbf{E}})\underset{\sim}{\mathbf{I}} + (\mu+\nu)\underset{\sim}{\mathbf{E}} + (\mu-\nu)\underset{\sim}{\mathbf{E}}^{\mathrm{T}} = \underset{\approx}{\mathbb{A}} : \underset{\sim}{\mathbf{E}} \quad , \tag{2.66}$$

$$T_{ij} = \lambda E_{kk}\delta_{ij} + (\mu+\nu)E_{ij} + (\mu-\nu)E_{ji} = \mathbb{A}_{ijkl}E_{kl} \quad ,$$

$${}^{\kappa}\underset{\sim}{\mathbf{T}} = \alpha \mathrm{tr}(\underset{\sim}{\boldsymbol{\mathscr{K}}})\underset{\sim}{\mathbf{I}} + (\beta+\gamma)\underset{\sim}{\boldsymbol{\mathscr{K}}} + (\beta-\gamma)\underset{\sim}{\boldsymbol{\mathscr{K}}}^{\mathrm{T}} = \underset{\approx}{\mathbb{B}} : \underset{\sim}{\boldsymbol{\mathscr{K}}} \quad , \tag{2.67}$$

$${}^{\kappa}T_{ij} = \alpha\mathscr{K}_{kk}\delta_{ij} + (\beta+\gamma)\mathscr{K}_{ij} + (\beta-\gamma)\mathscr{K}_{ji} = \mathbb{B}_{ijkl}\mathscr{K}_{kl} \quad ,$$

where λ and μ are the standard Lamé parameters, and $\nu, \alpha, \beta, \gamma$ are additional material moduli associated with the micropolar continuum. There does not exist a unique definition for these moduli as different definitions can be found in the literature, e.g., in [8, 28, 30], but need to satisfy a set of inequalities to ensure the quadratic form of the strain energy density to be non-negative, see, e.g., [30]. The elasticity tensors read

$$\underset{\approx}{\mathbb{A}} = \lambda \underset{\sim}{\mathbf{I}} \otimes \underset{\sim}{\mathbf{I}} + (\mu+\nu)\underset{\approx}{\mathbb{I}} + (\mu-\nu)\hat{\underset{\approx}{\mathbb{I}}} \quad , \tag{2.68}$$

$$\underset{\approx}{\mathbb{B}} = \alpha \underset{\sim}{\mathbf{I}} \otimes \underset{\sim}{\mathbf{I}} + (\beta+\gamma)\underset{\approx}{\mathbb{I}} + (\beta-\gamma)\hat{\underset{\approx}{\mathbb{I}}} \quad , \tag{2.69}$$

where $\underset{\approx}{\mathbb{I}} = \delta_{ik}\delta_{jl}\underline{\mathbf{e}}_i \otimes \underline{\mathbf{e}}_j \otimes \underline{\mathbf{e}}_k \otimes \underline{\mathbf{e}}_l$ and $\hat{\underset{\approx}{\mathbb{I}}} = \delta_{il}\delta_{jk}\underline{\mathbf{e}}_i \otimes \underline{\mathbf{e}}_j \otimes \underline{\mathbf{e}}_k \otimes \underline{\mathbf{e}}_l$. Note that for micropolar isotropic materials the relation $\mathbb{A}_{ijkl} = \mathbb{A}_{jilk}$ holds true. However, the minor symmetries are not satisfied and, consequently,

$\mathbb{A}_{ijkl} \neq \mathbb{A}_{jikl}$ and $\mathbb{A}_{ijkl} \neq \mathbb{A}_{ijlk}$. This also holds true for $\underset{\approx}{\mathbb{B}}$. In [44], the micropolar material moduli are related to their corresponding engineering parameters as

$$\lambda = 2\widetilde{n}\widetilde{G}/(1-2\widetilde{n}) \quad , \quad \mu = \widetilde{G} \quad , \quad \nu = \widetilde{G}\widetilde{N}^2/(1-\widetilde{N}^2) \quad , \tag{2.70}$$

$$\alpha = (2\widetilde{G}\widetilde{l}_t^2(1-\widetilde{\psi}))/\widetilde{\psi} \quad , \quad \beta = \widetilde{G}\widetilde{l}_t^2 \quad , \quad \gamma = \widetilde{G}(4\widetilde{l}_b^2 - \widetilde{l}_t^2) \quad , \tag{2.71}$$

where $\widetilde{n}$ is the Poisson ratio, $\widetilde{G}$ denotes the shear modulus, $\widetilde{l}_t$ and $\widetilde{l}_b$ are associated with the characteristic length for torsion and bending analyses, respectively, $\widetilde{N} \in [0,1]$ denotes the classical micropolar coupling number referring to the degree of coupling between displacement and rotation field, and $\widetilde{\psi} \in [0, 1.5]$ is associated with the polar ratio, which relates the torsional strains, i.e., the diagonal components of the curvature tensor, in a similar manner as the Poisson ratio does for the normal strains [26]. The CST is obtained for $\widetilde{N} = 1$ or $\nu \to \infty$. For a discussion on the physical interpretation of the micropolar material moduli, see, e.g., [55]. For material moduli given for various polymeric foams and a comparison to their classical material moduli, see, e.g., [47].

For plane strain problems, the material moduli of the linear micropolar isotropic material reduce to four, namely, $\lambda, \mu, \nu, \beta+\gamma$ according to the notation used in [44]. The elasticity tensors in vector-matrix notation as given in Eq. (2.63) reads as follows

$$[\underset{\approx}{\mathbb{D}}] = \begin{bmatrix} \lambda+2\mu & \lambda & & & & \\ \lambda & \lambda+2\mu & & & & \\ & & \mu+\nu & \mu-\nu & & \\ & & \mu-\nu & \mu+\nu & & \\ & & & & \beta+\gamma & \\ & & & & & \beta+\gamma \end{bmatrix} \quad . \tag{2.72}$$

2.6 Notes on the elasticity tensors

Right hand-side definition of elasticity tensors. The stress and strain measures defined for the derivation of the MECs are based on the definitions used in [53]. Therein, the left hand-side definition of stress components is used, cf. Section 2.3, and the strain measures are defined by applying the gradient from the left, cf. Section 2.2 Eq. (2.28). The resulting components of the elasticity tensors are related to these definitions through Eq. (2.54) and are further referred to as of left-hand side definition of elasticity tensors.

In order to obtain the components of the elasticity tensors based on the right hand-side definition of stress components (RSD), i.e., by using the right hand-side definition of stress components and strain measures defined via applying the gradient from the right, the following conversion rule can be applied

$$\mathbb{A}_{ijkl}^{\mathrm{RSD}} = \mathbb{A}_{jilk}^{\mathrm{LSD}} \quad . \tag{2.73}$$

For the right hand-side definition of stress components and strain measures based on applying the gradient from the left denoted by MD1 as well as vice versa referred to as MD2, the following conversion rule can be used

$$\mathbb{A}_{ijkl}^{\mathrm{MD1}} = \mathbb{A}_{jikl}^{\mathrm{LSD}} \quad , \tag{2.74}$$

$$\mathbb{A}_{ijkl}^{\mathrm{MD2}} = \mathbb{A}_{ijlk}^{\mathrm{LSD}} \quad , \tag{2.75}$$

respectively. These conversion rules should not be confused with the definition of minor symmetries of a fourth order tensor.

For the present thesis, only elasticity tensors according to LSD and RSD are needed. Based on the definition of stress and strain measures, the conversion rule given in Eq. (2.73) needs to be applied to the elasticity tensors obtained for the lattices in Chapter 3. Conversion is required for the PO lattice, but not for the PC lattice. No conversion is required for the BCC lattice, which also applies to isotropic materials, since $\mathbb{A}_{ijkl} = \mathbb{A}_{jilk}$ is satisfied.

Rotation of elasticity tensors. To study a given lattice in a configuration rotated with respect to the global coordinate system, the elasticity tenors need to be rotated accordingly. The rotation of an arbitrary tensor of fourth order reads

$$\bar{\underset{\approx}{\mathbb{Y}}} = \underset{\sim}{\mathbf{Q}}\underset{\sim}{\mathbf{Q}}\underset{\approx}{\mathbb{Y}}\underset{\sim}{\mathbf{Q}}^{\mathrm{T}}\underset{\sim}{\mathbf{Q}}^{\mathrm{T}} \quad , \qquad \bar{Y}_{ijkl} = Q_{ip}Q_{jq}Q_{kr}Q_{ls}Z_{pqrs} \quad , \tag{2.76}$$

with $\underset{\sim}{\mathbf{Q}}$ as a proper orthogonal second order tensor. For a mathematical positive rotation θ around a single axis of a defined coordinate system, e.g., 1-, 2-, and 3-axis, the following rotation matrices can be directly applied

$$\underset{\sim}{\mathbf{Q}}_1^+ = \begin{bmatrix} 1 & 0 & 0 \\ 0 & \cos\theta & -\sin\theta \\ 0 & \sin\theta & \cos\theta \end{bmatrix}, \qquad \underset{\sim}{\mathbf{Q}}_2^+ = \begin{bmatrix} \cos\theta & 0 & \sin\theta \\ 0 & 1 & 0 \\ -\sin\theta & 0 & \cos\theta \end{bmatrix}, \qquad \underset{\sim}{\mathbf{Q}}_3^+ = \begin{bmatrix} \cos\theta & -\sin\theta & 0 \\ \sin\theta & \cos\theta & 0 \\ 0 & 0 & 1 \end{bmatrix} \quad .$$

For the rotation about any axis, the rotation matrix can be determined using Eq. (2.9).

Elasticity tensors in Lagrangian and Eulerian description. Elasticity tensors based on different work-conjugate measures can be converted into each other based on pull-back and push-forward operations of strain measures according to Eqs. (2.22) and (2.23) as well as Piola transformations of stress measures Eq. (2.49). Whether the elasticity tensor in Lagrangian (or material) or Eulerian (or spatial) description is known, the following transformation rules can be applied

$$\mathbb{A}^t_{mnop} = \frac{1}{J} R_{mi} F_{nj} R_{ok} F_{pl} \mathbb{A}^0_{ijkl} \quad , \tag{2.77}$$

$$\mathbb{A}^0_{ijkl} = J R^{\mathrm{T}}_{im} F^{-1}_{jn} R^{\mathrm{T}}_{ko} F^{-1}_{lp} \mathbb{A}^t_{mnop} \quad , \tag{2.78}$$

respectively, where $(\cdot)^0$ denotes the Lagrangian and $(\cdot)^t$ refers to the Eulerian description. Note that this applies to all elasticity tensors given in Eq. (2.51).

For the lattice materials, the elasticity tensors are derived based on the linear micropolar theory, cf. Chapter 3. Hence, the constitutive laws based on these tensors are only suitable for predicting the response of linear elastic materials. To account for large displacements and rotations, either the Lagrangian or Eulerian strain measures need to be considered for the FEM implementation to get rid of rigid body rotations. For the usage of large strains, this implies that the response of the lattice material is correctly captured as long as these measures are small in magnitude. For the CET, smallness implies that the transformations reduce to mere (macro)rotations Eq. (2.77), see, e.g., [7]. For the micropolar continuum, this holds true as well, cf. Eq. (2.16), which gives $\underset{\sim}{\mathbf{R}}\underset{\sim}{\mathbf{R}}^{\mathrm{T}} \rightarrow \underset{\sim}{\mathbf{R}}^{\mathrm{mac}}\underset{\sim}{\mathbf{R}}^{\mathrm{mac\,T}} = \underset{\sim}{\mathbf{I}}$. For isotropic materials in small strain regimes, no transformation is needed due to isotropy. However, for anisotropic materials the transformation must be considered. As the components of the Lagrangian strain measures are invariant under rigid body rotations, it

follows that the elasticity tensors derived can be directly used in a pure Lagrangian description, i.e., $\underset{\approx}{\mathbb{A}}^0 = \underset{\approx}{\mathbb{A}}$ and $\underset{\approx}{\mathbb{B}}^0 = \underset{\approx}{\mathbb{B}}$. For Eulerian strain measures, the transformation given in Eq. (2.77) needs to be applied.

Chapter 3

Energy based homogenization

In the following, the homogenization method used to derive the components of the elasticity tensors, or micropolar elastic constants (MECs) of lattice structures for an equivalent micropolar continuum is presented. The method was originally introduced by [10] and applied to various centrosymmetric 2D lattices by [53]. The method yields two sets of MECs for the very same lattice material based on different assumptions during the derivation. The assumptions made and the characteristics of the two different sets have caused some controversy in the literature, which will be discussed after the method is presented. In this thesis, the method is used to obtain the MECs of 3D centrosymmetric lattices, namely, the primitive orthorhombic (PO), the body centered cubic (BCC), and the body centered cubic reinforced by primitive cubic (BCCCP) lattices. For the 2D lattices, the MECs are directly taken from [53], see Appendix D.

3.1 Method

The homogenization technique presented in [10] is a discrete energy based homogenization method. For a discrete base cell, the effective MECs of an equivalent micropolar continuum can be obtained. The method is restricted to lattices, for which a periodic unit cell can be found containing a single joint. It has been applied to various periodic centrosymmetric 2D lattices, see, e.g., [53].

An appropriate base cell of the discrete lattice is identified and its strain energy is constructed by the strain energy contributions of its individual members. The strain energy of each lattice member can be expressed as a function of its joint displacements and rotations

$$W_{IJ}(\underline{\mathbf{U}}_I, \underline{\mathbf{U}}_J, \underline{\mathbf{\Phi}}_I, \underline{\mathbf{\Phi}}_J) \quad , \tag{3.1}$$

where I and J denote the joints at both ends, see Figure 3.1. To obtain the approximation for the micropolar continuum, it is assumed that the joint displacements and rotations of each member can be expressed in terms of the origin of the base cell located at point O. The origin does not necessarily coincide with any joint of the lattice [53]. However, for the lattices studied in this work, all members of a base cell meet at a commonly shared origin joint, which is further denoted as O. The displacements and rotations at this origin joint O are denoted by $\underline{\mathbf{u}}\,(=\underline{\mathbf{U}}_\mathrm{O})$ and $\underline{\boldsymbol{\phi}}\,(=\underline{\mathbf{\Phi}}_\mathrm{O})$, respectively. A Taylor series expansion of the kinematics of

each remaining joint K of the lattice is then developed, where only terms up to the second order are retained, reading

$$\begin{aligned} \underline{\mathbf{U}}_K &\approx \underline{\mathbf{u}} + l_{OK}\frac{\partial \underline{\mathbf{u}}}{\partial t_{OK}} + \frac{1}{2} l_{OK}^2 \frac{\partial^2 \underline{\mathbf{u}}}{\partial t_{OK}^2} \quad , \\ \underline{\mathbf{\Phi}}_K &\approx \underline{\boldsymbol{\phi}} + l_{OK}\frac{\partial \underline{\boldsymbol{\phi}}}{\partial t_{OK}} + \frac{1}{2} l_{OK}^2 \frac{\partial^2 \underline{\boldsymbol{\phi}}}{\partial t_{OK}^2} \quad , \end{aligned} \tag{3.2}$$

with t_{OK} as the spatial coordinates along the directions OK and l_{OK} as the length of the member K. The strain energy density of the continuum approximation of a particular base cell is then constructed by summing the strain energies of each member K and referring the sum to the volume of the base cell, V_{bc}. It can be given as

$$\psi = \frac{1}{V_{\mathrm{bc}}} \sum_{K=1}^{n_{\mathrm{bc}}} W_{OK}(\underline{\mathbf{u}}, \underline{\boldsymbol{\phi}}, \underline{\mathbf{U}}_K, \underline{\mathbf{\Phi}}_K) \quad , \tag{3.3}$$

where n_{bc} is the number of members comprising the base cell. The first order direction derivatives in Eq. (3.2) with respect to the local beam coordinate system can be expressed as functions of first order spatial direction derivatives with respect to the global coordinate system as

$$\frac{\partial}{\partial t_{OK}} = f(a\frac{\partial}{\partial x_1}, b\frac{\partial}{\partial x_2}, c\frac{\partial}{\partial x_3}) \quad , \tag{3.4}$$

where a, b, c are constants. These constants are determined by the direction of the individual beam lying in space with respect to the global coordinate system. Any second order direction derivative is converted to first order direction derivative via integration by parts [10, 53]. Inserting the displacement and rotation fields of Eq. (3.2) into Eq. (3.3) and integration by parts for the second order spatial directions gives the strain energy density of the continuum approximation in terms of strain $\underset{\sim}{\boldsymbol{\varepsilon}}$ and curvature $\underset{\sim}{\boldsymbol{\kappa}}$ as

$$\psi(\underline{\mathbf{u}}, \underline{\boldsymbol{\phi}}, \frac{\partial \underline{\mathbf{u}}}{\partial x_i}, \frac{\partial \underline{\boldsymbol{\phi}}}{\partial x_i}) \Rightarrow \psi(\underline{\boldsymbol{\varepsilon}}, \underline{\boldsymbol{\kappa}}) \quad . \tag{3.5}$$

All further considerations are restricted to conservative systems, hence, the stresses, the couple stresses, and the MECs can be derived directly from the strain energy density by using Eqs. (2.53) and (2.54), respectively.

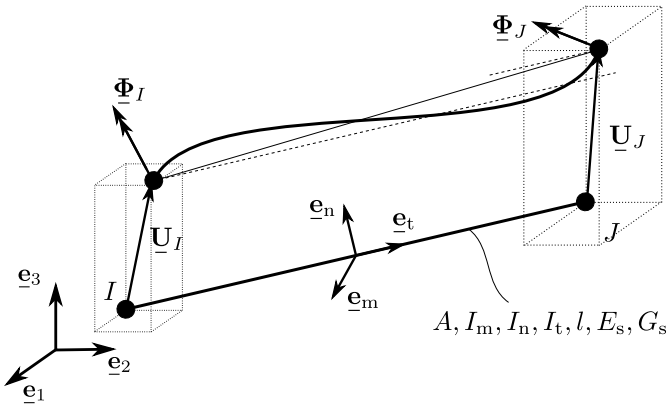

Figure 3.1: Schematic of beam element with end nodes I and J, and its local beam coordinate system with axes $\underline{\mathbf{e}}_t$, $\underline{\mathbf{e}}_n$, and $\underline{\mathbf{e}}_m$.

3.2 Controversy in the literature

The method presented yields two different sets of MECs for the very same lattice material, based on the number of higher order terms of the Taylor series expansion considered for the approximated displacement and rotation fields in Eq. (3.2). The two sets differ only in those MECs that link the couple stress and curvature, see Eq. (2.54). These MECs are different in both sign and magnitude. Neglecting the second order terms of the series leads to positive signs of these MECs, e.g., [6, 53], which are further referred to as *positive constants*. However, this set of constants does not give rise to an equilibrium of forces acting on the origin joint [10]. Retaining the second order terms of the series, leads to negative signs of the MECs, e.g., [10, 53], which are further referred to as *negative constants*. In some cases, the negative constants violate the positive definiteness of the strain energy defined for isotropic materials, see, e.g., [30]. This is the case for the equilateral triangular lattice, which motivated the discussion on the positive definiteness of the strain energy density given in [53]. Therein, it is argued that lattice materials show limited non-locality, which implies that the element size needs to be larger than the underlying internal characteristic length[1].

On the one hand, the necessity to ensure the equilibrium of forces at the origin joint, i.e., retaining the second order terms, has often been ignored in later works, e.g., for the strain gradient model for fracture analysis in [15], for obtaining MECs of a chiral auxetic lattice in [86], for studying the capability of accounting for size-effects of lattice materials in [97], and very recently for studying zigzag lattices in [16]. In [97], negative constants are even questioned with respect to consistency and stability.

On the other hand, some authors have presented homogenization approaches retaining the second order terms, e.g., for chiral lattices in [58] and for 2D and 3D lattices allowing more than a single joint in a base cell in [36]. The homogenization approach presented in [36] allows the authors to identify positive constants of the rectangular lattice when retaining second order terms. Not clearly classifiable is the homogenization approach presented in [72], where second order terms are retained in the first place, but at some point it is decided that second order derivatives can be neglected on the basis of the strain definition. However, the authors ensure that the compatibility of kinematics and equilibrium of forces and moments are guaranteed. Furthermore, the MECs based on first order terms for the regular hexagon honeycomb lattice presented in [15] do not agree with the well-established ones presented in [38], leading the authors in [46] to conclude that the validity of the Taylor series approach is in question. For their non-Taylor series based homogenization approach presented in [46], closed form expressions for the MECs with positive sign are found. However, positive constants of the rectangular lattice were identified in [36] using the Taylor series expansion even though second order terms were retained.

Both, the positive and negative constants derived in [53] are often used in the literature for the verification of MECs obtained by either new or similar homogenization methods and mainly serve as comparison for limiting cases of lattices. In [86], the MECs for a limiting case of the studied chiral auxetic lattice are compared with positive constants for the triangular lattice presented in [53]. The authors in [58] refer to both positive and negative constants for the triangular lattice presented in [53], which are shown to be obtained for a limiting case of the homogenization approach presented therein. In [16], the positive constants obtained for the triangular and square lattice in [53] are used for comparison with the MECs identified for limiting cases of zigzag chiral lattices. In [36], the MECs of the square lattice based on the presented homogenization approach are compared with positive and negative constants derived in [53].

[1] "The continuum material element cannot be less than the characteristic cell size over which the continuum strain energy density is defined." and "The strain energy function averaged over this volume of element should be positive definite and not the pointwise local strain energy function." [53]

Summarized, there is some controversy in the literature about the validity of the method in general. On the one hand, the resulting strain energy density appears to violate the positive definiteness criterion defined in [30] for certain cases when retaining second order terms in the Taylor series expansion of the kinematic fields. On the other hand, the derived MECs lead to a lack of equilibrium of forces when neglecting second-order terms [10]. Therefore, a numerical study is performed in Chapter 5 to evaluate the predictive capabilities of both positive and negative constants for the mechanical response of finite-sized lattice structures using discrete models as a basis for comparison.

For building a framework for further research rather than comparing homogenization methods, the homogenization method based on the Taylor series expansion [10, 53] is considered to be the most suitable method. It can be easily applied to various 3D lattice materials. Furthermore, only first order terms are retained. The reason for this is two-fold. Negative constants lead to oscillating solution fields, if the element size is smaller than the internal characteristic length of the lattice, which is not the case when using positive constants, cf. Chapter 5. Additionally, the positive constants are much easier to determine since no integration by parts is required in the derivation. Consequently, only positive constants are derived for the 3D lattices in the next section. The non-equilibrium of forces at the origin joint as a consequence of these constants is accepted on the basis of the results obtained for the 2D lattice simulations in Chapter 5. Therein, it is shown that positive constants have no disadvantages compared to negative constants at least for the lattices studied in this work.

3.3 Micropolar elastic constants of 3D centrosymmetric lattices

The configuration of each investigated lattice, namely, primitive orthorhombic, body centered cubic, and body centered cubic reinforced by primitive cubic, is schematically depicted in Figures 3.2, 3.3, and 3.4, respectively. Each lattice member is modeled as a Hermite beam showing two end nodes I and J, see Figure 3.1. The stiffness matrix of such a beam element, $[\underset{\sim}{\mathbf{k}}^{(e)}_{\text{local}}]$, and its corresponding vector of nodal kinematics, $[\underline{\mathbf{U}}^{(e)}_{\text{local}}]$, can be found in Appendix C. The stiffness matrix in Eq. (C.1) and the vector of nodal kinematics in Eq. (C.2) are given with respect to the local beam coordinate system. The transformation matrix, $[\underset{\sim}{\mathbf{T}}^{(e)}_{\text{r}}]$, given in Eq. (C.3) is used to transform the quantities to the global basis as

$$[\underset{\sim}{\mathbf{k}}^{(e)}_{\text{global}}] = [\underset{\sim}{\mathbf{T}}^{(e)}_{\text{r}}]^{\text{T}}[\underset{\sim}{\mathbf{k}}^{(e)}_{\text{local}}][\underset{\sim}{\mathbf{T}}^{(e)}_{\text{r}}] \quad , \tag{3.6}$$

$$[\underline{\mathbf{U}}^{(e)}_{\text{global}}] = [\underset{\sim}{\mathbf{T}}^{(e)}_{\text{r}}][\underline{\mathbf{U}}^{(e)}_{\text{local}}] \quad . \tag{3.7}$$

with the corresponding global vector of nodal kinematics

$$[\underline{\mathbf{U}}^{(e)}_{\text{global}}] = [\underline{\mathbf{U}}_I, \underline{\mathbf{\Phi}}_I, \underline{\mathbf{U}}_J, \underline{\mathbf{\Phi}}_J]^{\text{T}} = [U_{I1}, U_{I2}, U_{I3}, \Phi_{I1}, \Phi_{I2}, \Phi_{I3}, U_{J1}, U_{J2}, U_{J3}, \Phi_{J1}, \Phi_{J2}, \Phi_{J3}]^{\text{T}} \quad . \tag{3.8}$$

The strain energy of each lattice member in terms of joint displacements and rotations reads

$$\begin{aligned} W_{IJ}(\underline{\mathbf{U}}_I, \underline{\mathbf{\Phi}}_I, \underline{\mathbf{U}}_J, \underline{\mathbf{\Phi}}_J) &= \frac{1}{2}[\underline{\mathbf{U}}^{(e)}_{\text{local}}]^{\text{T}}[\underset{\sim}{\mathbf{k}}^{(e)}_{\text{local}}][\underline{\mathbf{U}}^{(e)}_{\text{local}}] \quad , \\ &= \frac{1}{2}[\underline{\mathbf{U}}^{(e)}_{\text{global}}]^{\text{T}}[\underset{\sim}{\mathbf{k}}^{(e)}_{\text{global}}][\underline{\mathbf{U}}^{(e)}_{\text{global}}] \quad . \end{aligned} \tag{3.9}$$

The strain energy density of the continuum approximation of the base cells studied are then obtained by using Eq. (3.3), which follows in terms of stiffness matrix and vector of nodal kinematics of each member OK as

$$\psi = \frac{1}{V_{\mathrm{bc}}} \left(\sum_{K=1}^{n_{\mathrm{bc}}} W_{OK}(\underline{\mathbf{u}}, \underline{\boldsymbol{\phi}}, \underline{\mathbf{U}}_K, \underline{\boldsymbol{\Phi}}_K) \right) = \frac{1}{V_{\mathrm{bc}}} \left(\sum_{(e)=1}^{n_{\mathrm{bc}}} \frac{1}{2} [\underline{\mathbf{U}}^{(e)}_{\mathrm{global}}]^{\mathrm{T}} [\underset{\sim}{\mathbf{k}}^{(e)}_{\mathrm{global}}] [\underline{\mathbf{U}}^{(e)}_{\mathrm{global}}] \right) . \tag{3.10}$$

The joint displacements and rotations of each member are then expressed in terms of the displacements, $\underline{\mathbf{u}}$, and rotations, $\underline{\boldsymbol{\phi}}$, of a commonly shared origin joint O located in the center of the base cell by using Eq. (3.2). Only terms up to the first order are considered based on the discussion in Section 3.2. The strain energy density of the continuum approximation can then be expressed in terms of strain and curvature, see Eq. (3.3).

From the strain energy density, the components of the fourth order elasticity tensors $\mathbb{A}_{ijkl}$, $\mathbb{B}_{ijkl}$, and $\mathbb{C}_{ijkl}$ can be determined by using Eq. (2.54), respectively. For centrosymmetric lattices, the elasticity tensor $\mathbb{C}_{ijkl}$ vanishes, see, e.g., [88], which is the case for the uniform periodically repeating 2D base cells discussed in [53]. This is also true for the 3D lattices studied in the present work, which is confirmed by the fact that no couple terms could be identified in the derived strain energy potential. Following [53], the components of the elasticity tensors are based on strain measures defined via applying the gradient from the left, which require the left hand-side definition of stress components. For the conversion of elasticity components in order to fit to strain measures based on the right gradient, see Section 2.6.

A comparison with ABAQUS is performed to verify a correct transformation of the local stiffness matrices given in Eq. (3.6), which enter Eq. (3.10). For each base cell, an overall stiffness matrix $[\underset{\sim}{\mathbf{K}}_{\mathrm{bc}}]$ is assembled, which is composed of the individual stiffness matrices, $[\underset{\sim}{\mathbf{k}}^{(e)}]$, of all its members, n_{bc}. The assembled global stiffness matrix reads

$$[\underset{\sim}{\mathbf{K}}_{\mathrm{bc}}] = \sum_{(e)=1}^{n_{\mathrm{bc}}} [\underset{\sim}{\mathbf{T}}^{(e)}_{\mathrm{k}}]^{\mathrm{T}} \underbrace{[\underset{\sim}{\mathbf{T}}^{(e)}_{\mathrm{r}}]^{\mathrm{T}} [\underset{\sim}{\mathbf{k}}^{(e)}_{\mathrm{local}}] [\underset{\sim}{\mathbf{T}}^{(e)}_{\mathrm{r}}]}_{[\underset{\sim}{\mathbf{k}}^{(e)}_{\mathrm{global}}]]} [\underset{\sim}{\mathbf{T}}^{(e)}_{\mathrm{k}}] \quad . \tag{3.11}$$

where $[\underset{\sim}{\mathbf{T}}^{(e)}_{\mathrm{k}}]$ accounts for the connectivity of the individual elements. The resulting stiffness matrix is compared to the stiffness matrix assembled by ABAQUS using Euler-Bernoulli two-node cubic beam elements (`B33`) provided by ABAQUS. These elements correspond to the Hermite beam element. To output the stiffness matrix assembled by ABAQUS, a substructure needs to be generated in a first step to be able to create a conventional .mtx file in a subsequent step. The stiffness matrix can then be obtained via the keyword `*SUBSTRUCTURE MATRIX OUTPUT`. The differences between the stiffness matrices obtained from the evaluation of Eq. (3.6) using numerical values for the analytical variables and for ABAQUS are considered negligible.

3.3.1 Primitive orthorhombic and primitive cubic lattice

The PO lattice is composed of six lattice members OK with end nodes, $K \in \{\mathrm{A}, \mathrm{B}, \mathrm{C}, \mathrm{D}, \mathrm{E}, \mathrm{F}\}$, connected at the center O of the base cell as depicted in Figure 3.2. For the derivation of the MECs, opposite members such as OA and OC need to show the same bending stiffness with respect to a common axis. The bending stiffness of an individual member is directly related to the definition of the local beam coordinate system. This needs to be considered when defining the local beam coordinate systems for each member, as shown for the PO lattice base cell in Figure 3.2. For example, the bending stiffnesses of members OA and OC according to their local beam axes $\underline{\mathbf{e}}_m$ and $\underline{\mathbf{e}}_n$ follow as $E_{\mathrm{s}} I_{\mathrm{mA}} = E_{\mathrm{s}} I_{\mathrm{mC}} = E_{\mathrm{s}} I_{\mathrm{m1}}$ and $E_{\mathrm{s}} I_{\mathrm{nA}} = E_{\mathrm{s}} I_{\mathrm{nC}} = E_{\mathrm{s}} I_{\mathrm{n1}}$, respectively, where E_{s} denotes the Young's modulus of the parent material and $I_{\mathrm{m}}, I_{\mathrm{n}}$ are the area moments of inertia corresponding to $\underline{\mathbf{e}}_m$ and $\underline{\mathbf{e}}_n$. Note that the indices for the area moments of inertia are not italicized to avoid confusion with tensorial quantities. It follows that only three sets of geometrical properties remain for the

lattice members, i.e., three unique lattice members composed of opposite members regarding the bending stiffness remain, OA=OC, OB=OD, and OE=OF. Otherwise, the centrosymmetry is broken and coupling terms are obtained. However, for different cross-sections or polar moments of inertia of opposite members, the centrosymmetry is preserved and the average values replace the individual values. In this thesis, opposite members are assumed to have the same cross-sections, area moments of inertia, and polar moments of inertia resulting in three sets of geometrical properties, i.e., OA=OC, OB=OD, and OE=OF.

The strain energy density for the PO lattice using Eq. (3.10) reads

$$\psi^{\mathrm{PO}} = \frac{1}{V_{\mathrm{bc}}} \sum_{K}^{n_{\mathrm{bc}}=6} W_{OK} \quad , \tag{3.12}$$

where $V_{\mathrm{bc}} = l_1 l_2 l_3$ is the volume occupied by the base cell. The strain energy density in terms of strain measures using Eq. (3.2) leads to

$$\begin{aligned}
\psi^{\mathrm{PO}} = {} & \frac{A_1 E_{\mathrm{s}} \varepsilon_{11}^2}{2 l_2 l_3} + \frac{A_2 E_{\mathrm{s}} \varepsilon_{22}^2}{2 l_1 l_3} + \frac{A_3 E_{\mathrm{s}} \varepsilon_{33}^2}{2 l_1 l_2} + \frac{2 E_{\mathrm{s}} I_{\mathrm{m1}} \kappa_{12}^2}{l_2 l_3} \\
& + \frac{6 E_{\mathrm{s}} I_{\mathrm{m1}} \varepsilon_{13}^2}{l_1^2 l_2 l_3} + \frac{2 E_{\mathrm{s}} I_{\mathrm{m2}} \kappa_{21}^2}{l_1 l_3} + \frac{6 E_{\mathrm{s}} I_{\mathrm{m2}} \varepsilon_{23}^2}{l_1 l_2^2 l_3} + \frac{2 E_{\mathrm{s}} I_{\mathrm{m3}} \kappa_{31}^2}{l_1 l_2} \\
& + \frac{6 E_{\mathrm{s}} I_{\mathrm{m3}} \varepsilon_{32}^2}{l_1 l_2 l_3^2} + \frac{2 E_{\mathrm{s}} I_{\mathrm{n1}} \kappa_{13}^2}{l_2 l_3} + \frac{6 E_{\mathrm{s}} I_{\mathrm{n1}} \varepsilon_{12}^2}{l_1^2 l_2 l_3} + \frac{2 E_{\mathrm{s}} I_{\mathrm{n2}} \kappa_{23}^2}{l_1 l_3} \\
& + \frac{6 E_{\mathrm{s}} I_{\mathrm{n2}} \varepsilon_{21}^2}{l_1 l_2^2 l_3} + \frac{2 E_{\mathrm{s}} I_{\mathrm{n3}} \kappa_{32}^2}{l_1 l_2} + \frac{6 E_{\mathrm{s}} I_{\mathrm{n3}} \varepsilon_{31}^2}{l_1 l_2 l_3^2} + \frac{G_{\mathrm{s}} I_{\mathrm{t1}} \kappa_{11}^2}{2 l_2 l_3} \\
& + \frac{G_{\mathrm{s}} I_{\mathrm{t2}} \kappa_{22}^2}{2 l_1 l_3} + \frac{G_{\mathrm{s}} I_{\mathrm{t3}} \kappa_{33}^2}{2 l_1 l_2} \quad ,
\end{aligned} \tag{3.13}$$

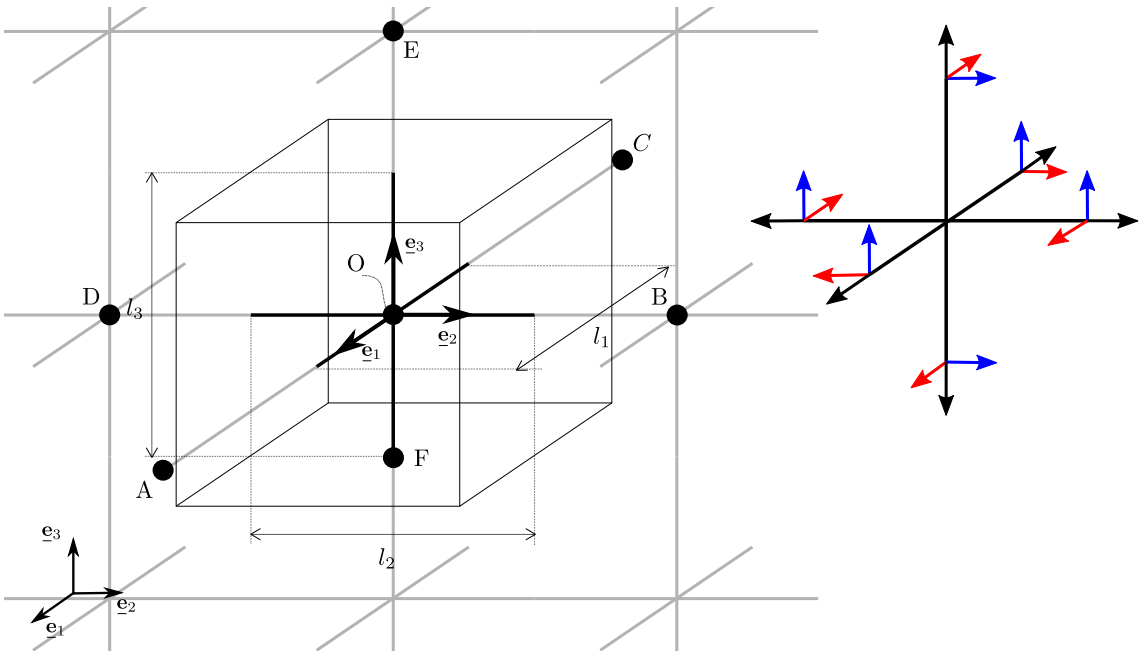

Figure 3.2: Schematic of base cell of PC lattice showing local beam coordinate systems with black, blue, and red arrows denoting axes $\underline{\mathbf{e}}_t$, $\underline{\mathbf{e}}_n$, and $\underline{\mathbf{e}}_m$, respectively.

where A_k, l_k, $I_{\mathrm{m}k}$, $I_{\mathrm{n}k}$, and $I_{\mathrm{t}k}$ denote the cross-section, length, area moment of inertia with respect to the local m- and n-axis, and polar moment of inertia for each lattice member $k = 1, 2, 3$, respectively. The length of the lattice members is shown in Figure 3.2. The MECs are determined by differentiating the strain energy density with respect to the strain measures according to Eq. (2.54). All non-zero components of the elasticity tensors, $\mathbb{A}_{ijkl}$ and $\mathbb{B}_{ijkl}$, are identified as

$$
\begin{aligned}
\mathbb{A}_{1111} &= \frac{A_1 E_\mathrm{s}}{l_2 l_3} \quad , & \mathbb{B}_{1111} &= \frac{G_\mathrm{s} I_{\mathrm{t}1}}{l_2 l_3} \quad , \\
\mathbb{A}_{1212} &= \frac{12 E_\mathrm{s} I_{\mathrm{n}1}}{l_1^2 l_2 l_3} \quad , & \mathbb{B}_{1212} &= \frac{4 E_\mathrm{s} I_{\mathrm{m}1}}{l_2 l_3} \quad , \\
\mathbb{A}_{1313} &= \frac{12 E_\mathrm{s} I_{\mathrm{m}1}}{l_1^2 l_2 l_3} \quad , & \mathbb{B}_{1313} &= \frac{4 E_\mathrm{s} I_{\mathrm{n}1}}{l_2 l_3} \quad , \\
\mathbb{A}_{2121} &= \frac{12 E_\mathrm{s} I_{\mathrm{n}2}}{l_1 l_2^2 l_3} \quad , & \mathbb{B}_{2121} &= \frac{4 E_\mathrm{s} I_{\mathrm{m}2}}{l_1 l_3} \quad , \\
\mathbb{A}_{2222} &= \frac{A_2 E_\mathrm{s}}{l_1 l_3} \quad , & \mathbb{B}_{2222} &= \frac{G_\mathrm{s} I_{\mathrm{t}2}}{l_1 l_3} \quad , \\
\mathbb{A}_{2323} &= \frac{12 E_\mathrm{s} I_{\mathrm{m}2}}{l_1 l_2^2 l_3} \quad , & \mathbb{B}_{2323} &= \frac{4 E_\mathrm{s} I_{\mathrm{n}2}}{l_1 l_3} \quad , \\
\mathbb{A}_{3131} &= \frac{12 E_\mathrm{s} I_{\mathrm{n}3}}{l_1 l_2 l_3^2} \quad , & \mathbb{B}_{3131} &= \frac{4 E_\mathrm{s} I_{\mathrm{m}3}}{l_1 l_2} \quad , \\
\mathbb{A}_{3232} &= \frac{12 E_\mathrm{s} I_{\mathrm{m}3}}{l_1 l_2 l_3^2} \quad , & \mathbb{B}_{3232} &= \frac{4 E_\mathrm{s} I_{\mathrm{n}3}}{l_1 l_2} \quad , \\
\mathbb{A}_{3333} &= \frac{A_3 E_\mathrm{s}}{l_1 l_2} \quad , & \mathbb{B}_{3333} &= \frac{G_\mathrm{s} I_{\mathrm{t}3}}{l_1 l_2} \quad .
\end{aligned}
\tag{3.14}
$$

No non-zero components corresponding to the coupling elasticity tensor $\mathbb{C}_{ijkl}$ could be identified, which is expected due to the considered centrosymmetry of the lattice. The elasticity tensors show orthotropic symmetry as expected, cf. Eq. (B.1). Note that for this lattice the effective Poisson's ratio is zero in all directions. Consequently, all off-diagonal components of the remaining elasticity tensors are zero. A comparison between the MECs derived for the primitive orthorhombic lattice and those derived for the 2D rectangular lattice in [53] can be found in Appendix E.

If all lattice members show the same geometrical properties, namely, $l_k = l$, $I_{\mathrm{m}k} = I_{\mathrm{n}k} = I$, $I_{\mathrm{t}k} = I_t$, and $A_k = A$, the strain energy density of the primitive cubic (PC) lattice, ψ^{PC}, is obtained. This lattice shows cubic symmetry, cf. Eq. (B.2).

3.3.2 Body centered cubic lattice

The BCC lattice is composed of eight lattice members OK with end nodes, $K \in \{\mathrm{A_{top}}, \mathrm{B_{top}}, \mathrm{C_{top}}, \mathrm{D_{top}}, \mathrm{A_{bot}}, \mathrm{B_{bot}}, \mathrm{C_{bot}}, \mathrm{D_{bot}}\}$, connected at the center, O, of the base cell as depicted in Figure 3.3. The BCC lattice spans a cubic base cell with side length, l, resulting in a length, $l_{\mathrm{BCC}} = \sqrt{3}l/2$, for each individual lattice member. For the sake of simplicity, all members possess the same geometrical properties. The local coordinate system of each member of the base cell is shown in Figure 3.3. The strain energy density for the BCC lattice using Eq. (3.10) reads

$$
\psi^{\mathrm{BCC}} = \frac{1}{V_{\mathrm{bc}}} \sum_{K}^{n_{\mathrm{bc}}=8} W_{OK} \quad , \tag{3.15}
$$

with $V_{\mathrm{bc}} = l^3$. The strain energy density in terms of strain measures using Eq. (3.2) leads to

$$\begin{aligned}
\psi^{\mathrm{BCC}} = \frac{2\sqrt{3}}{9l^4}(&AE_{\mathrm{s}}\varepsilon_{11}^2 l^2 + 2AE_{\mathrm{s}}\varepsilon_{11}\varepsilon_{22}l^2 + 2AE_{\mathrm{s}}\varepsilon_{11}\varepsilon_{33}l^2 + AE_{\mathrm{s}}\varepsilon_{12}^2 l^2 + 2AE_{\mathrm{s}}\varepsilon_{12}\varepsilon_{21}l^2 + AE_{\mathrm{s}}\varepsilon_{13}^2 l^2 \\
&+ 2AE_{\mathrm{s}}\varepsilon_{13}\varepsilon_{31}l^2 + AE_{\mathrm{s}}\varepsilon_{21}^2 l^2 + AE_{\mathrm{s}}\varepsilon_{22}^2 l^2 + 2AE_{\mathrm{s}}\varepsilon_{22}\varepsilon_{33}l^2 + AE_{\mathrm{s}}\varepsilon_{23}^2 l^2 + 2AE_{\mathrm{s}}\varepsilon_{23}\varepsilon_{32}l^2 \\
&+ AE_{\mathrm{s}}\varepsilon_{31}^2 l^2 + AE_{\mathrm{s}}\varepsilon_{32}^2 l^2 + AE_{\mathrm{s}}\varepsilon_{33}^2 l^2 + 32E_{\mathrm{s}}I\varepsilon_{11}^2 - 32E_{\mathrm{s}}I\varepsilon_{11}\varepsilon_{22} - 32E_{\mathrm{s}}I\varepsilon_{11}\varepsilon_{33} + 32E_{\mathrm{s}}I\varepsilon_{12}^2 \\
&- 32E_{\mathrm{s}}I\varepsilon_{12}\varepsilon_{21} + 32E_{\mathrm{s}}I\varepsilon_{13}^2 - 32E_{\mathrm{s}}I\varepsilon_{13}\varepsilon_{31} + 32E_{\mathrm{s}}I\varepsilon_{21}^2 + 32E_{\mathrm{s}}I\varepsilon_{22}^2 - 32E_{\mathrm{s}}I\varepsilon_{22}\varepsilon_{33} + 32E_{\mathrm{s}}I\varepsilon_{23}^2 \\
&- 32E_{\mathrm{s}}I\varepsilon_{23}\varepsilon_{32} + 32E_{\mathrm{s}}I\varepsilon_{31}^2 + 32E_{\mathrm{s}}I\varepsilon_{32}^2 + 32E_{\mathrm{s}}I\varepsilon_{33}^2 + 8E_{\mathrm{s}}I\kappa_{11}^2 l^2 - 8E_{\mathrm{s}}I\kappa_{11}\kappa_{22}l^2 - 8E_{\mathrm{s}}I\kappa_{11}\kappa_{33}l^2 \\
&+ 8E_{\mathrm{s}}I\kappa_{12}^2 l^2 - 8E_{\mathrm{s}}I\kappa_{12}\kappa_{21}l^2 + 8E_{\mathrm{s}}I\kappa_{13}^2 l^2 - 8E_{\mathrm{s}}I\kappa_{13}\kappa_{31}l^2 + 8E_{\mathrm{s}}I\kappa_{21}^2 l^2 + 8E_{\mathrm{s}}I\kappa_{22}^2 l^2 - 8E_{\mathrm{s}}I\kappa_{22}\kappa_{33}l^2 \\
&+ 8E_{\mathrm{s}}I\kappa_{23}^2 l^2 - 8E_{\mathrm{s}}I\kappa_{23}\kappa_{32}l^2 + 8E_{\mathrm{s}}I\kappa_{31}^2 l^2 + 8E_{\mathrm{s}}I\kappa_{32}^2 l^2 + 8E_{\mathrm{s}}I\kappa_{33}^2 l^2 + G_{\mathrm{s}}I_{\mathrm{t}}\kappa_{11}^2 l^2 \\
&+ 2G_{\mathrm{s}}I_{\mathrm{t}}\kappa_{11}\kappa_{22}l^2 + 2G_{\mathrm{s}}I_{\mathrm{t}}\kappa_{11}\kappa_{33}l^2 + G_{\mathrm{s}}I_{\mathrm{t}}\kappa_{12}^2 l^2 + 2G_{\mathrm{s}}I_{\mathrm{t}}\kappa_{12}\kappa_{21}l^2 + G_{\mathrm{s}}I_{\mathrm{t}}\kappa_{13}^2 l^2 + 2G_{\mathrm{s}}I_{\mathrm{t}}\kappa_{13}\kappa_{31}l^2 \\
&+ G_{\mathrm{s}}I_{\mathrm{t}}\kappa_{21}^2 l^2 + G_{\mathrm{s}}I_{\mathrm{t}}\kappa_{22}^2 l^2 + 2G_{\mathrm{s}}I_{\mathrm{t}}\kappa_{22}\kappa_{33}l^2 + G_{\mathrm{s}}I_{\mathrm{t}}\kappa_{23}^2 l^2 + 2G_{\mathrm{s}}I_{\mathrm{t}}\kappa_{23}\kappa_{32}l^2 + G_{\mathrm{s}}I_{\mathrm{t}}\kappa_{31}^2 l^2 \\
&+ G_{\mathrm{s}}I_{\mathrm{t}}\kappa_{32}^2 l^2 + G_{\mathrm{s}}I_{\mathrm{t}}\kappa_{33}^2 l^2) \quad .
\end{aligned} \tag{3.16}$$

All non-zero components of the elasticity tensors, $\mathbb{A}_{ijkl}$ and $\mathbb{B}_{ijkl}$, are identified as

$$\begin{aligned}
\mathbb{A}_{1111} &= \frac{4\sqrt{3}E_{\mathrm{s}}\left(Al^2 + 32I\right)}{9l^4} \quad , \qquad \mathbb{B}_{1111} = \frac{4\sqrt{3}\left(G_{\mathrm{s}}I_{\mathrm{t}} + 8E_{\mathrm{s}}I\right)}{9l^2} \quad , \\
\mathbb{A}_{1122} &= \frac{4\sqrt{3}E_{\mathrm{s}}\left(Al^2 - 16I\right)}{9l^4} \quad , \qquad \mathbb{B}_{1122} = \frac{4\sqrt{3}\left(G_{\mathrm{s}}I_{\mathrm{t}} - 4E_{\mathrm{s}}I\right)}{9l^2} \quad ,
\end{aligned} \tag{3.17}$$

with

$$\begin{aligned}
\mathbb{A}_{iiii} = \mathbb{A}_{ijij} = \mathbb{A}_{1111} \quad , \qquad \mathbb{B}_{iiii} = \mathbb{B}_{ijij} = \mathbb{B}_{1111} \quad , \\
\mathbb{A}_{iijj} = \mathbb{A}_{ijji} = \mathbb{A}_{1122} \quad , \qquad \mathbb{B}_{iijj} = \mathbb{B}_{ijij} = \mathbb{B}_{1122} \quad .
\end{aligned} \tag{3.18}$$

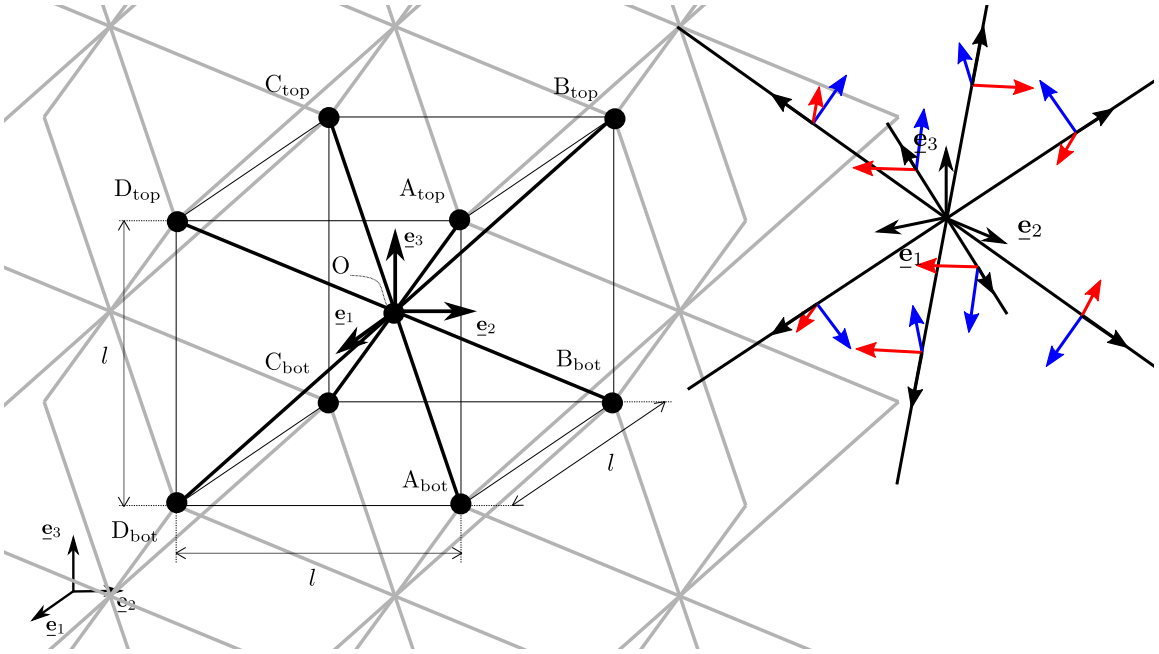

Figure 3.3: Schematic of base cell of BCC lattice showing local beam coordinate systems with black, blue, and red arrows denoting axes $\underline{\mathbf{e}}_t$, $\underline{\mathbf{e}}_n$, and $\underline{\mathbf{e}}_m$, respectively.

This results in 21 non-zero components for each of the two elasticity tensors. No non-zero components corresponding to the coupling elasticity tensor $\mathbb{C}_{ijkl}$ could be identified.

3.3.3 Body centered cubic reinforced by primitive cubic lattice

The BCCCP lattice is composed of 14 lattice members with end nodes of the BCC and PC lattices, which are connected at the center, O, of the base cell as depicted in Figure 3.4. The lattice represents a superposition of BCC and PC lattices. The base cell of the BCCCP lattice spans a cubic base cell with side length, l. The length of the lattice members belonging to the BCC lattice contribution is $l^{\mathrm{BCC}} = \sqrt{3}l/2$ whereas for the PC contribution the length of the members is $l_{\mathrm{PC}} = l/2$. For the sake of simplicity, the geometric properties of all members belonging to one of the contributing lattices are assumed to be the same. The local coordinate system of each member is shown in Figure 3.4. The strain energy density for the BCCCP lattice is obtained by the superposition of the individual strain energy densities of BCC and PC lattices

$$\psi^{\mathrm{BCCCP}} = \psi^{\mathrm{BCC}} + \psi^{\mathrm{PC}} \quad . \tag{3.19}$$

The contribution of the strain energy density ψ^{PC} follows from Eq. (3.13) with $l_k = l^{\mathrm{PC}}$, $A_k = A^{\mathrm{PC}}$, $I_{\mathrm{m}k} = I_{\mathrm{n}k} = I^{\mathrm{PC}}$, and $I_{\mathrm{t}k} = I_{\mathrm{t}}^{\mathrm{PC}}$ for $k = 1, 2, 3$. The contribution of the strain energy density ψ^{BCC} follows directly from Eq. (3.16), where quantities are superscripted by BCC. For the sake of brevity, the resulting strain energy density is not explicitly stated.

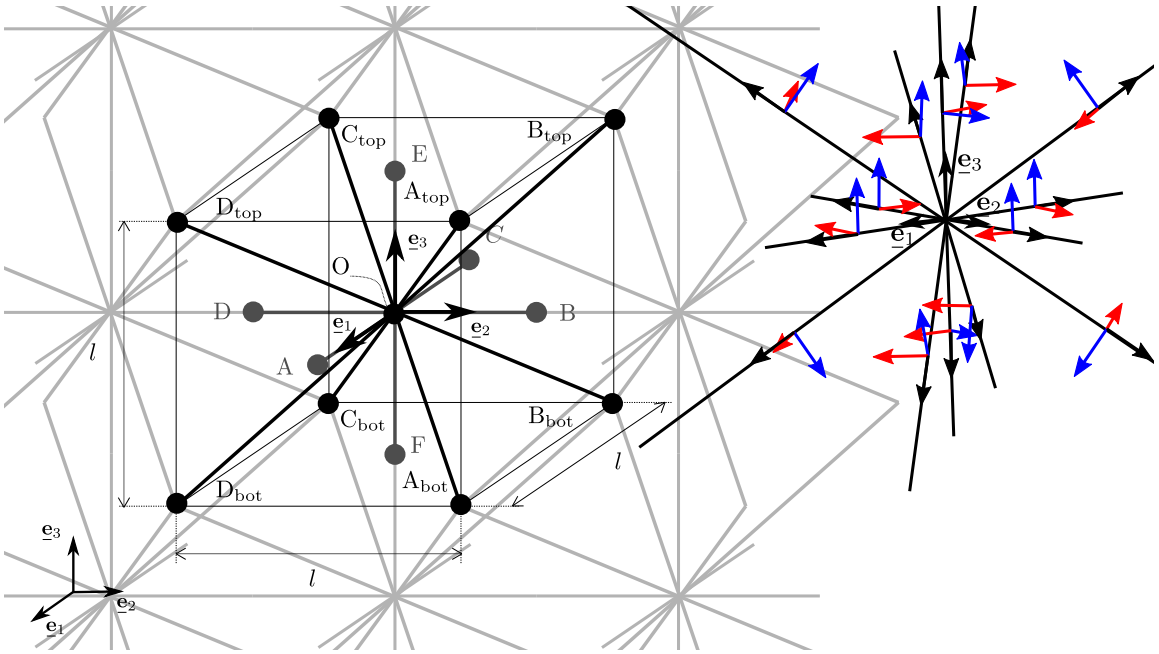

Figure 3.4: Schematic of base cell of BCCCP lattice showing local beam coordinate systems with black, blue, and red arrows denoting axes $\underline{\mathbf{e}}_t$, $\underline{\mathbf{e}}_n$, and $\underline{\mathbf{e}}_m$, respectively.

The MECs of this lattice can be determined either by differentiating the strain energy density given in Eq. (3.19) with respect to the strain measures or by superposition of the elasticity tensors of the BCC and PC lattice. The elasticity tensors of the BCCCP lattice read

$$\underset{\approx}{\mathbb{A}}^{\mathrm{BCCCP}} = \underset{\approx}{\mathbb{A}}^{\mathrm{PC}} + \underset{\approx}{\mathbb{A}}^{\mathrm{BCC}} \quad , \quad \underset{\approx}{\mathbb{B}}^{\mathrm{BCCCP}} = \underset{\approx}{\mathbb{B}}^{\mathrm{PC}} + \underset{\approx}{\mathbb{B}}^{\mathrm{BCC}} \quad . \tag{3.20}$$

Note that $\mathbb{C}_{ijkl}^{\mathrm{BCCCP}} = 0$. The components read

$$\begin{aligned}
\mathbb{A}_{1111} &= \frac{\sqrt{3}E_{\mathrm{s}}\left(4A^{\mathrm{BCC}}l^2 + 128I^{\mathrm{BCC}} + 3\sqrt{3}A^{\mathrm{PC}}l^2\right)}{9l^4} \quad , \quad \mathbb{B}_{1111} = \frac{\sqrt{3}\left(32E_{\mathrm{s}}I^{\mathrm{BCC}} + 4G_{\mathrm{s}}I_{\mathrm{t}}^{\mathrm{BCC}} + 3\sqrt{3}G_{\mathrm{s}}I_{\mathrm{t}}^{\mathrm{PC}}\right)}{9l^2} \quad , \\
\mathbb{A}_{1122} &= \frac{4\sqrt{3}E_{\mathrm{s}}\left(A^{\mathrm{BCC}}l^2 - 16I^{\mathrm{BCC}}\right)}{9l^4} \quad , \quad \mathbb{B}_{1122} = \frac{4\sqrt{3}\left(G_{\mathrm{s}}I_{\mathrm{t}}^{\mathrm{BCC}} - 4E_{\mathrm{s}}I^{\mathrm{BCC}}\right)}{9l^2} \quad , \\
\mathbb{A}_{1212} &= \frac{4\sqrt{3}E_{\mathrm{s}}\left(A^{\mathrm{BCC}}l^2 + 32I^{\mathrm{BCC}} + 9\sqrt{3}I^{\mathrm{PC}}\right)}{9l^4} \quad , \quad \mathbb{B}_{1212} = \frac{4\sqrt{3}\left(8E_{\mathrm{s}}I^{\mathrm{BCC}} + 3\sqrt{3}E_{\mathrm{s}}I^{\mathrm{PC}} + G_{\mathrm{s}}I_{\mathrm{t}}^{\mathrm{BCC}}\right)}{9l^2} \quad , \\
\mathbb{A}_{1221} &= \frac{4\sqrt{3}E_{\mathrm{s}}\left(A^{\mathrm{BCC}}l^2 - 16I^{\mathrm{BCC}}\right)}{9l^4} \quad , \quad \mathbb{B}_{1221} = \frac{4\sqrt{3}\left(G_{\mathrm{s}}I_{\mathrm{t}}^{\mathrm{BCC}} - 4E_{\mathrm{s}}I^{\mathrm{BCC}}\right)}{9l^2} \quad ,
\end{aligned} \tag{3.21}$$

with

$$\mathbb{A}_{iiii} = \mathbb{A}_{1111} \quad , \quad \mathbb{A}_{ijij} = \mathbb{A}_{1212} \quad , \quad \mathbb{A}_{ijji} = \mathbb{A}_{1221} \quad , \quad \mathbb{A}_{iijj} = \mathbb{A}_{1122} \quad . \tag{3.22}$$

As expected, the elasticity tensors show cubic symmetry, cf. Eq. (B.2). The off-diagonal components of these tensors are different from zero compared to the PC lattice, resulting from the contribution of the BCC lattice introducing Poisson effects.

Chapter 4

FEM implementation

In the following, the FEM implementation is outlined. Starting from the field equations of the micropolar continuum given in Chapter 2, the equations necessary for the FEM implementation are derived. Various implementations are made to accommodate geometrically nonlinear and linear micropolar boundary value problems. The implementation of the 3D geometrically nonlinear problem mainly follows [8, 26], where a discrete, i.e., a numerical consistent tangent matrix, is used instead of an analytical one to overcome excessive implementation work [8]. The framework for this implementation is ABAQUS, which is a robust and widely accepted commercial FEM program. The implementation of the linear problem considering two and three dimensions follows [53]. ABAQUS as well as the open-source FEM software NGSolve serve as the basis for the implementations to achieve the desired flexibility in post-processing of the simulation results and to employ their respective advantages. On the one hand, in ABAQUS, the postprocessing of results is tedious for user elements, which is the implementation interface used in this work. On the other hand, ABAQUS offers the possibility to employ user elements in conjunction with any other element from the element library and, hence, makes it interesting for industrial applications. In contrast, NGSolve provides convenient postprocessing capabilities based on the python based implementation interface. However, it does not provide any element library.

4.1 Geometrically nonlinear micropolar continuum in 3D

4.1.1 General concept

A total Lagrangian formulation for the FEM implementation is aimed for in order to overcome the necessity of transforming the elasticity tensors according to Eq. (2.77). The starting point is the weak form of the Lagrangian equations as derived, e.g., in [26, 28]. In [26], the derivation is based on introducing arbitrary vector valued weighting or test functions $\delta\underline{\mathbf{u}}$ and $\delta\underline{\boldsymbol{\phi}}$, which have to be sufficiently often differentiable and must vanish in regions of prescribed kinematic boundary conditions. The test functions are multiplied to the strong form of the BVP being composed of the Eulerian equilibrium equations given in Eqs. (2.36) and (2.37) including the corresponding boundary conditions given in Eqs. (2.45), (2.46), and (2.44). Integration by parts and some algebraic manipulations yield the principle of virtual work in the Eulerian description. By

integral and variable transformations, the principle of virtual work in the Lagrangian description is obtained, for further details see [26]. It reads

$$A_{\text{int}} - A_{\text{ext}} = G(\underline{\mathbf{u}}, \underline{\boldsymbol{\phi}}, \delta\underline{\mathbf{u}}, \delta\underline{\boldsymbol{\phi}}) = 0 \quad ,$$
$$\int_{\mathcal{R}_0} \underset{\sim}{\breve{\mathbf{T}}} : \delta\underset{\sim}{\mathbf{E}} + {}^{\kappa}\underset{\sim}{\breve{\mathbf{T}}} : \delta\underset{\sim}{\boldsymbol{\mathscr{K}}} \, \mathrm{d}V - \int_{\mathcal{R}_0} \rho_0 \underline{\mathbf{f}} \cdot \delta\underline{\mathbf{u}} + \rho_0 \underline{\mathbf{m}} \cdot \delta\underline{\boldsymbol{\phi}} \, \mathrm{d}V - \int_{\partial\mathcal{R}_0} \underline{\breve{\mathbf{t}}}^* \cdot \delta\underline{\mathbf{u}} + {}^{\kappa}\underline{\breve{\mathbf{t}}}^* \cdot \delta\underline{\boldsymbol{\phi}} \, \mathrm{d}S = 0 \quad , \tag{4.1}$$

where A_{int} and A_{ext} denote the virtual work of internal and external forces, respectively, G represents a functional based on displacement and rotation fields, $\delta\underset{\sim}{\mathbf{E}}$ and $\delta\underset{\sim}{\boldsymbol{\mathscr{K}}}$ represent the virtual relative Lagrangian stretch and wryness tensors, respectively. The virtual displacement and microrotation fields are denoted by $\delta\underline{\mathbf{u}}$ and $\delta\underline{\boldsymbol{\phi}}$, respectively. The applied surface tractions and moments given in Eq. (2.44) are denoted as $\underline{\breve{\mathbf{t}}}^*$ and ${}^{\kappa}\underline{\breve{\mathbf{t}}}^*$, respectively. In [26], the virtual strain measures are derived on the basis of expressing the external loads in Eq. (4.1) by using the Lagrangian equilibrium equations Eqs. (2.42) and (2.43) and subsequently equating the coefficients. The virtual strain measures read

$$\delta\underset{\sim}{\mathbf{E}} = \underset{\sim}{\mathbf{R}}^{\mathrm{T}}(\delta\underline{\mathbf{u}} \otimes \underline{\boldsymbol{\nabla}}_X + \mathrm{sk}(\delta\underline{\boldsymbol{\phi}})^{\mathrm{T}}\underset{\sim}{\mathbf{F}}) \quad , \tag{4.2}$$
$$\delta\underset{\sim}{\boldsymbol{\mathscr{K}}} = \underset{\sim}{\mathbf{R}}^{\mathrm{T}}\delta(\underline{\boldsymbol{\phi}} \otimes \underline{\boldsymbol{\nabla}}_X) \quad , \tag{4.3}$$

where $\mathrm{sk}(\cdot)$ takes an axial vector and gives the corresponding skew-symmetric matrix as given in Eq. (A.19). Inserting Eqs. (4.2) and (4.3) into the virtual work in Eq. (4.1) yields

$$G(\underline{\mathbf{u}}, \underline{\boldsymbol{\phi}}, \delta\underline{\mathbf{u}}, \delta\underline{\boldsymbol{\phi}}) = \int_{\mathcal{R}_0} \underset{\sim}{\breve{\mathbf{T}}} : (\underset{\sim}{\mathbf{R}}^{\mathrm{T}}(\delta\underline{\mathbf{u}} \otimes \underline{\boldsymbol{\nabla}}_X + \mathrm{sk}(\delta\underline{\boldsymbol{\phi}})^{\mathrm{T}}\underset{\sim}{\mathbf{F}})) + {}^{\kappa}\underset{\sim}{\breve{\mathbf{T}}} : \underset{\sim}{\mathbf{R}}^{\mathrm{T}}(\delta\underline{\boldsymbol{\phi}} \otimes \underline{\boldsymbol{\nabla}}_X) \, \mathrm{d}V$$
$$- \int_{\mathcal{R}_0} \rho_0 \underline{\mathbf{f}} \cdot \delta\underline{\mathbf{u}} + \rho_0 \underline{\mathbf{m}} \cdot \delta\underline{\boldsymbol{\phi}} \, \mathrm{d}V - \int_{\partial\mathcal{R}_0} \underline{\breve{\mathbf{t}}}^* \cdot \delta\underline{\mathbf{u}} + {}^{\kappa}\underline{\breve{\mathbf{t}}}^* \cdot \delta\underline{\boldsymbol{\phi}} \, \mathrm{d}S = 0 \quad . \tag{4.4}$$

To solve the nonlinear BVP by the FEM, the problem is discretized. The computational domain, $\Omega^h = \mathcal{R}_0$, is subdivided into a set of subdomains or finite elements, i.e., $\Omega^{(e)} \in \Omega^h$, reading

$$\Omega^h = \bigcup_{(e)=1}^{n_{\text{el}}} \Omega^{(e)} \quad , \tag{4.5}$$

where (e) is the element number, n_{el} denotes the number of elements, and $\bigcup$ refers to an assembly operator, which enforces the continuity of the kinematic fields between the elements. The superscript h denotes the approximation by finite elements, which will further be attached to quantities indicating their approximative character. To approximate the displacement and rotation fields within an element, the following interpolation functions are used

$$\underline{\mathbf{u}}^h(\underline{\mathbf{X}}, t) = N_I^u(\underline{\mathbf{X}})\underline{\mathbf{u}}_I(t) \quad , \tag{4.6}$$
$$\underline{\boldsymbol{\phi}}^h(\underline{\mathbf{X}}, t) = N_I^{\phi}(\underline{\mathbf{X}})\underline{\boldsymbol{\phi}}_I(t) \quad , \tag{4.7}$$

where I denotes a node at the element level with $I = \{1, ..., n^{(e)}\}$, where $n^{(e)}$ is the number of nodes comprising the element. The interpolation functions show the following properties

$$N_I^u(\underline{\mathbf{X}}_J) = \delta_{IJ} \quad , \quad N_I^{\phi}(\underline{\mathbf{X}}_J) = \delta_{IJ} \quad . \tag{4.8}$$

The virtual displacement and rotation fields are approximated in the same way as the kinematic fields given in Eqs. (4.6) and (4.7), respectively, i.e., Galerkin's method is applied. The approximation reads

$$\delta \underline{\mathbf{u}}^h(\underline{\mathbf{X}}) = N_I^u(\underline{\mathbf{X}})\delta \underline{\mathbf{u}}_I \quad , \tag{4.9}$$

$$\delta \underline{\boldsymbol{\phi}}^h(\underline{\mathbf{X}}) = N_I^\phi(\underline{\mathbf{X}})\delta \underline{\boldsymbol{\phi}}_I \quad . \tag{4.10}$$

An isoparametric element is aimed for, i.e., the geometry or position vectors are approximated in the same way as the displacement field, reading

$$\underline{\mathbf{x}}^h(\underline{\mathbf{X}}, t) = N_I^u(\underline{\mathbf{X}})\underline{\mathbf{x}}_I(t) \quad , \tag{4.11}$$

$$\underline{\mathbf{X}}^h(\underline{\mathbf{X}}, t) = N_I^u(\underline{\mathbf{X}})\underline{\mathbf{X}}_I(t) \quad . \tag{4.12}$$

In the following, the interpolation functions are also called shape functions.

To solve the discretized nonlinear BVP, the problem is linearized and solved employing an incrementally-iterative procedure, i.e., a sequence of linear problems is solved. Therefore, the virtual work given in Eq. (4.4) is prepared to be solved by the FEM. Following [69], this reads

$$[\delta \underline{\mathbf{y}}^a] \cdot [\underset{\sim}{\mathbf{K}}_{\mathrm{T}}([\underline{\mathbf{y}}^a])][\Delta \underline{\mathbf{y}}] = [\delta \underline{\mathbf{y}}^a] \cdot [\underline{\mathbf{r}}([\underline{\mathbf{y}}^a])] \Rightarrow [\underset{\sim}{\mathbf{K}}_{\mathrm{T}}([\underline{\mathbf{y}}^a])][\Delta \underline{\mathbf{y}}] = [\underline{\mathbf{r}}([\underline{\mathbf{y}}^a])] \quad , \tag{4.13}$$

where $[\underset{\sim}{\mathbf{K}}_{\mathrm{T}}]$ denotes the stiffness matrix, $[\underline{\mathbf{r}}] = [\underline{\mathbf{q}}_{\mathrm{int}}] - [\underline{\mathbf{q}}_{\mathrm{ext}}]$ is the generalized residual vector composed of internal, $[\underline{\mathbf{q}}_{\mathrm{int}}]$, and external force and moment vectors, $[\underline{\mathbf{q}}_{\mathrm{ext}}]$, and $[\underline{\mathbf{y}}] = [\underline{\mathbf{u}}, \underline{\boldsymbol{\phi}}]^{\mathrm{T}}$ denotes the solution vector of the problem, which is composed of the solution variables, namely, nodal displacements and rotations. The corresponding variation and the incremental value or linear change of the solution variables are denoted by $[\delta \underline{\mathbf{y}}] = [\delta \underline{\mathbf{u}}, \delta \underline{\boldsymbol{\phi}}]^{\mathrm{T}}$ and $[\Delta \underline{\mathbf{y}}] = [\Delta \underline{\mathbf{u}}, \Delta \underline{\boldsymbol{\phi}}]^{\mathrm{T}}$, respectively. The superscript a indicates the expansion point of the linearization. The solution variables must be isolated in Eq. (4.4) to be solved in the targeted set of linear equations as indicated by the right hand-side of Eq. (4.13), which is to be solved for $[\Delta \underline{\mathbf{y}}]$. Note that in the following the tensorial quantities are used to determine the components of the residual vector and of the tangent stiffness matrix instead of introducing an operator notation.

Following [69], the linearization of Eq. (4.4) by a Taylor series expansion around point a using the discretized kinematic fields reads

$$\mathrm{Lin}(G^h([\underline{\mathbf{y}}^a], [\delta \underline{\mathbf{y}}^a], [\Delta \underline{\mathbf{y}}])) = G^h([\underline{\mathbf{y}}^a], [\delta \underline{\mathbf{y}}^a]) + DG^h([\underline{\mathbf{y}}^a], [\delta \underline{\mathbf{y}}^a])[\Delta \underline{\mathbf{y}}] \quad , \tag{4.14}$$

where DG^h represents the first order term of the Taylor series. No coupling between displacement and rotation is considered to obtain a linear system of equations as given in Eq. (4.13) [69]. For the linearization of G^h, the same applies as in Eq. (4.4) yielding

$$\mathrm{Lin}(G^h([\underline{\mathbf{y}}^a], [\delta \underline{\mathbf{y}}^a], [\Delta \underline{\mathbf{y}}])) = 0 \Rightarrow DG^h([\underline{\mathbf{y}}^a], [\delta \underline{\mathbf{y}}^a])[\Delta \underline{\mathbf{y}}] = -G^h([\underline{\mathbf{y}}^a], [\delta \underline{\mathbf{y}}^a]) \quad , \tag{4.15}$$

which is associated with the right hand-side of Eq. (4.13). The variation of the residual force and moment vectors for the given expansion point a reads

$$\begin{aligned} -G^h([\underline{\mathbf{y}}^a],[\delta\underline{\mathbf{y}}^a]) &= \bigcup_{(e)=1}^{n_{\mathrm{el}}} -G^h([\underline{\mathbf{y}}^{a(e)}],[\delta\underline{\mathbf{y}}^{a(e)}]) \\ &= \bigcup_{(e)=1}^{n_{\mathrm{el}}} -\int_{\mathcal{R}_0} \breve{\underset{\sim}{\mathbf{T}}} : (\underset{\sim}{\mathbf{R}}^{\mathrm{T}}(\delta\underline{\mathbf{u}}^h \otimes \underline{\boldsymbol{\nabla}}_X + \mathrm{sk}(\delta\underline{\boldsymbol{\phi}}^h)^{\mathrm{T}}\underset{\sim}{\mathbf{F}})) + {}^{\kappa}\breve{\underset{\sim}{\mathbf{T}}} : (\underset{\sim}{\mathbf{R}}^{\mathrm{T}}(\delta\underline{\boldsymbol{\phi}}^h \otimes \underline{\boldsymbol{\nabla}}_X)\,\mathrm{d}V \\ &\quad + \int_{\mathcal{R}_0} \rho_0\underline{\mathbf{f}}\cdot\delta\underline{\mathbf{u}}^h + \rho_0\underline{\mathbf{m}}\cdot\delta\underline{\boldsymbol{\phi}}^h\,\mathrm{d}V + \int_{\partial\mathcal{R}_0} \breve{\underline{\mathbf{t}}}^*\cdot\delta\underline{\mathbf{u}}^h + {}^{\kappa}\breve{\underline{\mathbf{t}}}^*\cdot\delta\underline{\boldsymbol{\phi}}^h\,\mathrm{d}S \quad , \end{aligned} \tag{4.16}$$

Note that the superscript h is not attached to the tensorial quantities for the sake of brevity. The same holds for the element identifier (e). After the isolation of the solution variables as shown in [26], Eq. (4.16) reads

$$-G^h([\underline{\mathbf{y}}^a],[\delta\underline{\mathbf{y}}^a]) = \bigcup_{(e)=1}^{n_{\mathrm{el}}} -[\delta\underline{\mathbf{y}}^{(e)}]\cdot[\underline{\mathbf{r}}^{(e)}] = \bigcup_{(e)=1}^{n_{\mathrm{el}}} -[\delta\underline{\mathbf{y}}^{(e)}]\cdot([\underline{\mathbf{q}}^{(e)}_{\mathrm{int}}]-[\underline{\mathbf{q}}^{(e)}_{\mathrm{ext}}]) \quad , \tag{4.17}$$

where the residual force and moment vector can be split into internal and external parts denoted by $[\underline{\mathbf{q}}^{(e)}_{\mathrm{int}}]$ and $[\underline{\mathbf{q}}^{(e)}_{\mathrm{ext}}]$, respectively. To not end up with matrices specific to a particular element, the residuals are given with respect to a single node I corresponding to a particular element comprised of a certain number of nodes, $n^{(e)}$. The corresponding nodal equations of the element level based on Eq. (4.17) read

$$[\delta\underline{\mathbf{y}}^{(e)}_I]\cdot[\underline{\mathbf{r}}^{(e)}_I] = [\delta\underline{\mathbf{y}}^{(e)}_I]\cdot([\underline{\mathbf{q}}^{(e)}_{\mathrm{int},I}]-[\underline{\mathbf{q}}^{(e)}_{\mathrm{ext},I}]) = \delta\underline{\mathbf{u}}^{(e)}_I\cdot({}^{u}\underline{\mathbf{q}}^{(e)}_{\mathrm{int},I} - {}^{u}\underline{\mathbf{q}}^{(e)}_{\mathrm{ext},I}) + \delta\underline{\boldsymbol{\phi}}^{(e)}_I\cdot({}^{\phi}\underline{\mathbf{q}}^{(e)}_{\mathrm{int},I} - {}^{\phi}\underline{\mathbf{q}}^{(e)}_{\mathrm{ext},I}) \quad , \tag{4.18}$$

where the nodal quantities are arranged as $[\underline{\mathbf{y}}^{(e)}_I] = [u_{1;I}, u_{2;I}, u_{3;I}, \phi_{1;I}, \phi_{2;I}, \phi_{3;I}]^{\mathrm{T}}$, the internal and external force and moment vectors at node I are comprised of $[\underline{\mathbf{q}}^{(e)}_{\mathrm{int};I}] = \left[{}^{u}\underline{\mathbf{q}}^{(e)}_{\mathrm{int};I}, {}^{\phi}\underline{\mathbf{q}}^{(e)}_{\mathrm{int};I}\right]^{\mathrm{T}}$ and $[\underline{\mathbf{q}}^{(e)}_{\mathrm{ext};I}] = \left[{}^{u}\underline{\mathbf{q}}^{(e)}_{\mathrm{ext};I}, {}^{\phi}\underline{\mathbf{q}}^{(e)}_{\mathrm{ext};I}\right]^{\mathrm{T}}$, respectively. In [26], the internal force and moment vectors at node I are given as

$${}^{u}\underline{\mathbf{q}}^{(e)}_{\mathrm{int};I} = \int_V \underset{\sim}{\mathbf{R}}\breve{\underset{\sim}{\mathbf{T}}}\underline{\boldsymbol{\nabla}}_X N^u_I\,\mathrm{d}V \quad , \tag{4.19}$$

$${}^{\phi}\underline{\mathbf{q}}^{(e)}_{\mathrm{int};I} = \int_V \underset{\sim}{\mathbf{R}}{}^{\kappa}\breve{\underset{\sim}{\mathbf{T}}}\underline{\boldsymbol{\nabla}}_X N^{\phi}_I + 2N^{\phi}_I\mathrm{axl}(\mathrm{skew}(\underset{\sim}{\mathbf{F}}\breve{\underset{\sim}{\mathbf{T}}}^{\mathrm{T}}\underset{\sim}{\mathbf{R}}^{\mathrm{T}}))\,\mathrm{d}V \quad , \tag{4.20}$$

with $\mathrm{skew}((\cdot))$ giving the skew-symmetric part of $(\cdot)$, cf. Eq. (A.23), and the external force and moment vectors at node I are given as

$${}^{u}\underline{\mathbf{q}}^{(e)}_{\mathrm{ext};I} = \int_V \rho_0\underline{\mathbf{f}}N^u_I\,\mathrm{d}V + \int_{\partial\mathcal{R}_0}\breve{\underline{\mathbf{t}}}^* N^u_I\,\mathrm{d}S \quad , \tag{4.21}$$

$${}^{\phi}\underline{\mathbf{q}}^{(e)}_{\mathrm{ext};I} = \int_V \rho_0\underline{\mathbf{m}}N^{\phi}_I + \int_{\partial\mathcal{R}_0}{}^{\kappa}\breve{\underline{\mathbf{t}}}^* N^{\phi}_I\,\mathrm{d}S \quad . \tag{4.22}$$

Using Eq. (4.18) the residuals read

$${}^{u}\underline{\mathbf{r}}^{(e)}_I = \int_V \underset{\sim}{\mathbf{R}}\breve{\underset{\sim}{\mathbf{T}}}\underline{\boldsymbol{\nabla}}_X N^u_I - \rho_0\underline{\mathbf{f}}N^u_I\,\mathrm{d}V - \int_{\partial\mathcal{R}_0}\breve{\underline{\mathbf{t}}}^* N^u_I\,\mathrm{d}S \qquad \forall I \notin \partial\mathcal{R}^u_0 \quad , \tag{4.23}$$

$${}^{\phi}\underline{\mathbf{r}}^{(e)}_I = \int_V \underset{\sim}{\mathbf{R}}{}^{\kappa}\breve{\underset{\sim}{\mathbf{T}}}\underline{\boldsymbol{\nabla}}_X N^{\phi}_I + 2N^{\phi}_I\mathrm{axl}(\mathrm{skew}(\underset{\sim}{\mathbf{F}}\breve{\underset{\sim}{\mathbf{T}}}^{\mathrm{T}}\underset{\sim}{\mathbf{R}}^{\mathrm{T}})) - \rho_0\underline{\mathbf{m}}N^{\phi}_I\,\mathrm{d}V - \int_{\partial\mathcal{R}_0}{}^{\kappa}\breve{\underline{\mathbf{t}}}^* N^{\phi}_I\,\mathrm{d}S \qquad \forall I \notin \partial\mathcal{R}^{\phi}_0 \quad . \tag{4.24}$$

For further details on the derivation of the residuals, see [26].

The right term of the linearization of the variational formulation given in Eq. (4.15), DG^h, represents the linear change in the variational formulation around the expansion point $[\underline{\mathbf{y}}^a]$ from which the tangent stiffness matrix can be obtained. Note that for considering only conservative loads, which are independent of the displacement and rotation fields, only the internal forces contribute. The isolation of the solution variables in order to obtain the right hand-side of Eq. (4.13) is mathematically intricate. Furthermore, the analytical expression for the consistent tangent element matrix leads to excessive implementation work, see, e.g., [26, 43, 69]. In [26], the tangent stiffness matrix is derived considering isotropic material, which allows for some simplifications of the equations that are otherwise even more complex for considering anisotropic material.

This motivates to apply the approach suggested in [8] to alternatively determine the tangent stiffness matrix for micropolar problems using a central difference scheme. Therein, the individual element stiffness matrices associated with the assembled stiffness matrix given in Eq. (4.38) are determined numerically based on the element right hand-side residual vectors given in Eqs. (4.23) and (4.24) without external load contribution. The element stiffness matrix is determined via

$$[\underset{\sim}{\mathbf{K}}^{(k)}_{\mathrm{T};IJ}] = \left.\frac{\partial r_{iI}}{\partial y_{jJ}}\right|_k \approx \left.\frac{r_{iI}([\underline{\mathbf{y}}_J] + \vartheta[\underline{\mathbf{e}}_j]) - r_{iI}([\underline{\mathbf{y}}_J] - \vartheta[\underline{\mathbf{e}}_j])}{2\vartheta}\right|_k \quad , \tag{4.25}$$

where the solution vector, $[\underline{\mathbf{y}}]$, is perturbed in each DOF denoted by i, j by an perturbation of size ϑ denoted by the vector $[\underline{\mathbf{e}}]$. Throughout this thesis, the perturbation parameter is chosen as $\vartheta = 10^{-8}$, which depends on machine accuracy and typical values of the solution vector, for further details see [8]. In [8] it is stated that the computation time for the determination of the residuals is even lower than for the determination of the analytical tangent matrix given in [43], although the element residuals need to be computed $2\,(n_{\mathrm{el}}\, n^{(e)} \cdot 6)$ times.

The spatial discretization given in Eq. (4.5) allows the integration over $\mathcal{R}_0$ to be approximated by the sum of the integration over each subdomain, $\Omega^{(e)}$, reading

$$\int_{\mathcal{R}_0} (\cdot)(\underline{\mathbf{X}})\,\mathrm{d}V \approx \bigcup_{(e)=1}^{n_{\mathrm{el}}} \int_{\Omega^{(e)}} (\cdot)^{(e)}(\underline{\mathbf{X}})\,\mathrm{d}\Omega^{(e)} \quad . \tag{4.26}$$

In the following, the superscript (e) is not attached to the element quantities for the sake of brevity. Introducing a parent domain of each element, $\Omega^{(e)}_\xi$, the integration over the global domain can be given as

$$\bigcup_{(e)=1}^{n_{\mathrm{el}}} \int_{\Omega^{(e)}} (\cdot)^{(e)}(\underline{\mathbf{X}})\,\mathrm{d}\Omega^{(e)} = \bigcup_{(e)=1}^{n_{\mathrm{el}}} \int_{\Omega^{(e)}_\xi} (\cdot)^{(e)}(\underline{\boldsymbol{\xi}})\breve{J}_\xi(\underline{\boldsymbol{\xi}})\,\mathrm{d}\Omega^{(e)}_\xi \quad , \tag{4.27}$$

where $\breve{J}_\xi = \det(\partial\underline{\mathbf{X}}/\partial\underline{\boldsymbol{\xi}})$ denotes the determinant of the Jacobian of the element and represents the map between the element reference and its parent configuration. It reads

$$\begin{aligned} \underset{\sim}{\breve{\mathbf{J}}}_\xi(\underline{\boldsymbol{\xi}}) &= \underline{\mathbf{X}}_I \otimes \underline{\boldsymbol{\nabla}}_\xi N_I(\underline{\boldsymbol{\xi}}) \\ &= \begin{bmatrix} \frac{\partial N^{(e)}_I}{\partial\xi} X^{(e)}_{1I} & \frac{\partial N^{(e)}_I}{\partial\eta} X^{(e)}_{1I} & \frac{\partial N^{(e)}_I}{\partial\zeta} X^{(e)}_{1I} \\ \frac{\partial N^{(e)}_I}{\partial\xi} X^{(e)}_{2I} & \frac{\partial N^{(e)}_I}{\partial\eta} X^{(e)}_{2I} & \frac{\partial N^{(e)}_I}{\partial\zeta} X^{(e)}_{2I} \\ \frac{\partial N^{(e)}_I}{\partial\xi} X^{(e)}_{3I} & \frac{\partial N^{(e)}_I}{\partial\eta} X^{(e)}_{3I} & \frac{\partial N^{(e)}_I}{\partial\zeta} X^{(e)}_{3I} \end{bmatrix} \quad . \end{aligned} \tag{4.28}$$

Note that for the ABAQUS implementation in Section 4.1.2, the gradient is applied from the left, cf. Eq. (F.10), and, consequently, $\breve{\underset{\sim}{\mathbf{J}}}_\xi$ does not need to be transposed in the following equations. As the element parent configuration is the same for each element, the Gaussian quadrature scheme is used for the integration over the element domain reading as

$$\int_{\Omega_\xi^{(e)}} (\cdot)(\underline{\boldsymbol{\xi}}) \breve{J}_\xi(\underline{\boldsymbol{\xi}}) \, \mathrm{d}\Omega_\xi^{(e)} \approx \sum_{p=1}^{n_{\mathrm{int}}} (\cdot)(\underline{\boldsymbol{\xi}}_p) \breve{J}_\xi(\underline{\boldsymbol{\xi}}_p) w_p \quad , \tag{4.29}$$

where p denotes the integration point, n_{int} is the number of integration points, $\underline{\boldsymbol{\xi}}_p(\xi_p, \eta_p, \zeta_p)$ represents the vector of the element parent coordinates of each individual integration point, and w_p is the corresponding weighting factor. The element parent coordinates and the corresponding weighting factors of each integration point are known for certain types of elements and can be found in standard finite element text books, see , e.g., [7].

The consideration of conservative loads allows to introduce traction and surface traction boundary conditions at a later stage. Making use of Eqs.(4.26), (4.28), and (4.29), the nodal residual vectors at the element level based on Eqs. (4.23) and (4.24) follow as

$${}^{u}\underline{\mathbf{r}}_I^{(e)} = \sum_{p=1}^{n_{\mathrm{int}}} \left(\underset{\sim}{\mathbf{R}} \breve{\underset{\sim}{\mathbf{T}}}(\underline{\boldsymbol{\xi}}_p) \breve{\underset{\sim}{\mathbf{J}}}_\xi^{-\mathrm{T}}(\underline{\boldsymbol{\xi}}_p) \underline{\boldsymbol{\nabla}}_\xi N_I^u(\underline{\boldsymbol{\xi}}_p) - \rho_0 \underline{\mathbf{f}}(\underline{\boldsymbol{\xi}}_p) N_I^u(\underline{\boldsymbol{\xi}}_p) \right) \breve{J}_\xi(\underline{\boldsymbol{\xi}}_p) w_p \quad , \tag{4.30}$$

$${}^{\phi}\underline{\mathbf{r}}_I^{(e)} = \sum_{p=1}^{n_{\mathrm{int}}} \left(\underset{\sim}{\mathbf{R}}^{\kappa} \breve{\underset{\sim}{\mathbf{T}}}(\underline{\boldsymbol{\xi}}_p) \breve{\underset{\sim}{\mathbf{J}}}_\xi^{-\mathrm{T}}(\underline{\boldsymbol{\xi}}_p) \underline{\boldsymbol{\nabla}}_\xi N_I^\phi(\underline{\boldsymbol{\xi}}_p) - {}^{\chi}\breve{\underline{\mathbf{t}}}(\underline{\boldsymbol{\xi}}_p) N_I^\phi(\underline{\boldsymbol{\xi}}_p) - \rho_0 \underline{\mathbf{m}}(\underline{\boldsymbol{\xi}}_p) N_I^\phi(\underline{\boldsymbol{\xi}}_p) \right) \breve{J}_\xi(\underline{\boldsymbol{\xi}}_p) w_p \quad , \tag{4.31}$$

where in each equation the last term is associated with external forces and moments and the other terms are associated with stresses and couple stresses. The axial stress vector is introduced as ${}^{\chi}\breve{\underline{\mathbf{t}}} = -2\mathrm{axl}(\mathrm{skew}(\mathbf{F}\breve{\underset{\sim}{\mathbf{T}}}^{\mathrm{T}}\mathbf{R}^{\mathrm{T}})) = 2\mathrm{axl}(\mathrm{skew}(\mathbf{R}\breve{\underset{\sim}{\mathbf{T}}}\mathbf{F}^{\mathrm{T}})) = \mathrm{axl}(\mathbf{R}\breve{\underset{\sim}{\mathbf{T}}}\mathbf{F}^{\mathrm{T}} - \mathbf{F}\breve{\underset{\sim}{\mathbf{T}}}^{\mathrm{T}}\mathbf{R}^{\mathrm{T}})$. Introducing auxiliary vectors

$$\breve{\underline{\mathbf{B}}}_I^u(\underline{\boldsymbol{\xi}}_p) = \breve{\underset{\sim}{\mathbf{J}}}_\xi^{-\mathrm{T}}(\underline{\boldsymbol{\xi}}_p) \underline{\boldsymbol{\nabla}}_\xi N_I^u(\underline{\boldsymbol{\xi}}_p) \quad , \tag{4.32}$$

$$\breve{\underline{\mathbf{B}}}_I^\phi(\underline{\boldsymbol{\xi}}_p) = \breve{\underset{\sim}{\mathbf{J}}}_\xi^{-\mathrm{T}}(\underline{\boldsymbol{\xi}}_p) \underline{\boldsymbol{\nabla}}_\xi N_I^\phi(\underline{\boldsymbol{\xi}}_p) \quad , \tag{4.33}$$

the residual vectors given in Eqs. (4.30) and (4.31) read

$${}^{u}\underline{\mathbf{r}}_I^{(e)} = \sum_{p=1}^{n_{\mathrm{int}}} \left(\underset{\sim}{\mathbf{R}} \breve{\underset{\sim}{\mathbf{T}}} \breve{\underline{\mathbf{B}}}_I^u - \rho_0 \underline{\mathbf{f}} N_I^u \right) \breve{J}_\xi w_p \quad , \tag{4.34}$$

$${}^{\phi}\underline{\mathbf{r}}_I^{(e)} = \sum_{p=1}^{n_{\mathrm{int}}} \left(\underset{\sim}{\mathbf{R}}^{\kappa} \breve{\underset{\sim}{\mathbf{T}}} \breve{\underline{\mathbf{B}}}_I^\phi - {}^{\chi}\breve{\underline{\mathbf{t}}} N_I^\phi - \rho_0 \underline{\mathbf{m}} N_I^\phi \right) \breve{J}_\xi w_p \quad . \tag{4.35}$$

respectively, where the dependencies of the variables on $\underline{\boldsymbol{\xi}}_p$ are not explicitly stated. For the sake of brevity, the residuals are summarized in a single column vector

$$[\underline{\mathbf{r}}_I^{(e)}] = [{}^{u}\underline{\mathbf{r}}_I^{(e)}, {}^{\phi}\underline{\mathbf{r}}_I^{(e)}]^{\mathrm{T}} \tag{4.36}$$

as given in Eq. (4.18) with the dimension of (6x1).

The element stiffness matrices as well as the element residual vectors are then assembled reading

$$[\underset{\sim}{\mathbf{K}}_{\mathrm{T}}] = \bigcup_{(e)=1}^{n_{\mathrm{el}}} [\underset{\sim}{\mathbf{K}}_{\mathrm{T}}^{(e)}] \quad , \qquad [\underline{\mathbf{r}}] = \bigcup_{(e)=1}^{n_{\mathrm{el}}} [\underline{\mathbf{r}}^{(e)}] \quad . \tag{4.37}$$

Finally, for the incrementally-iterative procedure, the Newton-Raphson scheme is used, where the load is incrementally applied and an equilibrium iteration within each increment is performed. On the global or assembled level in terms of nodes following [8], this reads

$$[\underline{\mathbf{r}}_I^{(k+1)}] = [\underline{\mathbf{r}}_I^{(k)}] + \frac{[\partial \underline{\mathbf{r}}_I^{(k)}]}{[\partial \underline{\mathbf{y}}_J^{(k)}]}[\Delta \underline{\mathbf{y}}_J^{(k)}] = [\underline{\mathbf{0}}]$$

$$\Rightarrow [\underset{\sim}{\mathbf{K}}_{\mathrm{T};IJ}^{(k)}][\Delta \underline{\mathbf{y}}_J^{(k)}] = [\underline{\mathbf{r}}_I^{(k)}] \quad \text{and solve for } [\Delta \underline{\mathbf{y}}_J^{(k)}] \qquad , \tag{4.38}$$

$$\text{repeat until} \quad \|[\underline{\mathbf{r}}_I^{(k+1)}]\| < \epsilon \quad \text{then} \quad [\underline{\mathbf{y}}_{(m+1)J}^{(1)}] \leftarrow [\underline{\mathbf{y}}_{(m)J}^{(k_{\mathrm{eq}})}] \left(= [\underline{\mathbf{y}}_J^{(k+1)}] \leftarrow [\underline{\mathbf{y}}_J^{(k)}] + [\Delta \underline{\mathbf{y}}_J^{(k)}]\right) \qquad , \tag{4.39}$$

where the superscript a from Eq. (4.13) is replaced by k, which is the step counter of the equilibrium iteration. The number of increments is denoted by m and represents the starting point based on the previously converged increment while $m+1$ is referred to as the current increment. Once a certain criterion is fulfilled, e.g., the norm of the residual vector at node I is below a predefined threshold value ϵ, the solution is considered as converged with a total number of iterations, k_{eq}, and the next load increment can be applied with setting the iteration step counter to $k = 1$. For highly nonlinear problems, the tangent matrix should be updated within every iteration as pointed out in [8].

Updated Lagrangian formulation. For the sake of completeness, the derivation of the equivalent updated Lagrangian formulation is obtained by starting from the Eulerian equations of motion given in Eqs. (2.42) and (2.43). In [44], the virtual work for this formulation is given as

$$A_{\mathrm{int}} - A_{\mathrm{ext}} = G(\underline{\mathbf{u}}, \underline{\boldsymbol{\phi}}, \delta\underline{\mathbf{u}}, \delta\underline{\boldsymbol{\phi}}) = 0 \qquad , \tag{4.40}$$

$$\int_{\mathcal{R}_t} \underset{\sim}{\mathbf{T}} : \delta\underset{\sim}{\mathbf{e}} + {}^{\kappa}\underset{\sim}{\mathbf{T}} : \delta\cancel{\underset{\sim}{\boldsymbol{\kappa}}} \,\mathrm{d}v - \int_{\mathcal{R}_t} \rho_t \underline{\mathbf{f}} \cdot \delta\underline{\mathbf{u}} + \rho_t \underline{\mathbf{m}} \cdot \delta\underline{\boldsymbol{\phi}} \,\mathrm{d}v - \int_{\partial\mathcal{R}_t} \underline{\mathbf{t}}^* \cdot \delta\underline{\mathbf{u}} + {}^{\kappa}\underline{\mathbf{t}}^* \cdot \delta\underline{\boldsymbol{\phi}} \,\mathrm{d}s = 0 \qquad .$$

The derivation is abbreviated and takes directly the residual force and moment vectors of the discrtized problem given in Eqs. (4.23) and (4.24), which are then expressed with respect to the current configuration. The volume, v, and the surface, s, both with respect to the current configuration are obtained by using Eqs. (2.15) and (2.14), respectively. The gradient with respect to the current configuration, $\mathrm{grad}_{\mathrm{R}}(\cdot) = (\cdot) \otimes \underline{\boldsymbol{\nabla}}_x$, is obtained by using Eq. (A.25). Furthermore, the boundary conditions given in Eq. (2.44) are considered. This leads to

$$\int_{\mathcal{R}_t} (\underset{\sim}{\mathbf{R}}\underset{\sim}{\breve{\mathbf{T}}}\underset{\sim}{\mathbf{F}}^{\mathrm{T}}\underline{\boldsymbol{\nabla}}_x N_I^u - \rho_0 \underline{\mathbf{f}} N_I^u)\frac{1}{J} \,\mathrm{d}v - \int_{\partial\mathcal{R}_t} \underset{\sim}{\mathbf{R}}\underset{\sim}{\breve{\mathbf{T}}} N_I^u \underset{\sim}{\mathbf{F}}^{\mathrm{T}} \frac{1}{J}\underline{\mathbf{n}} \,\mathrm{d}s = \underline{\mathbf{0}} \qquad \forall I \notin \partial\mathcal{R}_t^u \qquad , \tag{4.41}$$

$$\int_{\mathcal{R}_t} (\underset{\sim}{\mathbf{R}}{}^{\kappa}\underset{\sim}{\breve{\mathbf{T}}}\underset{\sim}{\mathbf{F}}^{\mathrm{T}}\underline{\boldsymbol{\nabla}}_x N_I^\phi + 2N_I^\phi \mathrm{axl}(\mathrm{skew}(\underset{\sim}{\mathbf{F}}\underset{\sim}{\breve{\mathbf{T}}}^{\mathrm{T}}\underset{\sim}{\mathbf{R}}^{\mathrm{T}})) - \rho_0 \underline{\mathbf{m}} N_I^\phi)\frac{1}{J} \,\mathrm{d}v$$

$$- \int_{\partial\mathcal{R}_t} \underset{\sim}{\mathbf{R}}{}^{\kappa}\underset{\sim}{\breve{\mathbf{T}}} N_I^\phi \underset{\sim}{\mathbf{F}}^{\mathrm{T}} \frac{1}{J}\underline{\mathbf{n}} \,\mathrm{d}s = \underline{\mathbf{0}} \qquad \forall I \notin \partial\mathcal{R}_t^\phi \qquad . \tag{4.42}$$

Making use of the Piola transformations of the stress measures given in Eq. (2.49) and considering ${}^{\chi}\underline{\mathbf{t}} = -2\frac{1}{J}\mathrm{axl}(\mathrm{skew}(\underset{\sim}{\mathbf{F}}\underset{\sim}{\breve{\mathbf{T}}}^{\mathrm{T}}\underset{\sim}{\mathbf{R}}^{\mathrm{T}})) = -2\mathrm{axl}(\mathrm{skew}(\underset{\sim}{\mathbf{T}}^{\mathrm{T}}))$ yield

$$\int_{\mathcal{R}_t} (\underset{\sim}{\mathbf{T}}\underline{\boldsymbol{\nabla}}_x N_I^u - \rho_t \underline{\mathbf{f}} N_I^u) \,\mathrm{d}v - \int_{\partial\mathcal{R}_t} \underline{\mathbf{t}}^* N_I \,\mathrm{d}s = \underline{\mathbf{0}} \qquad \forall I \notin \partial\mathcal{R}_0^u \qquad , \tag{4.43}$$

$$\int_{\mathcal{R}_t} ({}^{\kappa}\underset{\sim}{\mathbf{T}}\underline{\boldsymbol{\nabla}}_x N_I^\phi - {}^{\chi}\underline{\mathbf{t}} N_I^\phi - \rho_t \underline{\mathbf{m}} N_I^\phi) \,\mathrm{d}v - \int_{\partial\mathcal{R}_t} {}^{\kappa}\underline{\mathbf{t}}^* N_I \,\mathrm{d}s = \underline{\mathbf{0}} \qquad \forall I \notin \partial\mathcal{R}_0^\phi \qquad , \tag{4.44}$$

where all quantities are considered with respect to the current configuration. To obtain the updated Lagrangian formulation for the FEM implementation, these equations are integrated by the Gaussian quadrature rule given in Eq. (4.29), where the Jacobian of the element must now be considered as a mapping between current and element parent configuration reading

$$\underset{\sim}{\mathbf{J}}_{\xi}(\underline{\boldsymbol{\xi}}) = \underline{\mathbf{x}}_I \otimes \underline{\boldsymbol{\nabla}}_{\xi} N_I(\underline{\boldsymbol{\xi}}) \qquad , \tag{4.45}$$

where $\underline{\mathbf{x}}$ is the position vector in the current configuration. With this at hand, the nodal residual vectors can be given as

$${}^{u}\underline{\mathbf{r}}_I^{(e)} = \sum_{p=1}^{n_{\text{int}}} \left(\underset{\sim}{\mathbf{T}} \underline{\mathbf{B}}_I^{u} - \rho_t \underline{\mathbf{f}} N_I \right) J_{\xi} w_p \qquad , \tag{4.46}$$

$${}^{\phi}\underline{\mathbf{r}}_I^{(e)} = \sum_{p=1}^{n_{\text{int}}} \left({}^{\kappa}\underset{\sim}{\mathbf{T}} \underline{\mathbf{B}}_I^{\phi} - {}^{\chi}\underline{\mathbf{t}} N_I - \rho_t \underline{\mathbf{m}} N_I \right) J_{\xi} w_p \qquad , \tag{4.47}$$

where J_{ξ} is the determinant of $\underset{\sim}{\mathbf{J}}_{\xi}$ and $\underline{\mathbf{B}}_I^{u}(\underline{\boldsymbol{\xi}}_p) = \underset{\sim}{\mathbf{J}}_{\xi}^{-\mathrm{T}}(\underline{\boldsymbol{\xi}}_p) \underline{\boldsymbol{\nabla}}_{\xi} N_I^{u}(\underline{\boldsymbol{\xi}}_p)$ as well as $\underline{\mathbf{B}}_I^{\phi}(\underline{\boldsymbol{\xi}}_p) = \underset{\sim}{\mathbf{J}}_{\xi}^{-\mathrm{T}}(\underline{\boldsymbol{\xi}}_p) \underline{\boldsymbol{\nabla}}_{\xi} N_I^{\phi}(\underline{\boldsymbol{\xi}}_p)$ represent auxiliary vectors. The nodal residual vectors are the same as given, e.g., in [8]. The resulting nodal residual vectors based on the updated, cf. Eqs. (4.46) and (4.47), and total Lagrangian formulations, cf. Eqs. (4.34) and (4.35), must be equal. Note that for the ABAQUS implementation in Section 4.1.2, the gradient in Eq. (4.45) is applied from the left and, consequently, $\underset{\sim}{\mathbf{J}}_{\xi}$ does not need to be transposed in the equations above.

Update of strain measures. The nodal residual vector corresponding to Eq. (4.36) is determined based on the updated or estimated values of the solution variables, i.e., nodal displacements and rotations. First, the approximated deformation gradient tensor and the approximated microrotation tensor are determined from which the strain measures are calculated. Once the strain measures are available, the stress measures can be determined based on the constitutive laws. Since the present thesis aims at a total Lagrangian formulation, only the updates of the Lagrangian strain measures are presented.

The deformation gradient tensor given in Eq. (2.13) using Eq. (4.6) is approximated by

$$\underset{\sim}{\mathbf{F}}^{h}(\underline{\mathbf{X}}, t) = \underset{\sim}{\mathbf{I}} + \underline{\mathbf{u}}_I(t) \otimes \underline{\boldsymbol{\nabla}}_X N_I^{u}(\underline{\mathbf{X}}) \qquad . \tag{4.48}$$

The microrotation tensor given in Eq. (2.6) using Eq. (4.7) is approximated by

$$\underset{\sim}{\mathbf{R}}^{h}(\underline{\mathbf{X}}, t) = \exp\left(\mathrm{sk}(N_I^{\phi}(\underline{\mathbf{X}}) \underline{\boldsymbol{\phi}}_I(t))\right) \qquad . \tag{4.49}$$

Note that the superscript h is not attached to the following tensorial quantities for the sake of brevity.

The update of the deformation gradient tensor is performed by directly using the updated nodal displacement vectors. It reads

$$\underset{\sim}{\mathbf{F}}^{(k+1)} = \underset{\sim}{\mathbf{I}} + \underline{\mathbf{u}}_I^{(k+1)} \otimes \underline{\boldsymbol{\nabla}}_X N_I^{u} \qquad , \tag{4.50}$$

where dependencies are not explicitly stated.

To ensure proper convergence of the solution, the microrotation tensor is updated as follows

$$\underset{\sim}{\mathbf{R}}^{(k+1)} = \Delta\underset{\sim}{\mathbf{R}}^{(k)} \underset{\sim}{\mathbf{R}}^{(k)} \tag{4.51}$$

where $\Delta\underset{\sim}{\mathbf{R}}^{(k)}$ denotes the incremental rotation and reads

$$\Delta\underset{\sim}{\mathbf{R}}^{(k)} = \exp\left(\mathrm{sk}(N_I^{\phi}\Delta\underline{\boldsymbol{\phi}}_I^{(k)})\right) \quad , \tag{4.52}$$

corresponding to Eq. (4.49).

For the update of the relative Lagrangian stretch tensor in Eqs. (2.18), (4.50), and (4.51) are used to obtain

$$\underset{\sim}{\mathbf{E}}^{(k+1)} = \underset{\sim}{\mathbf{R}}^{(k+1)\mathrm{T}}\underset{\sim}{\mathbf{F}}^{(k+1)} - \underset{\sim}{\mathbf{I}} \quad . \tag{4.53}$$

For the update of the relative Lagrangian wryness tensor given in Eq. (2.19), different approaches are found in [8] and [26]. Following [26], the tensor is updated as follows

$$\underset{\sim}{\boldsymbol{\mathscr{K}}}^{(k+1)} = \underset{\sim}{\boldsymbol{\mathscr{K}}}^{(k)} + \Delta\underset{\sim}{\boldsymbol{\mathscr{K}}}^{(k)} = \underset{\sim}{\boldsymbol{\mathscr{K}}}^{(k)} + \underset{\sim}{\mathbf{R}}^{(k+1)\mathrm{T}}\underset{\sim}{\boldsymbol{\mathcal{H}}}(\Delta\underline{\boldsymbol{\phi}}^{(k)})(\Delta\underline{\boldsymbol{\phi}}^{(k)} \otimes \underline{\boldsymbol{\nabla}}_X) \quad , \tag{4.54}$$

where $\underset{\sim}{\boldsymbol{\mathscr{K}}}^{(k)}$ represents the wryness tensor of the previous increment. The second order tensor, $\underset{\sim}{\boldsymbol{\mathcal{H}}}$, reads

$$\underset{\sim}{\boldsymbol{\mathcal{H}}}(\Delta\underline{\boldsymbol{\phi}}) = \underset{\sim}{\mathbf{I}} + \frac{1-\cos(\|\Delta\underline{\boldsymbol{\phi}}\|)}{\|\Delta\underline{\boldsymbol{\phi}}\|^2}(\Delta\underline{\boldsymbol{\phi}} \times \underset{\sim}{\mathbf{I}}) + \frac{\|\Delta\underline{\boldsymbol{\phi}}\| - \sin(\|\Delta\underline{\boldsymbol{\phi}}\|)}{\|\Delta\underline{\boldsymbol{\phi}}\|^3}(\Delta\underline{\boldsymbol{\phi}} \times \underset{\sim}{\mathbf{I}})^2 \quad , \tag{4.55}$$

with its derivation given in [37]. Following [8], the update of the relative Lagrangian wryness tensor reads

$$\underset{\sim}{\boldsymbol{\mathscr{K}}}^{(k+1)} = (\mathrm{axl}(\underset{\sim}{\mathbf{R}}^{(k+1)\mathrm{T}}\frac{\partial\underset{\sim}{\mathbf{R}}^{(k+1)}}{\partial X_k})) \otimes \underline{\mathbf{E}}_k \quad , \tag{4.56}$$

where the gradient of the microrotation tensor with respect to each spatial direction, X_k, is obtained by applying the chain rule to Eq. (4.51) and follows as

$$\frac{\partial\underset{\sim}{\mathbf{R}}^{(k+1)}}{\partial X_k} = \frac{\partial\Delta\underset{\sim}{\mathbf{R}}^{(k)}}{\partial X_k}\underset{\sim}{\mathbf{R}}^{(k)} + \Delta\underset{\sim}{\mathbf{R}}^{(k)}\frac{\partial\underset{\sim}{\mathbf{R}}^{(k)}}{\partial X_k} \quad . \tag{4.57}$$

Note that in [8] also a different approximation of the microrotation tensor is used, which reads

$$\underset{\sim}{\mathbf{R}}^{h}(\underline{\mathbf{X}}, t) = N_I^{\phi}(\underline{\mathbf{X}})\exp\left(\mathrm{sk}(\underline{\boldsymbol{\phi}}_I(t))\right) \quad , \tag{4.58}$$

where the interpolation functions are not within the exponent compared to Eq. (4.49). It gives a slightly different approximation not only for the microrotation tensor, but also for the strain measures. The gradient of the microrotation tensor using Eq. (4.58) is given in Eq. (F.12) in the Appendix F. Which of the definitions of the microrotation tensors given in Eqs. (4.49) and (4.58) is used for the implementation, is specified in Section 4.1.2. The same applies to the updates of $\underset{\sim}{\boldsymbol{\mathscr{K}}}$ given in Eqs. (4.54) and (4.57).

In the first iteration, $k = 1$, no deformation is assumed, reading

$$\underline{\mathbf{u}} = \underline{\mathbf{0}} \quad , \quad \underline{\boldsymbol{\phi}} = \underline{\mathbf{0}} \quad \rightarrow \quad \underset{\sim}{\mathbf{F}} = \underset{\sim}{\mathbf{I}} \quad , \quad \underset{\sim}{\mathbf{R}} = \underset{\sim}{\mathbf{I}} \quad , \quad \underset{\sim}{\mathbf{E}} = \underset{\sim}{\mathbf{0}} \quad , \quad \underset{\sim}{\boldsymbol{\mathscr{K}}} = \underset{\sim}{\mathbf{0}} \quad . \tag{4.59}$$

The system of equations is then solved for $[\Delta\underline{\mathbf{y}}^1]$, then $[\underline{\mathbf{y}}^{(2)}] \leftarrow [\underline{\mathbf{y}}^{(1)}] + [\Delta\underline{\mathbf{y}}^{(1)}]$, see Eq. (4.38). If an equilibrium for an increment is achieved for k_{eq} iterations, the quantities are stored as $(\cdot)^{(1)}_{(m+1)} \leftarrow (\cdot)^{(k_{\mathrm{eq}})}_{(m)}$.

Strain energy. On the element level, the incremental strain energy is approximated based on a trapezoidal rule reading

$$\Delta E_{\mathrm{se}}^{(k)} \approx \sum_{p=1}^{n_{\mathrm{int}}} \frac{1}{2} \left((\breve{\underset{\sim}{\mathbf{T}}}^{(k+1)} + \breve{\underset{\sim}{\mathbf{T}}}^{(k)}) : (\underset{\sim}{\mathbf{E}}^{(k+1)} - \underset{\sim}{\mathbf{E}}^{(k)}) + ({}^{\kappa}\breve{\underset{\sim}{\mathbf{T}}}^{(k+1)} + {}^{\kappa}\breve{\underset{\sim}{\mathbf{T}}}^{(k)}) : (\underset{\sim}{\boldsymbol{\mathscr{K}}}^{(k+1)} - \underset{\sim}{\boldsymbol{\mathscr{K}}}^{(k)}) \right) \breve{J}_{\xi} w_p \quad , \tag{4.60}$$

and updated accordingly

$$E_{\mathrm{se}}^{(k+1)} = \Delta E_{\mathrm{se}}^{(k)} + E_{\mathrm{se}}^{(k)} \quad , \tag{4.61}$$

with all quantities evaluated at the integration points ($\underline{\boldsymbol{\xi}}_p$). Optionally, the strain energy can be directly determined via

$$E_{\mathrm{se}}^{(k+1)} = \sum_{p=1}^{n_{\mathrm{int}}} \frac{1}{2} \left(\breve{\underset{\sim}{\mathbf{T}}}^{(k+1)} : \underset{\sim}{\mathbf{E}}^{(k+1)} + {}^{\kappa}\breve{\underset{\sim}{\mathbf{T}}}^{(k+1)} : \underset{\sim}{\boldsymbol{\mathscr{K}}}^{(k+1)} \right) \breve{J}_{\xi} w_p \quad . \tag{4.62}$$

Due to the absence of any energy dissipation, the strain energy must be equal to the work done by the external loads, i.e., $E_{\mathrm{se}} + E_{\mathrm{ext}} = 0$.

4.1.2 Implementation as user element

The implementation of the geometrically nonlinear micropolar continuum is performed in ABAQUS and is done on the element level via the ABAQUS user element (UEL) interface. This is the only interface provided by ABAQUS that allows to define the necessary additional rotational DOFs of the micropolar continuum. This element is capable of dealing with 3D problems involving large displacements and rotations in the small strain regime. For the present implementation, RSD of stress measures is used and the gradients are applied from the right side except for the Jacobian matrix defined in Eq. (F.10). Note that for some anisotropic materials the corresponding conversion rule of elasticity tensors needs to be considered, cf. Eq. (2.73). The advantage of an implementation in ABAQUS is the possibility of the user element to be used in combination with the elements available in the ABAQUS element library.

The UEL interface is provided by ABAQUS in the form of a subroutine written in Fortran77 or Fortran90, the latter being chosen for implementation. The interface provides information that is passed to the UEL subroutine. The most important information are the arrays containing the current estimates of the basic solution variables, i.e., total and incremental nodal values for the active DOF of the element at the end of the current increment/iteration. For the micropolar continuum, the active DOFs, y_N, are displacements u_N and microrotations ϕ_N with N denoting the DOF, see Eq. (F.4). The subroutine contains variables to be updated when passing through the subroutine. These variables are the right hand-side vector, `RHS`, with components F_N defined as external minus internal forces or moments, the consistent tangent matrix, `amatrx`, with components defined as $K_{\mathrm{T};NM} = -\partial F_N/\partial y_M$, the user-defined solution-dependent state variables (SDVs), such as stresses and strains, the energy variables, such as the strain energy, and an optional time incrementation parameter to change the step size if convergence issues show up. The element residuals are determined via Eqs. (4.34) and (4.35). The element tangent stiffness matrices are determined based on Eq. (4.25). Both quantities are assembled to form a global system of equations, taking into account all boundary conditions, which is performed by ABAQUS. The global system of equations in each increment and iteration, k, reads

$$[\underset{\sim}{\mathbf{K}}_{\mathrm{T}}^{(k)}][\Delta \underline{\mathbf{y}}^{(k)}] = [\underline{\mathbf{r}}^{(k)}] + \mathrm{NBC}|_{\underline{\mathbf{t}},^{\kappa}\underline{\mathbf{t}}} \quad , \tag{4.63}$$

where $\mathrm{NBC}|_{\underline{\mathbf{t}},^{\kappa}\underline{\mathbf{t}}}$ denotes the Neumann-type boundary conditions incorporated at this stage, cf. the additional terms associated with the traction and surface traction boundary conditions in Eqs. (4.23) and (4.24) with Eqs. (4.34) and (4.35). In general, $[\underset{\sim}{\mathbf{K}}] \neq [\underset{\sim}{\mathbf{K}}]^{\mathrm{T}}$, which requires the use of the unsymmetric matrix storage and solution capabilities of ABAQUS. The UEL is implemented such that it must be used in conjunction with the Newton-Raphson scheme as outlined in Eqs. (4.38) and (4.39). To use the Riks solution procedure capabilities of ABAQUS, an incremental load vector needs to be defined additionally, which is beyond of the scope of this thesis.

In the present thesis, a hexahedral element with linear shape functions is implemented. The shape functions used for the implementation are given in Eq. (F.1) with nodes following the convention used for solid elements available in the ABAQUS element library, cf. Figure 4.2. The displacements and rotations are approximated with the same interpolation functions, namely,

$$N_I^u(\underline{\mathbf{X}}) = N_I^{\phi}(\underline{\mathbf{X}}) = N_I(\underline{\mathbf{X}}) \quad . \tag{4.64}$$

The geometry uses the same interpolation functions as the solution variables, hence, the element is referred to being an isogeometric element, cf. Eq. (4.11). A Gaussian integration scheme is used, cf. Eq. (4.29), with the corresponding integration point coordinates and weighting factors given in Table F.1 in the Appendix F. This element is further referred to as `C3D8MP`.

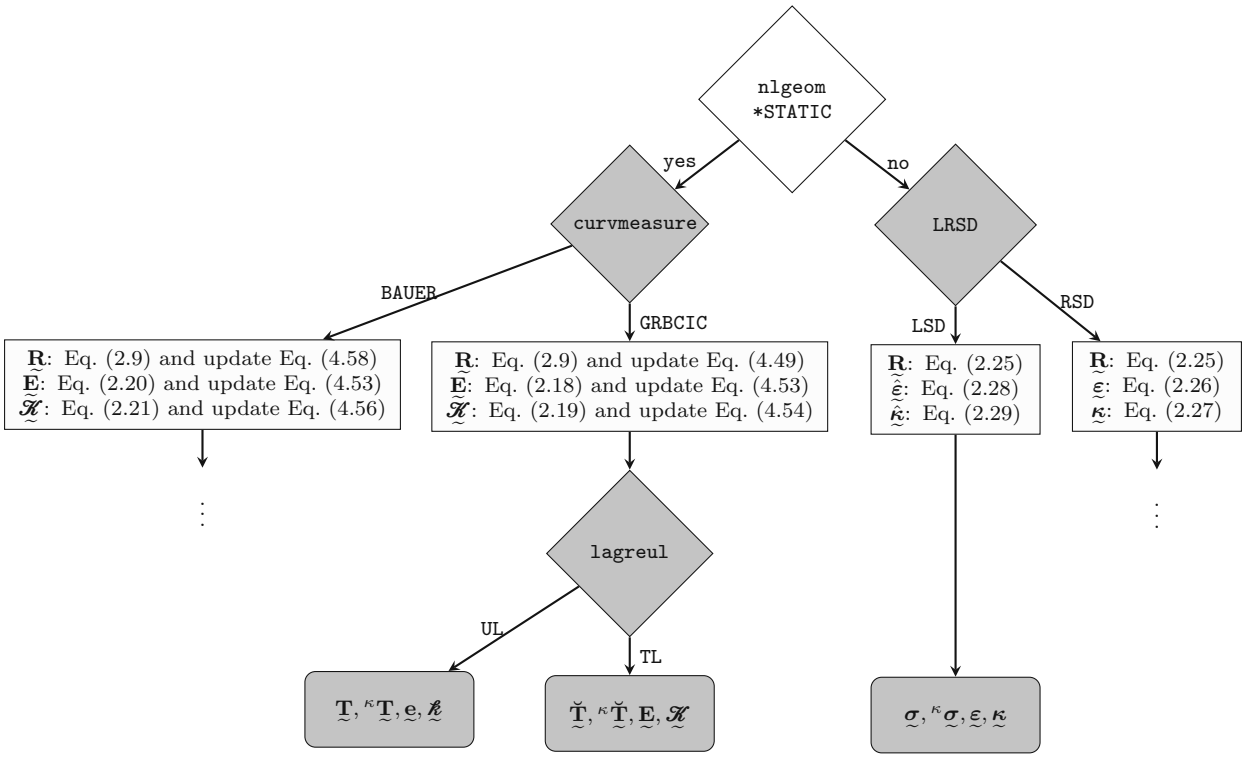

Figure 4.1: Flowchart of variables to be defined by the user (diamond-shaped tiles) and resulting output (grey rectangular tiles). The `*STATIC` step setting is to be specified in the input file (white) and the UEL `C3D8MP` user variables are to be set within the UEL subroutine (grey), where `TL` and `UL` denote total and updated Lagrangian descriptions, respectively. Vertical paths indicate the default setting of the user variables.

The right hand-side vector as well as the consistent tangent matrix can either be determined by using Eqs. (4.34) and (4.35) for the total Lagrangian formulation or by using Eqs. (4.46) and (4.47) for the updated Lagrangian formulation. The total Lagrangian formulation does not require the transformation of the elasticity tensors according to Eq. (2.77). To handle the transformations necessary for the updated Lagrangian formulation, pullback operations on the Eulerian strain measures given in Eq. (2.23) are used to determine PK2-like stress measures, which are then pushed forward via Piola transformations given in Eq. (2.49) to obtain the Cauchy-like stress tensors. Which formulation is used depends on the choice of the internal UEL user variable `lagreul`, cf. Figure 4.1. The default setting is the total Langrangian formulation. The linear micropolar continuum can be directly obtained by using small instead of large strain measures. This is enabled by defining the step setting `*STATIC` in the input file accordingly, cf. Figure 4.1. Both strain measures based on left and right gradients can be considered, cf. Eqs. (2.28) and (2.26), respectively. Consequently, the output, i.e., the SDVs, of the micropolar continuum element depends on the choice of internal UEL user variables as well as parameters provided by the input file, see Figure 4.1.

External body forces and moments can be considered as distributed loads and are accessible via the ABAQUS keyword `*DLOAD`. For further information on the user element variables, see Appendix F, while in particular for the element usage, see Appendix F.5.

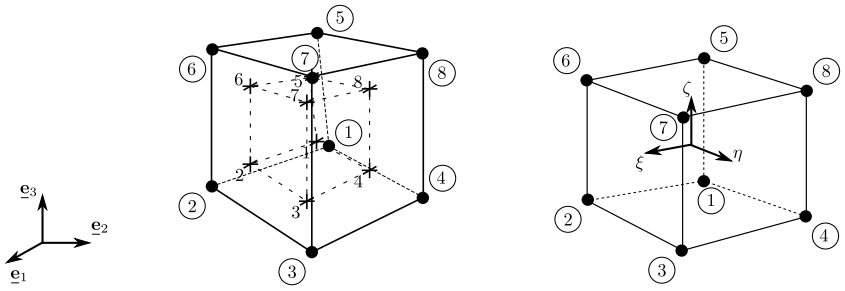

Figure 4.2: Trilinear hexahedral element with node and integration point numbering.

4.2 Linear micropolar continuum

A purely linear micropolar continuum in three as well as two dimensions is implemented using a vector-matrix notation, which leads to a more familiar way of implementing finite element matrices within the framework of ABAQUS. Following the implementation of 2D linear finite elements presented in [53], the starting point for the finite element implementation is the principle of virtual work, cf. Eq. (4.1). For the linear micropolar continuum, this reads

$$\int_{\mathcal{R}_0} \underset{\sim}{\boldsymbol{\sigma}} : \delta\underset{\sim}{\boldsymbol{\varepsilon}} + {}^{\kappa}\underset{\sim}{\boldsymbol{\sigma}} : \delta\underset{\sim}{\boldsymbol{\kappa}} \,\mathrm{d}V = \int_{\mathcal{R}_0} \rho\underline{\mathbf{f}} \cdot \delta\underline{\mathbf{u}} + \rho\underline{\mathbf{m}} \cdot \delta\underline{\boldsymbol{\phi}} \,\mathrm{d}V + \int_{\partial\mathcal{R}_0} \underline{\mathbf{t}}^* \cdot \delta\underline{\mathbf{u}} + {}^{\kappa}\underline{\mathbf{t}}^* \cdot \delta\underline{\boldsymbol{\phi}} \,\mathrm{d}S \quad , \tag{4.65}$$

$$\int_{\mathcal{R}_0} \sigma_{ij}\delta\varepsilon_{ij} + {}^{\kappa}\sigma_{ij}\delta\kappa_{ij} \,\mathrm{d}V = \int_{\mathcal{R}_0} \rho f_i\delta u_i + \rho m_i\delta\phi_i \,\mathrm{d}V + \int_{\partial\mathcal{R}_0} t_i\delta u_i + m_i\delta\phi_i \,\mathrm{d}S \quad ,$$

where $\underset{\sim}{\boldsymbol{\sigma}}, {}^{\kappa}\underset{\sim}{\boldsymbol{\sigma}}$ and $\underset{\sim}{\boldsymbol{\varepsilon}}, \underset{\sim}{\boldsymbol{\kappa}}$ refer to linear stress and strain measures, respectively, $\underline{\mathbf{t}}^*$ denotes applied surface tractions, ${}^{\kappa}\underline{\mathbf{t}}^*$ refers to applied surface moments, and $\rho(=\rho_0)$ is the density. Note that the stress measures are based on LSD and the strain measures are based on applying the gradient from the left, cf. Eq. (2.28). For the linear case, the volume, V, and surface, S, are to be integrated with respect to the undeformed or reference configuration. Using Eqs. (2.28) and (2.29), Eq. (4.65) reads

$$\int_{\mathcal{R}_0} \sigma_{ij}\delta u_{j,i} - \epsilon_{ijk}\sigma_{ij}\delta\phi_k + {}^{\kappa}\sigma_{ij}\delta\phi_{j,i} \,\mathrm{d}V = \int_{\mathcal{R}_0} \rho f_i\delta u_i + \rho m_i\delta\phi_i \,\mathrm{d}V + \int_{\partial\mathcal{R}_0} t_i\delta u_i + m_i\delta\phi_i \,\mathrm{d}S \quad , \tag{4.66}$$

where the separation of solution variables easily succeeds as these are neither multiplicatively coupled nor arguments of nonlinear functions. The problem is discretized and set up to be solved on the basis of Eq. (4.13). It serves as the basis for the derivation of the right-hand side vector and the stiffness matrix on the element level required for the ABAQUS implementation. Again, the Neumann-type boundary conditions are considered later in the global system of equations, cf. Eq. (4.63).

4.2.1 In 3D - ABAQUS implementation

Introducing the generalized vectors of linear stress and linear strain measure components as given in Eq. (2.61) with components arranged as given in Eq. (2.62), a differential operator matrix for the 3D case can be defined as

$$[\underset{\sim}{\mathbf{d}}] = (18 \times 6) \quad , \tag{4.67}$$

which is outlined in Eq. (F.13), with $[\underset{\approx}{\boldsymbol{\varepsilon}}] = [\underset{\sim}{\mathbf{d}}]\vec{y}$, where $\vec{y}$ denotes the physical continuous displacement and rotation field summarized as $\vec{y} = [u_1, u_2, u_3, \phi_1, \phi_2, \phi_3]^{\mathrm{T}}$. Both kinematic fields as well as the geometry are

approximated by interpolation functions within the element as done for the nonlinear element, cf. Eqs. (4.6), (4.7), and (4.64). With Eq. (4.67) at hand, the matrix of derivatives of shape functions on the element level is determined by

$$[\underset{\sim}{\mathbf{B}}_{\mathrm{N}}^{(e)}] = [\underset{\sim}{\mathbf{d}}][\underset{\sim}{\mathbf{N}}^{(e)}] \quad , \tag{4.68}$$

where $[\underset{\sim}{\mathbf{N}}^{(e)}]$ denotes the matrix of shape functions corresponding to a particular element, cf. Eq. (F.2). Using Eq. (4.68), Eq. (4.66) on the element level gives the sought local system of equations

$$[\underset{\sim}{\mathbf{K}}_{\mathrm{T}}^{(e)}][\Delta\underline{\mathbf{y}}^{(e)}] = [\underline{\mathbf{r}}^{(e)}] \Rightarrow [\underset{\sim}{\mathbf{K}}_{0}^{(e)}][\underline{\mathbf{y}}^{(e)}] = [\underline{\mathbf{q}}_{\mathrm{ext}}^{(e)}] \quad . \tag{4.69}$$

For the linear problem the stiffness matrix does not depend on the solution variable and the external forces are in equilibrium with the internal forces, so that the right-hand side of this equation can be directly introduced. Introducing the element parent domain, the element stiffness matrix and the right hand-side vector are determined by using a Gaussian quadrature scheme, cf. Eq. (4.29). The element stiffness matrix reads

$$[\underset{\sim}{\mathbf{K}}_{0}^{(e)}] = \int_{\mathcal{R}_0} [\underset{\sim}{\mathbf{B}}_{\mathrm{N}}^{(e)}]^{\mathrm{T}} [\underset{\approx}{\mathbb{D}}] [\underset{\sim}{\mathbf{B}}_{\mathrm{N}}^{(e)}] \,\mathrm{d}V \tag{4.70}$$

$$= \int_{-1}^{+1}\int_{-1}^{+1}\int_{-1}^{+1} [\underset{\sim}{\mathbf{B}}_{\mathrm{N}}^{(e)}]^{\mathrm{T}}(\underline{\boldsymbol{\xi}}) [\underset{\approx}{\mathbb{D}}] [\underset{\sim}{\mathbf{B}}_{\mathrm{N}}^{(e)}](\underline{\boldsymbol{\xi}}) \,\mathrm{d}\xi\,\mathrm{d}\eta\,\mathrm{d}\zeta \tag{4.71}$$

$$\approx \sum_{p=1}^{n_{\mathrm{int}}} [\underset{\sim}{\mathbf{B}}_{\mathrm{N}}^{(e)}]^{\mathrm{T}}(\underline{\boldsymbol{\xi}}_p) [\underset{\approx}{\mathbb{D}}] [\underset{\sim}{\mathbf{B}}_{\mathrm{N}}^{(e)}](\underline{\boldsymbol{\xi}}_p) J_{\xi}^{(e)}(\underline{\boldsymbol{\xi}}_p) w_p \quad , \tag{4.72}$$

as well as the element residual or right hand-side force and moment vector, which is comprised of external minus internal force and moment vector, and is determined via

$$[\underline{\mathbf{r}}^{(e)}] = \int_{\mathcal{R}_0} [\underset{\sim}{\mathbf{N}}^{(e)}]^{\mathrm{T}} \rho [\underline{\mathbf{f}}, \underline{\mathbf{m}}]^{\mathrm{T}} - [\underset{\sim}{\mathbf{B}}_{\mathrm{N}}^{(e)}]^{\mathrm{T}} [\boldsymbol{\sigma}] \mathrm{d}V \tag{4.73}$$

$$= \int_{-1}^{+1}\int_{-1}^{+1}\int_{-1}^{+1} [\underset{\sim}{\mathbf{N}}^{(e)}]^{\mathrm{T}}(\underline{\boldsymbol{\xi}}) \rho [\underline{\mathbf{f}}, \underline{\mathbf{m}}]^{\mathrm{T}} - [\underset{\sim}{\mathbf{B}}_{\mathrm{N}}^{(e)}]^{\mathrm{T}}(\underline{\boldsymbol{\xi}}) [\boldsymbol{\sigma}](\underline{\boldsymbol{\xi}}) \,\mathrm{d}\xi\,\mathrm{d}\eta\,\mathrm{d}\zeta \tag{4.74}$$

$$\approx \sum_{p=1}^{n_{\mathrm{int}}} \left([\underset{\sim}{\mathbf{N}}^{(e)}]^{\mathrm{T}}(\underline{\boldsymbol{\xi}}_p) \rho [\underline{\mathbf{f}}, \underline{\mathbf{m}}]^{\mathrm{T}} - [\underset{\sim}{\mathbf{B}}_{\mathrm{N}}^{(e)}]^{\mathrm{T}}(\underline{\boldsymbol{\xi}}_p) [\boldsymbol{\sigma}](\underline{\boldsymbol{\xi}}_p) \right) J_{\xi}^{(e)}(\underline{\boldsymbol{\xi}}_p) w_p \quad , \tag{4.75}$$

with $\rho[\underline{\mathbf{f}}, \underline{\mathbf{m}}]^{\mathrm{T}} = \rho[f_1, f_2, f_3, m_1, m_2, m_3]^{\mathrm{T}}$ and $[\underset{\approx}{\mathbb{D}}]$ the elasticity matrix, cf. Eq. (2.61). Note that the residual vector is given instead of the external force vector at this is point as this is required by ABAQUS. All quantities are evaluated at the integration point with corresponding coordinates $\underline{\boldsymbol{\xi}} = [\xi_p, \eta_p, \zeta_p]^{\mathrm{T}}$, where p describes the integration point number. The derivative matrix shows derivatives of the shape functions with respect to the global coordinate system. To obtain the derivatives of the shape functions with respect to the parent configuration, the mapping given in Eq. (4.28) needs to be considered, cf. Eq. (F.8). Note that the equations above are valid for any type of element to be implemented.

A hexahedral element with linear shape functions is implemented, cf. Figure 4.2. The shape functions are given in Eq. (F.1) and the matrix of shape functions is given in Eq. (F.2), which allows to form the matrix of derivatives of shape functions, cf. Eq. (4.68). This matrix is of size (18x48), which is not explicitly stated for the sake of brevity. The stiffness matrix and the right hand-side vector are determined according to Eqs. (4.72) and (4.75), respectively, where a full Gaussian quadrature scheme is used, see Table F.1 in Appendix F for the integration point data. The resulting 3D isoparametric finite element is further called `C3D8MPlin`. Body forces and moments can be considered as distributed loads and are accessible via the ABAQUS keyword `*DLOAD`.

4.2.2 In 2D - ABAQUS implementation

To consider 2D linear BVPs considering plane strain assumptions, the finite element implementation is set up analogously to the 3D case. Therefore, the 2D strain measures based on applying the gradient from the left as given in Eq. (2.65) and stress measures based on LSD are taken into account. Introducing the generalized vectors of linear stress and linear strain measure components as given in Eq. (2.63), a differential operator matrix can be defined as

$$[\underset{\sim}{\mathbf{d}}] = \begin{bmatrix} \frac{\partial}{\partial x_1} & 0 & 0 & \frac{\partial}{\partial x_2} & 0 & 0 \\ 0 & \frac{\partial}{\partial x_2} & \frac{\partial}{\partial x_1} & 0 & 0 & 0 \\ 0 & 0 & -1 & 1 & \frac{\partial}{\partial x_1} & \frac{\partial}{\partial x_2} \end{bmatrix}^{\mathrm{T}} \quad . \tag{4.76}$$

Accounting for 2D, the element stiffness matrix given in Eq. (4.70) reads

$$[\underset{\sim}{\mathbf{K}}_0^{(e)}] = \int_{-1}^{+1}\int_{-1}^{+1} [\underset{\sim}{\mathbf{B}}_{\mathrm{N}}^{(e)}]^{\mathrm{T}}(\underline{\boldsymbol{\xi}})\, [\underset{\approx}{\mathbb{D}}]\, [\underset{\sim}{\mathbf{B}}_{\mathrm{N}}^{(e)}](\underline{\boldsymbol{\xi}}) h \,\mathrm{d}\xi \,\mathrm{d}\eta \tag{4.77}$$

$$\approx \sum_{p=1}^{n_{\mathrm{int}}} [\underset{\sim}{\mathbf{B}}_{\mathrm{N}}^{(e)}]^{\mathrm{T}}(\underline{\boldsymbol{\xi}}_p)\, [\underset{\approx}{\mathbb{D}}]\, [\underset{\sim}{\mathbf{B}}_{\mathrm{N}}^{(e)}](\underline{\boldsymbol{\xi}}_p) h J_{\xi}^{(e)}(\underline{\boldsymbol{\xi}}_p) w_p \quad , \tag{4.78}$$

and the element residual or right hand-side force and moment vector given in Eq. (4.73) follows as

$$[\underline{\mathbf{r}}^{(e)}] = \int_{-1}^{+1}\int_{-1}^{+1} [\underset{\sim}{\mathbf{N}}^{(e)}]^{\mathrm{T}}(\underline{\boldsymbol{\xi}})[f_1, f_2, m_3]^{\mathrm{T}} - [\underset{\sim}{\mathbf{B}}_{\mathrm{N}}^{(e)}]^{\mathrm{T}}(\underline{\boldsymbol{\xi}})[\underline{\boldsymbol{\sigma}}](\underline{\boldsymbol{\xi}}) h \,\mathrm{d}\xi \,\mathrm{d}\eta \tag{4.79}$$

$$\approx \sum_{p=1}^{n_{\mathrm{int}}} \left([\underset{\sim}{\mathbf{N}}^{(e)}]^{\mathrm{T}}(\underline{\boldsymbol{\xi}}_p)[f_1, f_2, m_3]^{\mathrm{T}} - [\underset{\sim}{\mathbf{B}}_{\mathrm{N}}^{(e)}]^{\mathrm{T}}(\underline{\boldsymbol{\xi}}_p)[\underline{\boldsymbol{\sigma}}](\underline{\boldsymbol{\xi}}_p) \right) h J_{\xi}^{(e)}(\underline{\boldsymbol{\xi}}_p) w_p \quad , \tag{4.80}$$

where $\underline{\boldsymbol{\xi}}_p = [\xi_p, \eta_p]^{\mathrm{T}}$ represents the integration point coordinates with respect to the parent configuration of the element, h represents the thickness of the element, and $[\underset{\sim}{\mathbf{B}}_{\mathrm{N}}^{(e)}]$ denotes the matrix of derivatives of shape functions on the element level, cf. Eq. (4.68).

A quadrilateral element with linear shape functions is implemented, see Figure 4.3. The shape functions are given in Eq. (F.15) and the matrix of shape functions is given in Eq. (F.17), which allows to form the matrix of derivatives of shape functions, cf. Eq. (4.68), possessing dimensions of (6x12). The stiffness matrix and the right hand-side vector are determined according to Eqs. (4.78) and (4.80), respectively, where a Gaussian quadrature scheme is used, see Table F.2 in the Appendix F for the integration point data. The resulting 2D isoparametric finite element considers plane strain assumptions and is further called `CPE4MP`. The body forces and moments can be considered as distributed loads and are accessible via the ABAQUS keyword `*DLOAD`.

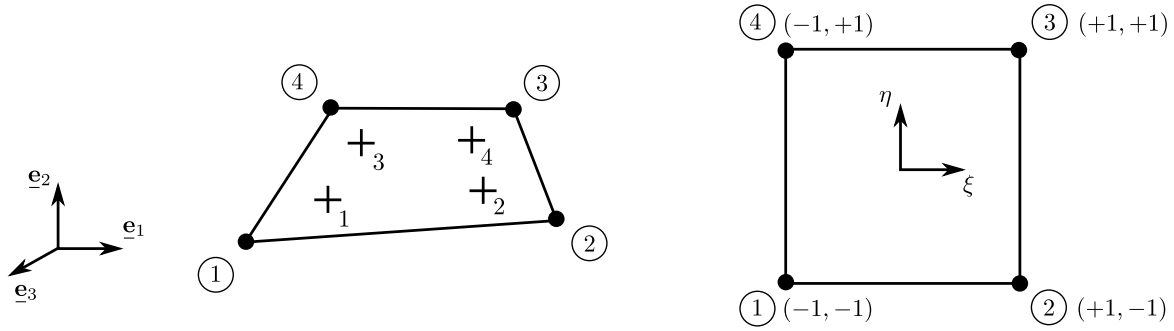

Figure 4.3: Linearly interpolated quadrilateral element with node and integration point numbering.

4.2.3 NGSolve implementation

For the numerical study on negative and positive constants in Chapter 5, the linear micropolar continuum is further implemented using the open-source software NGSolve V6.2.2302. The Python interface of NGSolve allows to directly change FEM features, such as the element size, h_e, and the interpolation order, p_e, which allows to easily perform parameter studies. Again, the implementation is based on [53] and has already been outlined in Section 4.2.

The strong form of the governing micropolar elasticity equations given in Section 2.3 via Eqs. (2.42) and (2.43) is turned into the weak form by multiplying with vector-valued test functions $\underline{\mathbf{v}}$ and $\underline{\mathbf{w}}$ and an integration over the domain. Using integration by parts and considering plane strain problems as well as no body forces and body moments, the weak form simplifies to

$$\int_\Omega \sigma_{ij} v_{j,i} + m_{i3} w_{,i} + \epsilon_{3ij} \sigma_{ij} w \, \mathrm{d}\Omega = 0 \quad , \tag{4.81}$$

where the vector-valued test function $\underline{\mathbf{w}}$ is reduced to a scalar-valued one, w, for 2D problems. Note that with $v_{j,i} = \delta u_{j,i}$ and $w = \delta \phi_3$ the virtual work can be obtained, cf. Eq. (4.66).

The introduction of a canonical notation for variational problems is handy and serves as the basis for the implementation in NGSolve. It reads as follows: Find $u_i \in U_i$ with $i = 1, 2$ and $\phi \in Q$ such that

$$a((u_i, \phi), (v_i, w)) = L((v_i, w)), \quad \forall v_i \in \hat{U}_i \quad \text{and} \quad \forall w \in \hat{Q} \quad , \tag{4.82}$$

with trail (unknown solution) and test function spaces

$$\begin{aligned} U_i &= \{v_i \in H^1(\Omega) : v_i = u_i^* \quad \text{on} \quad \partial\mathcal{R}_0^{u_i}\} \quad , \quad \hat{U}_i = \{v_i \in H^1(\Omega) : v_i = 0 \quad \text{on} \quad \partial\mathcal{R}_0^{u_i}\} \quad , \\ Q &= \{w \in H^1(\Omega) : w = \phi^* \quad \text{on} \quad \partial\mathcal{R}_0^{\phi}\} \quad , \quad \hat{Q} = \{w \in H^1(\Omega) : w = 0 \quad \text{on} \quad \partial\mathcal{R}_0^{\phi}\} \quad , \end{aligned} \tag{4.83}$$

respectively, where $H^1(\Omega)$ denotes the first order Sobolev space, u_i^* and ϕ^* are Dirichlet-type boundary conditions on the corresponding boundary portion $\partial\mathcal{R}_0$, cf. Eq. (2.45). In the case of Eq. (4.81), it follows

$$\begin{aligned} a((u_i, \phi), (v_i, w)) &= \int_\Omega \sigma_{ij} v_{j,i} + m_{i3} w_{,i} + \epsilon_{3ij} \sigma_{ij} w \, \mathrm{d}\Omega \quad , \\ L((v_i, w)) &= 0 \quad , \end{aligned} \tag{4.84}$$

with $a((u_i, \phi), (v_i, w))$ and $L((v_i, w))$ denoting the bilinear and linear form, respectively.

The procedure for the implementation consists of (i) declaring finite element spaces, i.e., the finite dimensional subspaces of U_i and Q, for each DOF, (ii) introducing test, trial, and grid functions, (iii) defining and assembling the linear and bilinear forms, and (iv) solving the system of equations obtained, cf. documentation NGSolve [1]. For the micropolar continuum, this reads

```
# (i)
U1 = H1(mesh, order=p_e, dim=1, dirichlet="bottom|top")
U2 = H1(mesh, order=p_e, dim=1, dirichlet="bottom|top")
Q  = H1(mesh, order=p_e, dim=1, dirichlet="bottom")
X  = U1*U2*Q
# (ii)
u1,u2,phi = X.TrialFunction()
v1,v2,w   = X.TestFunction()
# (iii)
a = BilinearForm(X)
a += InnerProduct(Sigma(Eps(u1,u2,phi),D), Gradv)*dx
a += InnerProduct(-Tt(Sigma(Eps(u1,u2,phi),D)), w)*dx
a += InnerProduct(Sigma_couple(Kap(phi),D), Gradw)*dx
gfu = GridFunction(X)
a.Assemble()
f = LinearForm(X)
f.Assemble()
# (iv)
r = f.vec.CreateVector()
r.data = f.vec - a.mat * gfu.vec
gfu.vec.data += a.mat.Inverse(freedofs=X.FreeDofs()) * r
```

where `#(·)` refers to the steps of the procedure given above. The finite element spaces use Legendre polynomials as basis functions, where p_e is associated with the order of the polynomials [1, 83]. The Dirichlet-type boundary conditions are introduced via the argument `"dirichlet=..."` using region identifiers predefined in the `mesh` object, e.g., `bottom`, with default setting $u_i^* = \phi^* = 0$. This only applies to the spaces of the trial functions. Note that all the variables that are not introduced in the code segment above, such as `Sigma` etc., are so-called coefficient functions and must be defined accordingly. For the sake of brevity, these declarations are not explicitly shown, which also applies to Dirichlet-boundary conditions differing from the default setting. The `gfu` represents functions in the finite element space and provides memory to hold for coefficient vectors, i.e., the nodal solution. For post-processing, values at any location X_1, X_2 inside the domain can be obtained via interpolation using functions provided by NGSolve, e.g., `gfu.components[DOF](mesh((`X_1`,` X_2`)))`.

Chapter 5

Competing length scales between micropolar continuum modeling of 2D periodic lattice materials and the finite element method

The two different sets of MECs derived in [10, 53] describing the very same lattice are investigated based on a numerical study. For this purpose, a micropolar continuum model is set up by means of the FEM and numerical simulations are performed. For comparison, discrete lattice models serve as reference. The types of lattices studied are the square, the triangular, and the 45° rotated square lattice. An extensive study is performed based on the square lattice, since its sets of constants derived in [10, 53] are often used for comparison with constants obtained by other homogenization approaches, e.g., [36, 46, 58, 86]. Various configurations of the lattices and different load cases are used to study the predictive capabilities and limitations of the micropolar continuum model with respect to the set of MECs used.

Furthermore, the influence of the *element size* and the *order of the interpolation functions* on the predicted mechanical response is studied. The mechanical response is evaluated on the basis of the strain energy and the rotation field. The simulations of the discrete models are carried out with ABAQUS/Standard 2019 (Dassault Systèmes Simulia Corp., Providence, RI, USA), while the simulations of the continuum model are performed either with ABAQUS/Standard 2019 or NGSolve V6.2.2302 based on the implementations given in Section 4.2.2 and Section 4.2.3, respectively.

5.1 Lattice models and method

5.1.1 Geometry and material properties

The overall geometric dimensions of the lattices are given by L_1 and L_2 for the spatial 1- and 2-directions, respectively. These dimensions are associated with the macroscopic domain, see Figure 5.1 (left, center left) for square, (center right) for triangular, and (right) for 45° rotated square lattice. For the square lattice, the macroscopic length is L ($= L_1 = L_2$). For this type of lattice, two possible base cell geometries are

shown in Figure 5.1 (top left, top center left). The periodic arrangement of the two base cells in the two spatial directions results either in a *closed-* or an *open-boundary* lattice for the closed-square or cross base cell, respectively. The base cells for the triangular and 45° rotated square lattices are shown in Figure 5.1 (top center right) and (top right), respectively. Note that for these two types of lattice, no differentiation is made between closed- and open-boundary configurations. The *internal* or *characteristic length* of the lattices is defined as the length of its lattice members, namely, l $(= l_1 = l_2)$, see Figure 5.1 (top). The macroscopic dimensions of the lattices are directly related to the characteristic length via the number of base cells, N_1xN_2, comprising the lattices, where N_1 and N_2 are the number of base cells in 1- and 2-direction, respectively. This leads to $L_i = lN_i$ for the square, $L_1 = L = lN_1$ and $L_2 = lN_2 \sin(\pi/3)$ for the triangular, and $L_i = lN_i\sqrt{2}$ for the 45° rotated square lattice, where $i = \{1, 2\}$ for each spatial direction. For an equal arrangement in both directions, i.e., $N_1 = N_2$ $(= N)$, it follows N_1x$N_2 = N$xN. For the sake of simplicity, the out-of-plane dimension is set to $h = 1$ for all lattices studied and the cross-section of each individual lattice member is assumed to be rectangular, $A_\square = t \cdot h$, where t denotes the corresponding thickness. The geometrical moment of inertia for each lattice member follows from $I_\square = (t^3 \cdot h)/12$. For each lattice type studied, the relative density, $\rho_\mathrm{r} = V_s/V$, is independent of the number of base cells, where V_s and V denote the volume of the parent material and the domain occupied by the lattice, respectively. For this purpose, a constant ratio of thickness to length of the lattice members of $t/l = 1/20$ is considered for all types of lattices. For the square and the 45° rotated square lattice, this gives $\rho_\mathrm{r} = 0.0975$ with $V_s = 4lth - t^2$ and $V = (l\sqrt{2})^2 h$. For the triangular lattice, the relative density follows as $\rho_\mathrm{r} \approx (2\sqrt{3}t)/l = \sqrt{3}/10 \approx 0.173$ with $V_s = 3tlh$ and $V = l^2(\sqrt{3}/2)h$, where no overlapping of the lattice members at the intersection points is considered.

The parent material of all the lattice structures, i.e., the material of the individual lattice members, is assumed to be an isotropic linear elastic material with a Young's modulus of $E_\mathrm{s} = 120000$ MPa and a Poisson ratio of $\nu_\mathrm{s} = 0.3$. The shear modulus for the isotropic material follows as $G_\mathrm{s} = E_\mathrm{s}/(2(1 + \nu_\mathrm{s}))$.

5.1.2 Discrete reference models

The influence of the number of base cells comprising a lattice alters the overall mechanical response in a severe way, especially when the macroscopic size of the structure is closer to the base cell size $l \not\ll L$, which is known as size effect. The size effect of repetitive lattices mainly depends on the topology of the free surfaces that is governed by the geometry of the base cell. For the square lattice, the free-surface shows either a

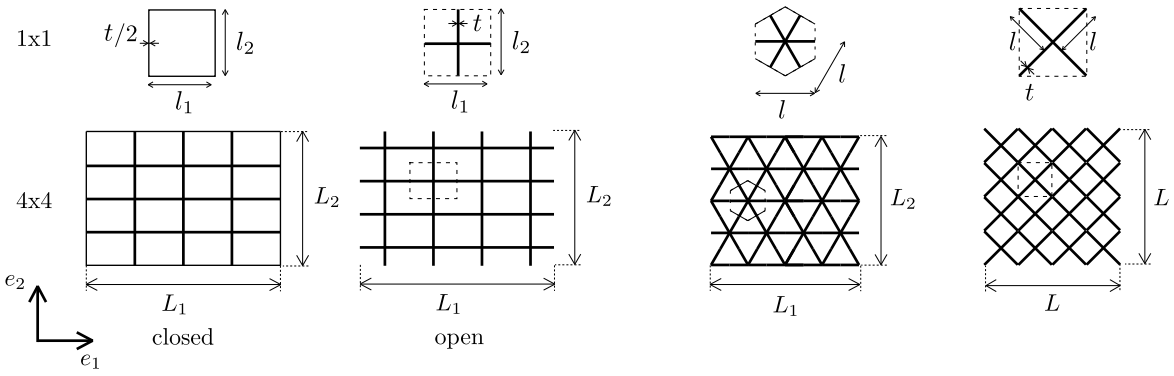

Figure 5.1: Closed-square, cross, triangular, and 45° rotated cross base cells (top) and corresponding closed-boundary square, open-boundary square, triangular, and 45° rotated square lattices exemplified for lattices consisting of NxN = 4x4 base cells (bottom), respectively.

closed- or an open-boundary for the periodic arrangements of the closed-square or the cross shaped base cells given in Figure 5.1 (left) and (center left), respectively. Therefore, two different discrete lattice models serve as references for the continuum model to address this issue and are further be called *closed-* or L and *open-boundary* or + *discrete models*. The elements representing the outer boundary of the closed-boundary model are assigned half of the cross-section and half of the geometrical moment of inertia, resulting in $A_\square/2$ and $I_\square/2$, respectively. Both models show the same relative density. The discrete models for the triangular and the 45° rotated square lattice are exemplified in the schematics given in Figure 5.1 (center right) and (right), respectively. The members of these lattices show the same geometrical properties as the members of the open-boundary square lattice. To account for the plane strain assumption as made for the micropolar continuum model, the Young's modulus $E_\mathrm{s} \to E$ and the shear modulus $G_\mathrm{s} \to G$ are converted according to Eq. (D.2).

All discrete lattice models are discretized by planar, linear Timoshenko beam elements accessible through the ABAQUS element library. Thereby, each strut of the lattice is discretized by six elements resulting in 12, 24, and 18 elements per base cell for the square, the 45° rotated square, and the triangular lattice, respectively. This discretization is considered appropriate to adequately capture the deformation state.

5.1.3 Methodology

Five different load cases and various configurations of the different types of lattices are used to evaluate the predictive capabilities and limitations of the micropolar continuum model with respect to the set of MECs used. The sets of constants of the individual lattices are given in Appendix D, where positive and negative MECs are denoted by $D_{55}^{\mathrm{pos}}, D_{66}^{\mathrm{pos}}$ or + and $D_{55}^{\mathrm{neg}}, D_{66}^{\mathrm{neg}}$ or −, respectively, since only these constants are different. The basis for the assessment is the comparison with discrete models in terms of strain energy and rotation field, ϕ_3 (= ϕ). The rotations at the midpoints, i.e., the origin joints O, of the base cells are of special interest for the comparison and are further denoted as MPBCs. The dimensions of the base cells range from sizes close to the overall dimensions of the lattice to sizes where the separation of scale is satisfied. Special focus is set on the influence of various FEM parameters of the continuum model on the predicted overall mechanical response, namely, the *finite element size*, h_e, and the *order of the interpolation functions*, or *interpolation order*, p_e. The rectangular domains occupied by the lattices are discretized by M_1xM_2 quadrilateral elements, where M_1 and M_2 are the number of elements in 1- and 2-direction, respectively. Considering the macroscopic dimensions, the side lengths of the elements with respect to the i-direction are obtained as $h_{e;i} = L_i/M_i$. This already indicates that the element size, h_e, is not unique, i.e., $h_{e;1} \neq h_{e;2}$. To study the competing length scales, it is meaningful to define the element size proportional to the characteristic length, i.e., $h_e \propto l$, and, additionally, to keep the ratio between the number of base cells and the number of elements the same for both spatial directions, i.e., $N_1/M_1 = N_2/M_2$. As both the microscopic dimensions of the base cell, l_i, and the corresponding element side lengths, $h_{e;i}$ are related to the macroscopic dimensions through $L_i = l_i N_i$ and $L_i = h_{e;i} M_i$, respectively, i.e., $h_{e;i}/l_i = N_i/M_i$ (no summation rule), it follows that $h_{e;1}/l_1 = h_{e;2}/l_2$ holds (no summation rule). The microscopic dimensions of the base cell in i-direction are $l_i = l$ for the square, $l_1 = l$ and $l_2 = l \sin(\pi/3)$ for the triangular, and $l_i = l\sqrt{2}$ for the 45° rotated square lattice. Even though for the triangular lattice two microscopic dimensions are obtained, i.e., $l_1 \neq l_2$, the ratio between $h_{e;i}$ and l_i is independent of the spatial direction, i.e., $h_{e;i}/l_i = N_i/M_i$ (no summation rule). Thus, which side length, $h_{e;i}$, is defined as the element size, h_e, does not matter as long as $N_1/M_1 = N_2/M_2$ is used. However, for the sake of clarity, the element size is defined with respect to 1-direction, i.e., $h_e = L_1/M_1$, for all lattices. Note that the number of elements is directly related to the number of base cells, e.g., using $h_e = l$ or equivalently $N_1 = M_1$ and $N_2 = M_2$ means that one base cell is represented by one element. In the following, h_e is used interchangeably with M_1 for a certain macroscopic dimension L_1. The same applies

to l and N_1. Furthermore, h_e will always be used in combination with l, since both are lengths. The same applies to M_1 and N_1, since both are positive natural numbers.

To ensure the comparability of discrete and continuum models and to additionally invoke the rotation field, two kinds of simple shear load cases, a compression, and a bending load case serve as the basis for the comparison. Distributed loads are preferred over point loads, such as the indentation load used in [53], as the length scale of the microstructure and the overall structure size are of the same order of magnitude for some of the lattice configurations studied. Local effects may dominate the overall response of the discrete lattice model due to the load application, which is hard to capture by continuum modeling. However, to support this assumption, the indentation load case presented in [53] is revisited.

The largest study is conducted on the basis of the simple shear load cases, which are schematically depicted in Figure 5.2. For both load cases, the displacements and rotations are fully clamped at the bottom boundary of the lattice. At the top boundary of the lattice, a displacement in 1-direction is prescribed with $U_1 = 0.2\text{mm}$, whereas the displacement in 2-direction is fixed. The difference for the two load cases can be found for the rotations at the top. These are left free for the more artificial simple shear load case to obtain a different gradient evolving from each boundary and are fixed for the other load case, cf. Figure 5.2 (left) and (right), respectively. The study mainly relies on different configurations of the square lattice. Additionally, a single configuration of the triangular lattice is examined to support the findings.

The indentation load case is schematically depicted in Figure 5.3 (left). The whole setting follows [53], expect that a prescribed displacement of $U_2 = 0.3\text{mm}$ is used instead of a point force. The displacement is applied at $X_1 = X_2 = 50\text{mm}$. The bottom of the lattice is fully clamped and the lattice investigated is a square lattice.

For the compression load case, the 45° rotated square lattice is used instead of the square lattice in order to invoke the rotation field and to obtain a problem dominated by bending rather than stretching. The load case is schematically depicted in Figure 5.3 (center), where the bottom and top are fully clamped except in 2-direction at the top. The prescribed displacement load is $U_2 = 0.1\text{mm}$.

To study the predictive capabilities of the continuum model considering a more realistic engineering problem, a bending load case on lattice beams is applied, see Figure 5.3 (right). The displacements and rotations are fully clamped at the left side while a displacement in 2-direction is prescribed with $U_2 = 20\text{mm}$ at the right side.

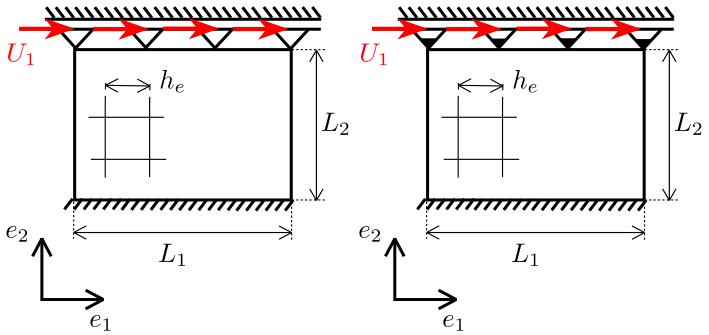

Figure 5.2: Schematics of the simple shear load cases with rotations free (left) and fixed (right) at the top. Regions where no displacements are prescribed are traction-free.

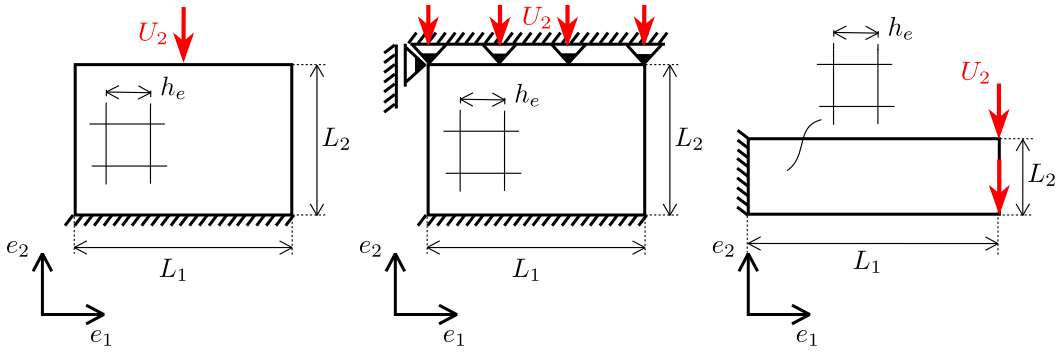

Figure 5.3: Schematic of the indentation (left), compression (center), and bending (right) load cases. Regions where no displacements are prescribed are traction-free.

A model based on CET also serves as reference for some of the investigations. It can be obtained by either using the corresponding classical equations in combination with classical elastic constants, which is done in the present work, or using a limit case of the micropolar continuum. Classical elastic constants of the square lattice can be found, e.g., in [34]. Note that these constants can also be obtained from the micropolar continuum by using the same constants relating normal stresses to strains, i.e., $D_{11}^{\mathrm{C}} = D_{11}$, $D_{12}^{\mathrm{C}} = D_{12}$, and $D_{22}^{\mathrm{C}} = D_{22}$, as well as using the average of the MECs coupling both shear stresses, i.e., $D_{33}^{\mathrm{C}} = (D_{33} + D_{34})/2$, see, e.g., [97]. The limit case is obtained by using classical elastic constants, e.g., $D_{33} = D_{44} = D_{33}^{\mathrm{C}}$ for the square lattice, in combination with either suppressing all rotational DOFs or setting $D_{55} \to \infty$ and $D_{66} \to \infty$. Alternatively, a very small characteristic length of the lattice, i.e., $l \to 0$, can be used with the rotational DOFs still present.

5.2 Results and discussion

5.2.1 Simple shear

The configurations of the square lattice used for the simple shear load cases are summarized in Table 5.1. *Closed-* and *open-boundary* discrete lattice models serve as references for comparison with the continuum models. The configuration of the triangular lattice can be found in Table 5.2. For the continuum model, the NGSolve implementation is used to facilitate the numerical study of the FEM parameters, cf. Section 4.2.3.

Investigation of the strain energy

The strain energy is investigated based on the results for the simple shear load case with rotations fixed at the top. To study the influence of the FEM parameters of the continuum model on the strain energy, the influence of the element size, h_e, is investigated in the first place. Second, the influence of the interpolation order is studied. The strain energies obtained for the discrete models of the square lattice are summarized in Table 5.3, except for NxN = 1000x1000, which needs to be considered computationally costly showing 12 million elements.

Table 5.1: Geometrical dimensions of the studied square lattices for the simple shear load cases.

NxN	L	h	l	t
(/)	in mm	in mm	in mm	in mm
4x4	1.0	1.0	0.25	0.0125
8x8	1.0	1.0	0.125	0.00625
16x16	1.0	1.0	0.0625	0.003125
32x32	1.0	1.0	0.0625	0.00078125
1000x1000	1.0	1.0	0.001	0.00005

Table 5.2: Geometrical dimensions of the studied triangular lattice for the simple shear load cases.

NxN	L_1	L_2	h	l	t
(/)	in mm	in mm	in mm	in mm	in mm
8x8	1.0	0.866	1.0	0.125	0.00625

Table 5.3: Strain energies of the closed- (L) and open-boundary (+) discrete models for various square lattices.

NxN	BTfixed		Bfixed	
	L	+	L	+
(/)	in N mm	in N mm	in N mm	in N mm
4x4	0.192928	0.180320	0.188140	0.155470
8x8	0.177621	0.170599	0.175566	0.160039
16x16	0.170458	0.167014	0.169506	0.162110
32x32	0.166572	0.165165	0.166116	0.162803

The evolution of the strain energy over the element size of the continuum model, h_e, is studied for various square lattices consisting of Nx$N = \{4\text{x}4, 8\text{x}8, 16\text{x}16, 32\text{x}32, 1000\text{x}1000\}$ base cells. Linear interpolation is used, i.e., $p_e = 1$. The results are shown in Figure 5.4 (top left) and (top right) for positive and negative MECs, respectively. For positive constants, it is shown that for an increasing number of elements, $M(= M_1 = M_2)$, i.e., decreasing element sizes, h_e, the strain energy shows convergence behavior corresponding to a certain lattice comprised of NxN base cells. Furthermore, for increasing $N(= N_1 = N_2)$, i.e., decreasing microscopic sizes, l, the strain energy converges towards a constant value of about 0.162N mm. This is expected due to the vanishing free-edge effect for increasing numbers of base cells. Information on the capability of the model to capture size effects it is referred to [97]. Note that for the CET continuum approximately the same results are obtained as for the micropolar continuum for NxN = 1000x1000, hence, the CET results are not explicitly shown in Figure 5.4 (top left). For the negative constants, once the element size reaches the characteristic length of the lattice, the strain energy starts to show oscillations, e.g., Nx$N = M$xM = 4x4 or Nx$N = M$xM = 8x8. Hence, using element sizes smaller than the characteristic length of the lattice is questionable. This observation has already been outlined and discussed in [53], and is revisited in Section 3.2.

For different interpolation orders, $p_e = \{1, 2, 3\}$, the evolution of the strain energy over the element size is studied for square lattices consisting of NxN = 8x8 and NxN = 16x16 base cells, see Figure 5.4 (bottom left)

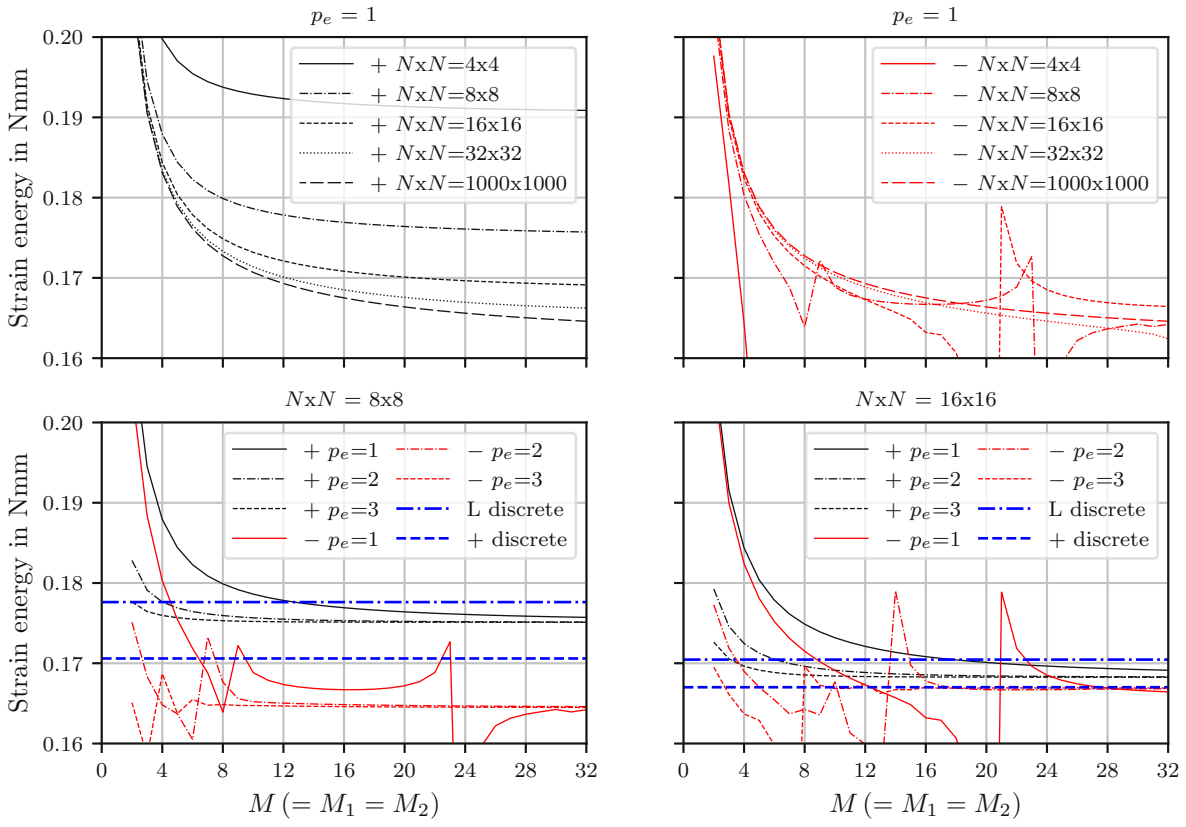

Figure 5.4: Simple shear with rotations fixed at top - Evolution of strain energies over element size for square lattices comprised of various base cells NxN with fixed interpolation order of $p_e = 1$ for positive (top left) and negative MECs (top right). Evolution of strain energy over element size of continuum model, $h_e = 1/M$, for lattices comprised of NxN = 8x8 (bottom left) and NxN = 16x16 base cells (bottom right) using various interpolation orders considering positive and negative constants.

and (bottom right), respectively. Both sets of MECs are considered and directly compared. For the positive constants, the strain energy converges faster to a constant value for higher interpolation orders. For negative constants, the oscillations occur for smaller values of MxM, the higher the interpolation order is. For the lattice NxN = 8x8, oscillation can be observed for the parameter sets composed of $\{p_e = 1, M\text{x}M = 8\text{x}8\}$, $\{p_e = 2, M\text{x}M = 4\text{x}4\}$, and $\{p_e = 3, M\text{x}M = 2\text{x}2\}$. For the lattice NxN = 16x16, oscillations start to occur for the parameter sets composed of $\{p_e = 1, M\text{x}M = 16\text{x}16\}$, $\{p_e = 2, M\text{x}M = 8\text{x}8\}$, and $\{p_e = 3, M\text{x}M = 4\text{x}4\}$. These results can be used to set up a condition for the element size considering a certain interpolation order. Considering interpolation orders up to $p_e = 3$, it follows that the finite element size must be chosen to satisfy

$$h_e > l \cdot (p_e + H(p_e - 3)) \quad , \tag{5.1}$$

where $H(x)$ is the Heaviside function, giving 0 for $x < 0$ and 1 for $x \geq 0$. Alternatively, this can be expressed in terms of the number of base cells and finite elements reading

$$N > M \cdot (p_e + H(p_e - 3)) \quad . \tag{5.2}$$

For very small internal dimensions, $l \ll L$, in combination with coarse element sizes compared to the characteristic length of the lattice, i.e., $l \ll h_e$ or $N \gg M$, the difference of the strain energy between positive and negative constants vanishes, cf. lattice NxN = 1000x1000 in Figure 5.4 (top left) and (top right). This is already indicated for $l < L$, cf. lattice NxN = 16x16 for $p_e = 1$ and Mx$M \approx$ 4x4, see Figure 5.4 (bottom right). This is expected as the values for the MECs relating curvature and couple stress are becoming small and the response is more dominated by the displacement based quantities. Note that the condition for the element size specified must be satisfied.

For the triangular lattice comprised of NxN = 8x8 base cells, the evolution of the strain energy over the element size of the continuum model is given in Figure 5.5. The interpolation order is varied using $p_e = \{1, 2\}$ for both positive and negative constants. Both positive and negative constants show approximately the same characteristics as was observed for the square lattice. Positive constants show convergence behavior for decreasing element sizes, negative constants show oscillating convergence behavior once the condition given in Eq. (5.1) defined for the square lattice is satisfied except for $p_e = 1$. For $p_e = 1$, the spike shows up for

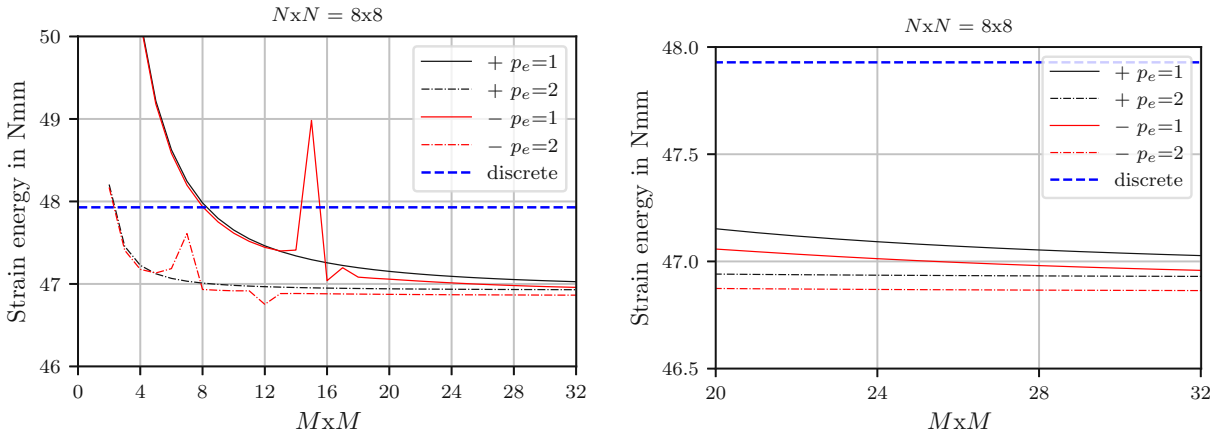

Figure 5.5: Simple shear with rotations fixed at top. Evolution of strain energies over element size for triangular lattice comprised of NxN = 8x8 base cells using interpolation orders of $p_e = \{1, 2\}$ for positive and negative MECs with detail (right).

MxM = 16x16 and does not appear for MxM = 8x8 as expected based on Eq. (5.1). However, the rotation field shows an oscillation pattern for MxM = 8x8, which will be discussed in the next Section. For very small element sizes, $h_e \ll l$, both positive and negative constants lead to approximately the same results.

Investigation of the rotation field

The rotation field is investigated on the basis of both simple shear load cases. Various FEM parameters are varied to study their influence on the predicted rotation field with special focus set on positive and negative MECs. A lattice comprised of NxN = 8x8 base cells is the basis for the investigations. Hence, the separation of scales cannot be considered fully satisfied, which is intended in order to study the capabilities of the micropolar continuum. For the square lattice, only the open-boundary discrete model is used for the comparison. In the following, the square lattice is treated first and then the triangular lattice.

In the first place, the simple shear load case with rotations fixed at top is considered. For the positive constants, the rotation fields are shown in Figure 5.6 for different parameter sets consisting of element size and interpolation order. For the set $\{p_e = 1, M\text{x}M = 4\text{x}4\}$ (top left), the rotation field is not completely resolved, whereas this is the case for the set $\{p_e = 2, M\text{x}M = 4\text{x}4\}$ (top right). For the set $\{p_e = 1, M\text{x}M = 8\text{x}8\}$

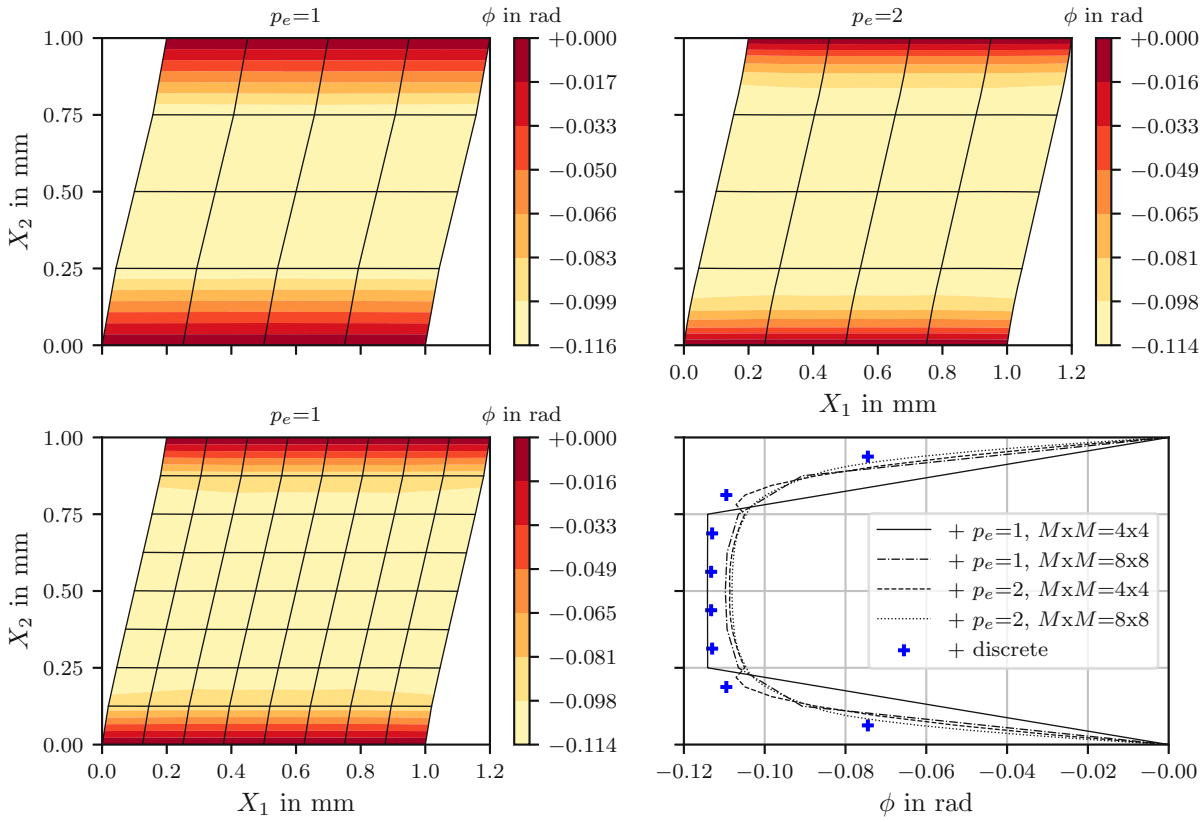

Figure 5.6: Positive constants - Rotation fields for square lattice comprised of NxN = 8x8 base cells for varying element size and interpolation order. Contour plots are given for the sets $\{p_e = 1, M\text{x}M = 4\text{x}4\}$ (top left), $\{p_e = 2, M\text{x}M = 4\text{x}4\}$ (top right), and $\{p_e = 1, M\text{x}M = 8\text{x}8\}$ (bottom left). Rotations over the height at $X_1 = 0.4375$mm, where + markers represent the solution of the discrete lattice at MPBCs (bottom right).

(bottom left), the field can be considered converged as well. In Figure 5.6 (bottom right), the corresponding rotations are given over the height at $X_1 = (N\text{x}N/2 - 1) \cdot l + l/2 = 0.4375\text{mm}$, which is associated with the mid left lattice column. The + markers represent the rotation of the discrete model at the MPBCs. The rotations of the continuum model agree well with the discrete model, especially for higher interpolation orders and finer meshes. Furthermore, the gradients of the rotation fields are well captured as long as the following condition for the element size,

$$h_e \lessapprox l \cdot (p_e + H(p_e - 3)) \quad , \tag{5.3}$$

is satisfied.

For negative constants, the rotation fields are shown in Figure 5.7. For the parameter set $\{p_e = 1, M\text{x}M = 4\text{x}4\}$ (top left), the rotation field is similar to its positive counterpart, cf. Figure 5.6 (top left), but already indicates the oscillation pattern at $X_2 = L/2$. This can be considered negligible. For the set $\{p_e = 2, M\text{x}M =$

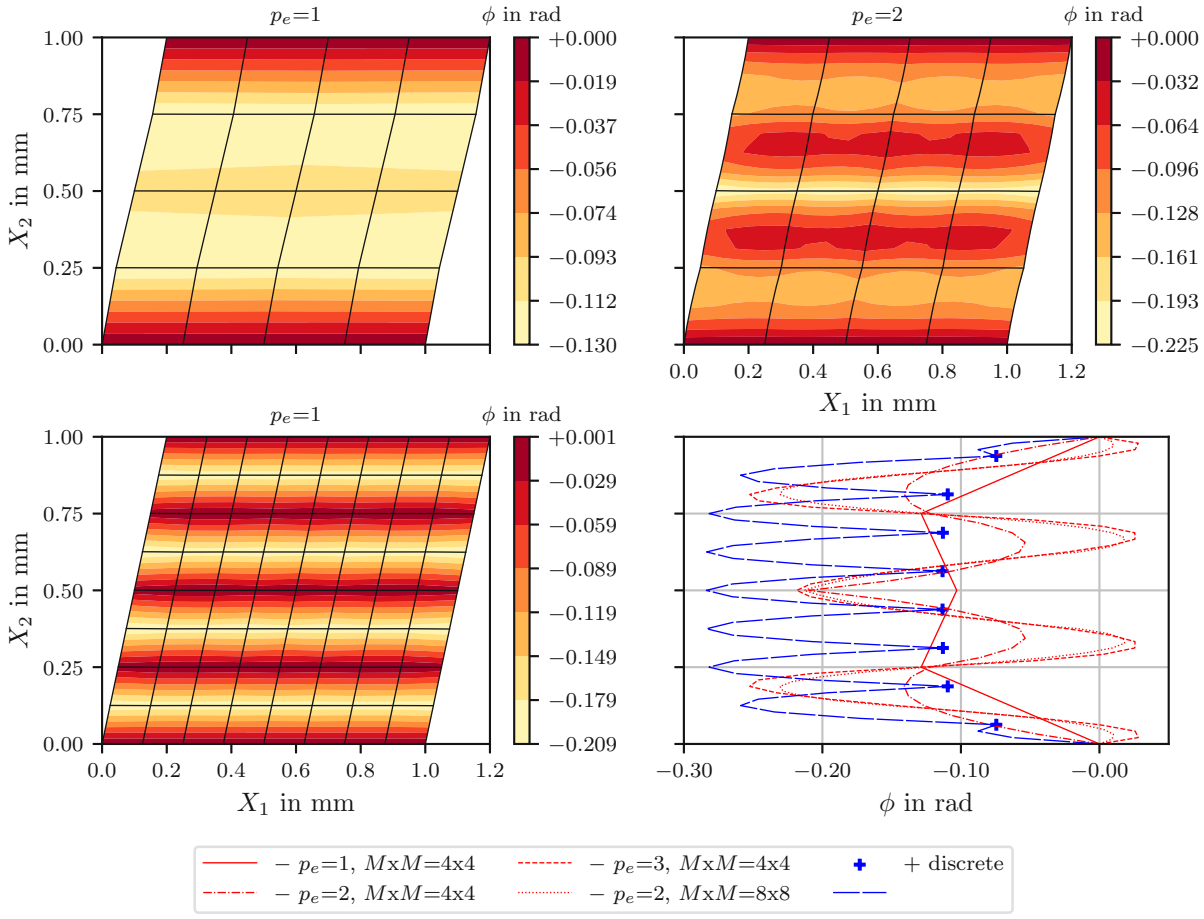

Figure 5.7: Negative constants - Rotation fields for square lattice comprised of $N\text{x}N$ = 8x8 base cells for varying element size and interpolation order. Contour plots are given for the sets $\{p_e = 1, M\text{x}M = 4\text{x}4\}$ (top left), $\{p_e = 2, M\text{x}M = 4\text{x}4\}$ (top right), and $\{p_e = 1, M\text{x}M = 8\text{x}8\}$ (bottom left). Rotations over the height at $X_1 = 0.4375\text{mm}$ (bottom right), where + markers represent the solution of the discrete lattice at MPBCs and blue dashes indicate the corresponding local rotation field along the fourth column of the lattice.

4x4} (top right), the rotation field already shows a developing oscillation pattern. For the set $\{p_e = 1, M\text{x}M = 8\text{x}8\}$ (bottom left), the rotation field shows a pattern with short wavelength oscillations. In Figure 5.6 (bottom right), the corresponding rotations are given over the height at $X_1 = (N\text{x}N/2-1)\cdot l+l/2 = 0.4375$mm, where the + markers represent the rotation of the discrete model at the MPBCs. The rotations of the continuum model only agrees with the discrete model as long as the condition for the element size given in Eq. (5.1) is satisfied. Otherwise, the rotation field shows a pattern with oscillations. This pattern converges for very small element sizes $M\text{x}M = 64\text{x}64$, cf. Figure 5.8 for $p_e = 1$ (top left) and $p_e = 2$ (top right). This also holds true for the lattice comprised of $N\text{x}N = 16\text{x}16$ base cells given in Figure 5.8 (bottom), where the oscillation shows approximately half the wavelength obtained for the lattice with $N\text{x}N = 8\text{x}8$ base cells. Although the wavelength seems to be directly linked to the characteristic length, the oscillations cannot be explained by the local rotation field obtained for the open-boundary discrete lattice, where the wavelength of the oscillation is too long to fit to the discrete counterpart, cf. Figure 5.7 (bottom right). To capture the gradient of the rotation field, a proper discretization of the continuum model is necessary regarding the element size in combination with the interpolation order. This necessity is in conflict with the condition necessary for the element size. Hence, the gradients of the rotation fields can hardly be captured using negative constants.

It is worth noting that both sets of MECs give approximately the same rotation fields as long as the condition, $h_e > l \cdot (p_e + H(p_e - 3))$, is satisfied, cf. Figure 5.6 (top left) and Figure 5.7 (top left).

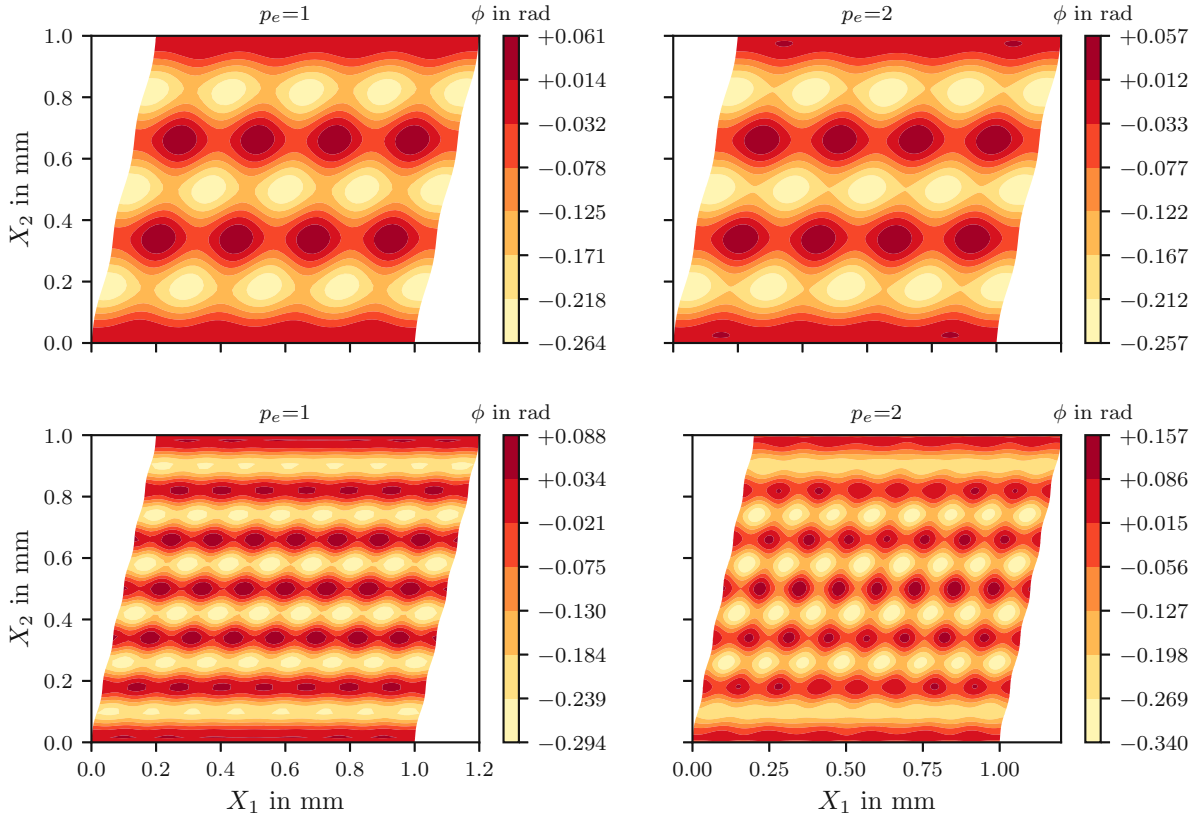

Figure 5.8: Rotation fields for square lattices comprised of $N\text{x}N = 8\text{x}8$ (top) and $N\text{x}N = 16\text{x}16$ (bottom) base cells. Contour plots are given for the sets $\{p_e = 1, M\text{x}M = 64\text{x}64\}$ (left), $\{p_e = 2, M\text{x}M = 64\text{x}64\}$ (right) using negative constants only.

For the simple shear load case with rotations free at the top and various parameter sets, the rotation fields and their corresponding line plots are presented in Figure 5.9. For positive constants (top left and right), the rotation field is already resolved for the set $\{p_e = 2, M\text{x}M = 4\text{x}4\}$. Furthermore, the gradient in the rotation field is well captured for sufficiently fine mesh sizes, cf. $\{p_e = 1, M\text{x}M = 8\text{x}8\}$, or coarse meshes using higher interpolation orders, cf. $\{p_e = 2, M\text{x}M = 4\text{x}4\}$. This meets the condition for the element size using positive constants given in Eq. (5.3). For negative constants, the gradient cannot be resolved for the given parameter sets.

For the triangular lattice, the simple shear load case with rotations fixed at top is used for the comparison between continuum and discrete models, see Figure 5.10. The contour plots show the rotation fields obtained for an interpolation order of $p_e = 1$ and a number of elements of $M\text{x}M8$ ($h_e = 0.125$) for positive (top left) and negative constants (bottom left). The rotation field shows the same characteristics as obtained for the square lattice with respect to the constants used. Convergence behavior for decreasing element sizes is obtained for the positive constants, whereas for negative constants, once the element size is equal or lower than the characteristic length, the rotation field shows an oscillation pattern. The rotations are given over the height at $X_1 = 0.0625$mm (top right) and $X_1 = 0.4375$mm (bottom right) for different FEM parameter sets permuting $\{p_e = 1, M\text{x}M = 8\text{x}8, 16\text{x}16\}$ for both positive and negative constants. Good agreement between

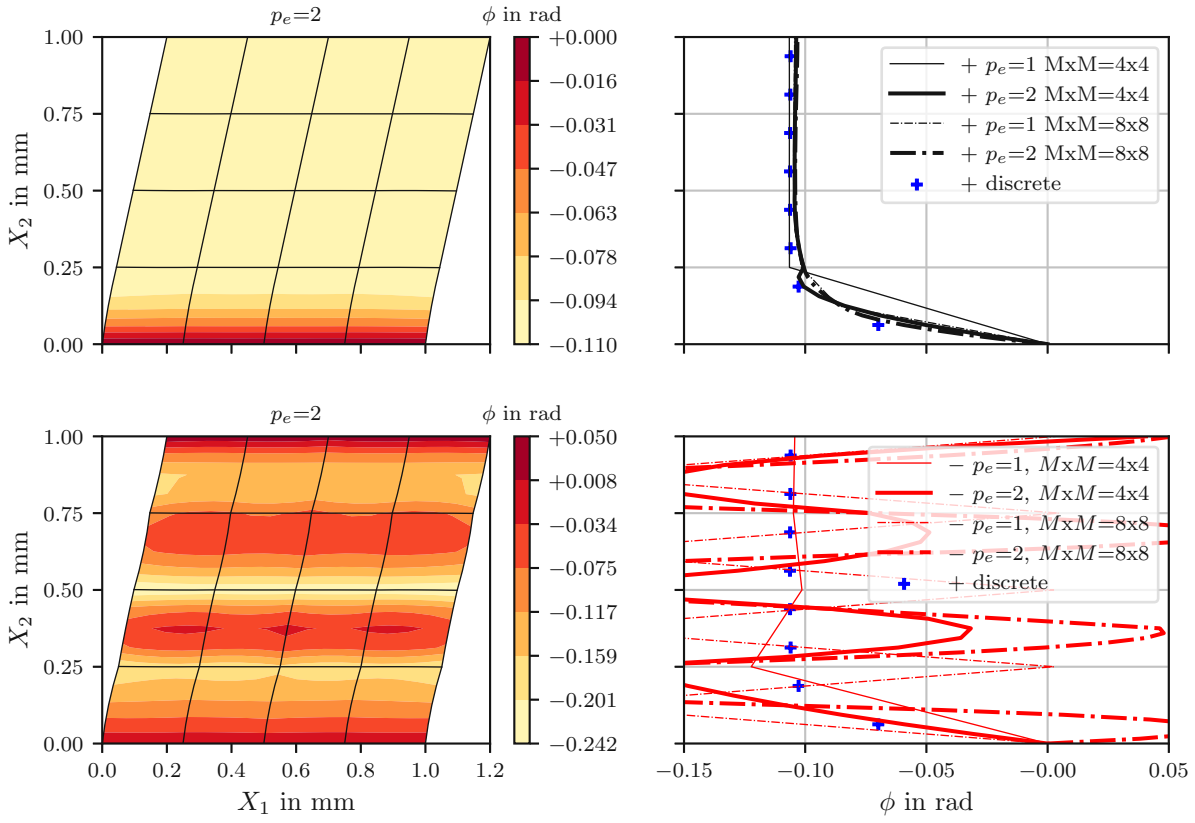

Figure 5.9: Simple shear with rotations free at top - Rotation fields for square lattice comprised of $N\text{x}N = 8\text{x}8$ base cells for the set $\{p_e = 2, M\text{x}M = 4\text{x}4\}$ considering positive (top left) and negative constants (bottom left). Rotations over the height at $X_1 = 0.4375$mm for different parameter sets permuting $\{p_e = 1, 2, M\text{x}M = 2, 4, 8\}$ for positive (top right) and negative constants (bottom right), where + markers represent the solution of the discrete lattice at MPBCs.

the continuum and the discrete model is obtained for distances close to the boundary while even very good agreement is achieved in the far-field region, i.e., the region with sufficient distance to the boundary, where the influence of the boundary declines.

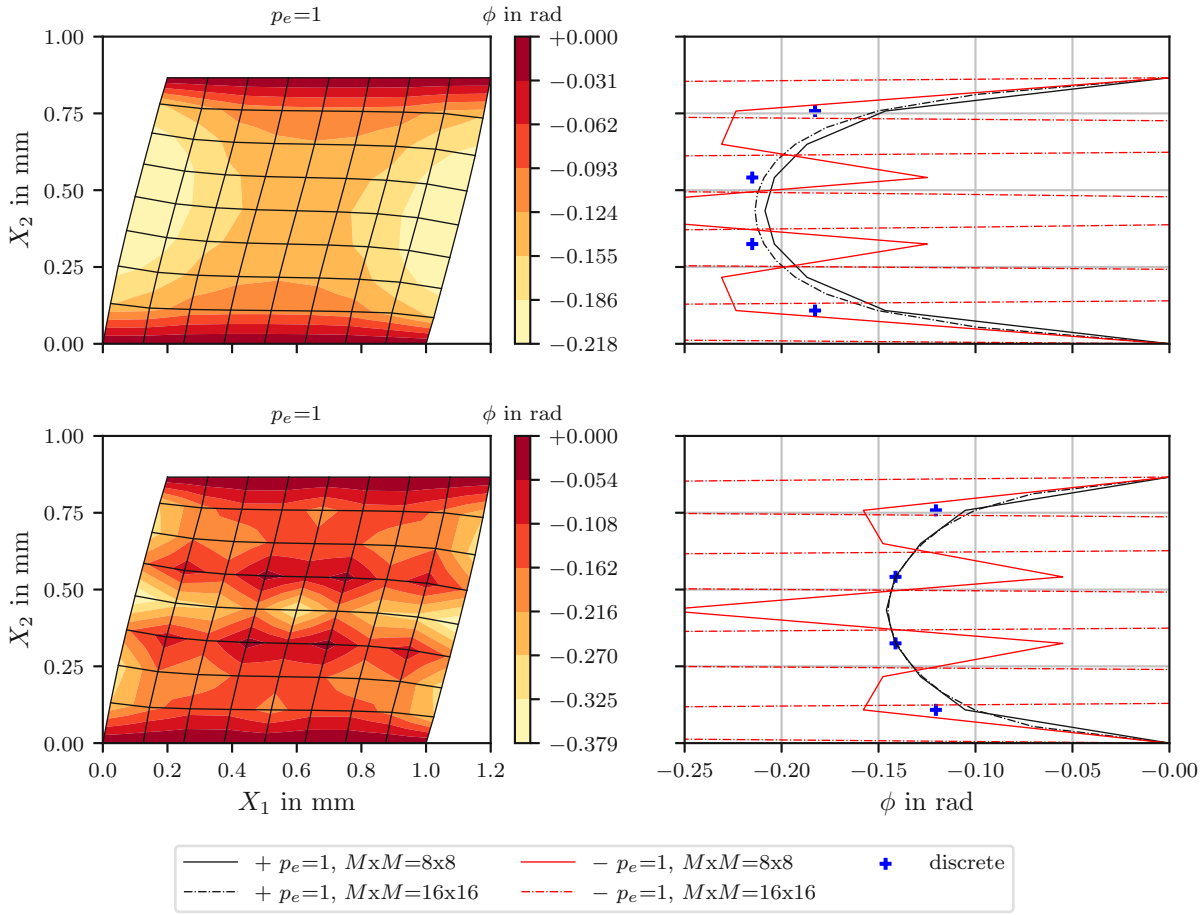

Figure 5.10: Simple shear with rotations fixed at top - Rotation fields for the triangular lattice comprised of NxN = 8x8 base cells for the set $\{p_e = 1, M\text{x}M = 8\text{x}8\}$ considering positive (top left) and negative MECs (bottom left). Rotations over the height at $X_1 = 0.0625$mm (top right) and $X_1 = 0.4375$mm (bottom right) for different parameter sets permuting $\{p_e = 1, M\text{x}M = 8\text{x}8, 16\text{x}16\}$ for both positive and negative constants, where + markers represent the solution of the discrete lattice at MPBCs.

5.2.2 Indentation

A single configuration of the square lattice is used for the indentation load case following [53]. The geometrical properties are summarized in Table 5.4. An open-boundary discrete lattice model serves as reference for comparison with the continuum models. Note that the exact load application for the discrete model is at $X_1 = 50\text{mm}$ and $X_2 = 49\text{mm}$, in contrast to the continuum model where the load is applied at $X_1 = 50\text{mm}$ and $X_2 = 50\text{mm}$. For the continuum model, the NGSolve implementation is used, cf. Section 4.2.3.

Investigation of the strain energy

The evolution of the strain energy over various element sizes and interpolation orders of the continuum model is given in Figure 5.11. Independent of the chosen set of FEM parameters, the overall response is much stiffer compared to the discrete reference model. With an increasing number of elements, the response of the continuum model becomes more compliant. Nevertheless, the strain energy differs by about a factor of two even for the smallest element size studied. This discrepancy is mainly driven by the fact that the continuum model does not provide any information about the exact situation at the point of load application. This information is crucial for this kind of load case. To account for this effect, information must be provided, e.g., using hybrid forms of modeling, such as using beam elements to resolve the discrete lattice structure in a region around the point of load application discrete elements to discretize the domain of the boundary layer. This is beyond the scope of the present thesis.

Table 5.4: Geometrical dimensions of the studied square lattice for the indentation load case.

NxN	L_1	L_2	h	l	t
(/)	in mm	in mm	in mm	in mm	in mm
50x25	100.0	50.0	1.0	2.0	0.1

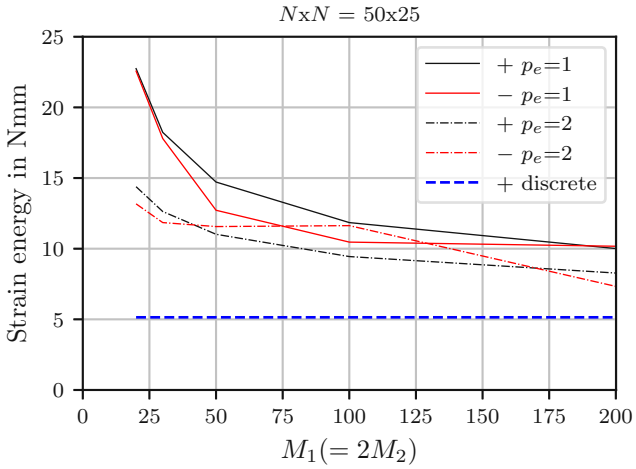

Figure 5.11: Indentation - Evolution of strain energies over element sizes MxM = {30x15, 50x25, 100x50, 200x100} for a square lattice comprised of NxN = 50x25 base cells using interpolation orders of $p_e = \{1, 2\}$ for both positive and negative constants.

Investigation of the rotation and stress fields

Following [53], the rotations along the top row of the lattice at $X_2 = 49$mm are given for various element sizes in Figure 5.12 (a) and (b) for positive and negative constants, respectively. For positive constants, the rotations are too small in magnitude compared to the discrete model and the gradient cannot be completely resolved even for the smallest element size, i.e., $h_e = l/4$ or $M_1 = 200$. This is in accordance with the results for the much stiffer response of the continuum model already indicated by the strain energy. For negative constants, the rotations show an oscillation pattern once the element size is smaller than the characteristic length of the lattice. For $h_e > l$ or $M_1 > 50$, the results are in agreement with those obtained for the positive constants. For $h_e \leq l$ or $M_1 \leq 50$, the rotations at the load application point show the same order of magnitude for continuum and discrete model. The magnitudes are also high in the far-field region for the continuum model using negative constants, where no rotations are obtained for the discrete model. These findings are in agreement with those presented in [53], which are solely based on using first order interpolation functions. Based on the findings of the simple shear load cases, second order interpolation functions are used as well to investigate their influence on the rotation field, which has not been presented in [53]. Figure 5.13 shows that the condition for the element size derived for the simple shear load cases given in Eq. (5.1) is still valid. When the condition is fulfilled, as it is the case for the largest element sizes, almost no oscillation within the rotation field occurs for negative constants. Once the condition is not satisfied anymore, the field shows an oscillation pattern, which is the case for $\{p_e = 2, M_1\text{x}M_2 = 30\text{x}15\}$, cf. Figure 5.13 (b).

Additionally, various stress fields of the continuum model are shown in Figure 5.12 for positive (c,e) and negative constants (d,f) for $\{p_e = 1, M_1\text{x}M_2 = 200\text{x}100\}$. The contours of the stress component σ_{22} given in Figure 5.12 (c,d) are only slightly different for using positive (c) and negative constants (d). This is based on the fact that this stress component is hardly affected by the different constants linking curvature and couple stress. Contrary, the contours of the stress component ${}^{\kappa}\sigma_{23}$ given in Figure 5.12 for positive (e) and negative constants (f) show significant differences. For negative constants, an oscillation pattern of the stress component ${}^{\kappa}\sigma_{23}$ over the entire lattice can be observed. For positive constants, the gradients in the stress field are limited to the region close to the indentation point.

Similar findings are obtained for $\{p_e = 2, M_1\text{x}M_2 = 30\text{x}15\}$, see Figure 5.13 (c,d,e,f) for various stress fields. Note that the condition on the element size given in Eq. (5.1) is intentionally chosen not to be satisfied. The field of the stress component σ_{22} given in Figure 5.13 (c,d) shows a different pattern for using positive (c) and negative constants (d). For negative constants, an oscillation pattern over the entire lattice domain can be observed. In contrast, when linear interpolation with FEM parameter set $\{p_e = 1, M_1\text{x}M_2 = 200\text{x}100\}$ was used, no oscillation pattern has been observed in such a distinct manner, cf. Figure 5.12 (d). For $\{p_e = 2, M_1\text{x}M_2 = 30\text{x}15\}$, the field of the stress component ${}^{\kappa}\sigma_{23}$ is shown in Figure 5.13 for using positive (e) and negative constants (f). Again, for negative constants, an oscillation pattern over the entire lattice domain can be observed, which is similar to the one obtained for the linear interpolation with FEM parameter set $\{p_e = 1, M_1\text{x}M_2 = 200\text{x}100\}$ shown in Figure 5.12 (f).

Summarizing, the results reveal that the condition for the element size given in Eq. (5.1) needs to be satisfied when using negative constants to prevent the prediction of unfeasible oscillations not only in the rotation field but also in the stress fields. This means that there is not only a restriction on the element size but also on the interpolation order, which has not been considered in [53].

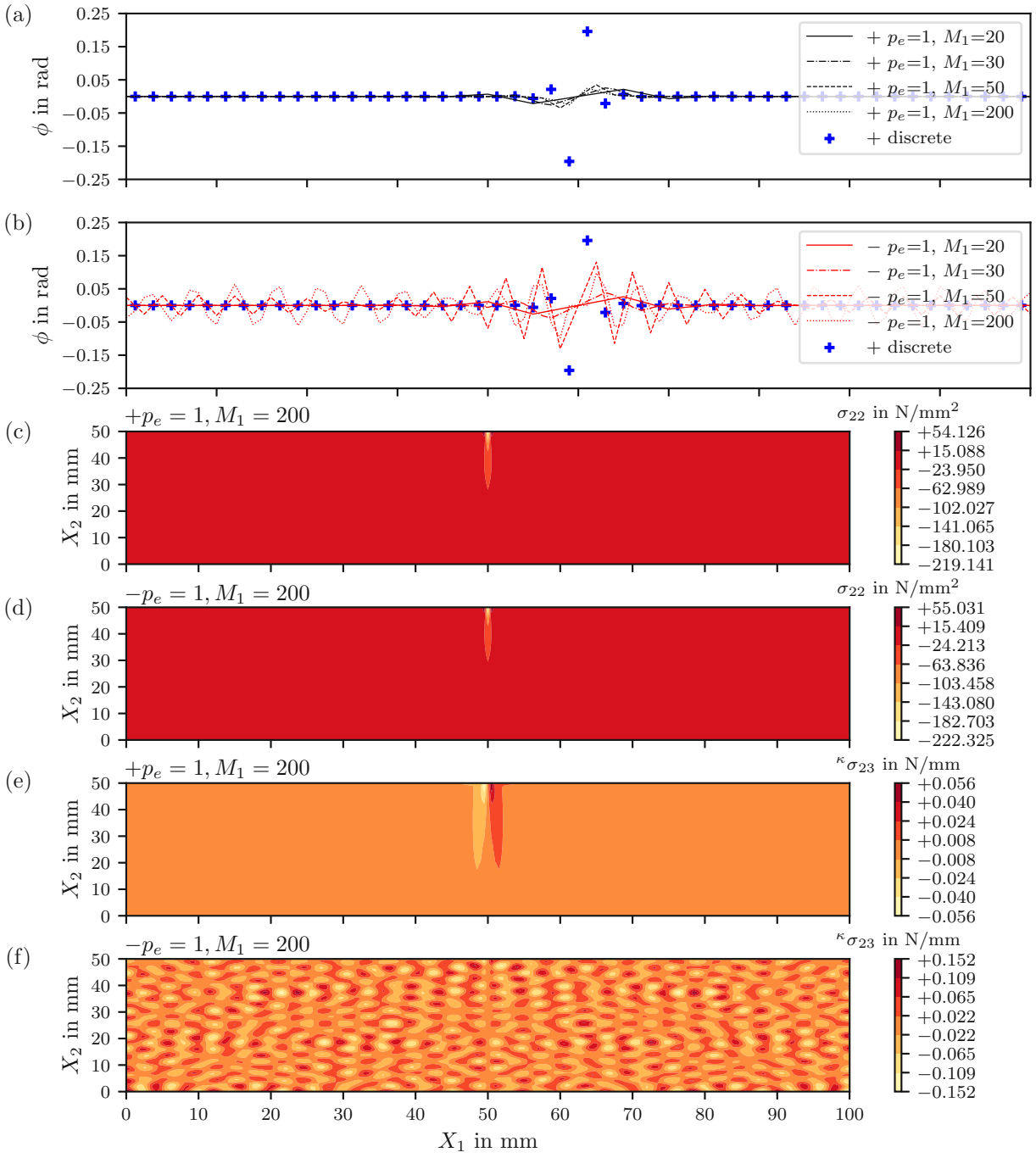

Figure 5.12: Indentation - Rotations along the width at $X_2 = 49$mm for interpolation order $p_e = 1$ and different numbers of elements for positive (a) and negative constants (b), where + markers represent the solution of the discrete lattice at MPBCs. Stress fields σ_{22} (c,d) and $^{\kappa}\sigma_{23}$ (e,f) for the continuum model with a number of elements of M_1xM_2 = 200x100 ($h_e = 0.5$) using an interpolation order of $p_e = 1$ for positive (c,e) and negative constants (d,f).

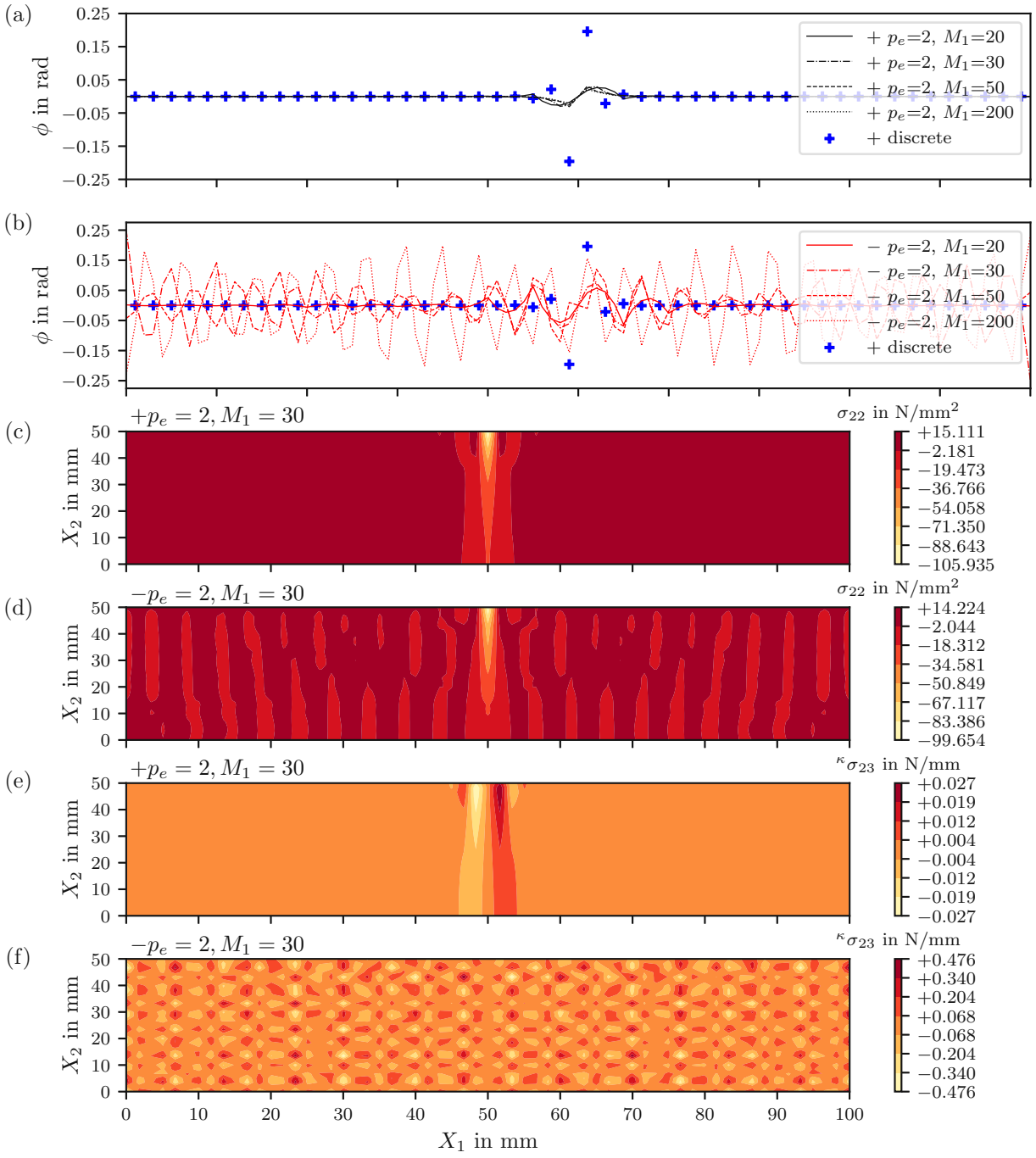

Figure 5.13: Indentation - Rotations along the width at $X_2 = 49$mm for interpolation order $p_e = 2$ and different numbers of elements for positive (a) and negative constants (b), where + markers represent the solution of the discrete lattice at MPBCs. Stress fields σ_{22} (c,d) and $^{\kappa}\sigma_{23}$ (e,f) for the continuum model with a number of elements of M_1xM_2 = 30x15 ($h_e = 3 + 1/3$) using an interpolation order of $p_e = 2$ for positive (c,e) and negative constants (d,f).

5.2.3 Compression

A single configuration of the 45° rotated square lattice is used for the compression load case. The geometrical properties are summarized in Table 5.5. For the continuum model, the NGSolve implementation is used, cf. Section 4.2.3.

Investigation of the strain energy

The evolution of the strain energy over the element size of the continuum model using an interpolation order of $p_e = 1$ is shown in Figure 5.14 for both positive and negative constants. For positive constants, it is shown that for an increasing number of elements, MxM, the strain energy shows convergence behavior. This also holds true for using negative constants until Mx$M \approx$ 36x36, where the strain energy starts to slightly deviate from the overall decreasing tendency. In contrast to the results obtained for the square lattice in particular, both positive and negative constants give approximately the same predictions across the element sizes studied where the strain energies predicted by the continuum models are far lower than for the discrete model.

Investigation of the rotation field

The rotation fields for both positive (top left) and negative constants (bottom left) are given for parameter sets $\{p_e = 1, M\text{x}M = 8\text{x}8\}$ and $\{p_e = 1, M\text{x}M = 16\text{x}16\}$ in Figures 5.15 and 5.16, respectively. For the coarse mesh, i.e., $\{p_e = 1, M\text{x}M = 8\text{x}8\}$, the rotation fields for both positive and negative constants show

Table 5.5: Geometrical dimensions of the studied 45° rotated square lattice for the compression load case.

NxN	L	h	l	t
(/)	in mm	in mm	in mm	in mm
8x8	1.0	1.0	$0.125/\sqrt{2}$	$0.00625/\sqrt{2}$

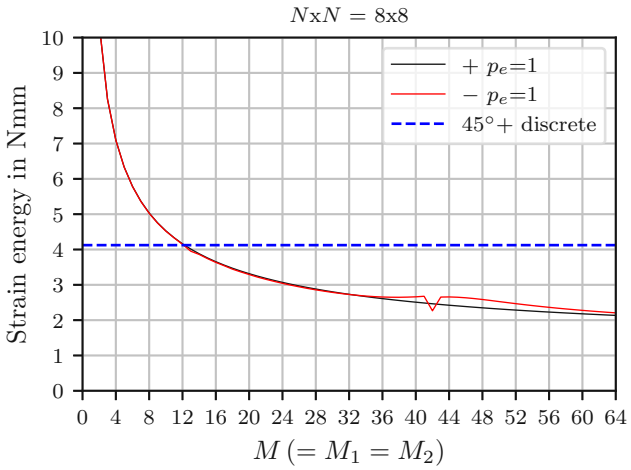

Figure 5.14: Compression load case - Evolution of strain energies over element size for the 45° rotated square lattice comprised of Nx$N = 8$ base cells using an interpolation order of $p_e = 1$ for both positive and negative constants.

a similar pattern, but different magnitudes. Differences of about 60% are obtained. For the fine mesh, i.e., $\{p_e = 1, M\text{x}M = 16\text{x}16\}$ with $h_e < l$, the rotation field obtained for negative constants shows an oscillation pattern with the rotations being almost twice as large as those of the corresponding coarse mesh. The rotation field obtained for positive constants is clearly better resolved by the fine mesh. The rotations are comparable to those obtained for the coarse mesh.

Additionally, the rotations are presented over the height of the lattice for two positions fixed at $X_1 = 0.0625$mm (top right) and $X_1 = 0.4375$mm (bottom right) for both parameter sets. For positive constants, the rotation field shows convergence behavior under mesh refinement. The characteristics of the high gradients that are present from the corners of the lattice to its center, forming a X-like pattern, are qualitatively captured. Note that for this load case in combination with the current lattice, the gradients strongly depend on the free surface conditions of the lattice. This cannot be properly captured by continuum modeling as has already been observed for the indentation load case described in Section 5.2.2. This causes the underestimation of the strain energy shown in Figure 5.14. For negative constants, the rotation field does not show convergence behavior under mesh refinement. For $h_e > l$, i.e., $\{p_e = 1, M\text{x}M = 8\text{x}8\}$, the results are comparable to those obtained for positive constants and show the same order of magnitude, cf. Figure 5.15 (top left) and (bottom left), respectively. For $h_e < l$, i.e., $\{p_e = 1, M\text{x}M = 16\text{x}16\}$, the rotation field shows an oscillation pattern.

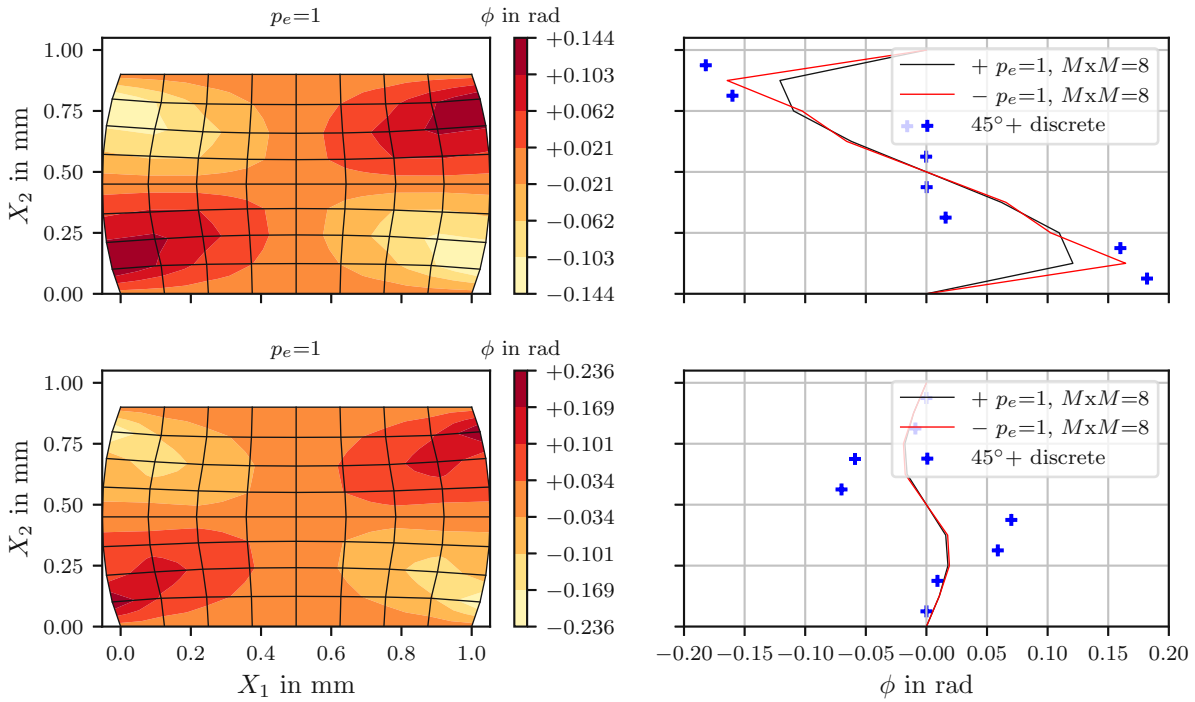

Figure 5.15: Compression - Rotation fields for the 45° rotated square lattice comprised of $N\text{x}N = 8\text{x}8$ base cells for element sizes of $M\text{x}M = 8\text{x}8$ ($h_e = 0.125$) and an interpolation order $p_e = 1$ for positive (top left) and negative MECs (bottom left). Rotations over the height at $X_1 = 0.0625$mm (top right) and $X_1 = 0.4375$mm (bottom right) for a parameter set of $\{p_e = 1, M\text{x}M = 16\}$ for positive and negative constants, where + markers represent the solution of the discrete lattice at MPBCs.

In Figure 5.17, the rotations at the MPBCs of the lattice are shown for the discrete (top left) as well as continuum models for positive (top center) and negative constants (top right). For the continuum models, a parameter set of $\{p_e = 1, M\text{x}M = 16\text{x}16\}$ is used. The rotations of the discrete models are extracted at nodes located at the MPBCs while those of the continuum models are obtained by interpolation. Furthermore, absolute error values with respect to the discrete model are given for positive (second row center) and negative constants (second row right). For positive constants, the error values are of high magnitude along the gradients of the rotation field. For the negative constants, the error values seems to be randomly distributed in terms of magnitude, which is a consequence of the oscillation pattern of the rotation field. Furthermore, relative error values with respect to the discrete model are given for positive (third row center) and negative constants (third row right). For both positive and negative constants, the error values are of very high magnitudes close to the boundaries. This indicates that the gradients in the rotation field forming the X-pattern decay more slowly for the continuum model than for the discrete model. This leads to rotations of $\phi \approx 0$ for the discrete models close to the boundaries, which cannot be properly captured by the continuum models, hence, large relative error values are observed.

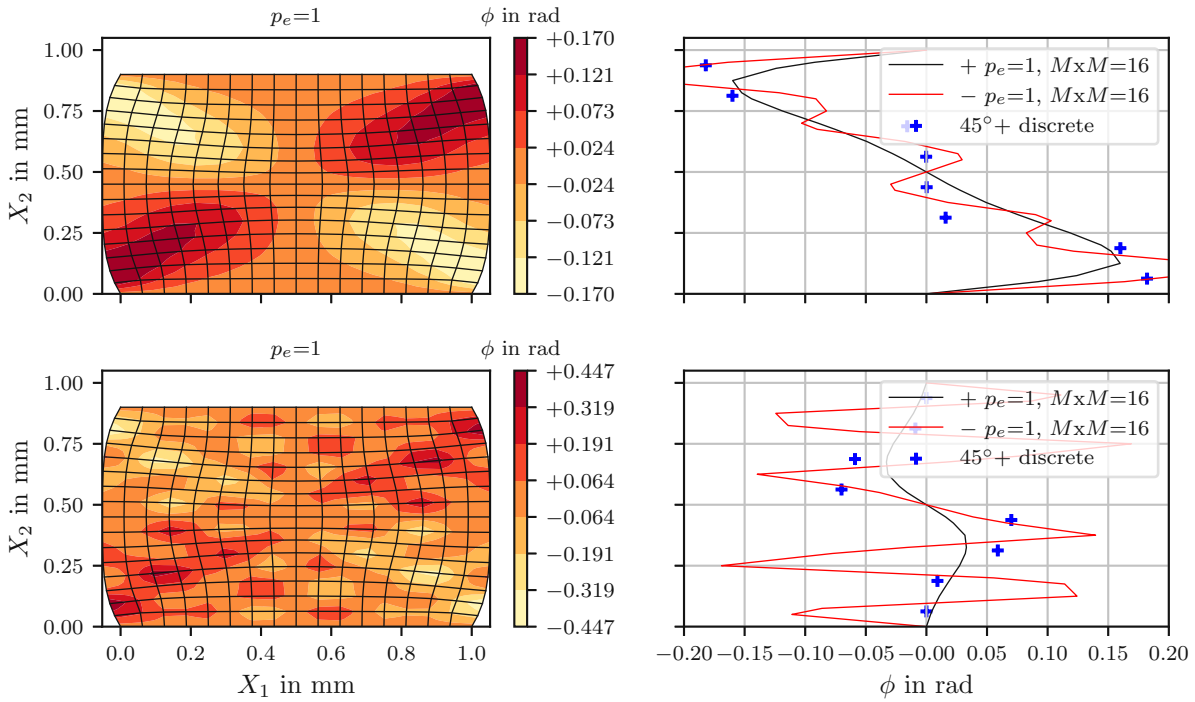

Figure 5.16: Compression - Rotation fields for the 45° rotated square lattice comprised of $N\text{x}N = 8\text{x}8$ base cells for element sizes of $M\text{x}M = 16\text{x}16$ ($h_e = 0.0625$) and an interpolation order $p_e = 1$ for positive (top left) and negative MECs (bottom left). Rotations over the height at $X_1 = 0.0625$mm (top right) and $X_1 = 0.4375$mm (bottom right) for a parameter set of $\{p_e = 1, M\text{x}M = 16\}$ for both positive and negative constants, where + markers represent the solution of the discrete lattice at MPBCs.

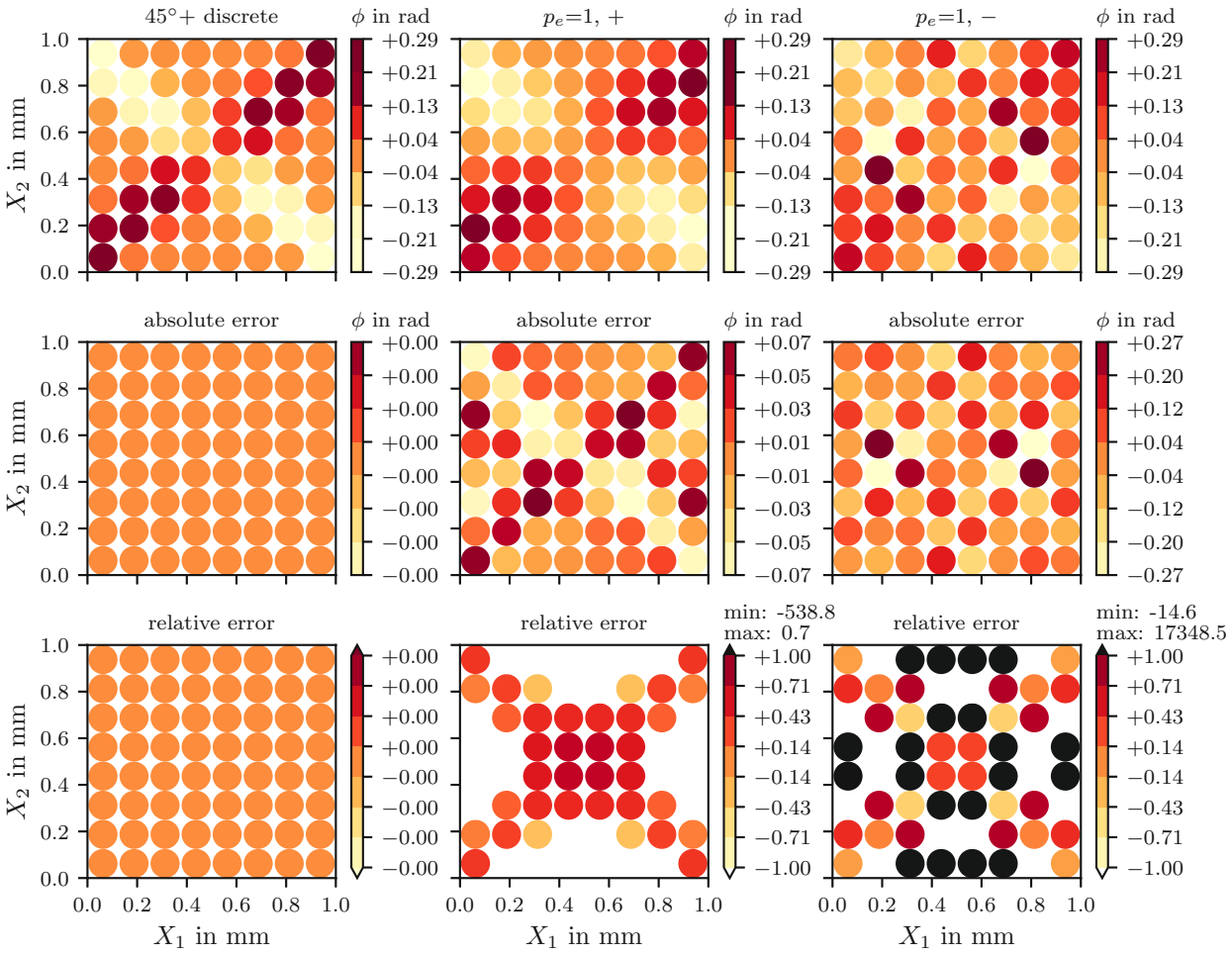

Figure 5.17: Compression - Rotations at MPBCs for the 45° rotated square lattice comprised of NxN = 8x8 base cells for the discrete model (top left), continuum model using positive (top center), and negative constants (top right) for $\{p_e = 1, M$xM = 16x16$\}$. Absolute error values (second row) and relative error values (third row) with respect to the discrete lattice for positive (center) and negative constants (right).

5.2.4 Bending

The configurations of the square lattice studied for the bending load case are summarized in Table 5.6. For the continuum model, the user element implemented in ABAQUS, `CPE4MP`, is used, cf. Section 4.2.2. No extensive numerical study is conducted, the element size is the only FEM parameter that is varied. The interpolation order is set to $p_e = 1$.

Investigation of the strain energy

The strain energies of *closed-* and *open-boundary* discrete lattice models comprising 50x5 and 100x10 base cells are compared to the corresponding continuum counterparts, cf. Figure 5.18 for positive (left) and negative constants (right) for different mesh sizes M_1xM_2. The *closed-* and *open-boundary* discrete lattice represent the lower and upper estimate of the lattice, respectively. The strain energy of the continuum model shows the same convergence behavior with respect to the MECs that is similar to the observations made for the other load cases. For positive constants, the strain energies of the continuum models are in good agreement with the corresponding discrete models. Furthermore, the strain energies are within the lower and upper estimates for all levels of discretization M_1xM_2. For negative constants, this is not the case if the element size is below the characteristic length, i.e., $h_e < l$. It is worth noting that both positive and negative constants give similar strain energies for very coarse meshes, i.e., $h_e \gg l$, cf. M_1x$M_2 = 20$x2.

Table 5.6: Geometrical dimensions of the square lattices for the bending load case.

N_1xN_2 (/)	L_1 in mm	L_2 in mm	h in mm	l in mm	t in mm
50x5	200.0	20.0	1.0	4.0	0.2
100x10	200.0	20.0	1.0	2.0	0.1

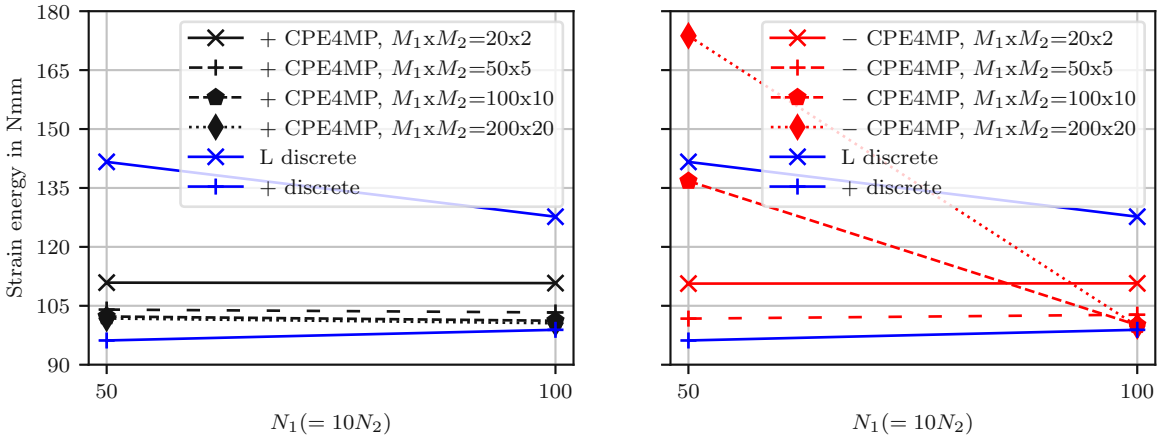

Figure 5.18: Comparison of strain energies of *closed-* and *open-boundary* discrete lattice models comprising 50x5 and 100x10 base cells as well as corresponding continuum counterparts for various mesh sizes M_1xM_2 using positive (left) and negative constants (right).

Investigation of the rotation field

All further investigations are based on the lattice comprising N_1xN_2 = 100x10 base cells with the *open-boundary* discrete model as reference. For the continuum model, two different mesh sizes are used, namely, M_1xM_2 = 20x2 ($h_e = 10 > l$) and M_1xM_2 = 100x10 ($h_e = 2 = l$), to assess the behavior under mesh refinement.

A direct comparison of the rotations between discrete and continuum model is given in Figure 5.19. The rotations are evaluated along the first row below the neutral axis of the physical lattice at $X_2 = 9$mm. For the discrete model, nodal values are directly extracted. For the continuum model, interpolated values are determined with respect to the MPBCs of the lattice. For positive constants, the rotations of the continuum model are in good agreement with the discrete model for both discretizations as given in Figures 5.19 (top). For $h_e > l$, there is a small offset in the rotations between the discrete and continuum models along the entire length in 1-direction, cf. Figures 5.19 (a). Furthermore, the gradient of the rotations with respect to the MPBCs cannot be accurately captured. For $h_e = l$, no offset is obtained and the gradient can be accurately captured, cf. Figures 5.19 (b). For negative constants, the rotations are in acceptable agreement with the discrete model only for the coarse mesh with $h_e > l$ as given in Figure 5.19 (c). For $h_e = l$, the rotations show an oscillation pattern, which is indicated by the nodal values taken at $X_2 = 9 + l/2$mm. However, the rotations at the MPBCs are in good agreement with those of the discrete ones, see Figure 5.19 (d). Element sizes smaller than the characteristic length are not considered based on the findings of the other load cases. Note that the local variations of the rotation field obtained for the discrete model cannot be captured independently of the set of constants used. For the sake of completeness, a contour of the rotation field of the continuum model for a discretization using M_1xM_2 = 100x10 is given in Figure 5.20 for positive (left) and negative constants (right). It is shown that the rotation field obtained for the negative constants shows an oscillation pattern. The rotation field has similar characteristics to the one obtained for the simple shear load case, resulting from similar boundary conditions and loads, cf. Figure 5.7. For positive constants, the rotation field shows only negative rotations, which is to be expected for the load case considered.

Additionally, the rotations at the MPBCs are compared for discrete and continuum models along the rows of the lattice at fixed positions $X_2 = 11, 13, 17, 19$ mm to study the influence of the free surface, see Figure 5.21. The continuum model uses a discretization of M_1xM_2 = 100x10 and only positive constants are considered. The rotations are captured fairly well by the continuum model when compared to the discrete model, except for positions close to the free surface of the lattice at $X_1 = 19$mm. This is expected since free edge effects cannot be correctly captured using continuum modeling. However, the results are not far off and can be considered acceptable.

In Figure 5.22, the displacements in 1-direction, U_1, and rotations, ϕ, are studied at the rightmost column of the lattice at $X_1 = 199$mm for the discrete and continuum models, where the latter use a discretization of M_1xM_2 = 100x10. The continuum model with positive constants captures the S-shaped macroscopic shear deformation well as indicated by U_1, see Figure 5.22 (top left). This also applies to the use of negative constants, see Figure 5.22 (bottom left). The rotations are shown for positive and negative constants in Figure 5.22 (top right) and (bottom right), respectively. For both positive and negative constants, the rotations at the MPBCs are in good agreement with the discrete model. However, the oscillation of the rotation field is already indicated by the offset between the markers + and • using negative constants as the element size equals the characteristic length of the lattice, $h_e = l$, see Figure 5.22 (bottom right).

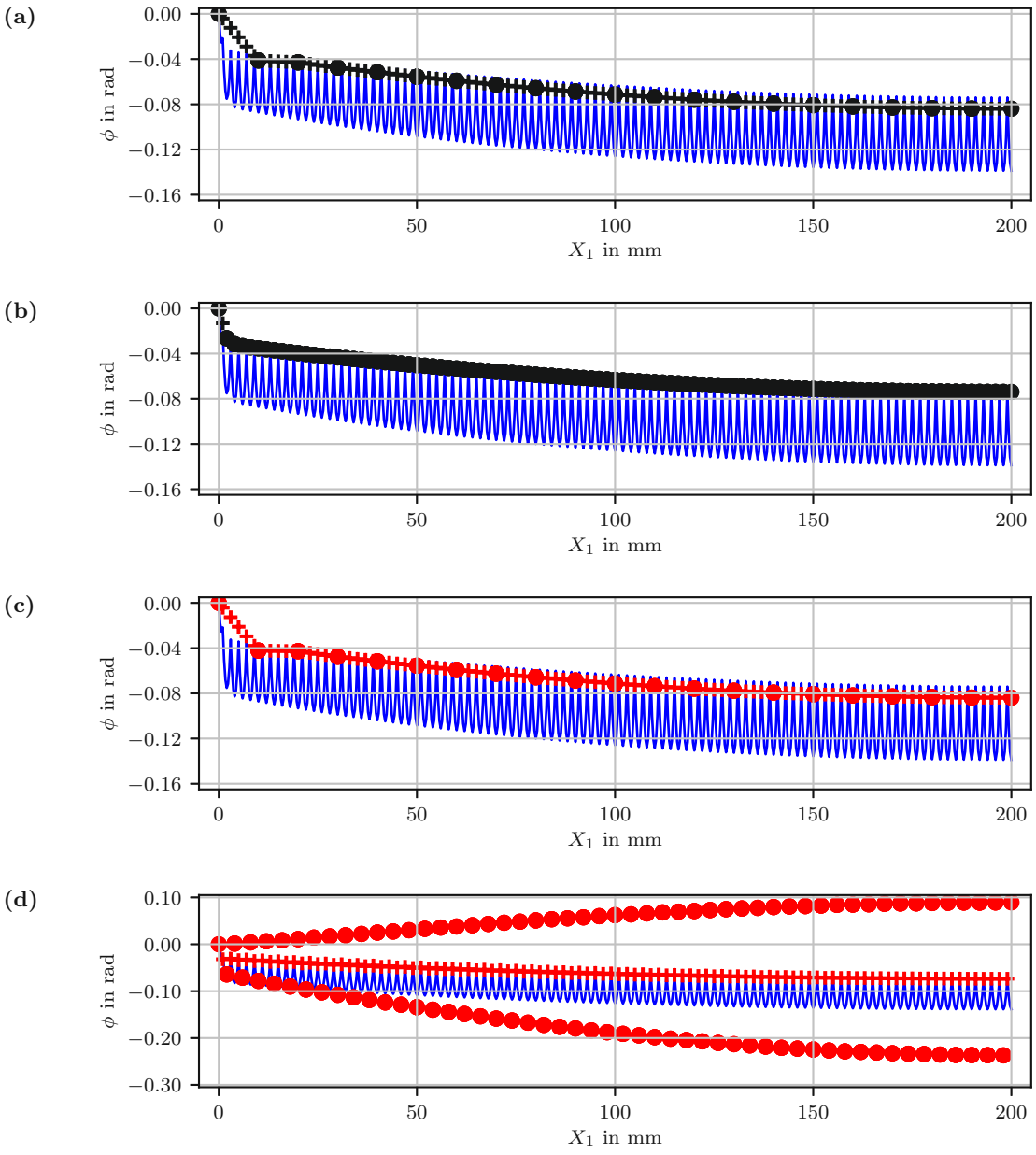

Figure 5.19: Rotations ϕ of discrete model along neutral axis at $X_2 = 9$mm indicated by the solid line and of continuum model with positive (a,b) and negative constants (c,d) indicated by the markers. The markers + and • correspond to MPBCs of the lattice at $X_2 = 9$mm and to nodes at $X_2 = 9 + l/2$mm, respectively. Discretization of continuum model with M_1xM_2 = 20x2 (a,c) and M_1xM_2 = 100x10 (b,d).

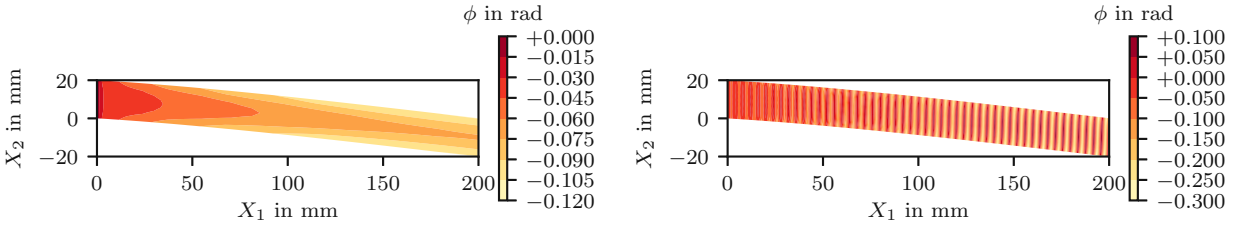

Figure 5.20: Rotation field of continuum model for M_1xM_2 = 100x10 using positive (left) and negative constants (right).

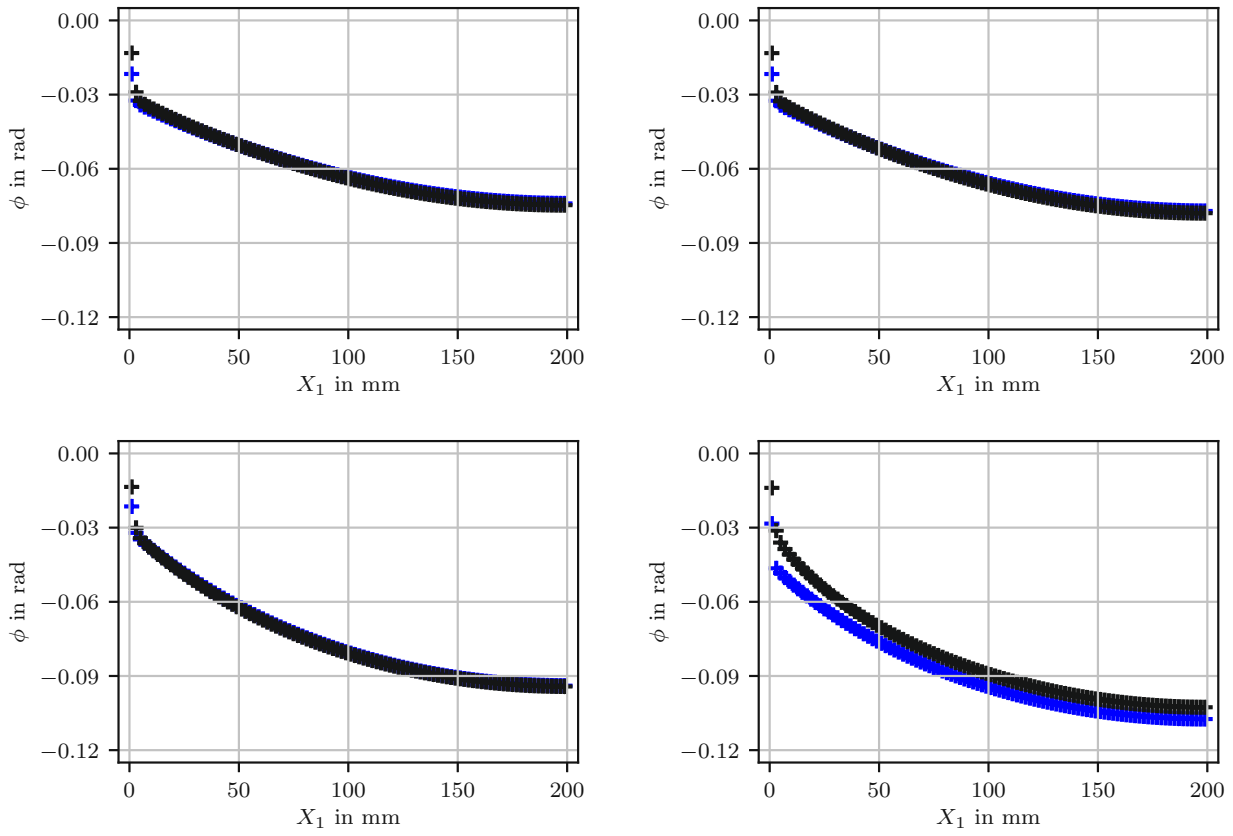

Figure 5.21: Rotations ϕ at MPBCs of discrete model along the rows of the lattice at X_2 = 11mm (top left), 13mm (top right), 17mm (bottom left), and 19mm (bottom right) indicated by the blue + markers and of continuum model with M_1xM_2 = 100x10 using positive constants indicated by the black + markers.

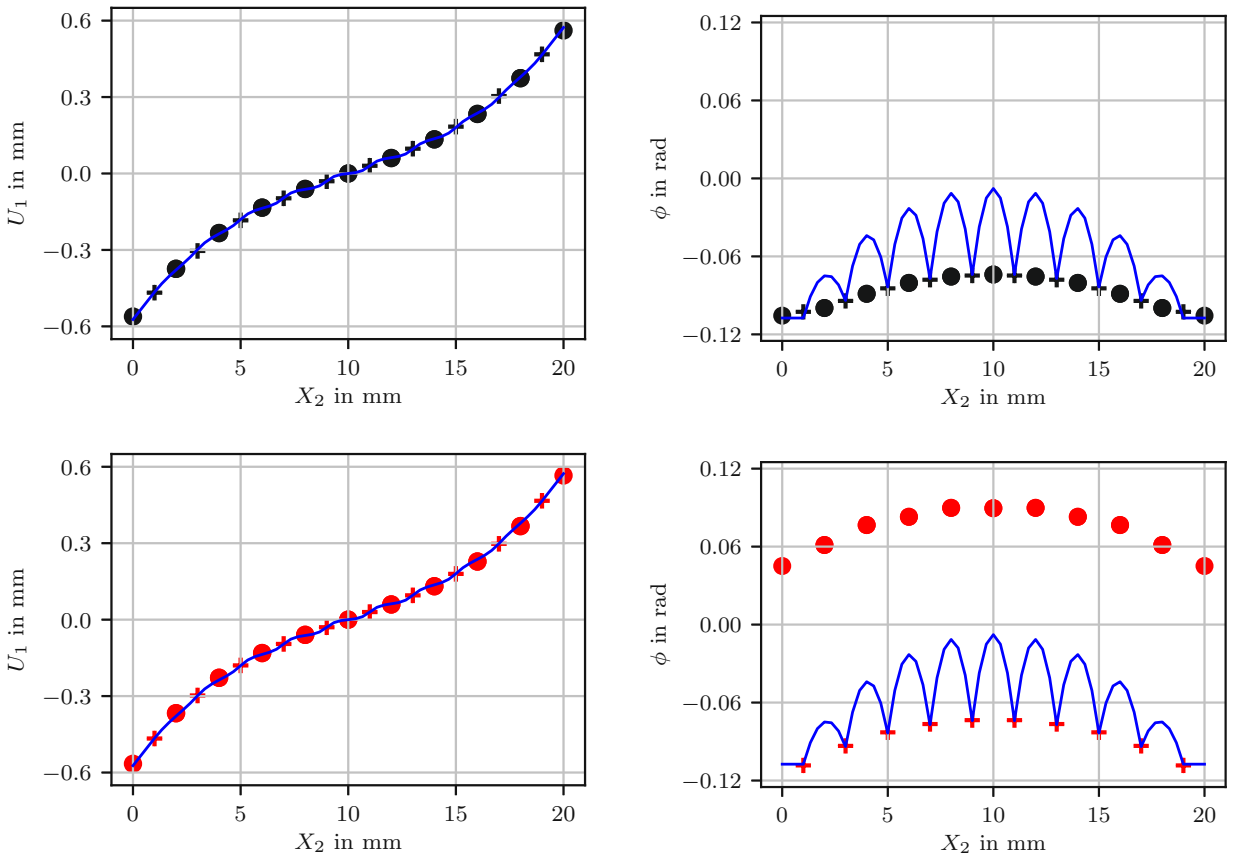

Figure 5.22: Displacements U_1 and rotations ϕ of discrete model along the column at $X_1 = 199$mm indicated by the solid line and of continuum counterpart with positive (top) and negative constants (bottom) indicated by the markers. The markers + and • correspond to MPBCs of the lattice at $X_1 = 199$mm and to nodes at $X_1 = (199 + l/2)$mm, respectively.

5.3 Summary

The mechanical response predicted by using the positive and the negative set of MECs obtained in [10, 53] for the very same lattice are studied based on numerical simulations by means of the Finite Element Method. The micropolar continuum model used for the investigations is implemented within the frameworks of NGSolve and ABAQUS. Various types of lattices showing different configurations are subjected to various load cases. The predictive capabilities of the micropolar continuum model with respect to the mechanical response are evaluated by comparisons with discrete models in terms of the strain energy and the rotation field. Special focus is set on two FEM parameters of the continuum model, namely, the element size and the interpolation order.

For negative constants, it is found that there is not only a constraint on the element size as given in [53], but there is also a constraint on the order of the interpolation functions used in combination with the element size. Converging strain energies are obtained only as long as the condition $h_e/(p_e + H(p_e - 3)) > l$ is fulfilled, i.e., the finite element size must be chosen to satisfy $h_e > l \cdot (p_e + H(p_e - 3))$, where interpolation orders are considered up to $p_e = 3$. Note that there are deviations from this condition either in terms of the lattice type or with respect to the load case, e.g., for the triangular lattice the effect is not as pronounced as for the square lattice. In contrast, no restriction on FEM parameters is observed for positive constants regarding convergence of the strain energy. Note that the strain energies are approximately the same for both sets of constants as long as the condition is satisfied.

The rotation fields obtained for both sets of constants are the same as long as the condition, $h_e > l \cdot (p_e + H(p_e - 3))$, is satisfied. For positive constants, the gradients of the rotation field regarding the midpoints of base cells of the lattice can be captured for $h_e \lessapprox l \cdot (p_e + H(p_e - 3))$, for which also the rotation field can be considered to be converged. This is observed for almost all the load cases with the corresponding lattice types studied, except for the compression and the indentation load case. For the compression load case, the rotation field is governed by local deformations, which cannot be quantitatively captured by the continuum model. For the indentation load case, continuum modeling must be considered not to be best suited due to the load application at the free surface and its point load character. Nevertheless, for both load cases the gradients can be qualitatively captured. For negative constants, the gradients are hardly captured. On the one hand, the gradients are not resolved properly as long as the condition is fulfilled. On the other hand, once the condition $h_e > l \cdot (p_e + H(p_e - 3))$ is no longer satisfied, the rotation field and the stress field start to show patterns with oscillations. Although some kind of a converged field can be obtained for $h_e \ll l \cdot (p_e + H(p_e - 3))$, it is not physically interpretable based on the current investigations. In addition, small geometrical deviations from the perfect quadrilateral elements used for the discretization in this work can strongly affect the results once the condition is no longer satisfied for every single element, e.g., quadrilateral in combination with triangular continuum elements.

It is worth noting that the condition derived for h_e is not unique as it is based on the characteristic length, l, of the lattice, which can be defined in different ways. Furthermore, the condition is based on quadrilateral elements using full integration only. The condition may be relaxed for using reduced integration, see [82] for investigations on the reduced integration and must be revisited for other element types, such as triangular elements.

In a nutshell, the FEM parameters of the continuum model and the characteristic length of the lattice must be considered as two competing length scales when using negative constants. Consequently, this must be taken into account in the modeling. This is not the case for positive constants, which can be used without any constraints as long as a proper discretization is ensured to resolve the kinematic fields, as also required for classical continuum modeling.

Chapter 6

Linear micropolar continuum modeling in 3D

The MECs derived for the 3D lattices in Section 3.3 are evaluated on the basis of numerical simulations in the linear regime. For this purpose, the corresponding micropolar continuum (MC) is set up by means of the Finite Element Method. Discrete lattice models serve as reference for the comparison. Various configurations of the lattices and different load cases are used to study the predictive capabilities and limitations of the MC model. The simulations of the discrete and continuum models are carried out with ABAQUS/Standard 2019 (Dassault Systèmes Simulia Corp., Providence, RI, USA). Information on the implementation of the continuum model can be found in Section 4.2.1.

6.1 Lattice models and method

6.1.1 Geometry and material properties

The lattice structures studied are the PC and BCC lattices with overall geometric dimensions L_1, L_2, and L_3 for all three spatial directions. The overall dimension is associated with the macroscopic domain, cf. Figure 6.1. Each lattice is set up via periodic arrangements of its base cells in all three spatial directions. The base cells of the PC and the BCC lattices are displayed in Figures 3.2 and 3.3 in Section 3.3, respectively. The periodic arrangement of the base cell for the PC lattice leads to an open-boundary surface. Note that for this type of lattice, no closed-boundary surface model is used. The *internal* or *characteristic length* of each lattice is defined as the size of its base cell and is set to $l\,(= l_1 = l_2 = l_3)$ for all lattices studied, resulting in a cubic material symmetry system for each lattice. Again, the macroscopic dimensions of the lattices are directly related to the characteristic length via the number of base cells comprising the lattices, which are further denoted as $N_1\text{x}N_2\text{x}N_3$, where N_1, N_2, and N_3 are the numbers of base cells in 1-,2-, and 3-directions, respectively. This leads to $L_i = lN_i$ for all lattices, where $i = \{1, 2, 3\}$ for each spatial direction. For an equal arrangement in all three directions, it follows $N_1\text{x}N_2\text{x}N_3 = N\text{x}N\text{x}N$, cf. Figure 6.1 for lattices comprised of 4x4x4 base cells. Note that either l or N_i is used in the following. The cross-sections of the lattice members are assumed to be circular, $A = r^2\pi$, where r denotes the radius. The area moment of inertia is defined as $I = (r^4/4)\pi(= I_\text{m} = I_\text{n})$ and the polar moment of inertia is given as $I_\text{t} = I_\text{m} + I_\text{n}$. The relative density of each type of lattice studied, $\rho_\text{r} = V_s/V$, is kept constant, where V_s and V denote the volume of the parent

material and the domain occupied by the lattice, respectively. For this purpose, a constant ratio of radius to length of the lattice members of $r/l_{LT} = 1/20$ is considered with LT = PC, BCC. Neglecting overlapping regions of the parent material, this results in $\rho_\mathrm{r} \approx 3\pi/400 = 0.024$ for the PC lattice with $L_\mathrm{PC} = l$ and $\rho_\mathrm{r} \approx 3\sqrt{3}\pi/400 = 0.041$ for the BCC lattice with $l_\mathrm{BCC} = \sqrt{3}l/2$. Note that for the BCC, the lengths of the lattice members are different from the base cell lengths, l, and, therefore, is to be accounted for accordingly. This is independent of the number of base cells involved.

The parent material of the lattice structures, i.e., the material of the individual lattice members, is an isotropic linear elastic material with a Young's modulus of $E_\mathrm{s} = 120000$ MPa and a Poisson ratio of $\nu_\mathrm{s} = 0.3$. The shear modulus for the isotropic material follows as $G_\mathrm{s} = E_\mathrm{s}/(2(1+\nu_\mathrm{s}))$.

6.1.2 Discrete reference models

The discrete lattice models are discretized by linear Timoshenko beam elements accessible through the ABAQUS element library, where each strut of the lattice is discretized by six elements. This leads to 18 elements for the PC and 48 elements for the BCC per base cell. This discretization allows the deformation state to be adequately captured.

6.1.3 Methodology

Two different load cases are used to study the mechanical response of the lattices and to evaluate the predictive capabilities and limitations of the MC model. The basis for the assessment is a comparison with discrete models in terms of strain energy and kinematic fields. To obtain a single scalar value that provides a rough estimate of the accuracy of the MC model predicting the kinematic fields, the following variable is introduced

$$\chi_y = \frac{1}{N}\sum_{i=1}^{N}\left|\frac{y_i^\mathrm{discrete} - y_i^\mathrm{MC}}{y_i^\mathrm{discrete}}\right| \quad , \tag{6.1}$$

where N is the number of MPBCs taken into account and y_i represents a DOF at MPBC i. The greater the value of χ_y, the poorer the predicitive capability of the MC model compared to the discrete reference model with respect to DOF y. Note that the fraction term represents the relative error. If $\chi = 0$, both MC and discrete model will show the same results.

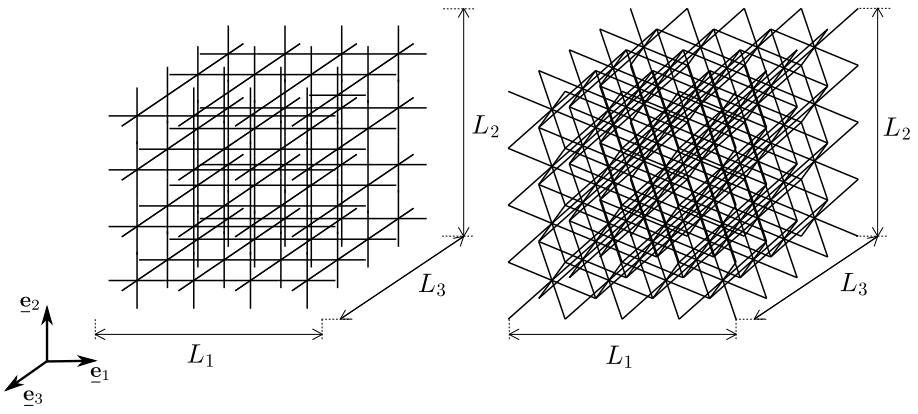

Figure 6.1: PC (left) and BCC (right) lattices comprised of 4x4x4 base cells.

The microscopic dimensions of the lattices are chosen such that the separation of scales is not fully satisfied in order to use micropolar modeling in a meaningful way. The cuboid domain is discretized by M_1xM_2xM_3 elements showing a cubic shape, where M_1, M_2, and M_3 are the numbers of elements in 1-, 2-, and 3-directions, respectively. Considering the macroscopic dimensions, the element size or side length of the elements with respect to the i-direction are obtained as L_i/M_i. For using cubic elements, the element size, h_e, or the side lengths of the elements are chosen to be the same in all three spatial directions. With the cubic shape of the base cells of the lattices studied, a ratio can be given that describes how many elements are used to discretize a single base cell. It is defined as the ratio between the number of base cells and the number of elements in each spatial direction, or, alternatively, using the element size and the characteristic length of the lattice, and reads

$$\mathcal{M}_i = M_i/N_i \; (= M/N = l/h_e) \qquad , \tag{6.2}$$

respectively (no summation rule).

The load cases considered are a simple shear and a torsion load case, cf. Figure 6.2. For the simple shear, the boundary conditions are applied in the planes parallel to the 1-3-plane at $X_2 = 0$ and $X_2 = L_2$. The lattice is fully clamped at $X_2 = 0$ and a displacement in 1-direction is prescribed at $X_2 = L_2$ with $U_1 = 0.2$mm while all other DOFs are fixed. For the torsion load case, the boundary conditions are applied in the planes parallel to the 1-2-plane at $X_3 = 0$ and $X_3 = L_3$. The lattice is fully clamped at $X_3 = 0$, while at $X_3 = L_3$ a reference node is introduced at $X_1 = L_1/2$ and $X_2 = L_2/2$ and tied to the nodes in this plane, i.e., the ABAQUS `*RIGID BODY, REF NODE= , TIE NSET=` keyword is used. A rotation of $\phi_3 = 1\,$rad is prescribed at the reference node.

The FEM parameters of the continuum model are chosen based on the conditions specified for positive constants to capture the expected gradients of the rotation fields shown for the 2D case in Chapter 5. For an interpolation order of $p_e = 1$, the element size needs to satisfy $h_e \leq l$, or, i.e., $\mathcal{M} \geq 1$.

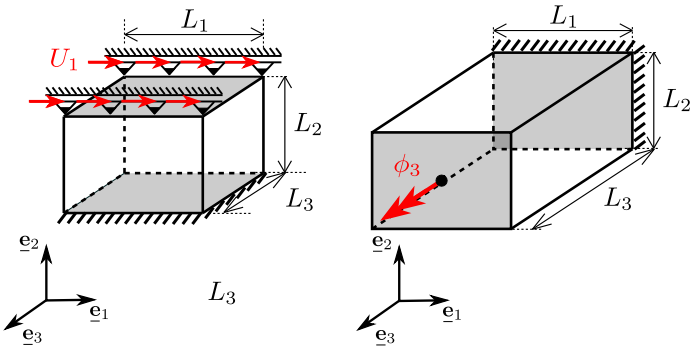

Figure 6.2: Schematics of the simple shear (left) and torsion load case (right) with free surfaces in white and surfaces with boundary conditions applied in grey. The free surfaces are traction-free.

6.2 Results and discussion

6.2.1 Simple shear

The configurations of the PC and the BCC lattices used for the simple shear load case are summarized in Table 6.1.

Investigation of the strain energy

The strain energies obtained for discrete and continuum models are summarized in Table 6.2. Different element sizes are used for the continuum model, namely, $h_e = l$, $h_e = l/2$, and $h_e = l/4$. As expected, the continuum model shows a more compliant behavior for smaller element sizes than for larger ones. This is more pronounced for the BCC than for the PC lattice. The relative error for the smallest element size studied is about 10.9% for the PC and -1.0% for the BCC lattice.

Investigation of the kinematic fields

The continuum models with element sizes of $h_e = l$ and $h_e = l/2$ are the basis for comparing the kinematic fields with the corresponding discrete models. First, the PC lattice is analyzed, then the BCC lattice.

PC. The displacements and the rotations of the MPBCs of the PC lattice along the 2-axis are shown in Figure 6.3 for two locations at $X_1 = X_3 = l/2 = 0.5\,\text{mm}$ (first and second row) and $X_1 = X_3 = 7l/2 = 3.5\,\text{mm}$ (third and fourth row). Significant changes occur only in the rotations ϕ_3 with respect to the studied locations and this is the only DOF that will be investigated further. The larger the distance to the free surface of the lattice, the continuum model is better able to capture these rotations, cf. Figure 6.4 for $X_1 = X_3 = l/2 = 0.5\,\text{mm}$ (top left), $X_1 = X_3 = 3l/2 = 1.5\,\text{mm}$ (top right), $X_1 = X_3 = 5l/2 = 2.5\,\text{mm}$ (bottom left), and $X_1 = X_3 = 7l/2 = 3.5\,\text{mm}$ (bottom right). In the far-field regions, i.e., at $X_1 = X_3 > l/2 = 0.5\,\text{mm}$ and $l/2 = 0.5\,\text{mm} < X_2 < 15l/2 = 7.5\,\text{mm}$, the rotations of the continuum model for both element sizes studied are in good agreement with the discrete model. For the element size being smaller than the *characteristic*

Table 6.1: Geometrical dimensions of the PC and BCC lattices studied for the simple shear load case.

	NxNxN (/)	$L_1 = L_2 = L_3$ in mm	l in mm	r in mm
PC	8x8x8	8	1	$l/20$
BCC	8x8x8	8	1	$l\sqrt{3}/2/20$

Table 6.2: Simple shear - Strain energies of discrete and micropolar continuum models for the PC and BCC lattices studied with relative error values for continuum models.

	NxNxN (/)	discrete in N mm	MC $\mathcal{M} = 1$ in N mm	rel. err. in %	MC $\mathcal{M} = 2$ in N mm	rel. err. in %	MC $\mathcal{M} = 4$ in N mm	rel. err. in %
PC	8x8x8	0.536652	0.611687	14.0	0.599748	11.8	0.595382	10.9
BCC	8x8x8	15.586239	25.284204	62.2	18.931805	21.3	15.429715	-1.0

length of the lattice, i.e., $h_e = l/2$, even the evolution of the gradients from the boundaries at $X_2 = 0$ and $X_2 = 8\,\text{mm}$ is captured reasonably well in the far field.

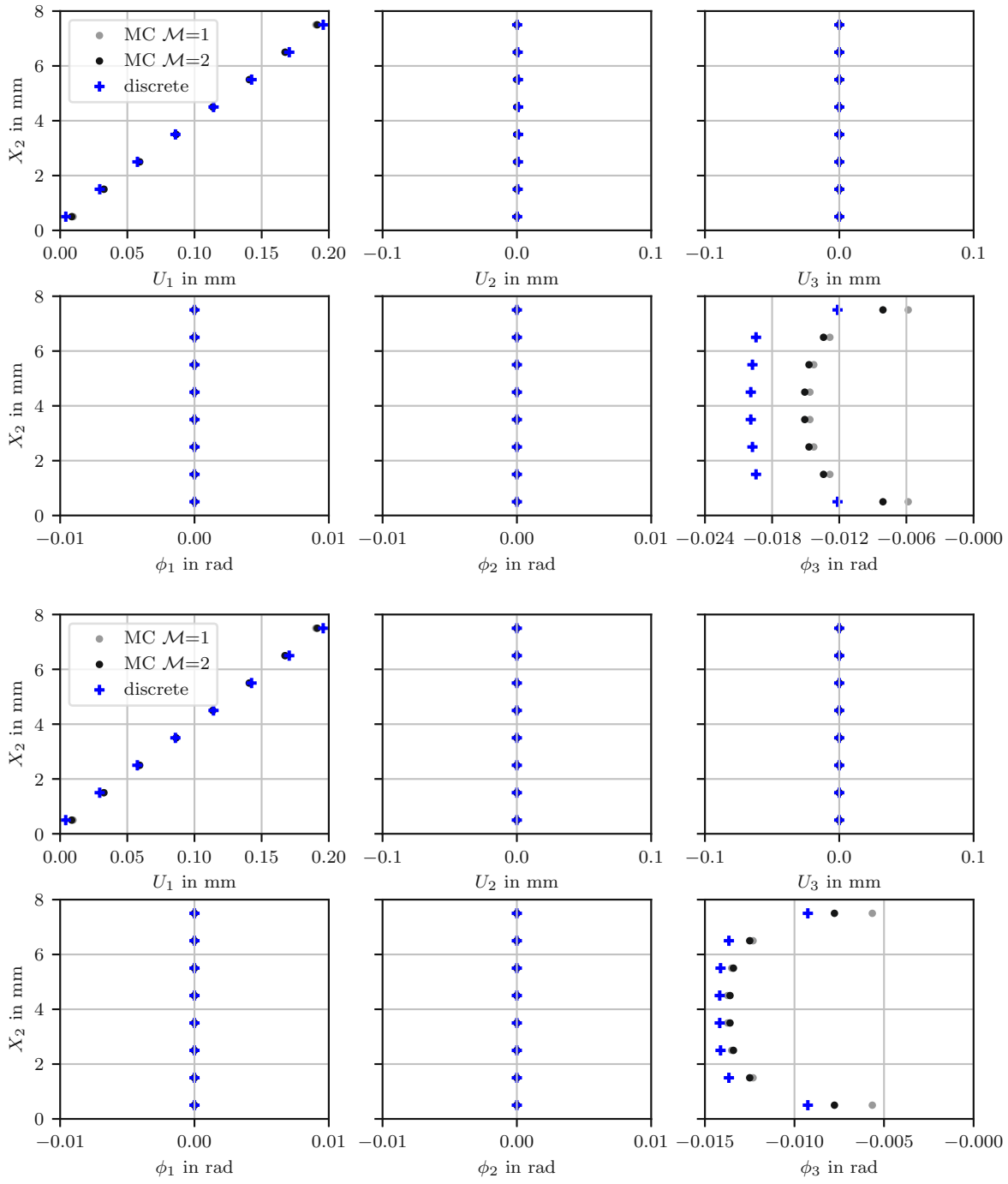

Figure 6.3: Simple shear - Displacements and rotations of MPBCs of the PC lattice, comprised of 8x8x8 base cells, along the 2-axis at locations $X_1 = X_3 = l/2 = 0.5\,\text{mm}$ (first and second row) and $X_1 = X_3 = 7l/2 = 3.5\,\text{mm}$ (third and fourth row).

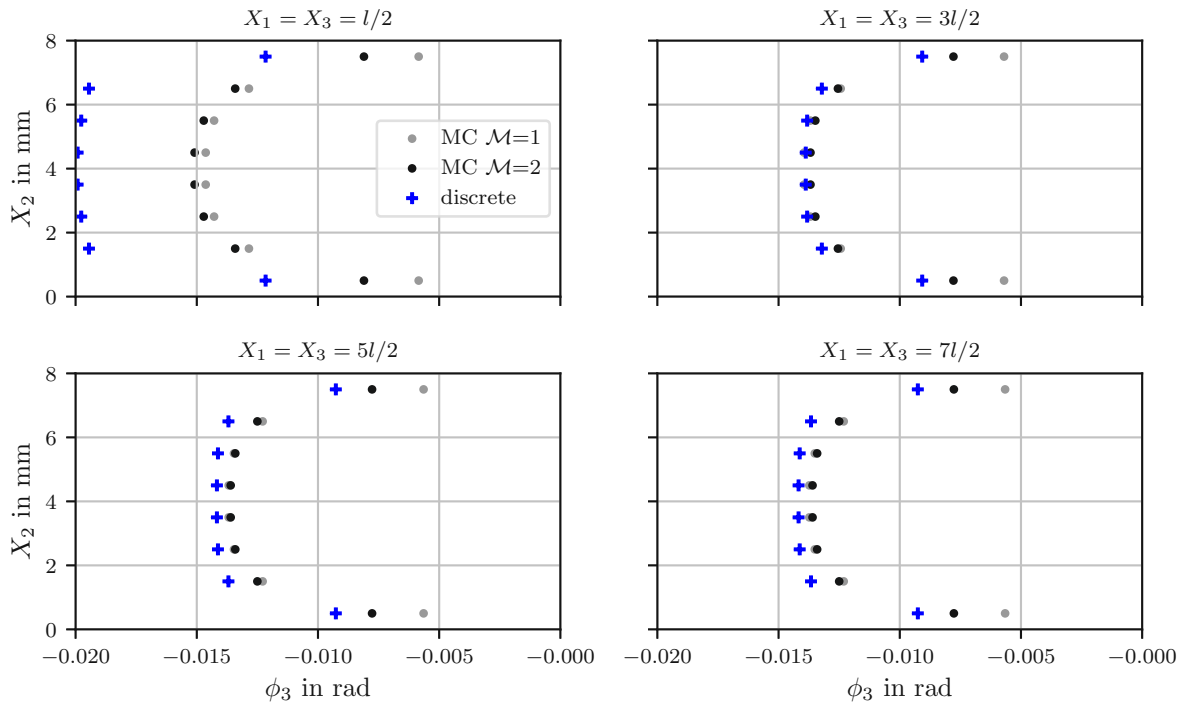

Figure 6.4: Simple shear - Rotations ϕ_3 of MPBCs of the PC lattice, comprised of 8x8x8 base cells, along the 2-axis at four different locations.

To gain further insight, the rotations ϕ_3 at the MPBCs are given with respect to three different planes in Figure 6.5. The first plane is parallel to the 1-2-plane for the location $X_3 = 7l/2 = 3.5\,\text{mm}$ (top), i.e., the surface normal is parallel to the 3-axis. The second and third planes are both parallel to the 2-3-plane for locations $X_1 = l/2$ (center) and $X_1 = 7l/2 = 3.5\,\text{mm}$ (bottom), i.e., the surface normals are parallel to the 1-axis. The discrete model (left column) and the continuum model with an element size of $h_e = l/2$ (center column) are directly compared via relative error values (right column).

For the load cases studied, the rotations in the 1-2-plane do not significantly change over the location X_3. Consequently, only a single plane at the location $X_3 = 7l/2 = 3.5\,\text{mm}$ is considered. The error values of the rotations in this plane are small in the far-field regions $l/2 = 0.5\,\text{mm} < X_1 < 15l/2 = 7.5\,\text{mm}$ and range between -0.01 and -0.11. For being close to the free surface at $X_1 = l/2 = 0.5\,\text{mm}$ and $X_1 = 15l/2 = 7.5\,\text{mm}$, the relative errors range between -0.20 and -0.33.

For the planes parallel to the 2-3-planes, the error values of the rotations are significantly smaller in the far-field region at $X_1 = 7l/2 = 3.5\,\text{mm}$ than close to the free surface at $X_1 = l/2 = 0.5\,\text{mm}$. In numbers, the error values range between -0.04 and -0.16 in the far-field region while those closer to the free surface range between -0.24 and -0.33. In the far-field region, even the gradients evolving from the boundaries at $X_2 = 0$ and $X_2 = 8\,\text{mm}$ are captured reasonably well.

To further obtain a rough estimate on how well the MC model captures the rotations ϕ_3 at the MPBCs with respect to various planes, a representative relative error value, $\chi_{\phi 3}$, according to Eq. (6.1) is evaluated for each plane showing a surface normal parallel to one of the three spatial dimensions. The relative error values of the planes are shown in Figure 6.6, where values are given for parallel planes over the corresponding spatial axis. For planes with surface normals parallel to the 3-axis, $\chi_{\phi 3}$ is the same for all planes, as expected. As

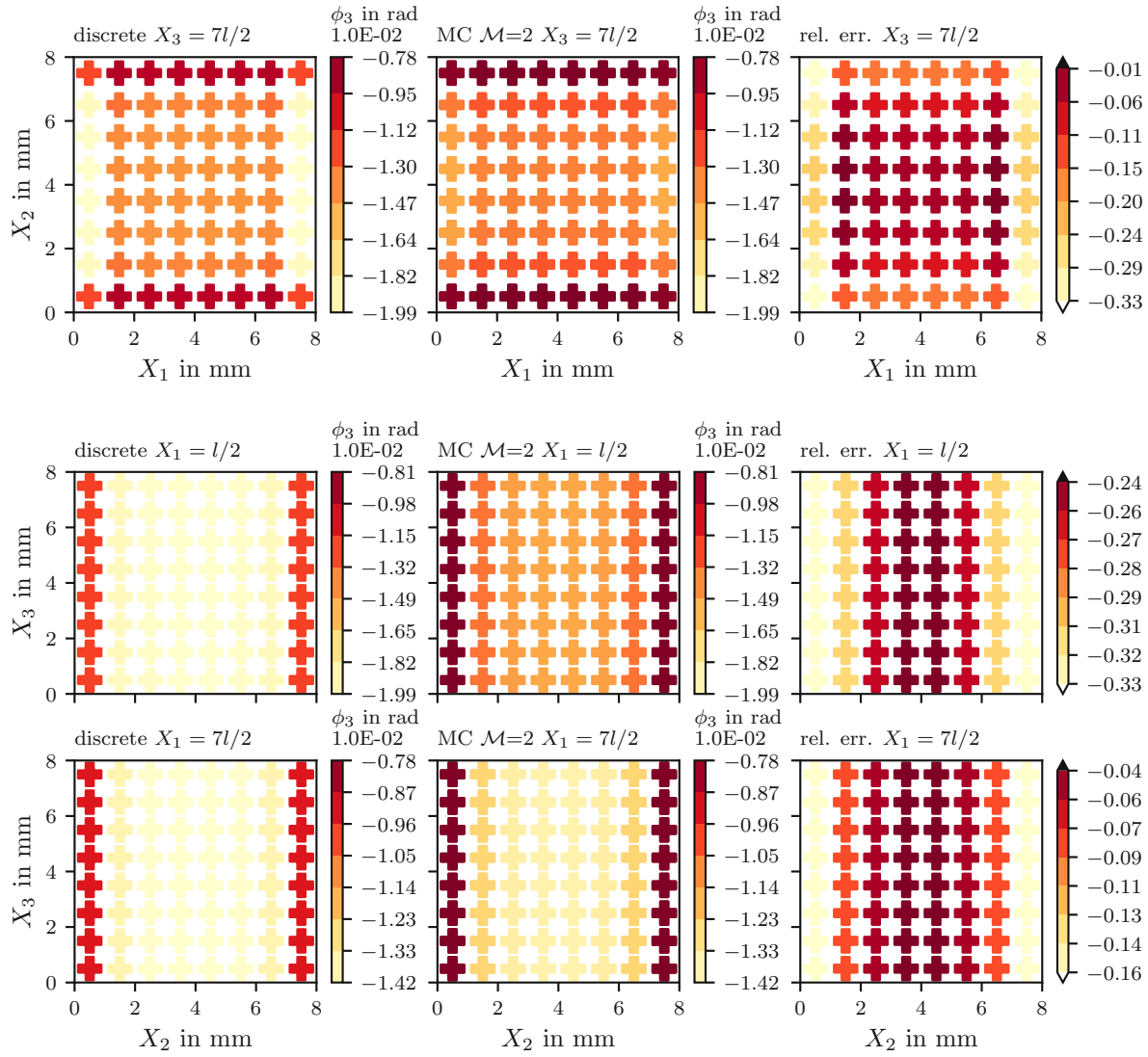

Figure 6.5: Simple shear - Rotations fields ϕ_3 of MPBCs of the PC lattice, comprised of 8x8x8 base cells, in 1-2-plane at location $X_3 = 7l/2 = 3.5\,\text{mm}$ (top) and in 2-3-plane at locations $X_1 = l/2 = 0.5\,\text{mm}$ (center) and $X_1 = 7l/2 = 3.5\,\text{mm}$ (bottom).

the average of these values gives $\chi_{\phi 3}$ of the whole lattice, the same value is obtained for the whole lattice. For planes with surface normals parallel to the 2-axis, $\chi_{\phi 3}$ decreases for increasing distance to the free surface. The same holds true for planes with surface normals parallel to the 1-axis, except for the planes at $X_1 = 3l/2 = 1.5\,\text{mm}$ and $X_1 = L - 3l/2 = 6.5\,\text{mm}$, which show lower values of $\chi_{\phi 3}$ compared to those obtained for planes with more distance to the free surface. Overall, the relative error values obtained for all planes are within an acceptable range, considering that the influence of the free surface is present in all planes. The results are almost exactly the same for using $\mathcal{M} = 4$, which is not shown for the sake of clarity. This indicates that the kinematic fields are already fully resolved for $\mathcal{M} = 2$.

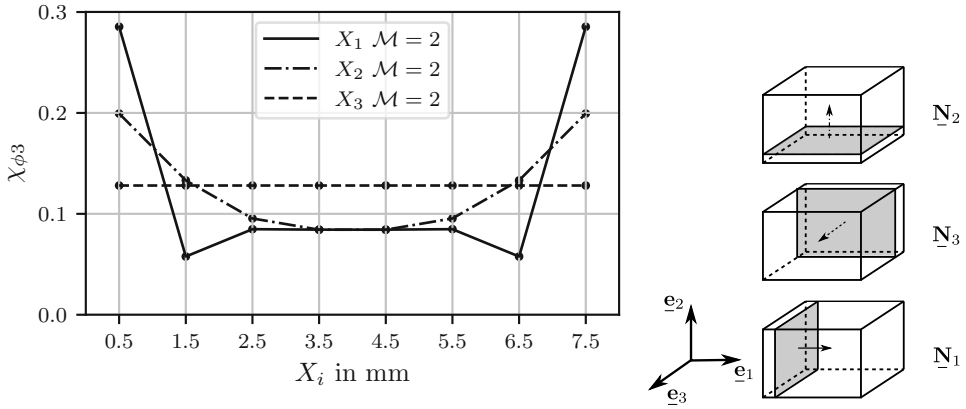

Figure 6.6: Simple shear - Relative error values of the rotations $\chi_{\phi 3}$ on various planes with surface normals parallel to the spatial directions $i = 1, 2, 3$ evaluated along the normals at locations of MPBCs of the PC lattice (left) and sketch of such planes including their surface normals (right).

BCC. For the BCC lattice, the displacements and the rotations of the MPBCs along the 2-axis are shown in Figure 6.7 for two locations at $X_1 = X_3 = l/2 = 0.5\,\text{mm}$ (first and second row) and $X_1 = X_3 = 7l/2 = 3.5\,\text{mm}$ (third and fourth row). Overall, the kinematics are qualitatively captured by the continuum model. Closer to the free surface at $X_1 = X_3 = l/2 = 0.5\,\text{mm}$ (first and second row), the displacements U_2 and U_3 are about an order of magnitude larger than in the far-field region at $X_1 = X_3 = 7l/2 = 3.5\,\text{mm}$ (third and fourth row). The same holds true for rotations ϕ_1 and ϕ_2. Contrarily, the rotations ϕ_3 do not decay in the far-field region and show the same order of magnitude at both locations. To study the evolution of the rotations ϕ_3 along the 2-axis from close to the free surface to the far-field region, four different locations are analyzed and shown in Figure 6.8, namely, $X_1 = X_3 = l/2 = 0.5\,\text{mm}$ (top left), $X_1 = X_3 = 3l/2 = 1.5\,\text{mm}$ (top right), $X_1 = X_3 = 5l/2 = 2.5\,\text{mm}$ (bottom left), and $X_1 = X_3 = 7l/2 = 3.5\,\text{mm}$ (bottom right). The free surface strongly influences the evolution of the rotations ϕ_3 over the 2-axis. Closer to the free surface at locations $X_1 = X_3 = l/2 = 0.5\,\text{mm}$ and $X_1 = X_3 = 3l/2 = 1.5\,\text{mm}$, completely different patterns are obtained when compared to those in the far-field region at locations $X_1 = X_3 = 5l/2 = 2.5\,\text{mm}$ and $X_1 = X_3 = 7l/2 = 3.5\,\text{mm}$. This means that the influence of the free surface decays much more slowly for the BCC than for the PC lattice, cf. Figure 6.4. The gradients evolving from the boundaries $X_2 = 0$ and $X_2 = 8\,\text{mm}$ are captured quite well by the continuum model in the far-field regions for both locations. However, the model is not able to capture the peak in the rotations at the center of the lattice at $X_2 = 7l/2 = 3.5\,\text{mm}$ and $X_2 = 9l/2 = 4.5\,\text{mm}$.

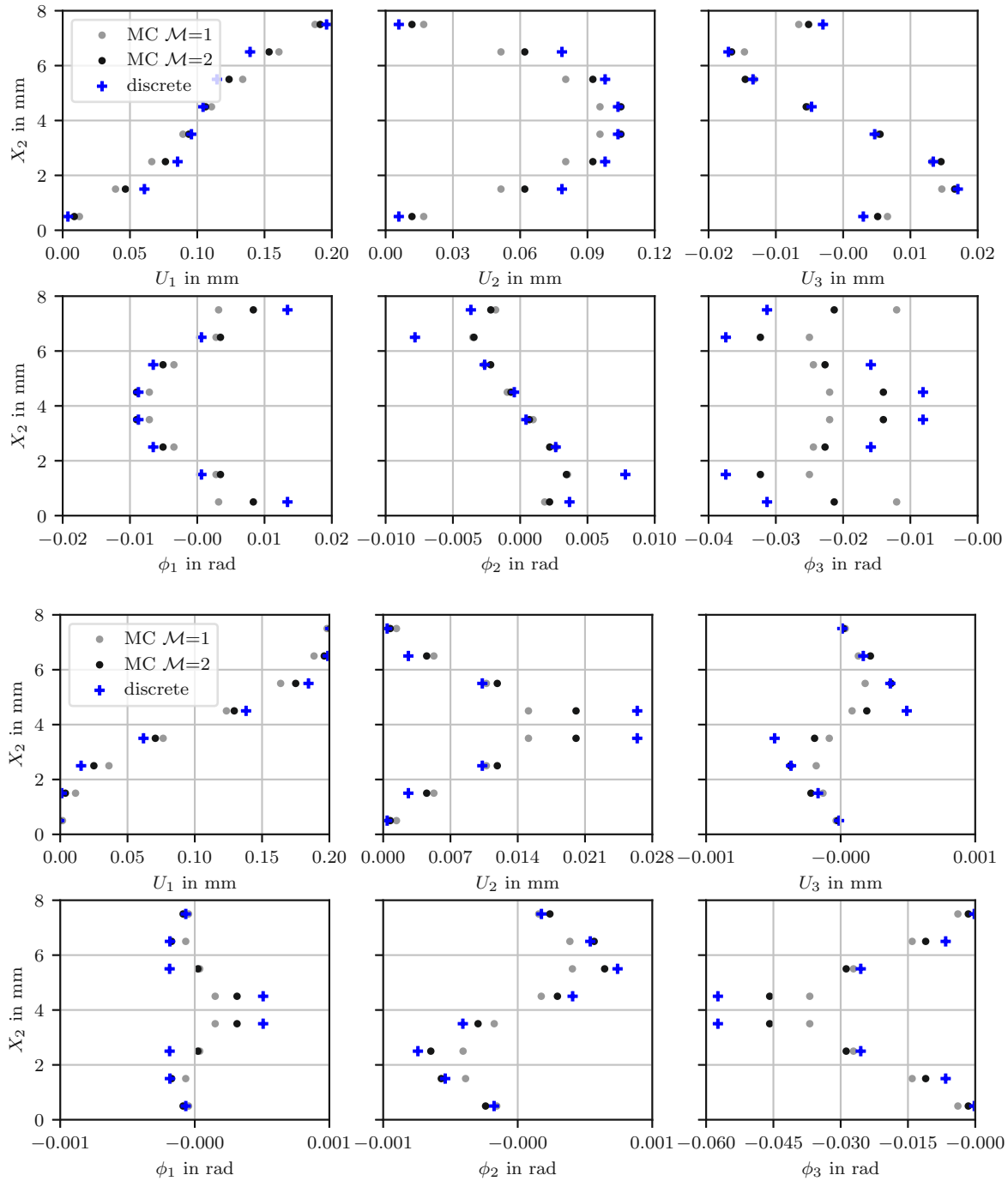

Figure 6.7: Simple shear - Displacements and rotations of MPBCs of the BCC lattice, comprised of 8x8x8 base cells, along the 2-axis at locations $X_1 = X_3 = l/2$ (first and second row) and $X_1 = X_3 = 7l/2$ (third and fourth row).

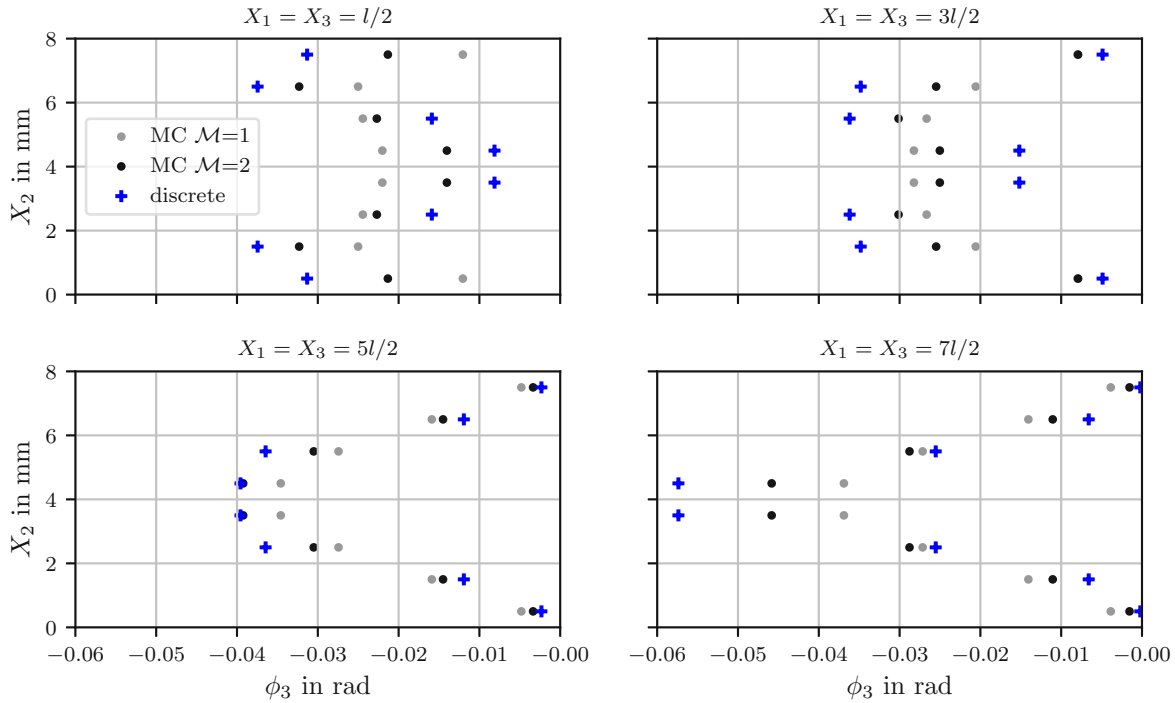

Figure 6.8: Simple shear - Rotations ϕ_3 of MPBCs of the BCC lattice, comprised of 8x8x8 base cells, along the 2-axis at four different locations.

To gain further insight, the rotations ϕ_3 at the MPBCs are given with respect to three different planes in Figure 6.9. The first plane is parallel to the 1-2-plane for the location $X_3 = 7l/2 = 3.5\,\text{mm}$ (top), i.e., the surface normal is parallel to the 3-axis. The second and third planes are both parallel to the 2-3-plane for locations $X_1 = l/2$ (center) and $X_1 = 7l/2 = 3.5\,\text{mm}$ (bottom), i.e., the surface normals are parallel to the 1-axis. The discrete model (left column) and the continuum model with an element size of $h_e = l/2$ (center column) are directly compared via relative error values (right column). For all planes, the rotations ϕ_3 are qualitatively captured by the continuum model, but show quite large error values. For the first plane, the error values are acceptable only in the far-field region with respect to both free surfaces, namely, for $3l/2 = 1.5\,\text{mm} < X_1$ and $X_2 < 13l/2 = 6.5\,\text{mm}$. Closer to the free surface, some of the error values are even larger than +1.0. For the plane parallel to the 2-3-plane at $X_1 = l/2 = 0.5\,\text{mm}$, the error values are quite large in the center, but small close to the free surface at $X_2 = l/2 = 0.5\,\text{mm}$ and $X_2 = 15l/2 = 7.5\,\text{mm}$. This may be a consequence of being quite close to the free surface at $X_1 = l/2 = 0.5\,\text{mm}$. In contrast, for the plane at $X_1 = 7l/2 = 3.5\,\text{mm}$, the error values decrease for increasing distance to the free surfaces, i.e., for $3l/2 = 1.5\,\text{mm} < X_2 < 13l/2 = 6.5\,\text{mm}$.

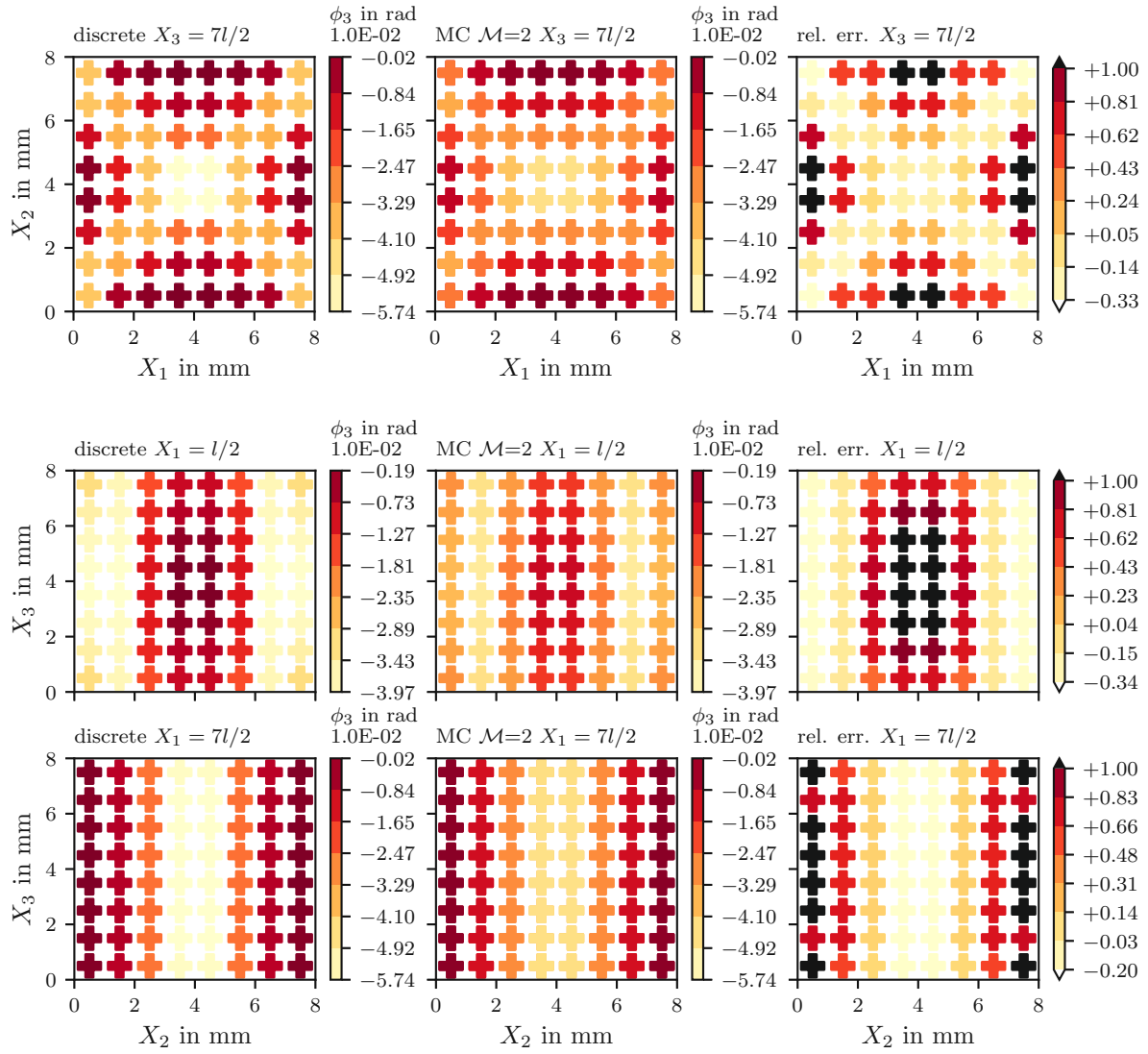

Figure 6.9: Simple shear - Rotation fields ϕ_3 of MPBCs of the BCC lattice, comprised of 8x8x8 base cells, in 1-2-plane at location $X_3 = 7l/2 = 3.5\,\text{mm}$ (top) and in 2-3-plane at locations $X_1 = l/2 = 0.5\,\text{mm}$ (center) and $X_1 = 7l/2 = 3.5\,\text{mm}$ (bottom).

To further obtain a rough estimate on the capability of the MC model to capture the rotations ϕ_3 at the MPBCs of the BCC lattice with respect to various planes, the relative error value, $\chi_{\phi 3}$, according to Eq. (6.1) is evaluated for planes with normals parallel to one of the three spatial dimensions. The representative error values are shown in Figure 6.10. For planes with surface normals parallel to the 3-axis, $\chi_{\phi 3}$ ranges between ≈ 0.35 and ≈ 0.85 and is not constant over X_3 as was observed for the PC lattice. Interestingly, planes with increasing distance to the free surface show larger error values. Similar results are obtained for planes parallel to the 1- and 2-axes. The lowest error values are obtained for $3l/2 = 1.5\,\text{mm} \leq X_i \leq 5l/2 = 2.5\,\text{mm}$. As was indicated by the strain energies given in Table 6.2, the relative error values are significantly reduced by using an element size of $h_e = l/4$ ($\mathcal{M} = 4$) instead of $h_e = l/2$ ($\mathcal{M} = 2$). The error values of rotation ϕ_3 for the whole lattice are ≈ 0.55 for $\mathcal{M} = 2$, and ≈ 0.29 for $\mathcal{M} = 4$. This means that for the present load case, the BCC lattice must be finer discretized than the PC lattice and that $\mathcal{M} = 4$ may not be sufficient.

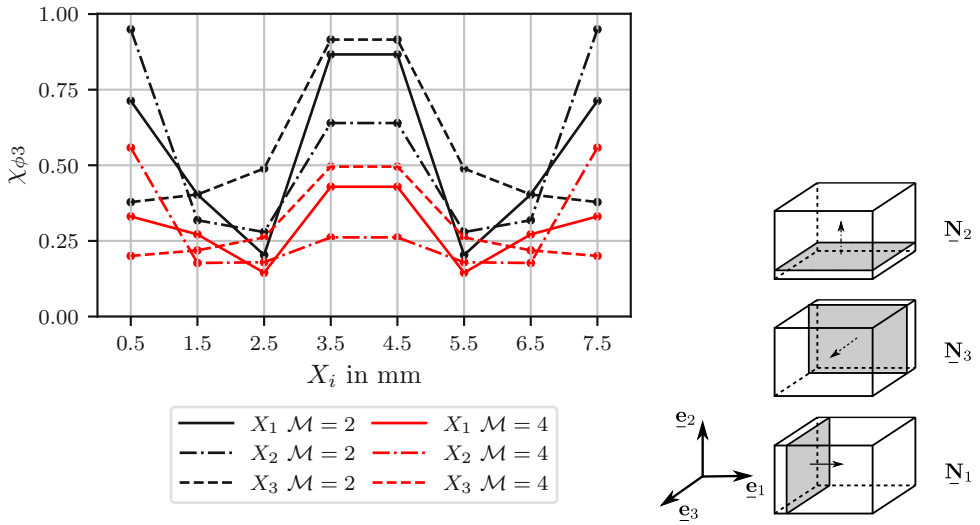

Figure 6.10: Simple shear - Relative error values of the rotations $\chi_{\phi 3}$ on various planes with surface normals parallel to the spatial directions $i = 1, 2, 3$ evaluated along the normals at locations of MPBCs of the BCC lattice (left) and sketch of such planes including their surface normals (right).

6.2.2 Torsion

The configurations of the PC and the BCC lattices used for the torsion load case are summarized in Table 6.3.

Investigation of the strain energy

The strain energies obtained for discrete and continuum models are summarized in Table 6.4. Different element sizes are used for the continuum model, namely, $h_e = l$ and $h_e = l/2$. As expected, the continuum model shows a more compliant behavior for the smaller element size than for the larger one. The relative error for the smallest element size studied is about 7.1% for the PC and 0.8% for the BCC lattice.

Investigation of the kinematic fields

The continuum models with element sizes of $h_e = l$ and $h_e = l/2$ are the basis for comparing the kinematic fields with the corresponding discrete models. First, the PC lattice is analyzed, then the BCC lattice.

PC. The displacements and the rotations of the MPBCs of the PC lattice along the 3-axis are shown in Figure 6.11 for two locations at $X_1 = X_2 = l/2 = 0.5\,\text{mm}$ (first and second rows) and $X_1 = X_2 = 7l/2 = 3.5\,\text{mm}$ (third and fourth rows). There are only differences in the rotations ϕ_1 and ϕ_2 for the locations studied. The larger the distance to the free surface of the lattice, the better the continuum model is able to capture these rotations. In the far-field region, i.e. at $X_1 = X_2 = 7l/2 = 3.5\,\text{mm}$, the rotations ϕ_1 and ϕ_2 of the continuum model for both element sizes studied are in good agreement with the discrete model. This also holds true for the gradients evolving from the boundaries at $X_3 = 0$ and $X_3 = 24\,\text{mm}$.

In Figure 6.12, the magnitudes of displacements (top) and rotations ϕ_3 at the MPBCs of the PC lattice (bottom) are given with respect to three different planes. All planes are parallel to the 1-2-plane and show different locations over the 3-axis, namely, $X_3 = 3l/2 = 1.5\,\text{mm}$ (first row), $X_3 = 23l/2 = 11.5\,\text{mm}$ (second row), and $X_3 = 45l/2 = 22.5\,\text{mm}$ (third row). The discrete model (left column) and the continuum model with an element size of $h_e = l/2$ (center column) are directly compared via relative error values (right column). The continuum model agrees well with its corresponding discrete model and shows small error values for both displacement magnitudes and rotations ϕ_3 in all three planes considered.

Table 6.3: Geometrical dimensions of the PC and BCC lattices studied for the torsion load case.

	N_1xN_2xN_3 (/)	$L_1 = L_2 = L_3/3$ in mm	l in mm	r in mm
PC	8x8x24	8	1	$l/20$
BCC	8x8x24	8	1	$l\sqrt{3}/2/20$

Table 6.4: Torsion - Strain energies of discrete and continuum models for the PC and BCC lattices studied.

	N_1xN_2xN_3 (/)	discrete in N mm	MC $\mathcal{M} = 1$ in N mm	rel. err. in %	MC $\mathcal{M} = 2$ in N mm	rel. err. in %
PC	8x8x24	46.201824	50.193474	8.6	49.481888	7.1
BCC	8x8x24	6550.92627	6679.807129	2.0	6602.644531	0.8

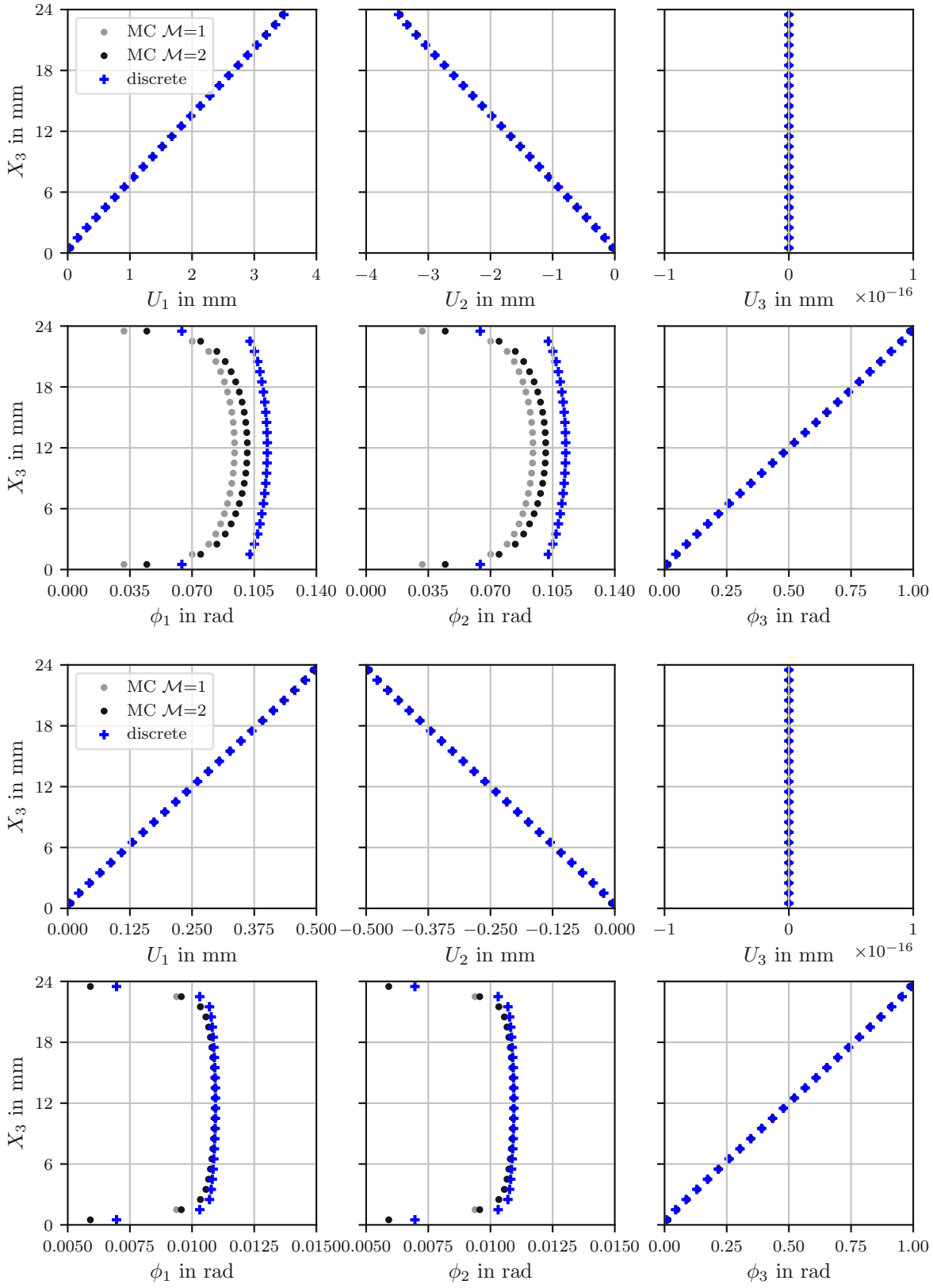

Figure 6.11: Torsion - Displacements and rotations of MPBCs along the 3-axis at location $X_1 = X_2 = l/2$ (first and second row) and $X_1 = X_2 = 7l/2$ (third and fourth row) for the PC lattice comprised of N_1xN_2xN_3 = 8x8x24 base cells.

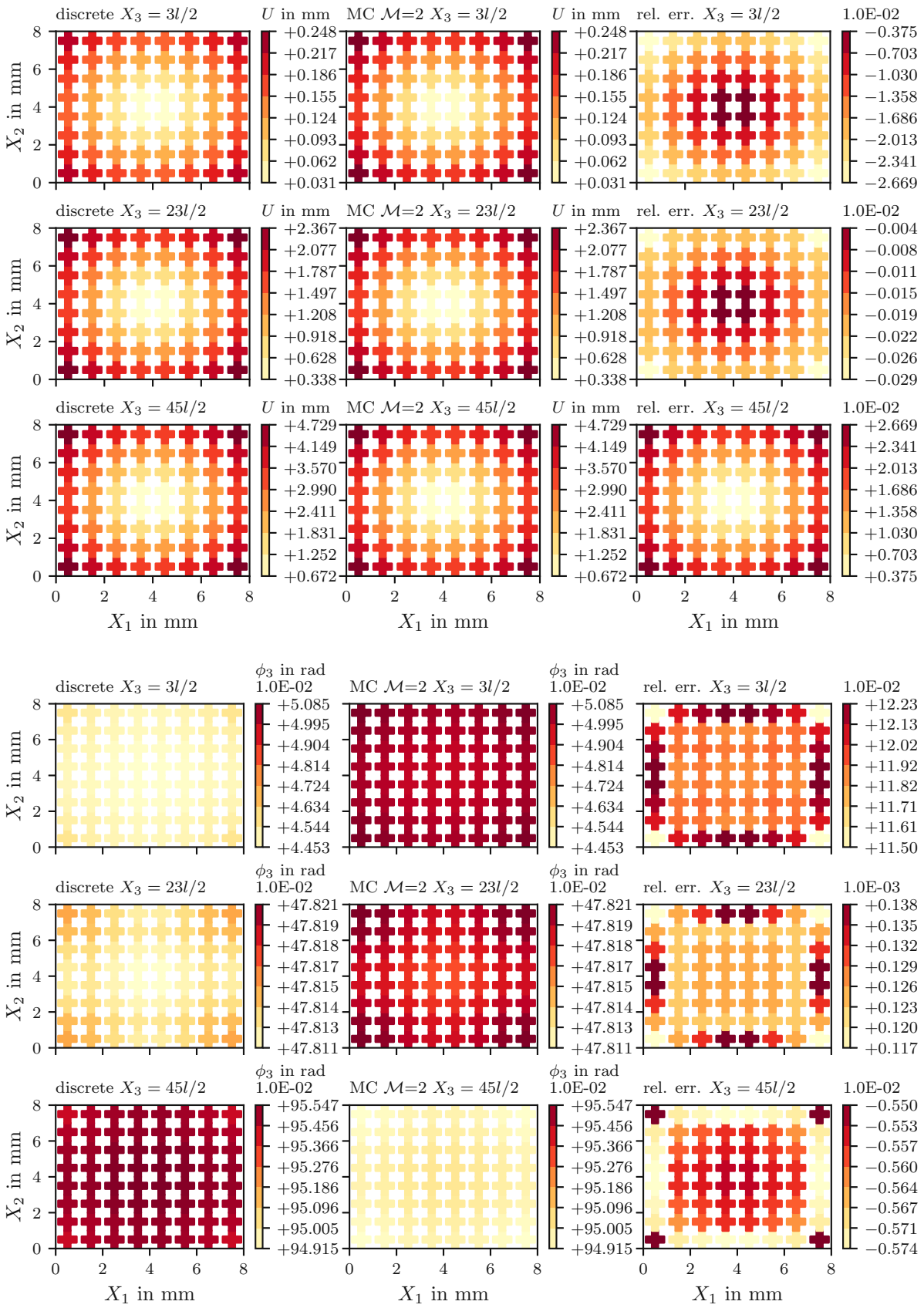

Figure 6.12: Torsion - Magnitudes of displacements U (top) and rotation fields ϕ_3 of MPBCs (bottom) in the 1-2-plane at various locations X_3 for the PC lattice comprised of N_1xN_2xN_3 = 8x8x24 base cells.

BCC. Similar results are obtained for the BCC lattice, cf. Figure 6.13 for displacements and rotations along the 3-axis for two locations at $X_1 = X_2 = l/2 = 0.5\,\text{mm}$ (first and second rows) and $X_1 = X_2 = 7l/23.5\,\text{mm}$ (third and fourth rows) and Figure 6.14 for displacement magnitudes (top) and rotations ϕ_3 of MPBCs (bottom) in three different planes parallel to the 1-2-plane.

Both PC and BCC. To further obtain a rough estimate on the capability of the MC model to capture the rotations ϕ_3 at the MPBCs with respect to various planes, the relative error value, $\chi_{\phi 3}$, according to Eq. (6.1) is evaluated for planes with normals parallel to one of the three spatial dimensions, cf. Figure 6.15 for the PC (left) and BCC lattices (right). For planes with surface normals parallel to the 1- and 2-axis, the representative error values $\chi_{\phi 3}$ are the same and are within an acceptable range between ≈ 0.045 and ≈ 0.05 for the PC and between ≈ 0.015 and ≈ 0.02 for the BCC lattice. For planes with surface normals parallel to the 3-axis, the error values are high very close to the boundary at $X_3 = l/2 = 0.5\,\text{mm}$. For increasing distance to the boundary, the error values decrease significantly and become very small. The values increase slightly closer to the boundary at $X_3 = 49l/2 = 24.5\,\text{mm}$. This holds true for both the PC and BCC lattices.

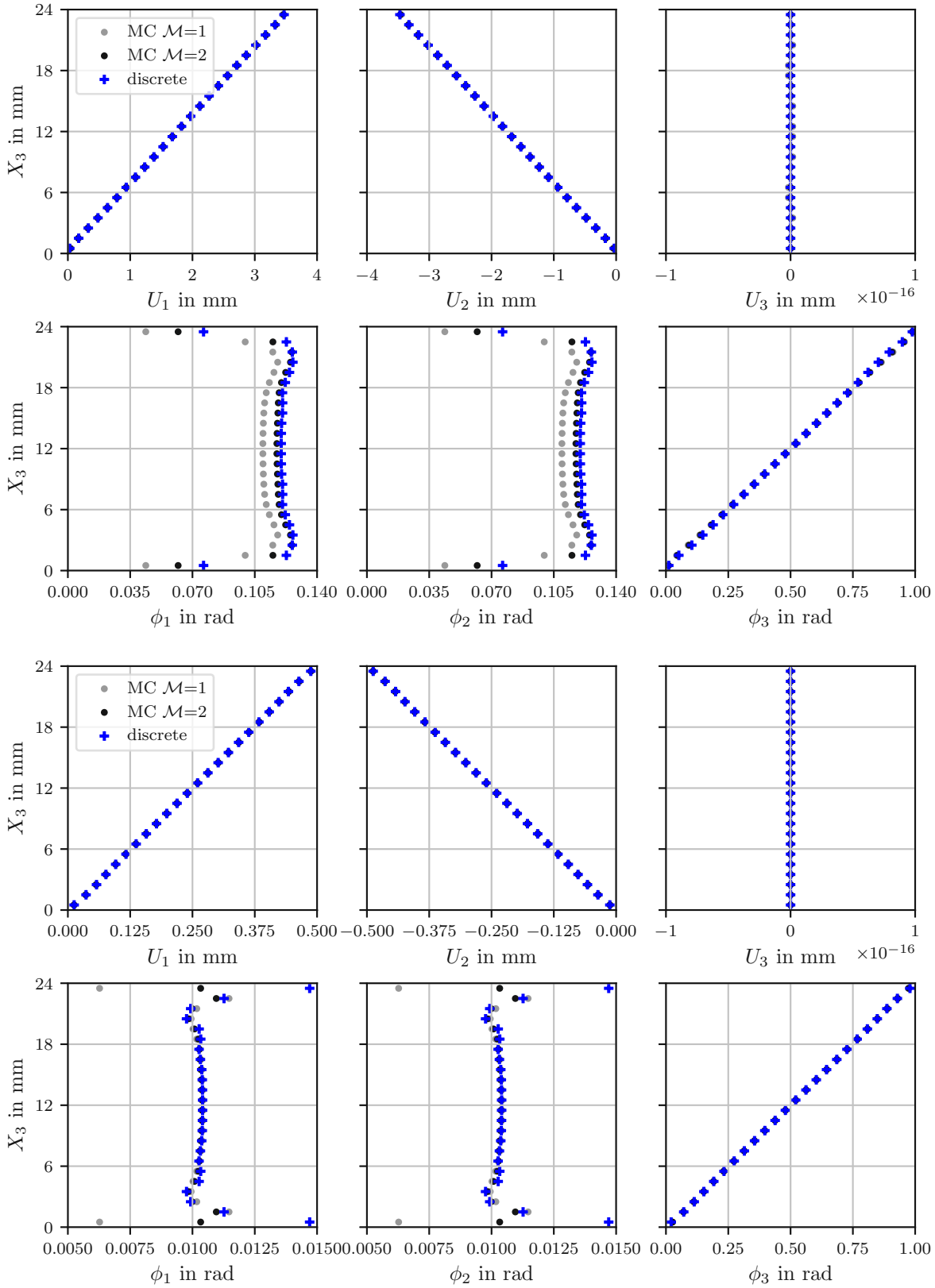

Figure 6.13: Torsion - Displacements and rotations of MPBCs along the 3-axis at location $X_1 = X_2 = l/2$ (first and second row) and $X_1 = X_2 = 7l/2$ (third and fourth row) for the BCC lattice comprised of N_1xN_2xN_3 = 8x8x24 base cells.

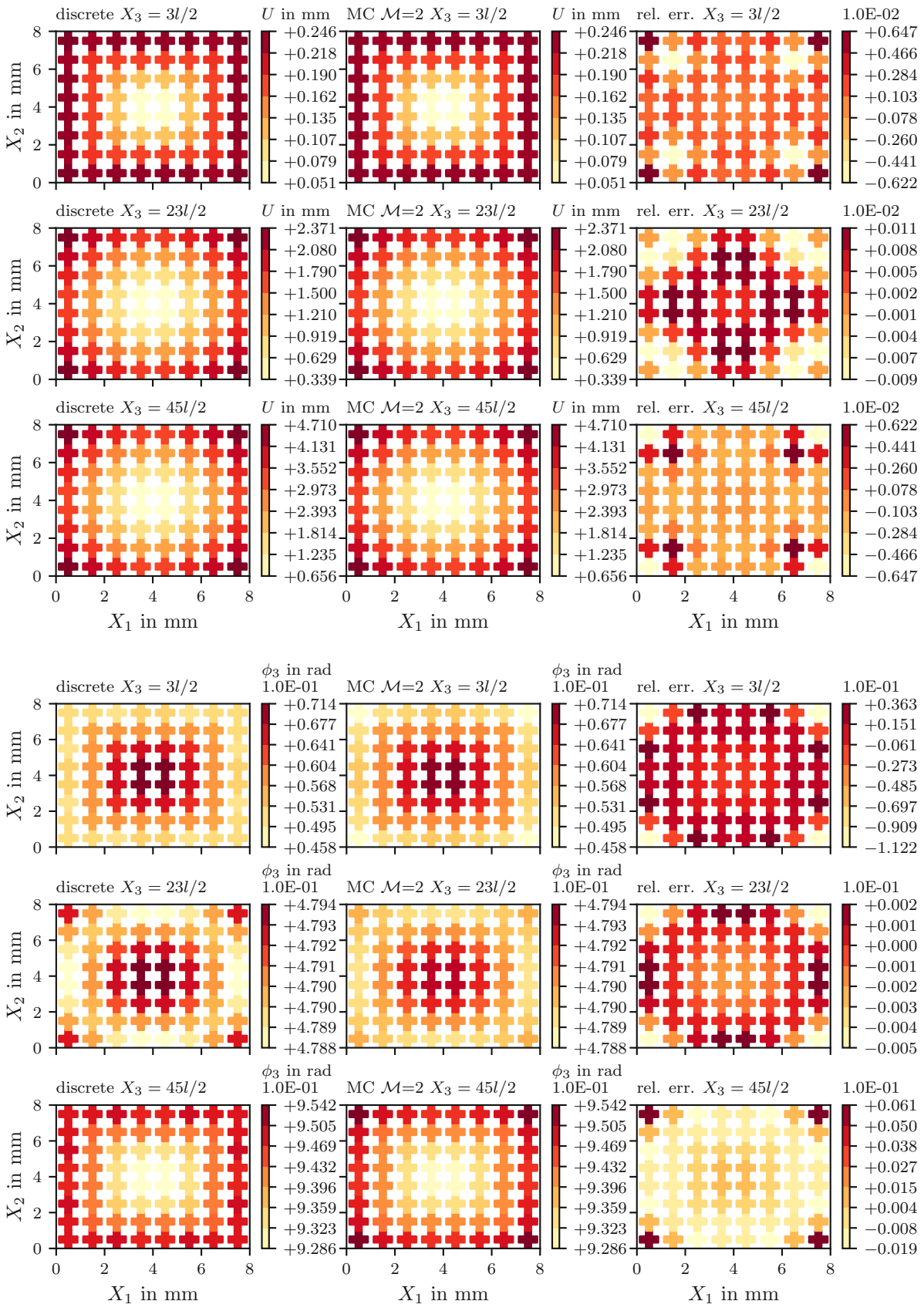

Figure 6.14: Torsion - Magnitudes of displacements U (top) and rotation fields ϕ_3 of MPBCs (bottom) in the 1-2-plane at various locations X_3 for the BCC lattice comprised of N_1xN_2xN_3 = 8x8x24 base cells.

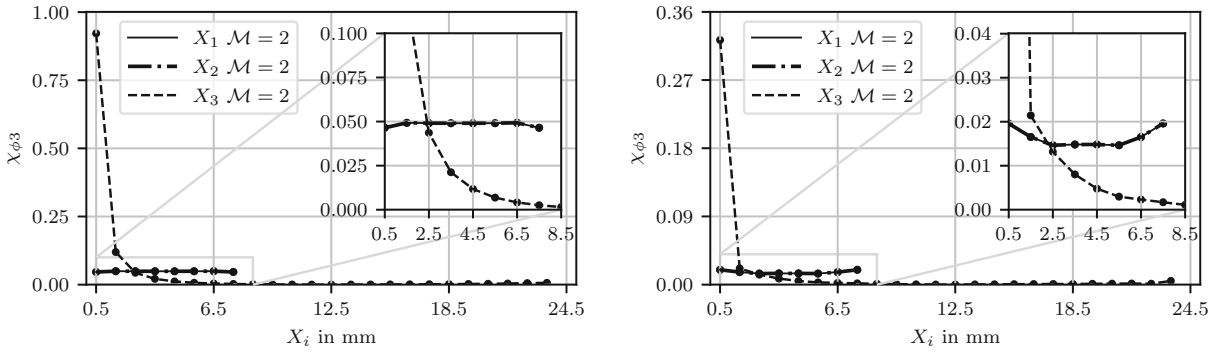

Figure 6.15: Torsion - Relative error values of rotations $\chi_{\phi 3}$ on various planes with surface normals parallel to the spatial directions $i = 1, 2, 3$ evaluated along the normals at locations of MPBCs of the PC lattice (left) and BCC lattice (right).

6.3 Summary

The MECs derived for the PC and the BCC lattices are evaluated on the basis of numerical simulations by comparison with discrete models. The implementation of the micropolar continuum model is performed in ABAQUS as a user element. For comparison, the mechanical response of the models is studied in terms of strain energy and kinematic fields. Therefore, different configurations of the PC and BCC lattices are subjected to a simple shear and a torsion load case. The FEM parameters chosen for the continuum model are based on the findings of Chapter 5.

The strain energy is captured quite well by the continuum models using element sizes smaller than the characteristic length of the lattice, $h_e < l$. For larger element sizes, it strongly depends on the type of lattice in combination with the load case studied, e.g., for the BCC lattice subjected to simple shear, the element size has to be at least $h_e < l/2$ to properly capture the strain energy, whereas subjected to torsion, an element size of $h_e = l$ is sufficient.

The kinematic fields of the midpoints of base cells of the lattice are studied with respect to different locations along various axes and planes and a direct comparison between continuum and discrete model is performed. The free surface of the lattice strongly influences the evolution of those fields excited by the load case. Close to the free surfaces, the continuum models are only able to qualitatively capture the kinematic fields. In the far field region, these fields can be captured quite well by the continuum model. When using element sizes smaller than the characteristic length of the lattice, e.g., $h_e < l/2$, even the gradients of the kinematic fields evolving from the boundaries are qualitatively captured reasonably well for both, PC and BCC lattice.

In summary, the micropolar continuum is able to capture the mechanical response of both PC and BCC lattices quite well when using element sizes smaller than the characteristic length of the lattice, i.e., $h_e < l$. For larger element sizes, this strongly depends on the type of lattice in combination with the load case studied. These findings coincide with those obtained for the 2D lattices presented in Chapter 5.

Chapter 7

Geometrically nonlinear micropolar continuum modeling in 3D

First, the geometrically nonlinear micropolar element presented in Section 4.1.2 is verified on the basis of three test cases taken from literature, where linear isotropic material behavior is considered. Next, the capabilities and limitations of the model are studied in terms of its ability to account for lattice materials in large displacement and rotation problems in the small strain regime. Buckling of slender lattice beams can be considered such a problem and serves as the basis for the evaluation. Different types and sizes of 3D periodic lattice structures are considered and subjected to global compressive loadings to study the capabilities of the model in estimating the critical loads as well as the postbuckling behavior.

7.1 Verification of UEL

The geometrically nonlinear micropolar element presented in Section 4.1.2 is verified by studying three specific structures, a T-shape structure, a curved cantilever beam, and an elbow cantilever, cf. Figure 7.1 for their schematics. Within the framework of nonlinear micropolar theory using the FEM, the T-shape structure test case was applied first by [8] while the other cases were first used in [44]. Note that all test cases were analyzed earlier in the context of classical elasticity, see [44] for more details. The T-shape structure is used to separately test torsion and bending. The curved cantilever beam is used to excite all rotations at once, which is realized by applying an out-of-plane load to the structure lying in-plane. For evaluating the ability of the model to account for rigid body rotations, the elbow cantilever is used. The elbow cantilever is subjected to torsion and bending while being additionally rotated. For the comparison with the literature, only the solution variables, namely, displacements and rotations, are evaluated. The convergence rate of the solution procedure is not of interest in the present work. For all test cases, the material behavior is considered to be linear isotropic, where the corresponding isotropic material moduli are taken from [44] and are summarized in Table 7.1. Details on the FEM models of the individual test cases can be found in the corresponding section. It is worth noting that the present FEM implementation shows the so-called non-invariance anomaly as observed in [44]. This anomaly describes the phenomenon that for interpolated rotations between two configurations the relative Lagrangian stretch and wryness tensors are non-invariant under rigid body rotations, even though their analytical expression is invariant as shown in [44]. The amount of non-invariance can be reduced by increasing the number of load increments used for the Newton-Raphson

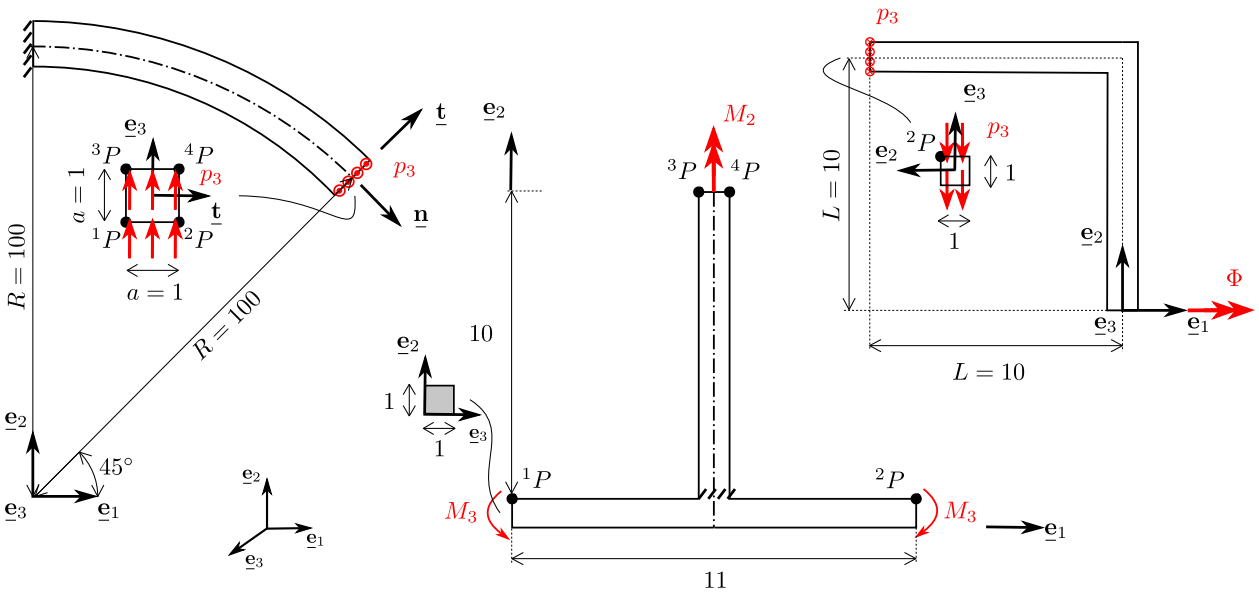

Figure 7.1: Schematics of the curved cantilever beam (left), T-shape structure (center), and elbow cantilever (right). The geometric dimensions are given in mm. (Taken and modified from [44])

procedure as well as a fine discretization of the domain [44]. The number of load increments and the discretization of the domain for all simulations performed in this work are chosen such that this invariance anomaly can be considered negligible. A solution to overcome this anomaly has been presented in [44], but has neither been applied therein nor in the present thesis. Where possible, the same incrementation is used as in [44] to ensure a proper comparison. All simulations are carried out with ABAQUS/Standard 2019 (Dassault Systèmes Simulia Corp., Providence, RI, USA) using its unsymmetric equation solution capability for which slightly better convergence behavior was found. The perturbation parameter in Eq. (4.25) for determining the tangential stiffness matrix is set to $\vartheta = 10^{-8}$ for all simulations performed. Note that for smaller values of ϑ no influence on the results can be observed, which is not shown for the sake of brevity.

7.1.1 T-shape structure

The T-shape structure is analyzed based on the second load case presented in [8] to stay within the limit of $||\underline{\phi}|| < 2\pi$. In [8], the T-shape structure was used to determine the convergence behavior of their FEM implementation. No results in terms of solution variables were presented. Therefore, the values of the very same load case presented in [44] are used for comparison. The isotropic material moduli are taken from [44] and can be found in Table 7.1. Note that slightly different material moduli have been used in [44] and in

Table 7.1: Isotropic micropolar material moduli for the various test cases, see Section 2.5 for their definition.

	λ	μ	ν	α	β	γ
T-bar	1.575E+04	1.05E+04	3.50000E+03	0.0E+00	5.25E+01	5.25E+01
Curv. Cant. (a)	5.000E+06	0.00E+00	5.05051E+04	0.0E+00	1.25E+04	3.75E+04
Curv. Cant. (b)	5.000E+06	0.00E+00	2.13158E+07	0.0E+00	1.25E+04	3.75E+04
Elbow Cant.	1.000E+04	0.00E+00	1.01010E+02	0.0E+00	2.50E+01	7.50E+01

Table 7.2: T-shape structure - Results from [44] (top) indicated by an asterisk $*$ and the present FEM implementation (bottom) are listed.

	U_1 mm	U_2 in mm	U_3 in mm	ϕ_1 in rad	ϕ_2 in rad	ϕ_3 in rad
$*^1P$	+1.2182E+00	−3.6278E+00	−1.1277E−02	−1.4940E−02	−5.2237E−03	+1.7303E+00
$*^2P$	−1.2182E+00	−3.6278E+00	−1.1277E−02	−1.4940E−02	+5.2237E−03	−1.7303E+00
$*^3P$	+1.0335E+00	+2.7191E−03	−9.7484E−01	−4.5819E−02	+3.2176E+00	−4.5027E−02
$*^4P$	−9.7484E−01	+2.7191E−03	−1.0335E+00	−4.5027E−02	+3.2176E+00	+4.5810E−02
^1P	+1.2182E+00	−3.6278E+00	−1.1277E−02	−1.6623E−02	−6.0958E−03	+1.7303E+00
^2P	−1.2182E+00	−3.6278E+00	−1.1277E−02	−1.6624E−02	+6.0993E−03	−1.7303E+00
^3P	+1.0336E+00	+2.7206E−03	−9.7479E−01	−1.1155E−01	+3.2135E+00	−1.1596E−01
^4P	−9.7479E−01	+2.7206E−03	−1.0336E+00	−1.1596E−01	+3.2135E+00	+1.1155E−01

[8]. The T-shape structure is fully clamped between rib and flange, i.e., the 1-3-plane at $X_2 = 1\,\text{mm}$. The loads are applied in two analysis steps. In the first step, the rib pointing in 2-direction is subjected to a resultant torsion moment of $M_2 = 600\,\text{N mm}$ at the free end at $X_2 = 11\,\text{mm}$. In the second step, two resultant bending moments each of $M_3 = 1125\,\text{N mm}$ are applied at the free ends of the flange pointing in 1-direction at $X_1 = 0\,\text{mm}$ and $X_1 = 11\,\text{mm}$, respectively. Similar to [44], the load is applied in 20 equal increments in both steps.

The element size for the discretization of the structure is $h_e = 1$, i.e., the structure is discretized by cube-shaped elements, where ten elements are used for the rib and eleven elements are used for the flange. The torsion and bending moments are applied in terms of concentrated nodal moments. Considering the discretization and the linearly interpolated elements, this results in ${}^iM_2 = M_2/4$ and ${}^iM_3 = M_3/4$ for each node i at the corresponding free ends, respectively.

The solution variables are evaluated at the end of the analysis at four different nodes, ${}^iP = [X_1, X_2, X_3]$, namely, at ${}^1P = [0, 1, 1]$, ${}^2P = [11, 1, 1]$, ${}^3P = [5, 11, 1]$, and ${}^4P = [6, 11, 1]$. The results are summarized in Table 7.2, see (top) for those presented in [44] and (bottom) for the present work. The displacements are in very good agreement with those presented in [44]. The same holds true for the rotations directly associated with the corresponding torsion or bending moment, i.e., ϕ_2 at ${}^3P$ and ${}^4P$ for the torsion moment and ϕ_3 at ${}^1P$ and ${}^2P$ for the bending moment. The other rotations deviate from the results presented in [44] by a factor of up to 3, cf. ϕ_1 at ${}^3P$ and ${}^4P$ as well as ϕ_3 at ${}^3P$ and ${}^4P$. Interestingly, the deviations are the very same for these rotations.

It is worth noting that for the first load case, the present FEM implementation gives the same results for the displacements as given in [44]. However, the rotations do not sum up properly as ABAQUS does not allow for rotations showing $||\underline{\phi}|| > 2\pi$.

7.1.2 Curved Cantilever Beam

The curved cantilever beam presented in [44] is fully clamped at the end parallel to the 2-3-plane. At the other end, a constant distributed surface load in 3-direction, $p_3 = 600\,\text{N/mm}^2$, is applied, which leads the curved cantilever beam to deflect in such a way that all three rotational DOFs are excited and show large magnitudes.

The structure is discretized by 14 and 256 elements along the neutral axis while both directions tangential to the cross-section of the beam are discretized by only one element. The surface load is applied through consistent nodal forces, see Eqs. (4.1)-(4.13). For the linear interpolated element and the discretization used, the force applied on each node, i, of the surface follows as ${}^{i}F_3 = p_3 A/4 = 150\,\mathrm{N}$ with the square cross-section $A = 1\,\mathrm{mm}^2$. The isotropic material moduli can be found in Table 7.1, where two different sets (a) and (b) are given. Set (a) represents a limit case of the micropolar theory to obtain results similar to those obtained by the classical elasticity theory whereas set (b) also considers micropolar effects.

For the comparison, the solution variables are evaluated at the free end at four different nodes, ${}^{i}P = [X_1, X_2, X_3]$, namely, at ${}^{1}P = [(R-a/2)\cos 45°, (R-a/2)\sin 45°, 0]$, ${}^{2}P = [(R+a/2)\cos 45°, (R+a/2)\sin 45°, 0]$, ${}^{3}P = [(R-a/2)\cos 45°, (R-a/2)\sin 45°, 1]$, and ${}^{4}P = [(R+a/2)\cos 45°, (R+a/2)\sin 45°, 1]$, where R denotes the radius of the structure and a is the side length of the square shaped cross-section. The values obtained for set (a) are summarized in Table 7.3, where two different discretizations are covered. The displacements are in very good agreement with those presented in [44] for both discretizations. The same holds true for the rotations ϕ_1. In contrast, deviations ranging from about -15% for ϕ_2 to about 15% for ϕ_3 are observed for the coarse discretization. However, the deviations decrease for using a finer discretization, where the highest deviation is about -5% for ϕ_3. Note that for the coarse discretization two increments instead of a single one as used in [44] are needed to obtain convergence considering the default settings of the ABAQUS Newton-Raphson solver, i.e., default values of `*CONTROLS, PARAMETERS=TIME INCREMENTATION`. For the fine discretization, 20 increments instead of ten as used in [44] are needed to achieve convergence. For material moduli set (b), the solution variables are only evaluated at node ${}^{1}P$, cf. Table 7.4. A deviation is only observed for the rotation ϕ_3, where they are about 28%. Note that 20 increments instead of five as used in [44] are needed to achieve convergence.

7.1.3 Elbow Cantilever

The elbow cantilever presented in [44] is fully clamped at the end parallel to the 1-3-plane. At the other end, a constant distributed surface load in negative 3-direction, $p_3 = -5\,\mathrm{N/mm}^2$, is applied. Additionally, the whole structure is subjected to a rigid body rotation around the 1-axis of $\Phi = 2\pi$. The analysis consists of two steps. In the first step, the surface load is applied in a single increment. In the second step, the rigid body rotation is applied using the minimum number of increments required for convergence.

The structure is discretized by 5 elements along each leg and a single element at the intersection of the two legs, i.e., in total eleven elements are used. The surface load is applied through concentrated nodal forces at each node, i, of the free end, which follows as ${}^{i}F_3 = p_3 A/4 = 1.25\,\mathrm{N}$ for the current FEM setting and with the square cross-section being $A = 1\,\mathrm{mm}^2$. The isotropic material moduli can be found in Table 7.1.

For the comparison, the solution variables are evaluated at the node, ${}^{2}P = [-10, 10.5, 0.5]$, and are summarized in Table 7.5, where the displacements are evaluated after the first and second load step. This is done in order to study the influence of the rigid body rotation on the response of the structure, where the first step is referred to as reference solution. For both steps, the results are in acceptable agreement with those presented in [44]. Considering the rigid body rotation, the results based on the FEM implementation in this work show slightly more deviations from its reference solutions than those presented in [44]. The deviations are associated with the non-invariance anomaly of strain measures of FEM implementations discussed in [44]. However, the deviations are considered to be acceptable. Note that approximately 30 to 40 increments are required for convergence with default settings of the ABAQUS Newton-Raphson solver instead of 20 increments as used in [44]. No rotations were presented in [44] and, hence, are not given.

Table 7.3: Curved cantilever beam - Results from [44] indicated by an asterisk $*$ and the present FEM implementation are listed for different element sizes and using material moduli set (a).

	U_1 mm	U_2 in mm	U_3 in mm	ϕ_1 in rad	ϕ_2 in rad	ϕ_3 in rad
	14x1x1					
$*^1P$	−1.28E+00	+1.91E+00	+1.61E+01	−5.08E−01	−6.06E−02	−3.56E−02
$*^2P$	−1.24E+00	+1.80E+00	+1.58E+01	−5.08E−01	−6.06E−02	−3.57E−02
$*^3P$	−1.32E+00	+2.40E+00	+1.59E+01	−5.08E−01	−6.06E−02	−3.57E−02
$*^4P$	−1.28E+00	+2.29E+00	+1.56E+01	−5.08E−01	−6.06E−02	−3.57E−02
^1P	−1.28E+00	+1.91E+00	+1.61E+01	−5.09E-01	−5.11E-02	−4.09E-02
^2P	−1.24E+00	+1.80E+00	+1.58E+01	−5.09E-01	−5.10E-02	−4.09E-02
^3P	−1.32E+00	+2.40E+00	+1.59E+01	−5.09E-01	−5.11E-02	−4.09E-02
^4P	−1.28E+00	+2.29E+00	+1.56E+01	−5.09E-01	−5.10E-02	−4.09E-02
	256x1x1					
$*^1P$	−2.15E+01	+1.25E+01	+5.22E+01	−5.67E−01	−9.66E−02	+4.78E−02
$*^2P$	−2.17E+01	+1.26E+01	+5.24E+01	−5.67E−01	−9.66E−02	+4.77E−02
$*^3P$	−2.23E+01	+1.29E+01	+5.16E+01	−5.67E−01	−9.66E−02	+4.78E−02
$*^4P$	−2.25E+01	+1.30E+01	+5.19E+01	−5.67E−01	−9.66E−02	+4.77E−02
^1P	−2.16E+01	+1.25E+01	+5.23E+01	−5.57E−01	−9.76E−01	+4.51E−02
^2P	−2.18E+01	+1.26E+01	+5.25E+01	−5.57E−01	−9.76E−01	+4.51E−02
^3P	−2.24E+01	+1.30E+01	+5.17E+01	−5.57E−01	−9.76E−01	+4.51E−02
^4P	−2.26E+01	+1.31E+01	+5.19E+01	−5.57E−01	−9.76E−01	+4.51E−02

Table 7.4: Curved cantilever beam - Results from [44] indicated by an asterisk $*$ and the present FEM implementation for 256x1x1 elements and using the material moduli set (b).

	U_1 mm	U_2 in mm	U_3 in mm	ϕ_1 in rad	ϕ_2 in rad	ϕ_3 in rad
$*^1P$	−1.874E+01	1.089E+01	4.927E+01	−5.60E−01	−8.82E−02	1.78E−02
^1P	−1.874E+01	1.089E+01	4.927E+01	−5.56E−01	−8.85E−02	1.28E−02

Table 7.5: Elbow cantilever - Results from [44] indicated by an asterisk $*$ and the present FEM implementation for 11 elements without (top) and with rotation around 1-direction (bottom).

	U_1 mm	U_2 in mm	U_3 in mm
$*^2P$	3.01094975−01	−8.04784620E−02	−3.32302580E+00
^2P	3.0107594E−01	−8.0521193E−02	−3.3230089E+00
$*^2P$	3.01116332E−01	−8.04918162E−02	−3.32321916E+00
^2P	3.0112722E−01	−8.0220205E−02	−3.3227509E+00

7.1.4 Summary

The present FEM implementation is successfully verified by comparing the results obtained for three different test cases to those presented in [44]. The displacements are in very good agreement for all cases studied. For the rotations, deviations are observed in the range of about $\pm 15\%$ for very coarse discretizations. For finer discretizations, the deviations decrease to about $\pm 5\%$ for the test cases studied. These deviations may be based on the slightly different FEM implementations and frameworks used, with the present work using ABAQUS instead of FEAP in [44]. The convergence criteria for the Newton-Raphson procedures may also play a role. However, the deviations are assumed to be acceptable for the applications presented in the next Section 7.2.

7.2 Postbuckling of lattice beams

The capabilities of the geometrically nonlinear micropolar continuum (MC) to estimate critical loads and to enter the postbuckling regime of lattice structures is studied by comparison with discrete models. Additionally, the continuum based on classical elasticity theory (CC) serves as reference to study advantages and disadvantages of the micropolar modeling. For this purpose, buckling of lattice beams is studied as shown in Figure 7.2. The boundary conditions are applied at the ends parallel to 1-2-plane. At $X_3 = 0\,\text{mm}$ the lattice beam is fully clamped and at $X_3 = L_3$ it is only free to move in 3-direction. Various configurations of the PC and BCC lattice serve as the basis for the comparison, where the geometrical properties and the parent material used are the same as outlined in Section 6.1.1. The description of the discrete lattice models can be found in Section 6.1.2, but to reduce the numerical effort a different discretization is used. For the BCC lattice, each strut is discretized by three elements instead of six, i.e., 24 elements per base cell, while for the PC lattice, four instead of six elements per strut are used, i.e., 12 elements per base cell. For the continuum models, discretizations with $\mathcal{M} \leq 1$ are used, cf. Eq. (6.2) in Section 6.1.3. The MECs of the PC lattice are based on Eq. (3.14) and for the BCC lattice on Eqs. (3.17) and (3.18). The classical elastic constants of the CET continuum are obtained based on the micropolar ones and are determined in the same way as outlined in Section 5.1.3 for 2D lattices. The elements used for the CET continuum are 8-node linearly interpolated, fully integrated, solid elements accessible through the ABAQUS element library. All simulations are carried out with ABAQUS/Standard 2019 (Dassault Systèmes Simulia Corp., Providence, RI, USA) with the micropolar continuum model using the implementation described in Section 4.1.2. Note that for the MC model, ABAQUS is used with its unsymmetric equation solution capability.

7.2.1 Methodology

Buckling as a bifurcation problem requires methods for leaving the trivial equilibrium solution path in order to access the postbuckling regime. This can be achieved by adding perturbations to the deformed configuration of the solution at the bifurcation point in an appropriate way, known as path-switching, e.g., [35], or using appropriate initial imperfections. In this thesis, initial imperfections are used to access the postbuckling regime. The imperfections are based on scaled eigenmodes of the corresponding eigenvalue problem of the discrete model. For the discrete model, the following analysis procedure is used, which consists of two individual analyses, (i) a buckling and (ii) a postbuckling analysis, respectively. For the continuum models, no buckling analysis is conducted as ABAQUS does not allow for this kind of analysis when user elements are

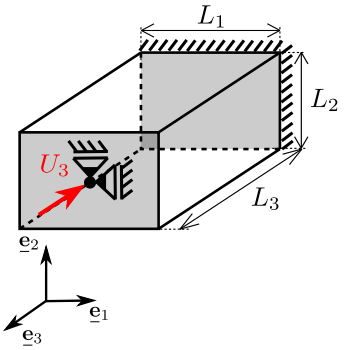

Figure 7.2: Schematic of the buckling load case with free surfaces in white and surfaces with boundary conditions applied in grey. The free surfaces are traction-free.

involved. The imperfections used are based on the results obtained from the buckling analysis of the discrete models.

The buckling analysis, represents a linear eigenvalue analysis with respect to a base state. In this work, the base state represents the undeformed configuration of the discrete model. The extracted eigenvalues correspond to load proportionality factors of a reference load, F_3^{ref}. The reference load is set to $F_3^{\text{ref}} = -1\,\text{N}$ with respect to the 3-axis. The critical load in 3-direction corresponding to the i^{th} eigenvalue, η_i, is estimated via

$$F_3^{*i} = \eta_i F_3^{\text{ref}} \quad . \tag{7.1}$$

In the postbuckling analysis, the postbuckling regime is accessed by imposing geometric imperfections onto the initial configuration. For the discrete models, these imperfections are based on the eigenmodes corresponding to the eigenvalues of the buckling analysis, further referred to as *eigenmode-affine imperfections*. The imperfections are applied to the undeformed FEM mesh through linear superposition of the extracted *eigenmodes* with the displacement

$$\underline{\boldsymbol{\Delta}} = \sum_{i=1}^{M} \xi_i \underline{\boldsymbol{H}}_i \quad , \tag{7.2}$$

where M is the number of eigenmodes taken into account, ξ_i corresponds to a proper scaling factor, and $\underline{\boldsymbol{H}}_i$ denotes the i^{th} eigenmode, which is normalized so that the maximum displacement component is 1. The scaling factors should be small enough such that the initial elastic response is not strongly influenced, but large enough to ensure access to the postbuckling regime. Note that only the displacement fields are used for the imperfection. Rotations are not taken into account.

For the continuum models, the eigenmodes of the discrete models serve as the basis for the imperfections, but with reduced information. Different procedures are required for the BCC and the PC lattice to superimpose the eigenmodes. For the BCC lattice, the displacement fields of all the base cell corner nodes are extracted and mapped onto the domain of the continuum model, i.e., are applied at the nodes of the continuum model showing the same coordinates. For meshes with element sizes smaller than the characteristic length of the lattice, i.e., $\mathcal{M} < 1$, linear interpolation is used. The procedure for the PC type lattice is different as there are no nodes of the discrete models coinciding with nodes of the continuum models when using, e.g., $\mathcal{M} = 1$. Therefore, the displacement fields of the MPBCs of the discrete models are extracted and directly mapped to the nodes of the continuum model associated with the corresponding base cell. For nodes that are associated with more than a single base cell, the mean value of all corresponding base cells is taken. These fields are then applied to the undeformed mesh of the continuum model, using linear interpolation if necessary, i.e., for $\mathcal{M} < 1$. Note that this procedure requires the boundary conditions to be enforced again, i.e., the displacement fields for the corresponding nodes must be set to zero accordingly.

For lattice structures manufactured by additive manufacturing, the mechanical response may be strongly influenced by imperfections based on the manufacturing process, such as deviations from the originally intended geometry or the original properties of the parent material, see, e.g., [99]. For investigating the capabilities of the model on capturing the mechanical response in the presence of such imperfections, geometric imperfections based on random radius deviations of struts are used. The radius of the lattice members corresponding to an individual base cell, j, of the lattice reads

$$r_j = r\xi\mathrm{r}_j \quad , \tag{7.3}$$

Table 7.6: Geometrical dimensions of the PC and BCC lattices studied for the postbuckling load case.

	N_1xN_2xN_3 (/)	$L_1 = L_2 = L_3/20$ in mm	l in mm	r in mm
PC	4x4x80	4	1	$l/20$
PC	8x8x160	8	1	$l/20$
BCC	4x4x80	4	1	$l\sqrt{3}/40$
BCC	8x8x160	8	1	$l\sqrt{3}/40$

Table 7.7: Identifiers and descriptions of imperfections, where L_1 is the overall length of the lattice in 1-direction and r is the radius of the lattice members of the geometrically perfect structure.

	description
Mi	eigenmode-affine imperfection with $\xi = i\%$ of $L_1 (= L_2)$
Ri	random-based imperfection with $\xi = i\%$ of r

where r is the radius of the geometrically perfect lattice member, ξ is a scaling factor, and r_j represents a function giving uniformly distributed numbers in the interval $[-1, +1]$. These imperfections are further referred to as *random-based imperfections*. The different radii used within individual base cells are directly applied through the cross-section definitions of the individual beam elements of the discrete models, whereas they are introduced on the level of the elasticity tensors for the continuum models, cf. Eq. (3.14) for PC and Eqs. (3.17)-(3.18) for the BCC lattices.

Note that for all postbuckling analyses a displacement controlled Newton-Raphson scheme is used.

7.2.2 Results and discussion

The configurations of the PC and the BCC lattices studied are summarized in Table 7.6. Critical loads and the corresponding eigenmodes are presented, which are estimated by buckling analyses of the discrete models. The post-buckling responses of discrete and continuum models is then compared for different imperfection types and amplitudes, see Table 7.7 for the notation used. The imperfection amplitudes used are given in the individual sections and are chosen to be as small as possible, but large enough to enable access to the post-buckling regime. Eigenmode-affine imperfections are used to study the postbuckling behavior of all configurations given in Table 7.6. Random-based imperfections are only applied to investigate the BCC lattice comprised of N_1xN_2xN_3 = 4x4x80 base cells.

Critical loads and corresponding eigenmodes

The eigenvalues of the buckling analyses of the discrete models are summarized in Table 7.8 and their corresponding eigenmodes are shown in Figures 7.3. The eigenvalues are equal to the critical loads except for the sign, since a reference load of $F_3^{\mathrm{ref}} = -1\,\mathrm{N}$ is used, cf. Eq. (7.1). The PC lattices show significantly higher critical loads compared to the BCC counterparts. For both BCC and PC lattices, the critical loads associated with the first and second as well as the third and fourth eigenvalues are the same, respectively. This also holds true for the overall characteristics of the corresponding eigenmodes, such as the wavelength. However, small differences in shape can be observed. As shown in Figures 7.3, the eigenmodes of the BCC (top) and PC (bottom) lattices are not aligned with a single global direction. They show displacements in

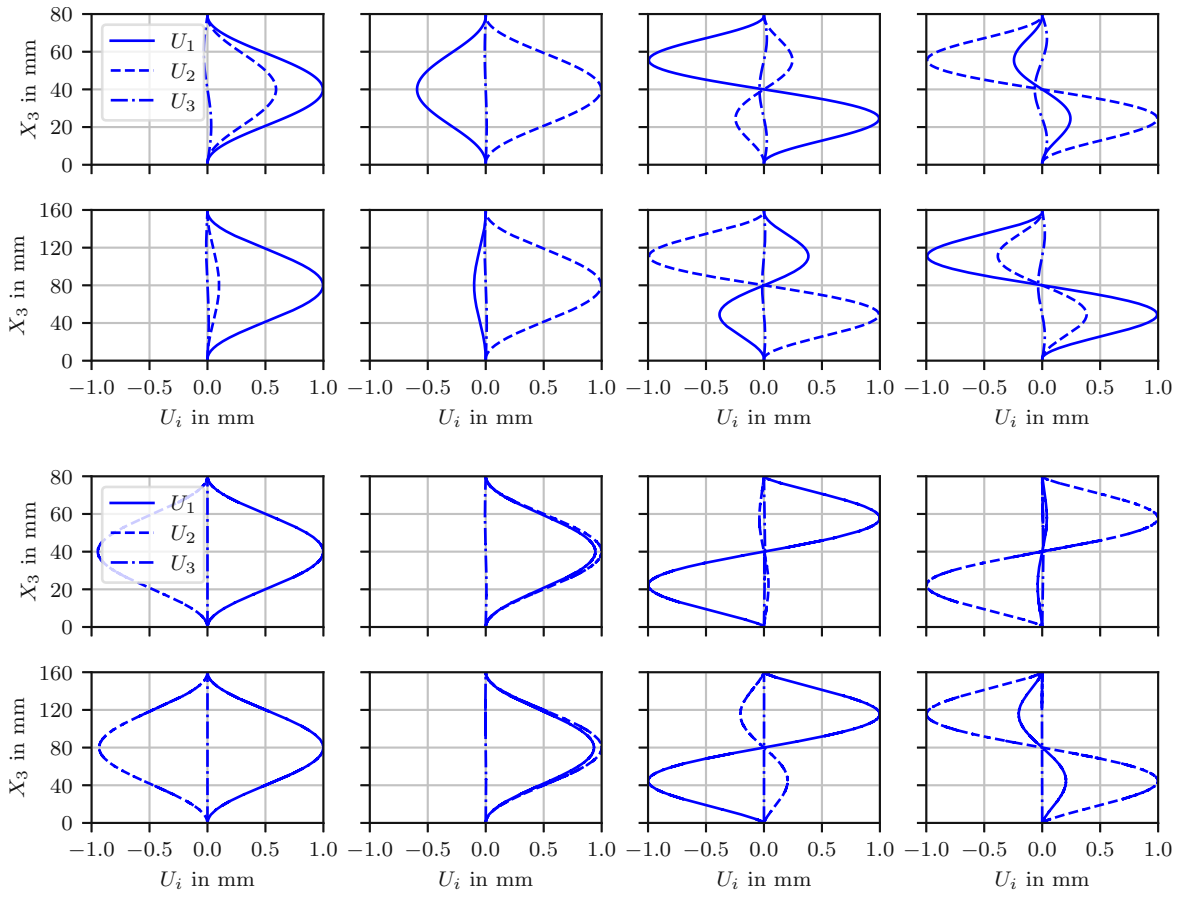

Figure 7.3: Displacements of MPBCs of discrete BCC (top) and PC lattices (bottom) comprised of N_1xN_2xN_3 = 4x4x80 (first and third row) and N_1xN_2xN_3 = 8x8x160 (second and fourth row) base cells representing the first (first column), second (second column), third (third column), and fourth eigenmode (fourth column). MPBCs are located at $X_1 = X_2 = L/2 - l/2$.

both directions perpendicular to the loading direction as indicated by the different amplitudes of the MPBCs displacements U_1 and U_2. For the BCC lattice, this is more pronounced for N_1xN_2xN_3 = 4x4x80 than for N_1xN_2xN_3 = 8x8x160 base cells. The PC lattice shows displacements in both directions independent of the number of base cells comprising the lattice. The deflection angle in the 1-2-plane is about $-45°$ for the first and 45° for the second eigenmode, i.e., $U_1 \approx -U_2$ and $U_1 \approx U_2$, respectively, cf. Figure 7.3 (bottom).

Table 7.8: The extracted eigenvalues η_i of the buckling analyses of the discrete model for a reference load of $F_3^{\text{ref}} = -1\,\text{N}$.

	N_1xN_2xN_3	$\eta_1 (= \eta_2)$	$\eta_3 (= \eta_4)$
BCC	4x4x80	2.72	5.62
BCC	8x8x160	10.76	22.23
PC	4x4x80	32.26	35.71
PC	8x8x160	134.67	149.91

Postbuckling behavior of BCC lattices

For the eigenmode-affine imperfections only the first eigenmode is used with an amplitude of 2% of $L_1(= L_2)$. The force-displacement curves of the two configurations of the BCC lattice are given in Figure 7.4. Considering the lattice comprised of N_1xN_2xN_3 = 4x4x80 base cells (left), the critical load is clearly overestimated by both the CC and the MC model and cannot even be captured for a discretization of $\mathcal{M} = 2$. Nevertheless, the continuum models are able to successfully enter the postbuckling regime and to qualitatively capture the stable postbuckling behavior of the lattice. For a lattice consisting of more base cells (right), i.e., N_1xN_2xN_3 = 8x8x160, the MC model using a discretization of $\mathcal{M} = 2$ is at least able to roughly estimate the critical load with a deviation of about 30% compared to the discrete model. The stable postbuckling behavior can be captured qualitatively well. For both lattices, the predictions of the CC model are slightly better than the ones of the MC model.

The displacement and rotation fields of the MPBCs of the BCC lattices are investigated for two different load levels, cf. Figure 7.5 for the lattice comprised of N_1xN_2xN_3 = 4x4x80 and Figure 7.6 for the lattice comprised of N_1xN_2xN_3 = 8x8x160 base cells. The load levels correspond to the critical load of each individual model (top) and to a displacement within the stable postbuckling regime (bottom). For the lattice comprised of N_1xN_2xN_3 = 4x4x80 base cells, the fields of the discrete and the MC models are in good qualitative agreement for both load levels. In the stable postbuckling regime, the discretization of $\mathcal{M} = 2$ yields fields that are also quantitatively in good agreement with those of the discrete models. When considering N_1xN_2xN_3 = 8x8x160 base cells comprising the lattice, the fields obtained by the MC model with $\mathcal{M} = 2$ are in very good agreement with the discrete model, with the exception of the displacement U_2. The CC model also shows similar results as those obtained from the other models, except for the rotation field, which cannot be provided by this model.

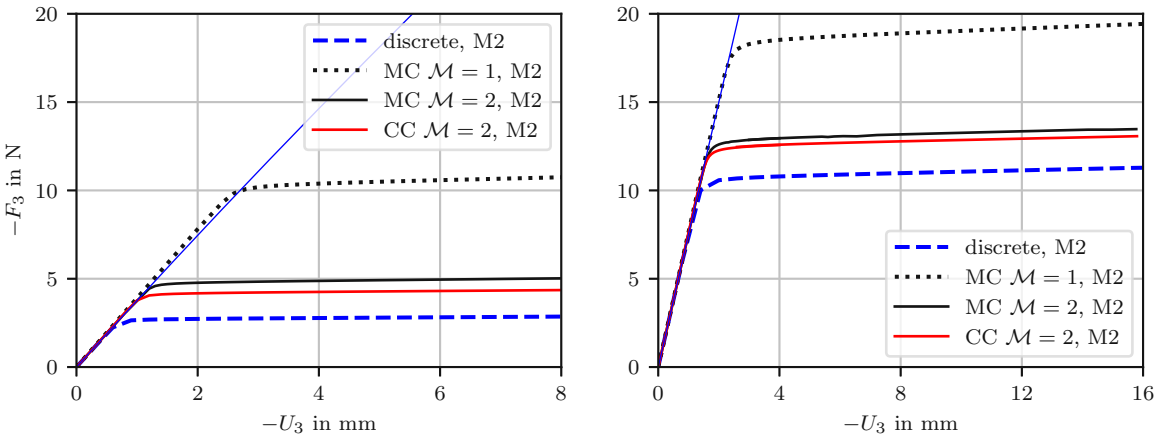

Figure 7.4: Force-displacement curves of the postbuckling analysis of BCC lattices comprised of N_1xN_2xN_3 = 4x4x80 (left) and N_1xN_2xN_3 = 8x8x160 base cells (right). The thin solid lines represent the trivial equilibrium paths of the discrete models.

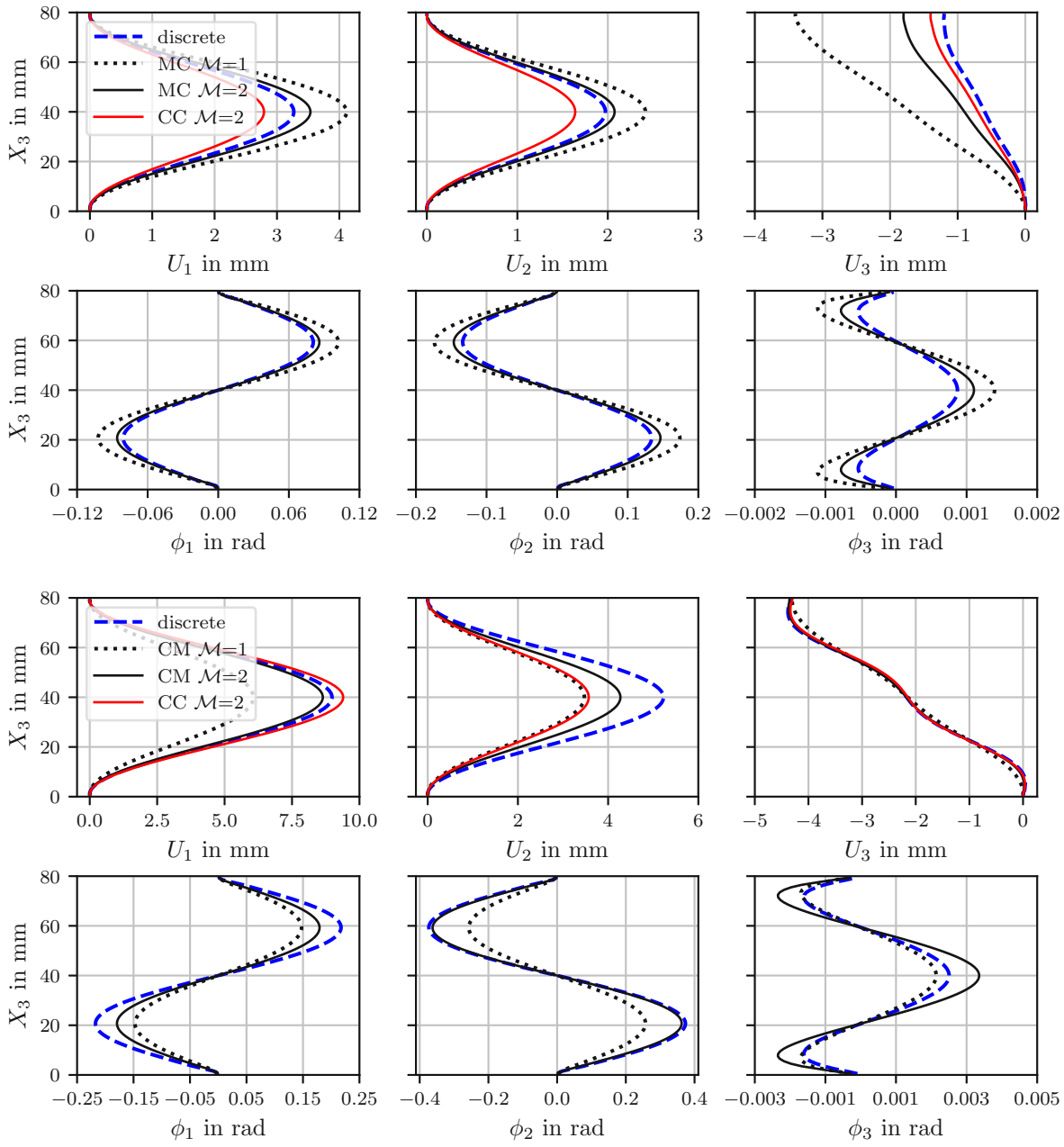

Figure 7.5: Displacements U_i and rotations ϕ_i of MPBCs of the BCC lattice with N_1xN_2xN_3 = 4x4x80 base cells of the discrete and the continuum model using discretizations of $\mathcal{M} = 1$ and $\mathcal{M} = 2$ for loads corresponding approximately to the critical load of each model (top), i.e., $U_3 \approx -1.2\,\text{mm}$ for the discrete model, $U_3 \approx -3.4\,\text{mm}$ for MC $\mathcal{M} = 1$, $U_3 \approx -1.8\,\text{mm}$ for MC $\mathcal{M} = 2$, and $U_3 \approx -1.4\,\text{mm}$ for CC $\mathcal{M} = 2$. The displacements and rotations in the stable postbuckling regime are evaluated at $U_3 \approx 4.3\,\text{mm}$ for all models (bottom). Results for MPBCs located at $X_1 = X_2 = L/2 - l/2 = 1.5\,\text{mm}$ are shown.

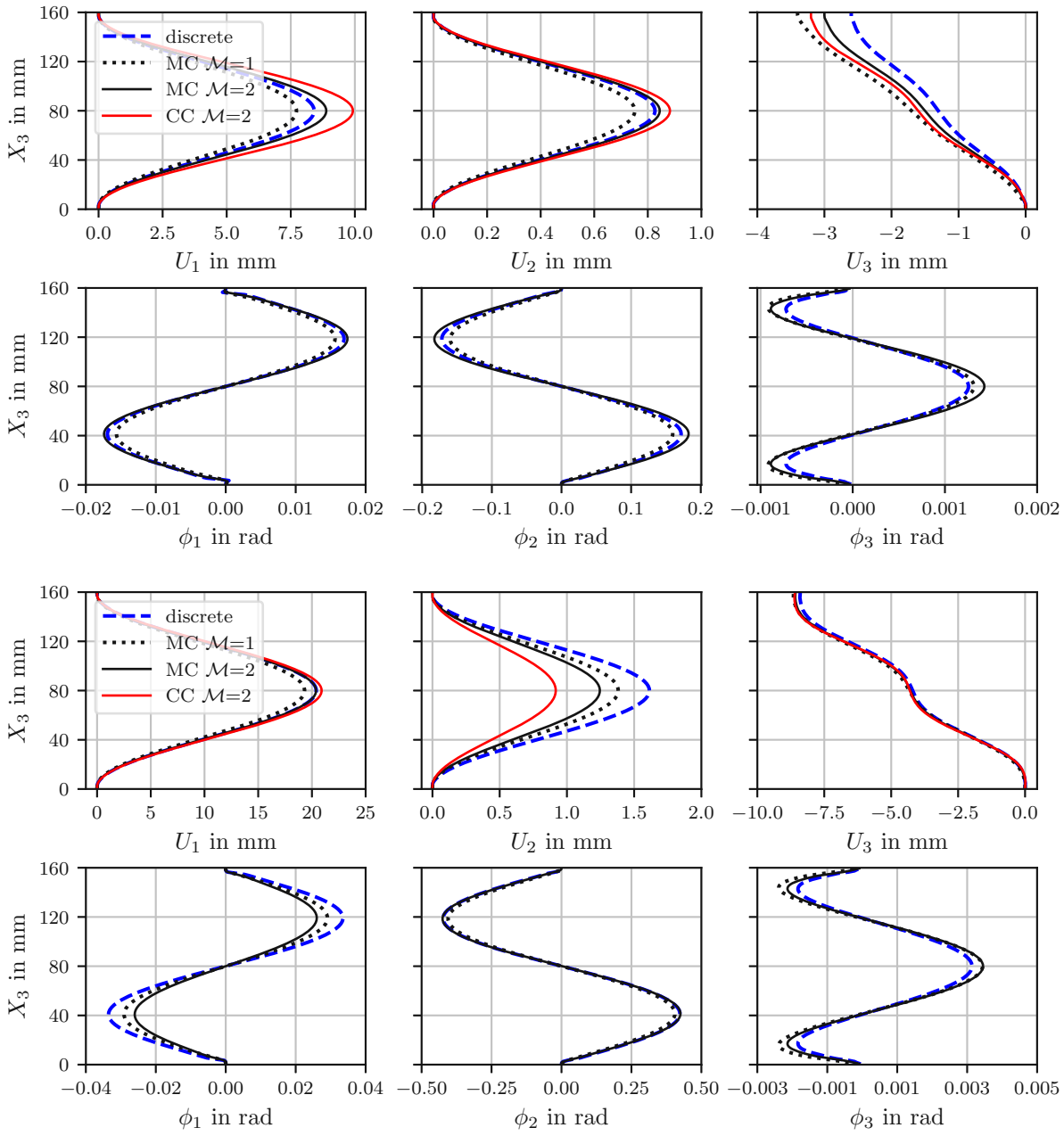

Figure 7.6: Displacements U_i and rotations ϕ_i of MPBCs of the BCC lattice with N_1xN_2xN_3 = 8x8x160 base cells of the discrete and the continuum model using discretizations of $\mathcal{M} = 1$ and $\mathcal{M} = 2$ for loads corresponding approximately to the critical load of each model (top), i.e., $U_3 \approx -2.6\,\text{mm}$ for the discrete model, $U_3 \approx -3.4\,\text{mm}$ for MC $\mathcal{M} = 1$, $U_3 \approx -3\,\text{mm}$ for MC $\mathcal{M} = 2$, and $U_3 \approx -3.2\,\text{mm}$ for CC $\mathcal{M} = 2$. The displacements and rotations in the stable postbuckling regime are evaluated at $U_3 \approx 8.5\,\text{mm}$ for all models (bottom). Results for MPBCs located at $X_1 = X_2 = L/2 - l/2 = 3.5\,\text{mm}$ are shown.

For the random-based imperfections, three different imperfections are used, which are denoted by ID1, ID2, and ID3. The imperfection amplitudes for ID1 and ID3 are up to 10% of the radius r whereas ID2 shows amplitudes up to 20% of r. Before discussing the postbuckling behavior of the models, the critical loads of the corresponding discrete models are estimated based on buckling analyses, which are summarized in Table 7.9. Contrary to the geometrically perfect lattice, the first and second eigenvalue of each of the three geometrically imperfect counterparts are not equal, which is also true for the third and fourth eigenvalue. However, these differences are small in magnitude and the differences compared to those obtained for the geometrically perfect counterpart are not significant. The corresponding eigenmodes are displayed in Figure 7.7 showing the same overall characteristics as the geometrically perfect counterparts, cf. Figure 7.3, e.g., the same wavelength. However, the angular deviations in the 1-2-plane are different for each imperfection studied, which already indicates that the imperfections strongly influence the deformation state in the postbuckling regime.

The force-displacement curves of all three random-based imperfect lattices are shown in Figure 7.8. The critical loads for all lattices correspond to the first or second critical load, which hardly differ from each other, cf. Table 7.9. To further study the postbuckling response, all three random-based imperfect lattices are evaluated along the 3-direction at $X_1 = X_2 = L_1/2 - l/2$ in terms of displacements and rotations, see

Table 7.9: The extracted eigenvalues η_i of the buckling analyses of the discrete model for a reference load of $F_3^{\text{ref}} = -1\,\text{N}$ and using random-based imperfections with ID denoting its identifier.

	η_1	η_2	η_3	η_4
ID1	2.721	2.755	5.567	5.636
ID2	2.722	2.735	5.735	5.772
ID3	2.736	2.766	5.627	5.684

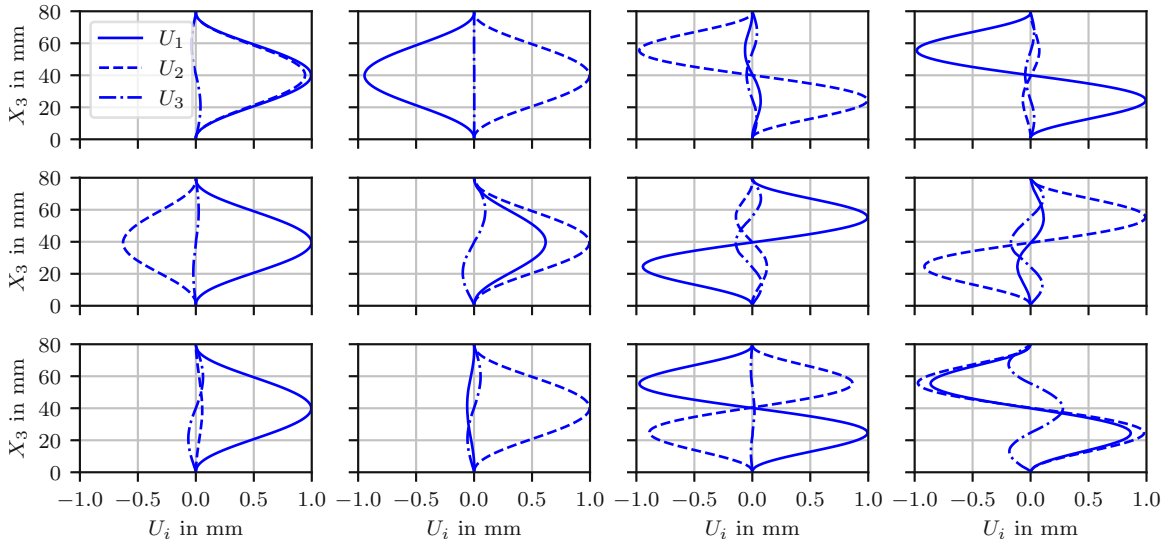

Figure 7.7: Displacements of MPBCs of discrete BCC lattices comprised of N_1xN_2xN_3 = 4x4x80 base cells for random-based imperfections ID1 (first row), ID2 (second row), and ID3 (third row) representing the first (first column), second (second column), third (third column), and fourth eigenmode (fourth column). Results for MPBCs located at $X_1 = X_2 = L/2 - l/2 = 1.5\,\text{mm}$ are shown.

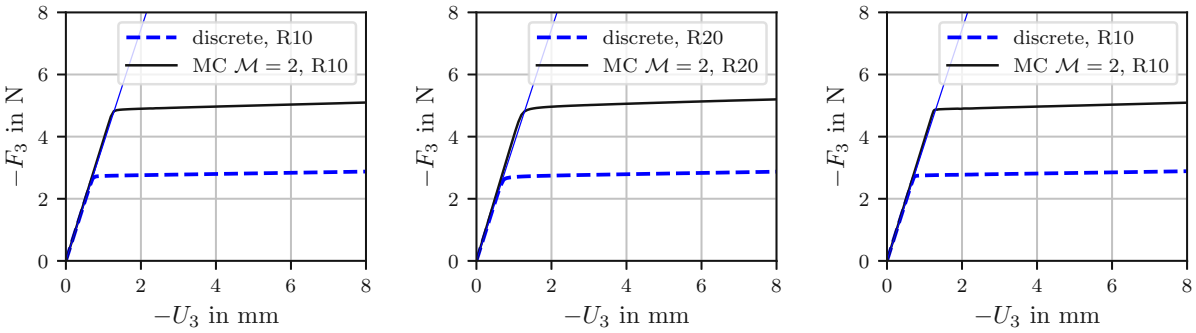

Figure 7.8: Force-displacement curves of the postbuckling analysis of BCC lattices comprised of N_1xN_2xN_3 = 4x4x80 base cells for different random-based imperfections, namely, ID1 (left), ID2 (center), and ID3 (right). The thin solid lines represent the trivial equilibrium paths of the discrete models.

Figure 7.9 for ID1, Figure 7.10 for ID2, and Figure 7.11 for ID3. The displacements and rotations are given for two different loading states, namely, approximately at the corresponding critical load as well as at a displacement load within the stable postbuckling regime. Note that for random-based imperfections, the CC model is not considered for comparison.

For ID1, the deformation of the MC model approximately coincides with the first eigenmode of the perfect lattice, cf. Figures 7.3 (top) and 7.9 (top). The eigenmodes of the imperfect discrete model do not coincide with any of the eigenmodes extracted for the perfect (Figure 7.3) or for the imperfect lattice (Figure 7.7). The deformation state of the imperfect discrete model shows a deflection angle of about $-115°$ with respect to the 1-axis in the 1-2-plane. However, the overall characteristics are the same. The differences may be caused by local effects that can only be captured by the discrete model. It is expected that if the buckling analysis is carried out with the imperfect lattice being preloaded close to the critical load, the same deformation will be predicted. The same deviations are observed for the rotations as expected. The postbuckling responses of both discrete and MC models are stable as displacements and rotations keep their overall characteristics also for the higher load level, which has already been indicated by the force-displacement curve given in Figure 7.8 (left).

For ID2, both the displacements and the rotations of the discrete and MC model show the same characteristics for both load levels with some deviations regarding the deflection angle. For the higher loading, the deviations decrease and the deformations are in good agreement, cf. Figure 7.10 (bottom). The deformation shapes of both models do not coincide with any of the eigenmodes displayed in Figure 7.7 (center). The deformations of the discrete model clearly show in the opposite direction of the first eigenmode of the imperfect lattice. Since the discrete and MC models show similar deformation states, the MC model also seems to be able to partially capture local geometric changes before reaching the critical load, resulting in a different deformation shape than predicted by the linear eigenvalue analysis of the unloaded structure.

For ID3, both the displacements and the rotations of the discrete and MC model are in good agreement for both load levels, cf. Figure 7.11. The displacement U_2 and the rotation ϕ_1 are small in magnitude compared to their in-plane counterparts U_1 and ϕ_2 and, hence, the differences between discrete and MC model can be considered acceptable. The deformation shapes of both discrete and MC model approximately coincide with the first eigenmode of the imperfect lattice.

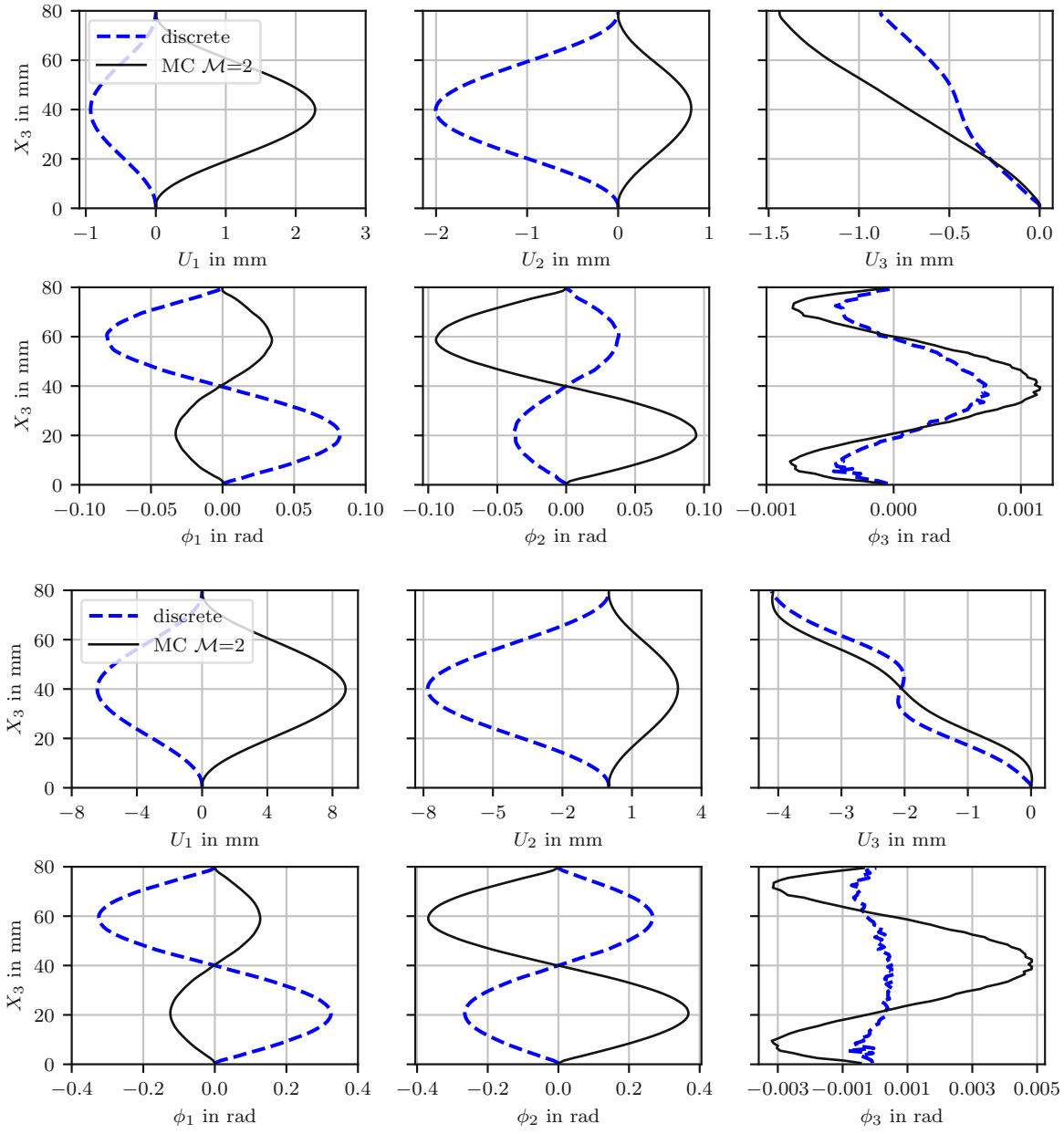

Figure 7.9: Imperfection ID1 - Displacements U_i and rotations ϕ_i of MPBCs of BCC lattice with N_1xN_2xN_3 = 4x4x80 base cells of the discrete and the MC model using a discretization $\mathcal{M} = 2$ for loads corresponding approximately to the critical load of each model (top), i.e., $U_3 \approx -0.9\,\text{mm}$ for the discrete and $U_3 \approx -1.4\,\text{mm}$ for MC $\mathcal{M} = 2$ model. The displacements and rotations in the stable postbuckling regime are evaluated at $U_3 \approx 4\,\text{mm}$ for all models (bottom). Results for MPBCs located at $X_1 = X_2 = L/2 - l/2 = 1.5\,\text{mm}$ are shown.

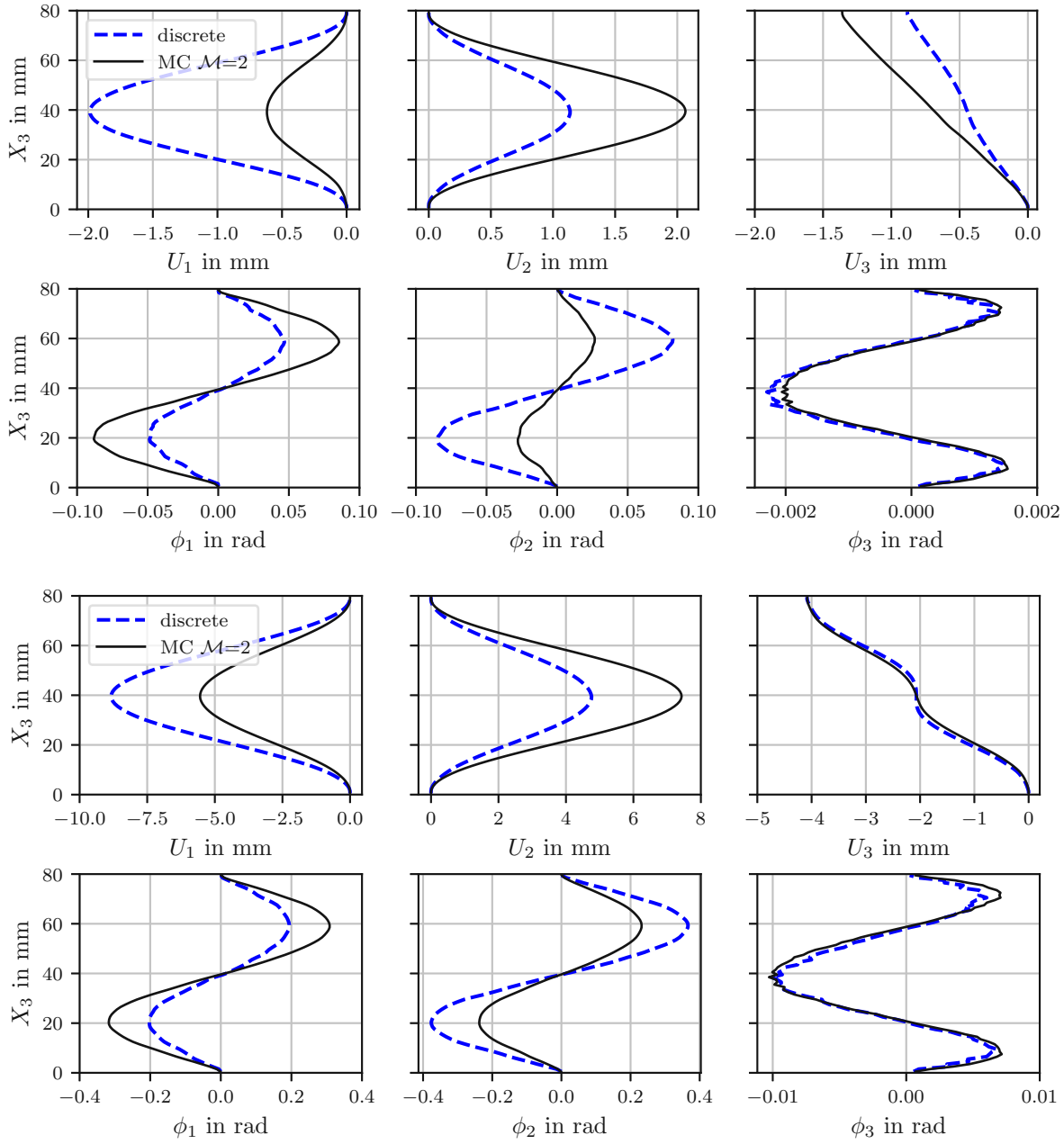

Figure 7.10: Imperfection ID2 - Displacements U_i and rotations ϕ_i of MPBCs of BCC lattice with N_1xN_2xN_3 = 4x4x80 base cells of the discrete and the MC model using a discretization $\mathcal{M} = 2$ for loads corresponding approximately to the critical load of each model (top), i.e., $U_3 \approx -0.9\,\text{mm}$ for the discrete and $U_3 \approx -1.4\,\text{mm}$ for MC $\mathcal{M} = 2$ model. The displacements and rotations in the stable postbuckling regime are evaluated at $U_3 \approx 4\,\text{mm}$ for all models (bottom). Results of MPBCs located at $X_1 = X_2 = L/2 - l/2 = 1.5\,\text{mm}$ are shown.

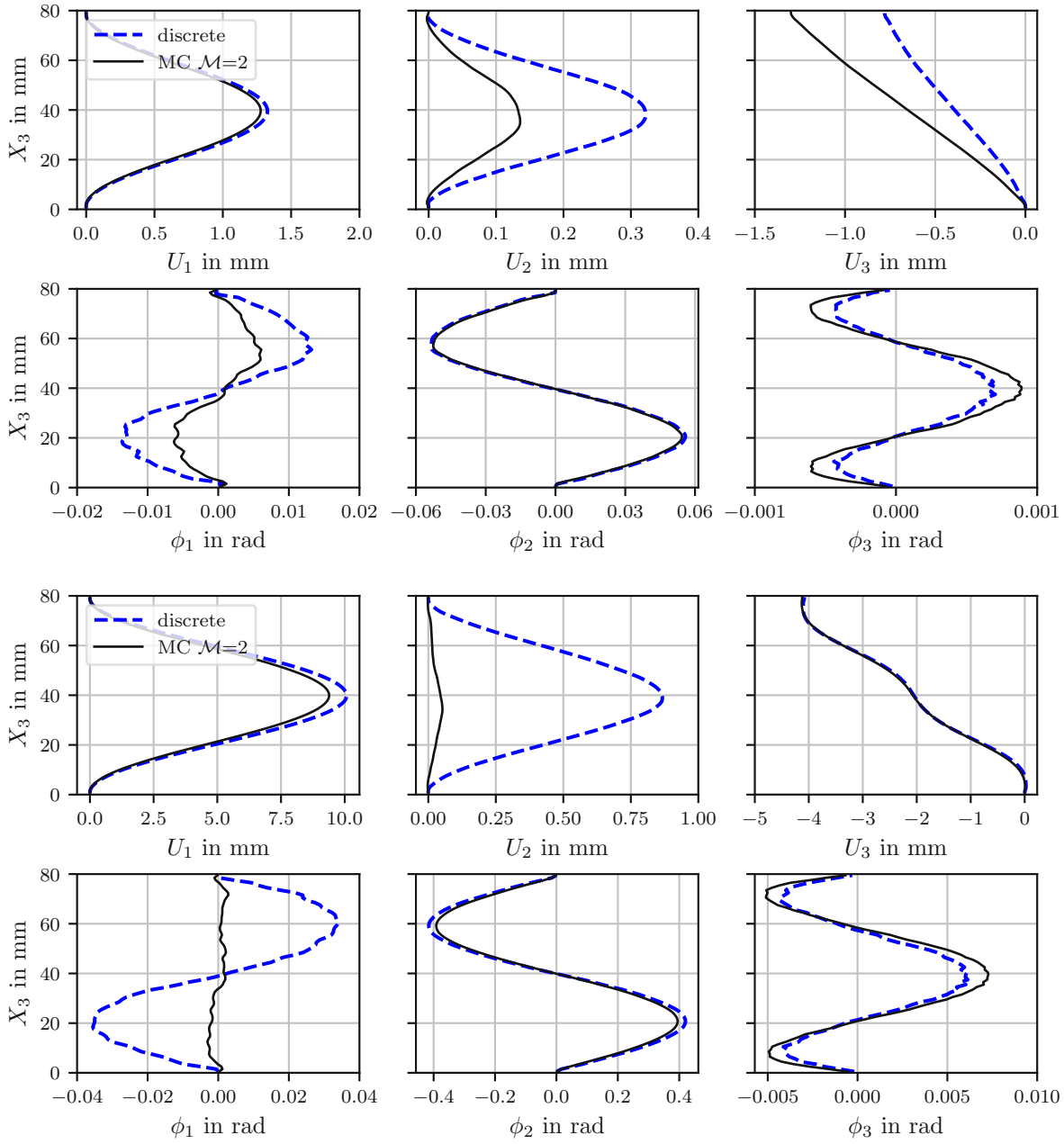

Figure 7.11: Imperfection ID3 - Displacements U_i and rotations ϕ_i of MPBCs of BCC lattice with N_1xN_2xN_3 = 4x4x80 base cells of the discrete and the MC model using a discretization $\mathcal{M} = 2$ for loads corresponding approximately to the critical load of each model (top), i.e., $U_3 \approx -0.8\,\text{mm}$ for the discrete and $U_3 \approx -1.3\,\text{mm}$ for MC $\mathcal{M} = 2$ model. The displacements and rotations in the stable postbuckling regime are evaluated at $U_3 \approx 4\,\text{mm}$ for all models (bottom). Results for MPBCs located at $X_1 = X_2 = L/2 - l/2 = 1.5\,\text{mm}$ are shown.

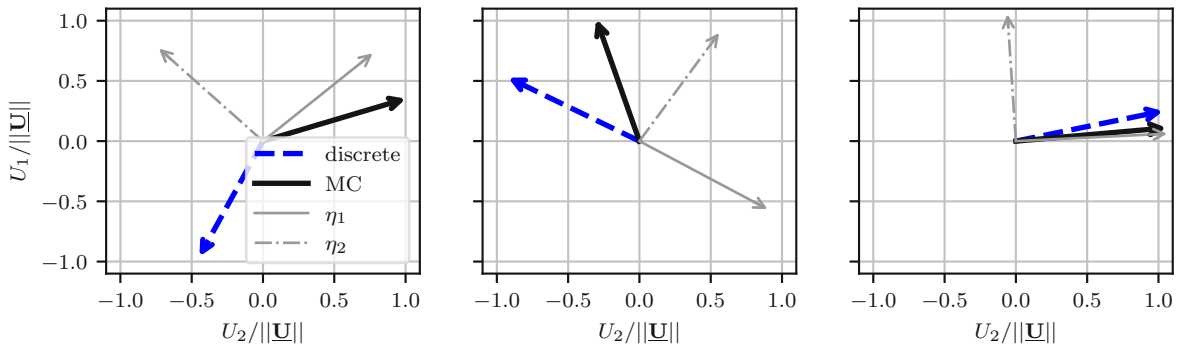

Figure 7.12: Normalized displacement vectors in the 1-2-plane at $X_1 = X_2 = L/2 - l/2 = 1.5\,\text{mm}, X_3 = L_3/2 - l/2 = 39.5\,\text{mm}$ evaluated approximately at the corresponding critical load of each model indicate the directions of the deformations of ID1 (left), ID2 (center), and ID3 (right) for both discrete and continuum models. The grey thin lines indicate the directions of the eigenmodes of the imperfect discrete models based on the linear eigenvalue analyses.

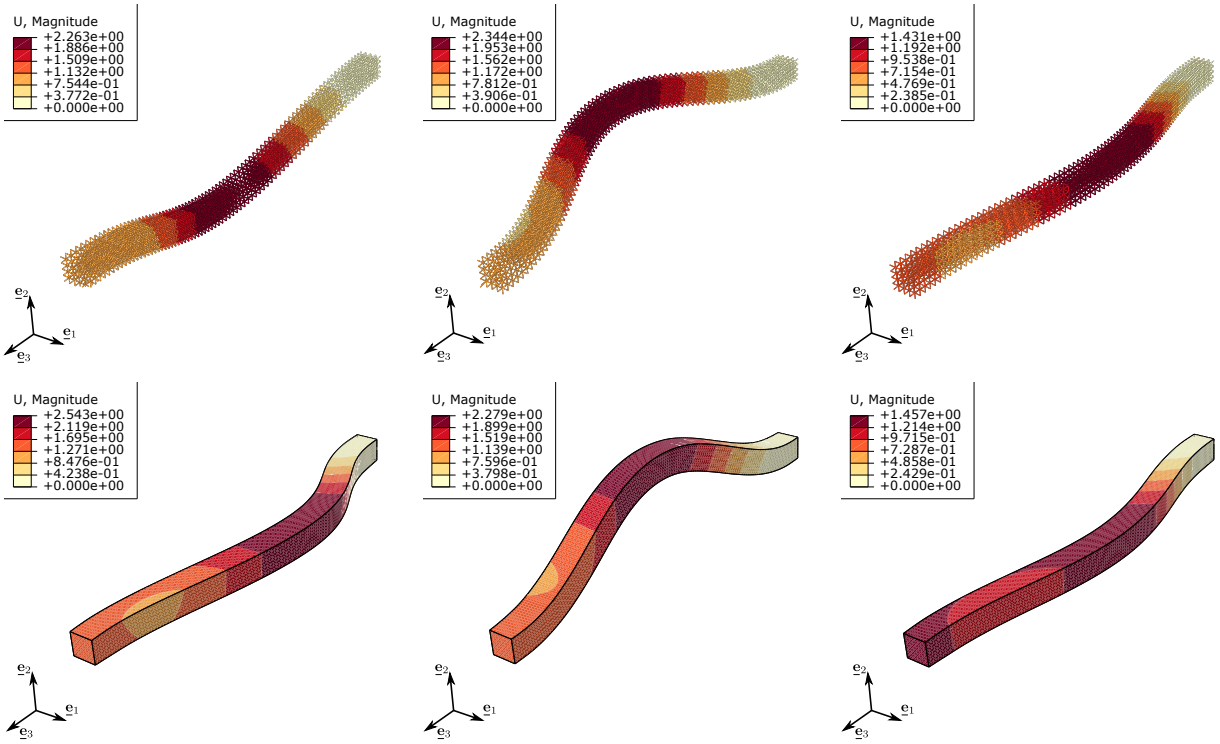

Figure 7.13: Contour of displacement magnitudes for loads that correspond approximately to the critical load of each model of ID1 (left), ID2 (center), and ID3 (right) for both discrete (top) and continuum models (bottom) with deformation scale factors of five.

For a better overview on the directions of the deformations of all models, the normalized displacement vectors in the 1-2-plane at $X_1 = X_2 = L/2 - l/2 = 1.5\,\text{mm}, X_3 = L_3/2 - l/2 = 39.5\,\text{mm}$ are shown in Figure 7.12 for ID1 (left), ID2 (center), and ID3 (right) for both discrete and continuum models. The normalized displacement vectors have been evaluated for loads that correspond approximately to the critical load of

each model. Additionally, the normalized displacements of the imperfect discrete models based on the linear eigenvalue analyses are given for comparison. The corresponding contour plots are shown in Figure 7.13.

Postbuckling behavior of PC lattices

The eigenmode-affine imperfections used for the PC lattices are only based on the first eigenmode with an amplitude of about 4% of $L_1(= L_2)$ for the discrete model and of 10% for the continuum models. For the continuum models, higher amplitudes were found to be necessary for entering the postbuckling regime. This is caused by the missing or reduced information available for the imperfections, which are only based on the displacements from the MPBCs of the discrete lattice model.

The force-displacement curves of the two configurations of the PC lattice are given in Figure 7.14. For N_1xN_2xN_3 = 4x4x80 base cells comprising the lattice (left), the MC models for both discretizations overestimate the critical load of the discrete model by about 25%. The response of the models is almost the same for both discretizations $\mathcal{M} = 1$ and $\mathcal{M} = 2$. Interestingly, the MC models are not only able to enter the postbuckling regime once the critical load is reached, but also to capture the unstable postbuckling response of the lattice, which is indicated by the negative slope of the curve. It is worth noting that the convergence behavior for obtaining a solution for the discrete models is very sensitive to the imperfection amplitude used, e.g., no converged solution for an imperfection of exactly 4% of $L_1(= L_2)$ is obtained while for 3.8% it is. Unfortunately, no converged solution is found for the discrete model of the lattice comprised of N_1xN_2xN_3 = 8x8x160 base cells (right). In contrast, the MC models show very good convergence behavior. Note that for $\mathcal{M} = 2$, the solution has been stopped manually due to time constraints. The critical load is estimated quite well by the MC models with deviations of about 10% compared to the last solution obtained for the discrete model. Comparing the MC models to their CC counterparts, they show a more compliant response and are in better agreement with the results of the discrete models. Furthermore, the CC models show convergence issues in the unstable postbuckling regime. For the N_1xN_2xN_3 = 8x8x160 lattice and using a discretization of $\mathcal{M} = 2$, the CC model is not able to enter the postbuckling regime for the same imperfection amplitude as used for its MC counterpart.

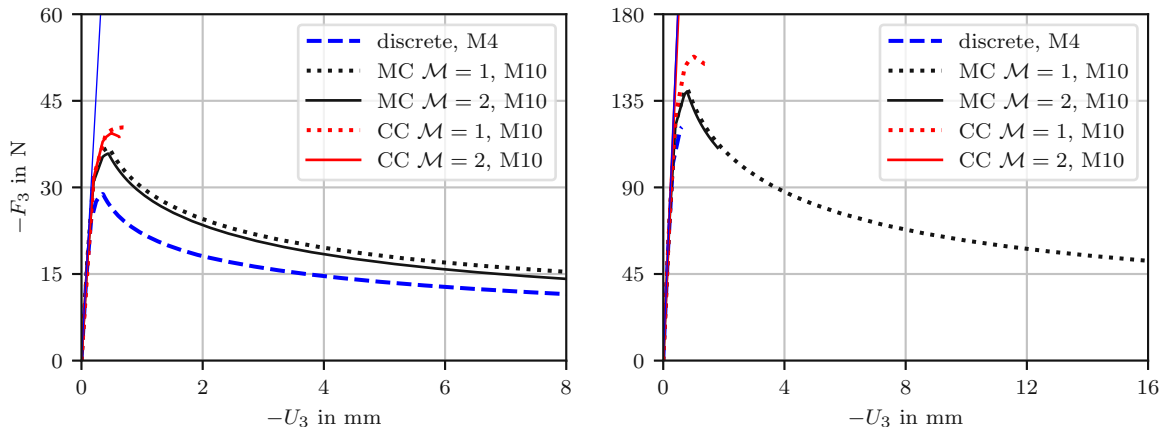

Figure 7.14: Force-displacement curves of the postbuckling analysis of PC lattices comprised of N_1xN_2xN_3 = 4x4x80 (left) and N_1xN_2xN_3 = 8x8x160 base cells (right). The thin solid lines represent the trivial equilibrium paths of the discrete models.

To further study the postbuckling behavior of the PC lattices, the displacements and rotations of the MPBCs of the PC lattices are given over the height in 3-direction and are investigated for different load levels, cf. Figure 7.15 for the lattice comprised of N_1xN_2xN_3 = 4x4x80 base cells and Figure 7.17 for N_1xN_2xN_3 = 8x8x160. The MPBCs are located at one of the center columns of the lattice, namely, at $X_1 = X_2 = L/2-l/2$. For the lattice N_1xN_2xN_3 = 4x4x80, two load levels are shown corresponding to the critical load of each individual model (top) and to a displacement of $U_3 \approx 1.6\,\mathrm{mm}$ (bottom), where the latter belongs to the unstable postbuckling behavior. At the critical load (top), the fields obtained by the MC model are in qualitative agreement with those of the discrete counterpart, except for the rotation ϕ_3, which is related to torsion. The deformation shapes of the models are in agreement with the first eigenmode, cf. Figure 7.3, which indicates that the procedure for applying the eigenmode-affine imperfections to the continuum models works. In the unstable postbuckling regime, the fields of the continuum model and the discrete model are starting to diverge qualitatively from each other, which can especially be seen for the displacements U_1 and U_2. This means that at some point the mechanisms driving the unstable postbuckling behavior cannot be captured anymore. These mechanisms seems to be mainly based on local instabilities at $X_3 \approx L_3/2$ and close to the boundaries at $X_3 \approx 5l$ and $X_3 \approx L_3 - 5l$, cf. Figure 7.15 (bottom) for displacements U_1 and U_2. The MC model cannot capture such instabilities in the current form. From a continuum point of view, this is related to the finite strain regime, where a fully nonlinear MC continuum model is necessary to account for such instabilities. For the lattice materials investigated in this work, these strains are related to the effective response of the lattice structure and are governed by large displacements or finite rotations of the underlying microstructure rather than to material nonlinearities of the parent material. Interestingly, the rotations ϕ_1 and ϕ_2 can be partly captured by the continuum model in a qualitative manner. Note that for higher load levels, the fields diverge further while keeping their overall characteristics shown in Figure 7.15 (bottom). This is not explicitly shown for the sake of brevity. For the lattice N_1xN_2xN_3 = 8x8x160, the displacements and rotations of the MPBCs are only evaluated at the critical loads due to the convergence issues of the discrete model at higher load levels. The MC models are in qualitative agreement with the discrete counterpart, except for the rotation ϕ_3. However, these differences can be considered negligible compared to the other rotations. Again, the fields are already fully resolved for the coarse discretization $\mathcal{M} = 1$. Interestingly, the CC model using a discretization of $\mathcal{M} = 2$ shows a deformation shape neither corresponding to the first nor to the second eigenmode. For a better overview on the deformations, contour plots of the displacement and rotation magnitudes are shown in Figure 7.16.

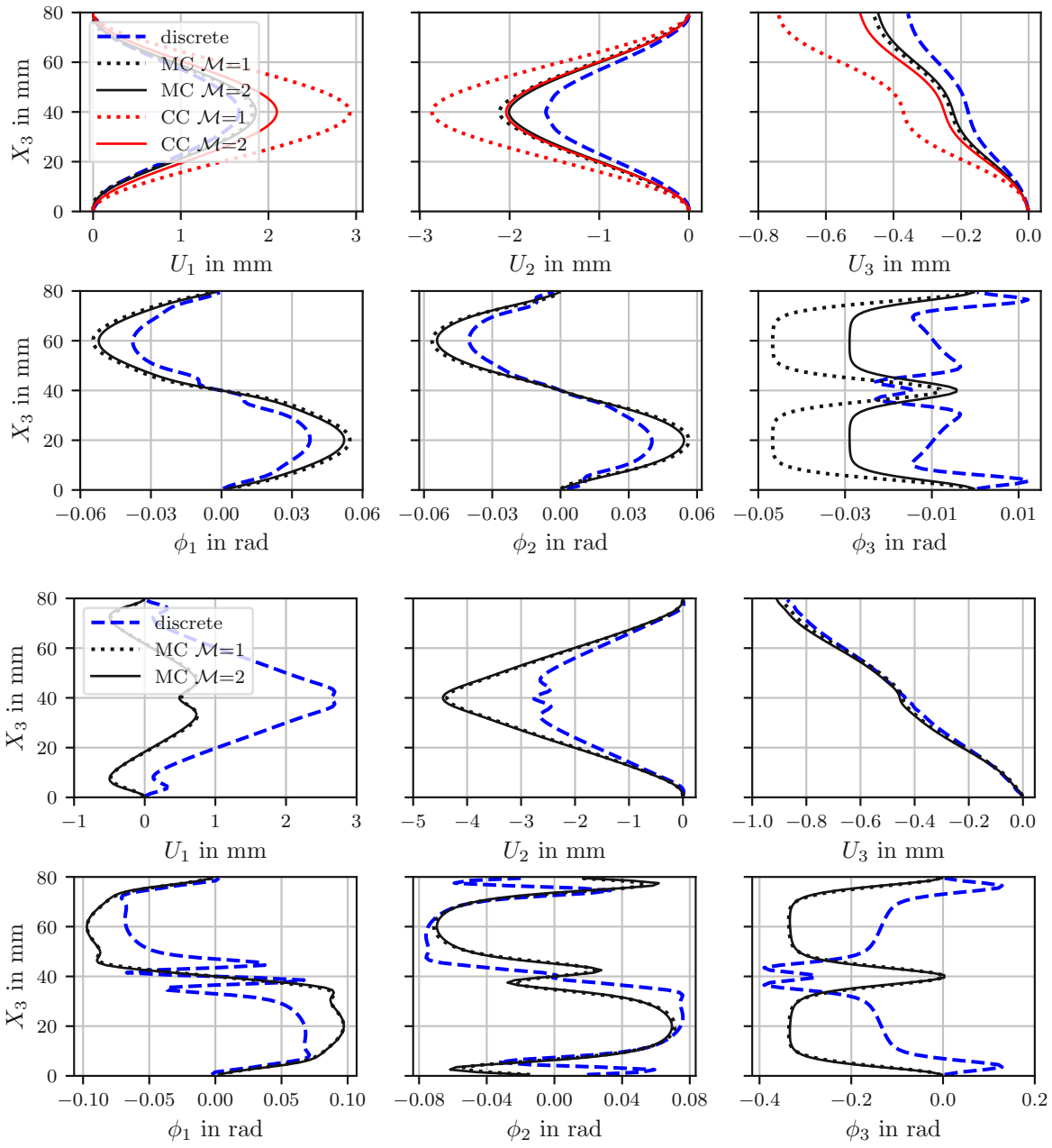

Figure 7.15: Displacements U_i and rotations ϕ_i of MPBCs of PC lattice with N_1xN_2xN_3 = 4x4x80 base cells of the discrete and the continuum model using discretizations of $\mathcal{M} = 1$ and $\mathcal{M} = 2$ for loads corresponding approximately to the critical load of each model (top), i.e., $U_3 \approx -0.35\,\text{mm}$ for the discrete model, $U_3 \approx -0.46\,\text{mm}$ for MC $\mathcal{M} = 1$, $U_3 \approx -0.44\,\text{mm}$ for MC $\mathcal{M} = 2$, $U_3 \approx -0.74\,\text{mm}$ for CC $\mathcal{M} = 1$, and $U_3 \approx -0.5\,\text{mm}$ for CC $\mathcal{M} = 2$. The displacements and rotations in the postbuckling regime are evaluated at $U_3 \approx 0.9\,\text{mm}$ for discrete and MC models (bottom). Results for MPBCs located at $X_1 = X_2 = L/2 - l/2 = 1.5\,\text{mm}$ are shown.

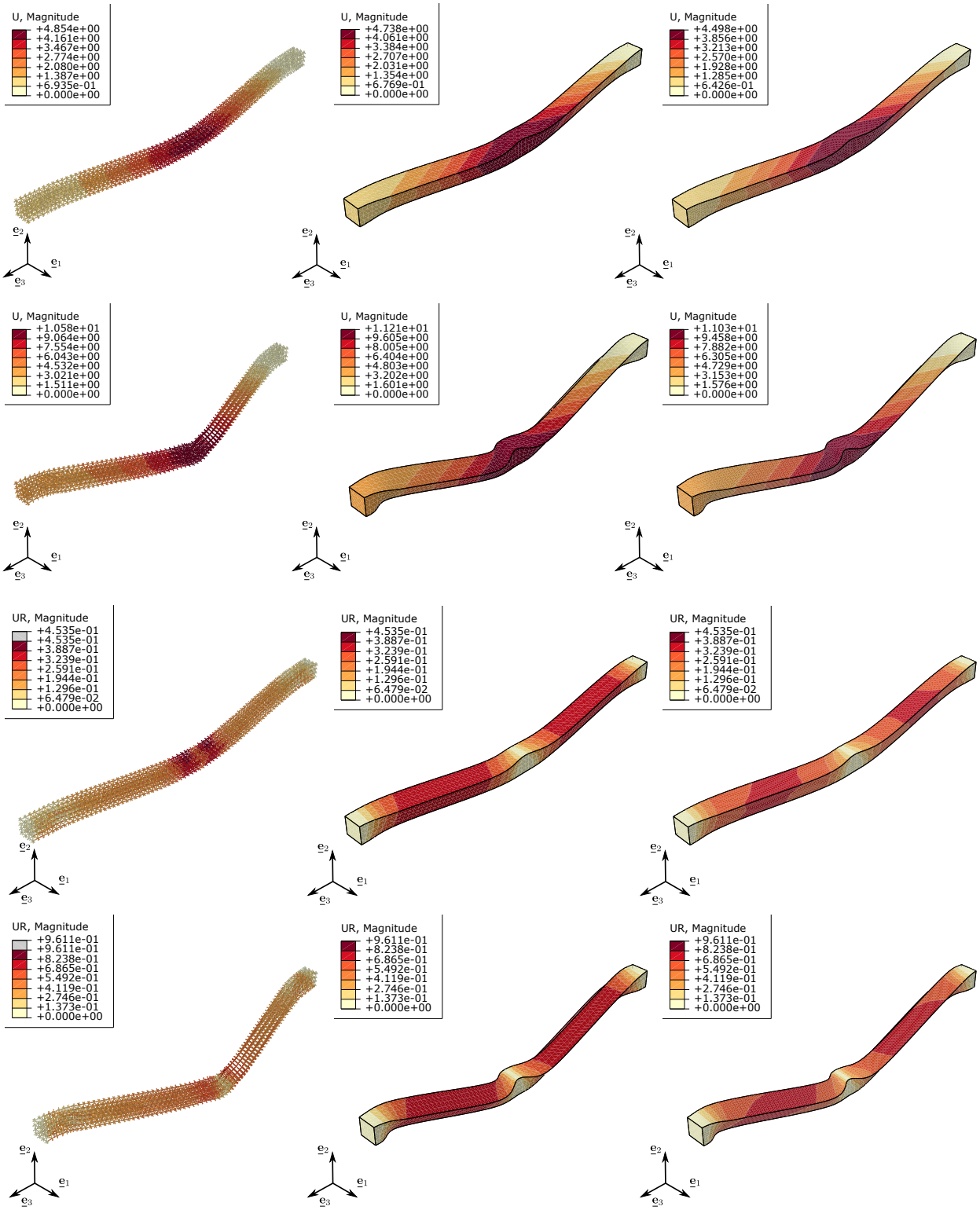

Figure 7.16: Contours of displacement magnitudes U (first and second row) and rotation magnitudes ϕ (third and fourth row) of the PC lattice with N_1xN_2xN_3 = 4x4x80 base cells. Results of the discrete (left) and the MC models using discretizations of $\mathcal{M} = 1$ (center) and $\mathcal{M} = 2$ (right) are shown. The displacement and rotation magnitudes are evaluated at $U_3 \approx -0.9\,\text{mm}$ (first and third row) and $U_3 \approx -4\,\text{mm}$ (second and fourth row). Note that the rotation magnitudes of the MC models are scaled to the rotation magnitude of the discrete models.

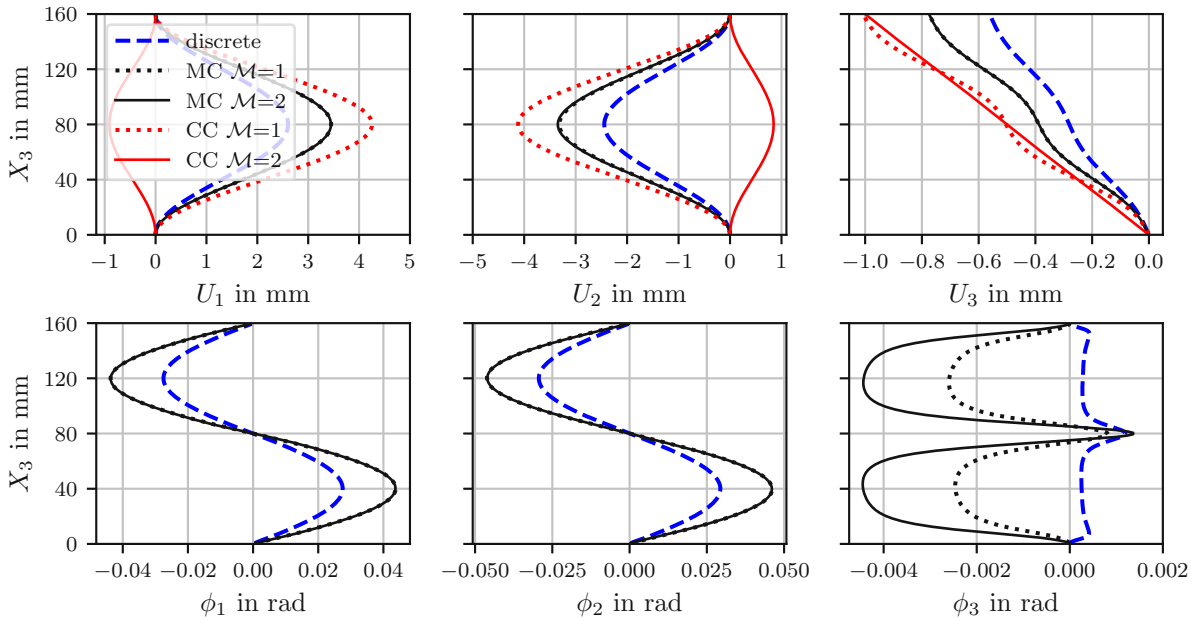

Figure 7.17: Displacements U_i and rotations ϕ_i of MPBCs of PC lattice with N_1xN_2xN_3 = 8x8x160 base cells of the discrete and the continuum model using discretizations of $\mathcal{M} = 1$ and $\mathcal{M} = 2$ corresponding to the critical load of each model, i.e., $U_3 \approx -0.57\,\text{mm}$ for the discrete model, $U_3 \approx -0.75\,\text{mm}$ for MC $\mathcal{M} = 1$ and $\mathcal{M} = 1$, and $U_3 \approx -1\,\text{mm}$ for CC $\mathcal{M} = 1$ and $\mathcal{M} = 2$. Results for MPBCs located at $X_1 = X_2 = L/2 - l/2 = 3.5\,\text{mm}$ are shown.

Computation time

The computational performance of all the models is of further interest and, therefore, the computation time and the number of user defined nodes of each model are summarized in Table 7.10. For practical reasons, the number of user defined nodes is given instead of the DOFs of the model, which provides a good estimate of the number of DOFs anyway. In contrast to the six DOFs per node of the discrete and the MC models, the CC model has only three DOFs per node. The basis for the evaluation are the postbuckling simulations using eigenmode-affine imperfections of both BCC and PC lattices. All simulations are conducted on a single core (1 CPU) of a standard workstation.

For the BCC lattice 4x4x80, the CC model shows a lower computation time than the corresponding discrete model by a factor ≈ 2.8 while for the BCC lattice 8x8x160 it shows higher computation times by a factor of ≈ 2. For the PC lattice, no convergence is achieved with the CC model. In contrast, the MC model shows good convergence behavior for both lattice types. However, the MC models are outperformed by the corresponding discrete models for all the lattices studied even though they show a smaller number of nodes, i.e., fewer DOFs. For coarse discretizations of the MC model, i.e., MC $\mathcal{M} = 1$, the differences are acceptable while for fine discretizations, i.e., MC $\mathcal{M} = 2$, the differences are significant, which is a result of the large number of nodes used for the MC model.

Furthermore, the computation times of simulations in the prebuckling regime are studied using a predefined number of increments. The basis for the evaluation is the BCC 8x8x160 lattice using the discrete, MC $\mathcal{M} = 1$, MC $\mathcal{M} = 2$, and CC $\mathcal{M} = 2$ models, where the number of nodes can be found in Table 7.10. Additionally, the symmetric equation solution procedure is used for the MC models. Simulations are conducted using a

Table 7.10: Number of user defined nodes and computation time of each model for the postbuckling simulations based on the eigenmode-affine imperfections, where a single core (1 CPU) of a standard workstation is used. The superscript * denotes manually aborted jobs, / indicates that no convergence of the job has been achieved, and - means that no job has been conducted.

		discrete	MC $\mathcal{M}=1$	MC $\mathcal{M}=2$	CC $\mathcal{M}=1$	CC $\mathcal{M}=2$	discrete	MC $\mathcal{M}=1$	MC $\mathcal{M}=2$	CC $\mathcal{M}=1$	CC $\mathcal{M}=2$
		user defined nodes					CPU time in s				
PC	4x4x80	21137	2026	13042	2026	13042	580	783	7085	/	/
PC	8x8x160	105025	13042	92770	13042	92770	/	7819	*141920	/	/
BCC	4x4x80	23786	2026	13042	-	13041	470	531	5053	-	167
BCC	8x8x160	187122	13042	92770	-	92770	1510	5216	58304	-	2725

Table 7.11: Computation times in s based on BCC lattice comprised of 8x8x160 base cells in the prebuckling regime. For the MC model, both the unsymmetric and symmetric equation solution techniques of ABAQUS are used, with the latter denoted by *sym*.

	discrete	MC $\mathcal{M}=1$	MC $\mathcal{M}=2$	MC *sym* $\mathcal{M}=1$	MC *sym* $\mathcal{M}=2$	CC $\mathcal{M}=2$
CPU time in total	218	398	5017	336	3834	443
number of iterations in total	8	6	6	6	6	11
CPU time per iteration	≈ 8	≈ 11	≈ 422	≈ 5	≈ 208	≈ 28
CPU time - solver	≈ 64	≈ 66	≈ 2532	≈ 30	≈ 1248	≈ 308
CPU time - not solver related	≈ 154	≈ 332	≈ 2485	≈ 306	≈ 2586	≈ 135

displacement load of $-0.5\,\mathrm{mm}$, which is applied in five equally large increments. The resulting total CPU times, the total numbers of iterations required for convergence, and the CPU times needed for solving the system of equations of the models are summarized in Table 7.11.

For the total CPU times, the discrete model outperforms the MC models by a factor of 2 to 23 depending on the discretization and the CC model with $\mathcal{M}=2$ by a factor of 2. The comparison of the total numbers of iterations required for convergence within the allowable (five) increments shows that the MC models show the best convergence behavior. The CPU times per iteration needed to solve the system of equations are similar for the discrete and the coarse MC models. Note that the symmetric solution procedure requires about half the computation time of the unsymmetric one. With respect to the number of DOFs, the CPU times per iteration of the discrete model for solving the system of equations is about 84 times lower than that of the fine MC model (unsymmetric). Not only solving the system of equations is time-consuming, but also the procedure for setting up this system, cf. fourth and fifth rows in Table 7.11. Note that this time is independent of the solution procedure, since the full stiffness matrix is determined within the UEL subroutine. This is particularly noticeable in the case of the coarse models. This is in contrast to the CC model, where more time is required to solve the system of equations than to build the system.

Summarized, the advantage of the MC models is more in modeling, such as geometry preparation and meshing, than in computation time. Since the MC models show smaller numbers of nodes compared to their discrete counterparts even for the fine discretization and the time spent for setting up the system of equations

is quite time-consuming, it is worth optimizing the FEM implementation presented in Section 4.1.2 to reduce the overall computation time. This is beyond the scope of the present thesis.

7.2.3 Summary

Simulations of various lattice beams of PC and BCC type are conducted to investigate the capabilities of the geometrically nonlinear micropolar continuum element in estimating critical loads and predicting the postbuckling behavior. Discrete lattice models serve as reference while CET continuum (CC) models are used to evaluate advantages and disadvantages of micropolar modeling. Linear eigenvalue analyses of the discrete models serve as the basis for eigenmode-affine imperfections, which are used to access the postbuckling regime. A strategy is presented for making use of these imperfections for the continuum models. Motivated by the imperfections present in additively manufactured lattices, three random-based geometric imperfections are further used to investigate the capabilities of the micropolar model to account for the postbuckling behavior of BCC type lattices in the presence of such imperfections.

The critical loads of the BCC type lattices studied can only be roughly estimated by the micropolar model. The predicted mechanical response is too stiff and shows deviations of about 30% compared to the discrete reference model for using element sizes two times smaller than the characteristic length of the lattice, i.e., $h_e = l/2$. The CC model shows a slightly more compliant response than the MC model. The deviations between micropolar and discrete model are smaller for the PC type lattices, which are about 10% for both discretizations used, i.e., $h_e = l$ and $h_e = l/2$. Contrary to the BCC type lattice, the CC model shows a stiffer response than the MC model.

The presented strategy for applying eigenmode-affine imperfections to the continuum models is successfully employed. All continuum models are able to access the postbuckling regime and show the expected deformations, which are governed by the first eigenmode. The stable postbuckling response of the BCC type lattices is qualitatively captured by the micropolar models in terms of both displacement and rotation fields. This is independent of the type of imperfection used. Interestingly, for two out of three random-based imperfections, the deformations of discrete and micropolar models do not coincide with the corresponding eigenmodes predicted by the linear eigenvalue analyses of the discrete models. Comparing the deformations predicted by the models of the imperfect lattice against each other it is found that for one random-based imperfection they do not coincide except for the wavelength whereas for the other random-based imperfections approximately the same deformations are obtained. The case where discrete and MC models show the same deformations but do not coincide with the corresponding first eigenmode indicates that the MC model seems to be able to partially capture local geometric changes before the critical load is reached, resulting in a different deformation shape than predicted by the linear eigenvalue analysis of the unloaded structure. It is remarkable that even the unstable postbuckling response of the PC type lattices can be captured to a certain extent. A comparison of the deformations of the models shows that some of the crucial characteristics that cause the unstable behavior can be captured. This is not the case for deformations far into the postbuckling regime, which is indicated by diverging displacement and rotation fields between micropolar and discrete models. It reveals that the micropolar continuum is not able to account for strong local instabilities. To capture these instabilities, a nonlinear MC model allowing to account for the finite strain regime must be considered. For the CET continuum, convergence issues occur at loads beyond the critical load, and it is not able to provide information about the unstable postbuckling behavior of the PC type lattice. In terms of computational performance, the current FEM implementation of the MC model is clearly outperformed by the discrete and MC model, which gives rise for optimization in future work.

In a nutshell, it is shown that the micropolar continuum can be successfully used to study the postbuckling behavior of lattice structures. With improvements in the implementation, the costly computation times of the MC models can be reduced, which makes the MC models advantageous over discrete models when considering the simpler geometry preparation and meshing. While further studies are necessary to identify the limits for their usage to ensure the reliability required for any engineering application, the current contribution provides evidence that the micropolar continuum offers the possibility of replacing discrete models for post-buckling prediction of lattice structures with improvements in future work.

Chapter 8

Summary

Lattice materials are becoming increasingly important in lightweight design, as advancing additive manufacturing techniques offer the opportunity to manufacture them in such a way that they meet desired properties while maintaining a low weight. To use them in engineering applications, reliable predictions of the mechanical response are essential for saving costs and time. In particular, continuum modeling of lattice materials is an ongoing trend towards numerical efficiency and time saving in model preparation. Reliability requires that the deformation mechanisms are properly captured by the models. Among the numerous failure mechanisms that may occur in lattice materials, this work focuses on buckling, which plays an important role in such materials. The micropolar continuum theory is a promising modeling approach, which possesses an internal length scale allowing to describe the required mechanisms, and is employed in this work to study 3D lattice materials.

To study 3D lattices in the context of micropolar continuum modeling, the corresponding micropolar elastic constants for the constitutive relations are determined based on the energy-based homogenization method presented in [10, 53]. This method yields two different sets of micropolar elastic constants for the same lattice type based on retaining (negative constants) or neglecting (positive constants) second order terms in the Taylor series expansion of the kinematic fields during the derivation. This has caused an ongoing debate in the literature about the validity of the method in general. Despite the controversy, it has been applied in various works using one of the two sets of constants with no intention of contributing to the discussion. To add some new flavor to the discussion and, additionally, to decide which set is used for the 3D lattices, the mechanical response of 2D lattices predicted by using the positive and the negative constants for the very same lattice are studied based on numerical simulations by means of the FEM. Various types of lattices showing different configurations are subjected to various load cases. The predictive capabilities of the models are evaluated by the comparison with discrete models in terms of strain energies and rotation fields. Special focus is set on two FEM parameters of the continuum model, namely, the element size and the order of interpolation function. The 2D linear micropolar continuum is implemented in NGSolve and as a user element in ABAQUS. It is shown that the FEM parameters of the continuum model and the characteristic length of the lattice must be considered as two competing length scales when negative constants are used. Consequently, this must be taken into account in the modeling. Therefore, based on the evaluation of the strain energies and the rotation fields, a condition is provided giving a rough estimate for the element size to be used in conjunction with the order of the interpolation functions. In contrast, no constraints are observed for positive constants as long as a proper discretization is ensured to resolve the kinematic fields, as is also required for classical continuum modeling.

Based on the findings of the numerical study carried out with 2D lattices, the positive micropolar elastic constants of 3D lattices are derived, namely, of the PC, the BCC, and the BCCCP lattice. To the best of the author's knowledge, these constants have not been reported in the literature before. To evaluate these constants, numerical simulations by means of the FEM are conducted, where the mechanical response of the continuum models is compared with the corresponding discrete models in terms of strain energy and kinematic fields. For this purpose, PC and BCC-type lattices subjected to simple shear and torsion serve as basis. The 3D linear micropolar continuum model is implemented in ABAQUS as a user element. It is shown that the model is able to capture the mechanical response of both PC and BCC lattices quite well for using elements smaller than the corresponding characteristic length of the lattice. For larger elements, this strongly depends on the type of lattice in combination with the load case studied.

For studying slender lattice beams undergoing large displacements and rotations under global compressive loading, geometrically nonlinear micropolar continuum models are required to capture the deformations. Therefore, the model presented in [8] is implemented in ABAQUS as a user element with some modifications based on [44]. The implementation is successfully verified against benchmark examples taken from literature, where linear isotropic material behavior is considered. Within the scope of the present thesis, it is investigated to which extent the model is able to estimate critical loads and predict the postbuckling behavior of 3D lattice materials remaining within the linear strain regime. To the best of the author's knowledge, such investigations have not yet been presented in the literature. The basis for evaluation are simulations of various lattice beams of PC and BCC type. For the anisotropic material behavior of the lattice materials, the previously derived micropolar constants are used. Discrete lattice models serve as reference while CET continuum models are used to evaluate advantages and disadvantages of micropolar modeling. Linear eigenvalue analyses of the discrete models serve as the basis for eigenmode-affine imperfections, which are used to access the postbuckling regime. A strategy is presented for making use of these imperfections for the continuum models. Motivated by the imperfections present in additive manufactured lattices, random-based geometric imperfections are additionally used to investigate the capabilities of the micropolar model to account for the postbuckling behavior of BCC type lattices in the presence of such imperfections. It is shown that the micropolar continuum can be successfully employed to study the postbuckling behavior of lattice structures. The localization of the deformation that determines the overall response can be captured to some extent as long as it is small. Even though the computation time for the micropolar model in the present stage is higher than for the discrete models, the time saved in model preparation may compensate for this drawback. While further studies are necessary to identify the limits for the usage of micropolar models to ensure the reliability required for any engineering application, the present contribution provides evidence that the micropolar continuum offers the possibility of replacing discrete models for post-buckling predictions of lattice structures.

Appendix A

Mathematical operators

The Levi-Civita symbol or the permutation tensor is defined as

$$\underset{\sim}{\boldsymbol{\epsilon}} = \epsilon_{ijk} = \begin{cases} 1 & i,j,k = 1,2,3;\ 2,3,1;\ 3,1,2 \\ -1 & i,j,k = 3,2,1;\ 1,3,2;\ 2,1,3 \\ 0 & i = j,\ i = k,\ j = k \end{cases} \quad , \tag{A.1}$$

with $\epsilon_{ijk} = \epsilon_{jki} = \epsilon_{kij}$, $\epsilon_{kji} = \epsilon_{jik} = \epsilon_{ikj}$, and $\epsilon_{ijk} = -\epsilon_{kji}$.

The Kronecker-Delta symbol is defined as follows

$$\delta_{ij} = \underline{\mathbf{e}}_i \cdot \underline{\mathbf{e}}_j = \begin{cases} 1 & i = j \\ 0 & i \neq j \end{cases} \quad . \tag{A.2}$$

where the following holds true, $\delta_{ij}\delta_{jk} = \delta_{ik}$.

The following mathematical operators between tensors of various order are given in tensor notation and the corresponding index notation. The inner product between two first order tensors reads

$$\begin{aligned} \underline{\mathbf{a}} \cdot \underline{\mathbf{b}} &= c \ (= \underline{\mathbf{a}}^{\mathrm{T}} \underline{\mathbf{b}}) \quad , \\ a_i b_i &= c \quad . \end{aligned} \tag{A.3}$$

The cross or vector product between two first order tensors reads

$$\begin{aligned} \underline{\mathbf{a}} \times \underline{\mathbf{b}} &= \underline{\mathbf{c}} \ (= -\underline{\mathbf{b}} \times \underline{\mathbf{a}}) \quad , \\ \epsilon_{ijk} a_i b_j &= c_k \quad , \\ \begin{bmatrix} a_2 b_3 - a_3 b_2 \\ a_3 b_1 - a_1 b_3 \\ a_1 b_2 - a_2 b_1 \end{bmatrix} &= \begin{bmatrix} c_1 \\ c_2 \\ c_3 \end{bmatrix} \quad . \end{aligned} \tag{A.4}$$

The dyadic product between two first order tensors reads

$$\underline{\mathbf{a}} \otimes \underline{\mathbf{b}} = \underset{\sim}{\mathbf{C}} \quad , \tag{A.5}$$
$$a_i b_j = C_{ij} \quad .$$

The product between second and first order tensors, i.e., matrix-vector multiplication, reads

$$\underset{\sim}{\mathbf{A}}\underline{\mathbf{b}} = \underline{\mathbf{c}} \neq \underline{\mathbf{b}}^{\mathrm{T}}\underset{\sim}{\mathbf{A}} \quad , \tag{A.6}$$
$$A_{ij} b_j = c_i \quad ,$$
$$\underline{\mathbf{a}}^{\mathrm{T}}\underset{\sim}{\mathbf{B}} = \underline{\mathbf{c}}^{\mathrm{T}} \quad , \tag{A.7}$$
$$b_i A_{ij} = c_j \quad .$$

The product between two second order tensors, i.e., matrix-matrix multiplication, reads

$$\underset{\sim}{\mathbf{A}}\underset{\sim}{\mathbf{B}} = \underset{\sim}{\mathbf{C}} \neq \underset{\sim}{\mathbf{B}}\underset{\sim}{\mathbf{A}} \quad , \tag{A.8}$$
$$A_{ik} B_{kj} = C_{ij} \quad .$$

The double contraction or double inner product between two second order tensors reads

$$\underset{\sim}{\mathbf{A}} : \underset{\sim}{\mathbf{B}} = c \quad , \tag{A.9}$$
$$A_{ij} B_{ij} = c \quad .$$

The inner product of second and third order tensors reads

$$\underset{\sim}{\underline{\mathbf{C}}} = \underset{\sim}{\underline{\mathbf{A}}} \cdot \underset{\sim}{\underline{\mathbf{B}}} \triangleq C_{ijk} = A_{il} B_{ljk} \quad . \tag{A.10}$$

The double contraction between third and second order tensors is defined as

$$\underline{\mathbf{c}} = \underset{\sim}{\underline{\mathbf{A}}} : \underset{\sim}{\mathbf{B}} \triangleq c_i = A_{ijk} B_{jk} \quad . \tag{A.11}$$

The double contraction between two third order tensors reads

$$\underset{\sim}{\mathbf{C}} = \underset{\sim}{\underline{\mathbf{A}}} : \underset{\sim}{\underline{\mathbf{B}}} \triangleq C_{ij} = A_{ilk} B_{lkj} \quad . \tag{A.12}$$

The double contraction between fourth and second order tensors reads

$$\underset{\sim}{\mathbf{C}} = \underset{\sim}{\underline{\underline{\mathbf{A}}}} : \underset{\sim}{\mathbf{B}} \triangleq C_{ij} = A_{ijkl} B_{kl} \quad . \tag{A.13}$$

In general, there exist a left and right cross or vector product between a second order tensor, $\underset{\sim}{\mathbf{A}} = \underline{\mathbf{a}} \otimes \underline{\mathbf{b}}$, and a vector, $\underline{\mathbf{c}}$, which are commonly defined as

$$\underline{\mathbf{c}} \times \underset{\sim}{\mathbf{A}} = \underline{\mathbf{c}} \times (\underline{\mathbf{a}} \otimes \underline{\mathbf{b}}) = (\underline{\mathbf{c}} \times \underline{\mathbf{a}}) \otimes \underline{\mathbf{b}} = c_k A_{ij} \epsilon_{kil} \underline{\mathbf{e}}_l \otimes \underline{\mathbf{e}}_j \quad , \tag{A.14}$$
$$\underset{\sim}{\mathbf{A}} \times \underline{\mathbf{c}} = (\underline{\mathbf{a}} \otimes \underline{\mathbf{b}}) \times \underline{\mathbf{c}} = \underline{\mathbf{a}} \otimes (\underline{\mathbf{b}} \times \underline{\mathbf{c}}) = c_k A_{ij} \epsilon_{jkl} \underline{\mathbf{e}}_i \otimes \underline{\mathbf{e}}_l \quad , \tag{A.15}$$

respectively, see [2]. The following properties hold

$$\underset{\sim}{\mathbf{c}} \times \underset{\sim}{\mathbf{A}} = -(\underset{\sim}{\mathbf{A}}^{\mathrm{T}} \times \underset{\sim}{\mathbf{c}})^{\mathrm{T}} \quad , \tag{A.16}$$

$$\underset{\sim}{\mathbf{A}} \times \underset{\sim}{\mathbf{c}} = -(\underset{\sim}{\mathbf{c}} \times \underset{\sim}{\mathbf{A}}^{\mathrm{T}})^{\mathrm{T}} \quad , \tag{A.17}$$

$$\underset{\sim}{\mathbf{A}} \times \underset{\sim}{\mathbf{c}} \neq \underset{\sim}{\mathbf{c}} \times \underset{\sim}{\mathbf{A}} \quad . \tag{A.18}$$

The difference between left and right product is superseded when using the identity tensor, $\underset{\sim}{\mathbf{A}} = \underset{\sim}{\mathbf{I}}$, which results in the relation $\underset{\sim}{\mathbf{I}} \times \underset{\sim}{\mathbf{c}} = \underset{\sim}{\mathbf{c}} \times \underset{\sim}{\mathbf{I}}$, e.g., [80]. This also applies to the skew-symmetric matrix, $\underset{\sim}{\mathbf{W}}$, of the axial vector, $\underline{\boldsymbol{\phi}}$, which can be expressed as $\underset{\sim}{\mathbf{W}} = \underline{\boldsymbol{\phi}} \times \underset{\sim}{\mathbf{I}} = \underset{\sim}{\mathbf{I}} \times \underline{\boldsymbol{\phi}}$. This also follows from the relation $\underset{\sim}{\mathbf{W}} = -\underset{\sim}{\mathbf{W}}^{\mathrm{T}}$ and equating the coefficients of Eqs. (A.16) and (A.17). It reads as follows

$$\underset{\sim}{\mathbf{W}} = \underline{\boldsymbol{\phi}} \times \underset{\sim}{\mathbf{I}} = \underset{\sim}{\mathbf{I}} \times \underline{\boldsymbol{\phi}} = \mathrm{sk}(\underline{\boldsymbol{\phi}}) = \begin{bmatrix} 0 & -\phi_3 & \phi_2 \\ \phi_3 & 0 & -\phi_1 \\ -\phi_2 & \phi_1 & 0 \end{bmatrix} \quad , \tag{A.19}$$

$$W_{ij} = -\epsilon_{ijk}\phi_k = \epsilon_{jik}\phi_k \quad ,$$

where $\mathrm{sk}(\cdot)$ takes an axial vector and gives the corresponding skew-symmetric matrix. In order to obtain the axial vector of a skew-symmetric tensor, the following mathematical operator is defined

$$\underline{\mathbf{w}} = \mathrm{axl}(\underset{\sim}{\mathbf{W}}) = -\frac{1}{2}\underset{\approx}{\boldsymbol{\epsilon}} : \underset{\sim}{\mathbf{W}} \quad , \tag{A.20}$$

$$w_i = \frac{1}{2}\epsilon_{ijk}W_{kj} = -\frac{1}{2}\epsilon_{ijk}W_{jk} \quad ,$$

$$\begin{bmatrix} w_1 \\ w_2 \\ w_3 \end{bmatrix} = \mathrm{axl}\left(\begin{bmatrix} 0 & -w_3 & w_2 \\ w_3 & 0 & -w_1 \\ -w_2 & w_1 & 0 \end{bmatrix} \right) \quad ,$$

where the double contraction is given in Eq. (A.11). In [28], a slightly different operator is defined, which reads

$$\underline{\mathbf{a}} = (\underset{\sim}{\mathbf{A}})_{\times} = (A_{mn}e_m \otimes e_n)_{\times} \triangleq A_{mn}e_m \times e_n \quad , \tag{A.21}$$

$$a_i = \epsilon_{ijk}A_{jk} \quad .$$

It follows that the axial vector of a skew-symmetric second order tensor can be given optionally to Eq. (A.20) as

$$\underline{\mathbf{w}} = -\frac{1}{2}(\underset{\sim}{\mathbf{W}})_{\times} \quad . \tag{A.22}$$

Note that $\mathrm{axl}(\underset{\sim}{\mathbf{W}}) = -1/2(\underset{\sim}{\mathbf{W}})_{\times}$. The skew-symmetric part of a second order tensor is obtained by introducing the following function

$$\mathrm{skew}(\underset{\sim}{\mathbf{A}}) = \frac{1}{2}(\underset{\sim}{\mathbf{A}} - \underset{\sim}{\mathbf{A}}^{\mathrm{T}}) \quad . \tag{A.23}$$

The nabla operators with respect to the reference or current configuration are defined as

$$\underline{\boldsymbol{\nabla}}_x = \frac{\partial}{\partial x_i}\underline{\mathbf{e}}_i = \nabla_i \underline{\mathbf{e}}_i = \ {}_{,i}\ \underline{\mathbf{e}}_i \quad , \qquad \underline{\boldsymbol{\nabla}}_X = \frac{\partial}{\partial X_I}\underline{\mathbf{E}}_I = \nabla_I \underline{\mathbf{E}}_I = \ {}_{,I}\ \underline{\mathbf{E}}_I \quad , \tag{A.24}$$

respectively. For the transformation of the gradients with respect to the reference and current configurations, e.g., [44], the transformation reads as follows

$$\underset{\sim}{\boldsymbol{\nabla}}_X = \underset{\sim}{\mathbf{F}}^{\mathrm{T}} \underset{\sim}{\boldsymbol{\nabla}}_x \leftrightarrow \underset{\sim}{\boldsymbol{\nabla}}_x = \underset{\sim}{\mathbf{F}}^{-\mathrm{T}} \underset{\sim}{\boldsymbol{\nabla}}_X \quad . \tag{A.25}$$

The divergences of first order tensors read

$$\begin{aligned} \mathrm{Div}_{\mathrm{R}}(\underset{\sim}{\mathbf{a}}) &= \underset{\sim}{\mathbf{a}} \cdot \underset{\sim}{\boldsymbol{\nabla}}_X = a_i \nabla_i = c \quad , \\ \mathrm{div}_{\mathrm{R}}(\underset{\sim}{\mathbf{a}}) &= \underset{\sim}{\mathbf{a}} \cdot \underset{\sim}{\boldsymbol{\nabla}}_x = a_i \nabla_i = c \quad , \\ \mathrm{Div}_{\mathrm{L}}(\underset{\sim}{\mathbf{a}}) &= \underset{\sim}{\boldsymbol{\nabla}}_X \cdot \underset{\sim}{\mathbf{a}} = a_i \nabla_i = c \ (= \mathrm{Div}_{\mathrm{R}}(\underset{\sim}{\mathbf{a}})) \quad , \\ \mathrm{div}_{\mathrm{L}}(\underset{\sim}{\mathbf{a}}) &= \underset{\sim}{\boldsymbol{\nabla}}_x \cdot \underset{\sim}{\mathbf{a}} = a_i \nabla_i = c \ (= \mathrm{div}_{\mathrm{R}}(\underset{\sim}{\mathbf{a}})) \quad . \end{aligned} \tag{A.26}$$

The gradients of first order tensors read

$$\begin{aligned} \mathrm{Grad}_{\mathrm{R}}(\underset{\sim}{\mathbf{a}}) &= \underset{\sim}{\mathbf{a}} \otimes \underset{\sim}{\boldsymbol{\nabla}}_X = a_i \nabla_j = C_{ij} \quad , \\ \mathrm{grad}_{\mathrm{R}}(\underset{\sim}{\mathbf{a}}) &= \underset{\sim}{\mathbf{a}} \otimes \underset{\sim}{\boldsymbol{\nabla}}_x = a_i \nabla_j = C_{ij} \quad , \\ \mathrm{Grad}_{\mathrm{L}}(\underset{\sim}{\mathbf{a}}) &= \underset{\sim}{\boldsymbol{\nabla}}_X \otimes \underset{\sim}{\mathbf{a}} = \nabla_i a_j = C_{ij} \ (= \mathrm{Grad}_{\mathrm{R}}(\underset{\sim}{\mathbf{a}})^{\mathrm{T}}) \quad , \\ \mathrm{grad}_{\mathrm{L}}(\underset{\sim}{\mathbf{a}}) &= \underset{\sim}{\boldsymbol{\nabla}}_x \otimes \underset{\sim}{\mathbf{a}} = \nabla_i a_j = C_{ij} \ (= \mathrm{grad}_{\mathrm{R}}(\underset{\sim}{\mathbf{a}})^{\mathrm{T}}) \quad . \end{aligned} \tag{A.27}$$

The divergences of second order tensors read

$$\begin{aligned} \mathrm{Div}_{\mathrm{R}}(\underset{\sim}{\mathbf{A}}) &= \underset{\sim}{\mathbf{A}} \underset{\sim}{\boldsymbol{\nabla}}_X = A_{ij} \nabla_j = b_i \quad , \\ \mathrm{div}_{\mathrm{R}}(\underset{\sim}{\mathbf{A}}) &= \underset{\sim}{\mathbf{A}} \underset{\sim}{\boldsymbol{\nabla}}_x = A_{ij} \nabla_j = b_i \quad , \\ \mathrm{Div}_{\mathrm{L}}(\underset{\sim}{\mathbf{A}}) &= \underset{\sim}{\boldsymbol{\nabla}}_X \underset{\sim}{\mathbf{A}} = A_{ij} \nabla_i = b_j \ (\neq \mathrm{Div}_{\mathrm{R}}(\underset{\sim}{\mathbf{A}}^{\mathrm{T}})) \quad , \\ \mathrm{div}_{\mathrm{L}}(\underset{\sim}{\mathbf{A}}) &= \underset{\sim}{\boldsymbol{\nabla}}_x \underset{\sim}{\mathbf{A}} = A_{ij} \nabla_i = b_j \ (\neq \mathrm{div}_{\mathrm{R}}(\underset{\sim}{\mathbf{A}}^{\mathrm{T}})) \quad . \end{aligned} \tag{A.28}$$

The gradients of second order tensors read

$$\begin{aligned} \mathrm{Grad}_{\mathrm{R}}(\underset{\sim}{\mathbf{A}}) &= \underset{\sim}{\mathbf{A}} \otimes \underset{\sim}{\boldsymbol{\nabla}}_X = A_{ij} \nabla_k = C_{ijk} \quad , \\ \mathrm{grad}_{\mathrm{R}}(\underset{\sim}{\mathbf{A}}) &= \underset{\sim}{\mathbf{A}} \otimes \underset{\sim}{\boldsymbol{\nabla}}_x = A_{ij} \nabla_k = C_{ijk} \quad , \\ \mathrm{Grad}_{\mathrm{L}}(\underset{\sim}{\mathbf{A}}) &= \underset{\sim}{\boldsymbol{\nabla}}_X \otimes \underset{\sim}{\mathbf{A}} = \nabla_i A_{jk} = C_{ijk} \quad , \\ \mathrm{grad}_{\mathrm{L}}(\underset{\sim}{\mathbf{A}}) &= \underset{\sim}{\boldsymbol{\nabla}}_x \otimes \underset{\sim}{\mathbf{A}} = \nabla_i A_{jk} = C_{ijk} \quad , \end{aligned} \tag{A.29}$$

e.g.

$$\mathrm{Grad}_{\mathrm{R}}(\underset{\sim}{\mathbf{A}}) = \underset{\sim}{\mathbf{A}} \otimes \underline{\boldsymbol{\nabla}}_X = A_{ij}\nabla_k = C_{ijk} = \underset{\approx}{\mathbf{C}} = \begin{bmatrix} \begin{bmatrix} \frac{\partial A_{11}}{\partial X_1} & \frac{\partial A_{11}}{\partial X_2} \\ \frac{\partial A_{12}}{\partial X_1} & \frac{\partial A_{12}}{\partial X_2} \end{bmatrix} \\ \begin{bmatrix} \frac{\partial A_{21}}{\partial X_1} & \frac{\partial A_{21}}{\partial X_1} \\ \frac{\partial A_{22}}{\partial X_1} & \frac{\partial A_{22}}{\partial X_2} \end{bmatrix} \end{bmatrix} \quad ,$$

$$\mathrm{Grad}_{\mathrm{L}}(\underset{\sim}{\mathbf{A}}) = \underline{\boldsymbol{\nabla}}_X \otimes \underset{\sim}{\mathbf{A}} = \nabla_i A_{jk} = C_{ijk} = \underset{\approx}{\mathbf{C}} = \begin{bmatrix} \begin{bmatrix} \frac{\partial A_{11}}{\partial X_1} & \frac{\partial A_{12}}{\partial X_1} \\ \frac{\partial A_{21}}{\partial X_1} & \frac{\partial A_{22}}{\partial X_1} \end{bmatrix} \\ \begin{bmatrix} \frac{\partial A_{11}}{\partial X_2} & \frac{\partial A_{12}}{\partial X_2} \\ \frac{\partial A_{21}}{\partial X_2} & \frac{\partial A_{22}}{\partial X_2} \end{bmatrix} \end{bmatrix} \quad .$$

The divergence identity reads

$$\mathrm{div}_{\mathrm{R}}(\underset{\sim}{\mathbf{A}}\underline{\mathbf{b}}) = \mathrm{div}_{\mathrm{R}}(\underset{\sim}{\mathbf{A}})\underline{\mathbf{b}} + \underset{\sim}{\mathbf{A}} : \mathrm{grad}_{\mathrm{R}}(\underline{\mathbf{b}}) \quad . \tag{A.30}$$

The divergence theorem or Gaussian theorem given in [2] reads

$$\int_V \mathrm{div}_{\mathrm{R}}(\underset{\sim}{\mathbf{A}})\, dV = \int_S \underset{\sim}{\mathbf{A}}\underline{\mathbf{n}}\, dS \quad , \quad \int_V A_{ij,j}\, dV = \int_S A_{ij}n_j\, dS \quad , \tag{A.31}$$

where V is the volume of the integration domain, $\underset{\sim}{\mathbf{A}}$ a second order tensor, S a surface domain, and $\underline{\mathbf{n}}$ the corresponding surface normal.

Appendix B

Vector-matrix representation

The vector-matrix representation of non-symmetric second and fourth order tensors follows the definition used in [27], where the components are arranged in the order given in Eq. (2.62). Consequently, second order tensors read

$$\underset{\sim}{\mathbf{A}} = A_{ij} \Rightarrow [\underset{\sim}{\mathbf{A}}] = [A_{11}\ A_{22}\ A_{33}\ A_{23}\ A_{31}\ A_{12}\ A_{32}\ A_{13}\ A_{21}]^T$$

and fourth order tensors follow as

$$\underset{\approx}{\mathbb{A}} = \mathbb{A}_{ijkl} \Rightarrow [\underset{\approx}{\mathbb{A}}] = \begin{bmatrix} A_{1111} & A_{1122} & A_{1133} & A_{1123} & A_{1131} & A_{1112} & A_{1132} & A_{1113} & A_{1121} \\ A_{2211} & A_{2222} & A_{2233} & A_{2223} & A_{2231} & A_{2212} & A_{2232} & A_{2213} & A_{2221} \\ A_{3311} & A_{3322} & A_{3333} & A_{3323} & A_{3331} & A_{3312} & A_{3332} & A_{3313} & A_{3321} \\ A_{2311} & A_{2322} & A_{2333} & A_{2323} & A_{2331} & A_{2312} & A_{2332} & A_{2313} & A_{2321} \\ A_{3111} & A_{3122} & A_{3133} & A_{3123} & A_{3131} & A_{3112} & A_{3132} & A_{3113} & A_{3121} \\ A_{1211} & A_{1222} & A_{1233} & A_{1223} & A_{1231} & A_{1212} & A_{1232} & A_{1213} & A_{1221} \\ A_{3211} & A_{3222} & A_{3233} & A_{3223} & A_{3231} & A_{3212} & A_{3232} & A_{3213} & A_{3221} \\ A_{1311} & A_{1322} & A_{1333} & A_{1323} & A_{1331} & A_{1312} & A_{1332} & A_{1313} & A_{1321} \\ A_{2111} & A_{2122} & A_{2133} & A_{2123} & A_{2131} & A_{2112} & A_{2132} & A_{2113} & A_{2121} \end{bmatrix} ,$$

where the brackets indicate the vector-matrix representation of the corresponding tensor.

In [27], the following material symmetries of the fourth order elasticity tensors in vector-matrix representation for the micropolar continuum are given. For the present thesis, the most important symmetries are outlined.

A representative of the elasticity tensors of the orthotropic material, which shows 30 independent MECs, reads

$$[\underset{\approx}{\mathbb{A}}] = \begin{bmatrix} A_{1111} & A_{1122} & A_{1133} & 0 & 0 & 0 & 0 & 0 & 0 \\ & A_{2222} & A_{2233} & 0 & 0 & 0 & 0 & 0 & 0 \\ & & A_{3333} & 0 & 0 & 0 & 0 & 0 & 0 \\ & & & A_{2323} & 0 & 0 & A_{2332} & 0 & 0 \\ & & & & A_{3131} & 0 & 0 & A_{3113} & 0 \\ & & & & & A_{1212} & 0 & & A_{1221} \\ & & \text{sym} & & & & A_{3232} & 0 & 0 \\ & & & & & & & A_{1313} & 0 \\ & & & & & & & & A_{2121} \end{bmatrix} . \tag{B.1}$$

For materials showing cubic symmetry, eight independent MECs are left and the representative elasticity tensor reads

$$[\underset{\approx}{\mathbb{A}}] = \begin{bmatrix} A_{1111} & A_{1122} & A_{1122} & 0 & 0 & 0 & 0 & 0 & 0 \\ & A_{1111} & A_{1122} & 0 & 0 & 0 & 0 & 0 & 0 \\ & & A_{1111} & 0 & 0 & 0 & 0 & 0 & 0 \\ & & & A_{1212} & 0 & 0 & A_{1221} & 0 & 0 \\ & & & & A_{1212} & 0 & 0 & A_{1221} & 0 \\ & & & & & A_{1212} & 0 & & A_{1221} \\ & & \text{sym} & & & & A_{1212} & 0 & 0 \\ & & & & & & & A_{1212} & 0 \\ & & & & & & & & A_{1212} \end{bmatrix} . \tag{B.2}$$

Appendix C

Local beam stiffness matrix

For the homogenization method in Chapter 3, the stiffness matrix of the beam element with respect to its local coordinate system reads

$$[\underset{\sim}{\mathbf{k}}^{(e)}_{\text{local}}] = \begin{bmatrix} \frac{(E_{\text{s}}A)}{l} & 0 & 0 & 0 & 0 & 0 \\ 0 & \frac{12(E_{\text{s}}I_{\text{m}})}{l^3} & 0 & 0 & 0 & \frac{6(E_{\text{s}}I_{\text{m}})}{l^2} \\ 0 & 0 & \frac{12(E_{\text{s}}I_{\text{n}})}{l^3} & 0 & \frac{-6(E_{\text{s}}I_{\text{n}})}{l^2} & 0 \\ 0 & 0 & 0 & \frac{(G_{\text{s}}I_{\text{t}})}{l} & 0 & 0 \\ 0 & 0 & \frac{-6(E_{\text{s}}I_{\text{n}})}{l^2} & 0 & \frac{4(E_{\text{s}}I_{\text{n}})}{l} & 0 \\ 0 & \frac{6(E_{\text{s}}I_{\text{m}})}{l^2} & 0 & 0 & 0 & \frac{4(E_{\text{s}}I_{\text{m}})}{l} \\ \frac{-(E_{\text{s}}A)}{l} & 0 & 0 & 0 & 0 & 0 \\ 0 & \frac{-12(E_{\text{s}}I_{\text{m}})}{l^3} & 0 & 0 & 0 & \frac{-6(E_{\text{s}}I_{\text{m}})}{l^2} \\ 0 & 0 & \frac{-12(E_{\text{s}}I_{\text{n}})}{l^3} & 0 & \frac{6(E_{\text{s}}I_{\text{n}})}{l^2} & 0 \\ 0 & 0 & 0 & \frac{-(G_{\text{s}}I_{\text{t}})}{l} & 0 & 0 \\ 0 & 0 & \frac{-6(E_{\text{s}}I_{\text{n}})}{l^2} & 0 & \frac{2(E_{\text{s}}I_{\text{n}})}{l} & 0 \\ 0 & \frac{6(E_{\text{s}}I_{\text{m}})}{l^2} & 0 & 0 & 0 & \frac{2(E_{\text{s}}I_{\text{m}})}{l} \end{bmatrix}$$

$$\begin{bmatrix}
\frac{-(E_\mathrm{s}A)}{l} & 0 & 0 & 0 & 0 & 0 \\
0 & \frac{-12(E_\mathrm{s}I_\mathrm{m})}{l^3} & 0 & 0 & 0 & \frac{6(E_\mathrm{s}I_\mathrm{m})}{l^2} \\
0 & 0 & \frac{-12(E_\mathrm{s}I_\mathrm{n})}{l^3} & 0 & \frac{-6(E_\mathrm{s}I_\mathrm{n})}{l^2} & 0 \\
0 & 0 & 0 & \frac{-(G_\mathrm{s}I_\mathrm{t})}{l} & 0 & 0 \\
0 & 0 & \frac{6(E_\mathrm{s}I_\mathrm{n})}{l^2} & 0 & \frac{2(E_\mathrm{s}I_\mathrm{n})}{l} & 0 \\
0 & \frac{-6(E_\mathrm{s}I_\mathrm{m})}{l^2} & 0 & 0 & 0 & \frac{2(E_\mathrm{s}I_\mathrm{m})}{l} \\
\frac{(E_\mathrm{s}A)}{l} & 0 & 0 & 0 & 0 & 0 \\
0 & \frac{12(E_\mathrm{s}I_\mathrm{m})}{l^3} & 0 & 0 & 0 & \frac{-6(E_\mathrm{s}I_\mathrm{m})}{l^2} \\
0 & 0 & \frac{12(E_\mathrm{s}I_\mathrm{n})}{l^3} & 0 & \frac{6(E_\mathrm{s}I_\mathrm{n})}{l^2} & 0 \\
0 & 0 & 0 & \frac{(G_\mathrm{s}I_\mathrm{t})}{l} & 0 & 0 \\
0 & 0 & \frac{6(E_\mathrm{s}I_\mathrm{n})}{l^2} & 0 & \frac{4(E_\mathrm{s}I_\mathrm{n})}{l} & 0 \\
0 & \frac{-6(E_\mathrm{s}I_\mathrm{m})}{l^2} & 0 & 0 & 0 & \frac{4(E_\mathrm{s}I_\mathrm{m})}{l}
\end{bmatrix} . \tag{C.1}$$

The corresponding vector of nodal kinematics with respect to the local coordinate system reads

$$[\underline{\mathbf{U}}^{(e)}_{\mathrm{local}}] = [U_{I\mathrm{t}}, U_{I\mathrm{n}}, U_{I\mathrm{m}}, \Phi_{I\mathrm{t}}, \Phi_{I\mathrm{n}}, \Phi_{I\mathrm{m}}, U_{J\mathrm{t}}, U_{J\mathrm{n}}, U_{J\mathrm{m}}, \Phi_{J\mathrm{t}}, \Phi_{J\mathrm{n}}, \Phi_{J\mathrm{m}}]^{\mathrm{T}} \quad , \tag{C.2}$$

where nodal displacements and rotations are denoted by U_I and Φ_I, respectively, with the local axes denoted by t, n, and m, see Figure 3.1. The stiffness quantities of the beam for stretching along the t-axis, bending about the m-axis and the n-axis, as well as torsion about the t-axis are referred to as, $(E_\mathrm{s}A)$, $(E_\mathrm{s}I_\mathrm{m})$, $(E_\mathrm{s}I_\mathrm{n})$, and $(G_\mathrm{s}I_\mathrm{t})$, respectively. The length of the beam is denoted by l, its cross-section is referred to as A, and its parent material parameters E_s and G_s denote the Young's and shear modulus, respectively.

The transformation matrix (from local to global) for the lattice members, to be used in conjunction with Eq. (3.6) or (3.7) in order to determine the strain energy density of the base cell given in Eq. (3.10), reads

$$[\underset{\sim}{\mathbf{T}}^{(e)}_{\mathrm{r}}] = \begin{bmatrix}
t_1 & n_1 & m_1 & 0 & 0 & 0 & 0 & 0 & 0 & 0 & 0 & 0 \\
t_2 & n_2 & m_2 & 0 & 0 & 0 & 0 & 0 & 0 & 0 & 0 & 0 \\
t_3 & n_3 & m_3 & 0 & 0 & 0 & 0 & 0 & 0 & 0 & 0 & 0 \\
0 & 0 & 0 & t_1 & n_1 & m_1 & 0 & 0 & 0 & 0 & 0 & 0 \\
0 & 0 & 0 & t_2 & n_2 & m_2 & 0 & 0 & 0 & 0 & 0 & 0 \\
0 & 0 & 0 & t_3 & n_3 & m_3 & 0 & 0 & 0 & 0 & 0 & 0 \\
0 & 0 & 0 & 0 & 0 & 0 & t_1 & n_1 & m_1 & 0 & 0 & 0 \\
0 & 0 & 0 & 0 & 0 & 0 & t_2 & n_2 & m_2 & 0 & 0 & 0 \\
0 & 0 & 0 & 0 & 0 & 0 & t_3 & n_3 & m_3 & 0 & 0 & 0 \\
0 & 0 & 0 & 0 & 0 & 0 & 0 & 0 & 0 & t_1 & n_1 & m_1 \\
0 & 0 & 0 & 0 & 0 & 0 & 0 & 0 & 0 & t_2 & n_2 & m_2 \\
0 & 0 & 0 & 0 & 0 & 0 & 0 & 0 & 0 & t_3 & n_3 & m_3
\end{bmatrix} , \tag{C.3}$$

where $\underline{\mathbf{e}}_t = [t_1, t_2, t_3]^{\mathrm{T}}$, $\underline{\mathbf{e}}_n = [n_1, n_2, n_3]^{\mathrm{T}}$, and $\underline{\mathbf{e}}_m = \underline{\mathbf{e}}_t \times \underline{\mathbf{e}}_n = [m_1, m_2, m_3]^{\mathrm{T}}$, cf., e.g., Figure 3.2. As an example, for the lattice member OB of the PO lattice, the local base vectors are $\underline{\mathbf{e}}_t = [0, 1, 0]^{\mathrm{T}}$, $\underline{\mathbf{e}}_n = [0, 0, 1]^{\mathrm{T}}$, and $\underline{\mathbf{e}}_m = \underline{\mathbf{e}}_t \times \underline{\mathbf{e}}_n = [1, 0, 0]^{\mathrm{T}}$, while for the lattice member $\mathrm{OA}_{\mathrm{top}}$ of the BCC lattice, the local base vectors are $\underline{\mathbf{e}}_t = [\sqrt{3}/3, \sqrt{3}/3, \sqrt{3}/3]^{\mathrm{T}}$, $\underline{\mathbf{e}}_n = [-\sqrt{6}/6, -\sqrt{6}/6, \sqrt{6}/3]^{\mathrm{T}}$, and $\underline{\mathbf{e}}_m = \underline{\mathbf{e}}_t \times \underline{\mathbf{e}}_n = [\sqrt{2}/2, -\sqrt{2}/2, 0]^{\mathrm{T}}$.

Appendix D

Micropolar elastic constants of rectangular, 45° rotated square, and triangular lattices

For the sake of completeness, the MECs of the 2D rectangular and triangular lattice under the plane strain assumption derived in [53] are outlined. Therein, the stress measures are based on LSD and the strain measures are obtained by using gradients applied from the left resulting in elasticity tensors according to LSD. Additionally, the MECs of the 45° rotated square lattice are determined based on the rectangular lattice and an appropriate rotation. Note that two different sets of MECs are obtained depending on the assumptions made during the derivation, cf. Chapter 3.

The rectangular lattice is composed of four lattice members OK with extremity nodes, $K \in \{\mathrm{A}, \mathrm{B}, \mathrm{C}, \mathrm{D}\}$, connected at the center, O, of the base cell as depicted in Figure D.1 (left). For the rectangular lattice, the MECs read [53]

$$\begin{aligned}
\mathbb{A}_{1111} &= \frac{E_1 l_1}{l_2} \quad (= D_{11}) \quad , \quad \mathbb{A}_{2222} = \frac{E_2 l_2}{l_1} \quad (= D_{22}) \quad , \\
\mathbb{A}_{1212} &= \frac{12 k_1}{l_1 l_2} \quad (= D_{33}) \quad , \quad \mathbb{A}_{2121} = \frac{12 k_2}{l_1 l_2} \quad (= D_{44}) \quad , \\
\mathbb{B}_{1313} &= \underbrace{-\frac{2k_1 l_1}{l_2} \quad \text{or} \quad \frac{4k_1 l_1}{l_2}}_{D_{55}^{\text{neg}} \text{ or } D_{55}^{\text{pos}}} \quad (= D_{55}) \quad , \quad \mathbb{B}_{2323} = \underbrace{-\frac{2k_2 l_2}{l_1} \quad \text{or} \quad \frac{4k_2 l_2}{l_1}}_{D_{66}^{\text{neg}} \text{ or } D_{66}^{\text{pos}}} \quad (= D_{66}) \quad ,
\end{aligned} \tag{D.1}$$

with $E_i = \dfrac{Et}{l_i}$, $k_i = \dfrac{Et^3}{12 l_i}$ for $i = 1, 2$, and

$$E = \frac{E_\mathrm{s}}{(1 - \nu_\mathrm{s}^2)}, \tag{D.2}$$

where E_s and ν_s denote the Young's modulus and the Poisson ratio of the parent material, respectively. The length of each beam is denoted by l_i and the cell wall thickness is t, which is assumed to be the same for all lattice members and constant along the length of each beam. The D_{ij} denote the components of the elasticity matrix given in Eq. (2.63). To obtain the MECs of the square lattice, the length of each beam is set to l, i.e., $l_1 = l_2 = l$. Note that the out-of-plane thickness with respect to the plane strain assumption has been defined as $h = 1$.

The MECs of the 45° rotated square lattice can be obtained either via rotation of the elasticity tensors of the corresponding square lattice with a length of l for the lattice members, cf. Eq. (2.76), or directly via Eq. (3.3). To obtain the same MECs via the direct derivation as via the rotation, the same length, namely l, must be used for the lattice members, the volume of the base cell must show $V_{\mathrm{bc}} = A_{\mathrm{bc}}h = (l\sqrt{2})^2$ with $h = 1$, and the full energy contribution of each lattice member must be considered. Full energy contribution means that no prefactor of 1/2 needs to be considered in Eq. (3.3) as required for the rectangular lattice shown in [53], cf. Figure D.1 (center). The two different sets of MECs obtained read

$$\begin{aligned}
\mathbb{A}_{1111} &= \frac{E_l}{2} + \frac{6k_l}{l^2} \quad (= D_{11}) \quad , & \mathbb{A}_{1122} &= \frac{E_l}{2} - \frac{6k_l}{l^2} \quad (= D_{12}) \quad , \\
\mathbb{A}_{2211} &= \frac{E_l}{2} - \frac{6k_l}{l^2} \quad (= D_{21}) \quad , & \mathbb{A}_{2222} &= \frac{E_l}{2} + \frac{6k_l}{l^2} \quad (= D_{22}) \quad , \\
\mathbb{A}_{1212} &= \frac{E_l}{2} + \frac{6k_l}{l^2} \quad (= D_{33}) \quad , & \mathbb{A}_{1221} &= \frac{E_l}{2} - \frac{6k_l}{l^2} \quad (= D_{34}) \quad , \\
\mathbb{A}_{2112} &= \frac{E_l}{2} - \frac{6k_l}{l^2} \quad (= D_{43}) \quad , & \mathbb{A}_{2121} &= \frac{E_l}{2} + \frac{6k_l}{l^2} \quad (= D_{44}) \quad , \\
\mathbb{B}_{1313} &= \underbrace{-2k_l \quad \text{or} \quad 4k_l}_{D_{55}^{\mathrm{neg}} \text{ or } D_{55}^{\mathrm{pos}}} \quad (= D_{55}) \quad , & \mathbb{B}_{2323} &= \underbrace{-2k_l \quad \text{or} \quad 4k_l}_{D_{66}^{\mathrm{neg}} \text{ or } D_{66}^{\mathrm{pos}}} \quad (= D_{66}) \quad ,
\end{aligned} \tag{D.3}$$

where $E_l = \dfrac{Et}{l}$ and $k_l = \dfrac{Et^3}{12l}$ with E as given in Eq. (D.2).

The triangular lattice is composed of six lattice members OK with extremity nodes, $K \in \{\mathrm{A}, \mathrm{B}, \mathrm{C}, \mathrm{D}, \mathrm{E}, \mathrm{F}\}$, connected at the center, O, of the base cell as depicted in Figure D.1 (right). The two different sets of MECs read [53]

$$\begin{aligned}
\mathbb{A}_{1111} &= \frac{\sqrt{3}}{4l^2}(3E_l l^2 + 12k_l) \quad (= D_{11}) \quad , & \mathbb{A}_{1122} &= \frac{\sqrt{3}}{4l^2}(E_l l^2 - 12k_l) \quad (= D_{12}) \quad , \\
\mathbb{A}_{2211} &= \mathbb{A}_{1122} \quad (= D_{21}) \quad , & \mathbb{A}_{2222} &= \mathbb{A}_{1111} \quad (= D_{22}) \quad , \\
\mathbb{A}_{1212} &= \frac{\sqrt{3}}{4l^2}(E_l l^2 + 36k_l) \quad (= D_{33}) \quad , & \mathbb{A}_{1221} &= \mathbb{A}_{1122} \quad (= D_{34}) \quad , \\
\mathbb{A}_{2112} &= \mathbb{A}_{1122} \quad (= D_{43}) \quad , & \mathbb{A}_{2121} &= \mathbb{A}_{1212} \quad (= D_{44}) \quad , \\
\mathbb{B}_{1313} &= \underbrace{-2\sqrt{3}k_l \quad \text{or} \quad 4\sqrt{3}k_l}_{D_{55}^{\mathrm{neg}} \text{ or } D_{55}^{\mathrm{pos}}} \quad (= D_{55}) \quad , & \mathbb{B}_{2323} &= \underbrace{-2\sqrt{3}k_l \quad \text{or} \quad 4\sqrt{3}k_l}_{D_{66}^{\mathrm{neg}} \text{ or } D_{66}^{\mathrm{pos}}} \quad (= D_{66}) \quad ,
\end{aligned} \tag{D.4}$$

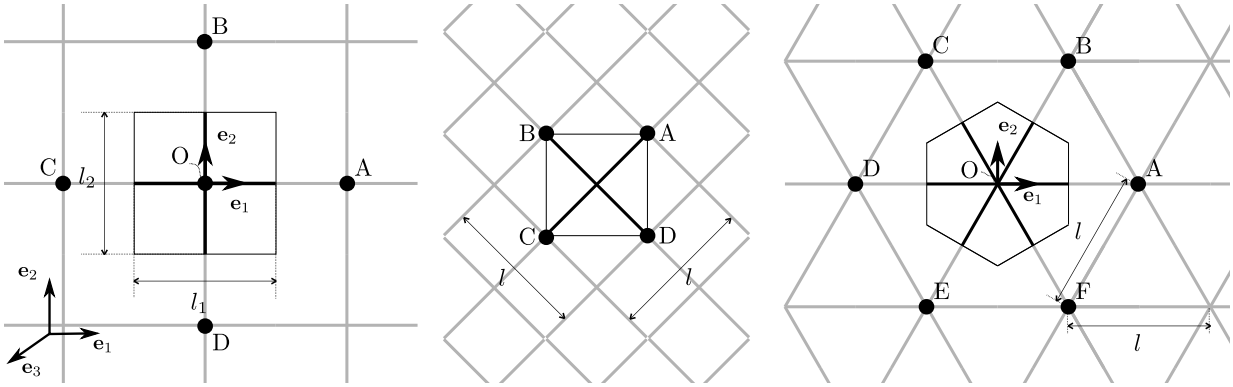

Figure D.1: Rectangular (left), 45° rotated square (center), and triangular lattice (right) with their corresponding base cells.

Appendix E

Comparison of micropolar elastic constants of primitive orthorhombic 3D and rectangular 2D lattice

A comparison between the MECs derived for the primitive orthorhombic lattice and those derived for the 2D rectangular lattice in [53] is aimed for. Therefore, various components of the fourth order elasticity tensors with respect to the in-plane directions $\underline{\mathbf{e}}_1$ and $\underline{\mathbf{e}}_2$ are compared to each other.

For the comparison, the 2D lattice needs to be considered under plane stress assumption instead of plane strain, i.e., $E = E_s$, see [53]. The components $\mathbb{A}_{1111}$ of the 2D lattice considering the plane stress assumption and the 3D lattice are given as

$$\mathbb{A}^{\mathrm{2D}}_{1111} = \frac{E_{\mathrm{s}} t}{l_2} \quad , \tag{E.1}$$

$$\mathbb{A}^{\mathrm{3D}}_{1111} = \frac{A_1 E_{\mathrm{s}}}{l_2 l_3} \quad , \tag{E.2}$$

respectively. The comparison aims to show that

$$\mathbb{A}^{\mathrm{3D}}_{1111} \to \mathbb{A}^{\mathrm{2D}}_{1111} \quad , \tag{E.3}$$

where the 3D lattice needs to be geometrically reduced. The cross-section A_1 of the corresponding 3D lattice member is determined by its thicknesses in 2- and 3-directions, i.e., $A_1 = t_2 t_3$. The out-of-plane thickness for the 3D lattice with respect to the plane stress assumption follows from the geometrical dimensions in 3-direction, $t_3 = l_3 \to h$, which is considered to be 1, i.e., $h = 1$. Furthermore, considering constant thicknesses, i.e., $t_2 = t_3 = t$, leads to

$$\mathbb{A}^{\mathrm{3D}}_{1111} = \mathbb{A}^{\mathrm{2D}}_{1111} = \frac{E_{\mathrm{s}} t}{l_2} \quad . \tag{E.4}$$

The components $\mathbb{A}_{1212}$ and $\mathbb{B}_{1313}$ for the 2D and 3D lattice are given as

$$\mathbb{A}^{\mathrm{2D}}_{1212} = \frac{Eh^3}{l_1^2 l_2} \qquad \text{and} \qquad \mathbb{A}^{\mathrm{3D}}_{1212} = \frac{12EI_{\mathrm{n1}}}{l_1^2 l_2 l_3} \quad , \tag{E.5}$$

$$\mathbb{B}^{\mathrm{2D}}_{1313} = \frac{4Eh^3}{12l_2} \qquad \text{and} \qquad \mathbb{B}^{\mathrm{3D}}_{1313} = \frac{4EI_{\mathrm{n1}}}{l_2 l_3} \quad , \tag{E.6}$$

respectively, where the area moment of inertia is given as $I_{\mathrm{n1}} = t_2^3 t_3/12$. Considering $t_2 = t$ as well as $t_3 = l_3 \to h$ it follows that $\mathbb{A}^{\mathrm{3D}}_{1212} = \mathbb{A}^{\mathrm{2D}}_{1212}$ and $\mathbb{B}^{\mathrm{3D}}_{1313} = \mathbb{B}^{\mathrm{2D}}_{1313}$.

All the other components $\mathbb{A}_{ijkl}$ for $i,j,k,l = \{1,2\}$ and $\mathbb{B}_{ijkl}$ for $i,k = \{1,2\}$ and $j,l = \{3\}$ can be compared analogously.

Appendix F

ABAQUS user elements

F.1 Geometrically nonlinear element in 3D

The interpolation or shape functions for the isoparametric hexahedral element (e) in the element parent space are given as

$$
\begin{aligned}
N_1^{(e)} &= \frac{1}{8}(1-\xi)(1-\eta)(1-\zeta) \quad , & N_2^{(e)} &= \frac{1}{8}(1+\xi)(1-\eta)(1-\zeta) \quad , \\
N_3^{(e)} &= \frac{1}{8}(1+\xi)(1+\eta)(1-\zeta) \quad , & N_4^{(e)} &= \frac{1}{8}(1-\xi)(1+\eta)(1-\zeta) \quad , \\
N_5^{(e)} &= \frac{1}{8}(1-\xi)(1-\eta)(1+\zeta) \quad , & N_6^{(e)} &= \frac{1}{8}(1+\xi)(1-\eta)(1+\zeta) \quad , \\
N_7^{(e)} &= \frac{1}{8}(1+\xi)(1+\eta)(1+\zeta) \quad , & N_8^{(e)} &= \frac{1}{8}(1-\xi)(1+\eta)(1+\zeta) \quad ,
\end{aligned}
$$

where ξ, η, and ζ denote the coordinates in the element parent space. The resulting vector of shape functions is

$$
[\underline{\mathbf{N}}^{(e)}] = \begin{bmatrix} N_1 & N_2 & N_3 & N_4 & N_5 & N_6 & N_7 & N_8 \end{bmatrix}^{\mathrm{T}} \tag{F.1}
$$

and the corresponding matrix of shape functions is

$$
[\underset{\sim}{\mathbf{N}}^{(e)}] = \begin{bmatrix}
\dots & N_I & 0 & 0 & 0 & 0 & 0 & \dots \\
\dots & 0 & N_I & 0 & 0 & 0 & 0 & \dots \\
\dots & 0 & 0 & N_I & 0 & 0 & 0 & \dots \\
\dots & 0 & 0 & 0 & N_I & 0 & 0 & \dots \\
\dots & 0 & 0 & 0 & 0 & N_I & 0 & \dots \\
\dots & 0 & 0 & 0 & 0 & 0 & N_I & \dots
\end{bmatrix} \quad , \tag{F.2}
$$

where I denotes nodes $1-8$.

The resulting matrix of derivatives of shape functions reads

$$[\underset{\sim}{\mathbf{N}}^{(e)}_{,\xi}] = \begin{bmatrix} \dots & \dfrac{\partial N_I^{(e)}}{\partial \xi} & \dots \\ \dots & \dfrac{\partial N_I^{(e)}}{\partial \eta} & \dots \\ \dots & \dfrac{\partial N_I^{(e)}}{\partial \zeta} & \dots \end{bmatrix} \quad . \tag{F.3}$$

The nodal displacements and rotations are stored in the displacement-rotation-vector of an element (e) in the form

$$[\underset{\sim}{\mathbf{y}}^{(e)}] = [\dots, U_{1I}^{(e)}, U_{2I}^{(e)}, U_{3I}^{(e)}, \phi_{1I}^{(e)}, \phi_{2I}^{(e)}, \phi_{3I}^{(e)}, \dots]^{\mathrm{T}} \quad . \tag{F.4}$$

This vector is an input of the UEL. This vector is rearranged for further usage into a nodal displacement and rotation matrix. The same is done for the vector containing the coordinates, which is also an input of the UEL. These matrices read as follows

$$[\underset{\sim}{\mathbf{U}}^{(e)}] = \begin{bmatrix} \dots & U_{1I} & \dots \\ \dots & U_{2I} & \dots \\ \dots & U_{3I} & \dots \end{bmatrix} \quad , \quad [\underset{\sim}{\mathbf{\Phi}}^{(e)}] = \begin{bmatrix} \dots & \phi_{1I} & \dots \\ \dots & \phi_{2I} & \dots \\ \dots & \phi_{3I} & \dots \end{bmatrix} \quad , \quad [\underset{\sim}{\mathbf{X}}^{(e)}] = \begin{bmatrix} \dots & X_{1I} & \dots \\ \dots & X_{2I} & \dots \\ \dots & X_{3I} & \dots \end{bmatrix} \quad . \tag{F.5}$$

Geometry, displacement, and rotation fields are then approximated by

$$\underline{\mathbf{u}} \approx [\underset{\sim}{\mathbf{U}}^{(e)}][\underline{\mathbf{N}}^{(e)}] \quad , \quad \underline{\boldsymbol{\phi}} \approx [\underset{\sim}{\mathbf{\Phi}}^{(e)}][\underline{\mathbf{N}}^{(e)}] \quad , \quad \underline{\mathbf{X}} \approx [\underset{\sim}{\mathbf{X}}^{(e)}][\underline{\mathbf{N}}^{(e)}] \quad . \tag{F.6}$$

The derivatives of the kinematic fields are needed with respect to the global coordinate system. Note that it is necessary to distinguish between updated and total Lagrangian formulations to consider the map between parent and reference configurations or between parent and current configurations, respectively. In the following, the map between parent and reference configuration is outlined. The following matrix, the so-called *bmatrix*, is introduced

$$[\underset{\sim}{\mathbf{B}}^{(e)}] = \begin{bmatrix} \dots & B_I^1 & \dots \\ \dots & B_I^2 & \dots \\ \dots & B_I^3 & \dots \end{bmatrix} = \begin{bmatrix} \dots & \dfrac{\partial N_I}{\partial X_1} & \dots \\ \dots & \dfrac{\partial N_I}{\partial X_2} & \dots \\ \dots & \dfrac{\partial N_I}{\partial X_3} & \dots \end{bmatrix} \quad , \tag{F.7}$$

where the derivatives of the shape functions are given with respect to global coordinates in the reference or material configurations X_1, X_2, and X_3 reading

$$\begin{aligned} \frac{\partial N_I}{\partial X_1} &= \frac{\partial N_I}{\partial \xi} J_{11}^{-1} + \frac{\partial N_I}{\partial \eta} J_{12}^{-1} + \frac{\partial N_I}{\partial \zeta} J_{13}^{-1} \quad , \\ \frac{\partial N_I}{\partial X_2} &= \frac{\partial N_I}{\partial \xi} J_{21}^{-1} + \frac{\partial N_I}{\partial \eta} J_{22}^{-1} + \frac{\partial N_I}{\partial \zeta} J_{23}^{-1} \quad , \\ \frac{\partial N_I}{\partial X_3} &= \frac{\partial N_I}{\partial \xi} J_{31}^{-1} + \frac{\partial N_I}{\partial \eta} J_{32}^{-1} + \frac{\partial N_I}{\partial \zeta} J_{33}^{-1} \quad , \end{aligned} \tag{F.8}$$

with J_{ij}^{-1} as the components of the inverse Jacobian matrix. The Jacobian is defined as

$$\begin{bmatrix} \frac{\partial}{\partial \xi} \\ \frac{\partial}{\partial \eta} \\ \frac{\partial}{\partial \zeta} \end{bmatrix} = \underbrace{\begin{bmatrix} \frac{\partial X_1}{\partial \xi} & \frac{\partial X_2}{\partial \xi} & \frac{\partial X_3}{\partial \xi} \\ \frac{\partial X_1}{\partial \eta} & \frac{\partial X_2}{\partial \eta} & \frac{\partial X_3}{\partial \eta} \\ \frac{\partial X_1}{\partial \zeta} & \frac{\partial X_2}{\partial \zeta} & \frac{\partial X_3}{\partial \zeta} \end{bmatrix}}_{[\underset{\sim}{\mathbf{J}}^{(e)}]} \begin{bmatrix} \frac{\partial}{\partial X_1} \\ \frac{\partial}{\partial X_2} \\ \frac{\partial}{\partial X_3} \end{bmatrix} \quad , \tag{F.9}$$

with

$$[\underset{\sim}{\mathbf{J}}^{(e)}] = \begin{bmatrix} \frac{\partial N_I^{(e)}}{\partial \xi} X_{1I}^{(e)} & \frac{\partial N_I^{(e)}}{\partial \xi} X_{2I}^{(e)} & \frac{\partial N_I^{(e)}}{\partial \xi} X_{3I}^{(e)} \\ \frac{\partial N_I^{(e)}}{\partial \eta} X_{1I}^{(e)} & \frac{\partial N_I^{(e)}}{\partial \eta} X_{2I}^{(e)} & \frac{\partial N_I^{(e)}}{\partial \eta} X_{3I}^{(e)} \\ \frac{\partial N_I^{(e)}}{\partial \zeta} X_{1I}^{(e)} & \frac{\partial N_I^{(e)}}{\partial \zeta} X_{2I}^{(e)} & \frac{\partial N_I^{(e)}}{\partial \zeta} X_{3I}^{(e)} \end{bmatrix} \quad . \tag{F.10}$$

With the above equations at hand, the update of the deformation gradient tensor given in Eq. (4.48) can be given as follows

$$\underset{\sim}{\mathbf{F}} = \underset{\sim}{\mathbf{I}} + \mathrm{Grad}_{\mathrm{R}}([\underset{\sim}{\mathbf{U}}^{(e)}][\underline{\mathbf{N}}^{(e)}]) = \underset{\sim}{\mathbf{I}} + \sum_{I=1}^{n_{\mathrm{el}}} \begin{bmatrix} U_{1I} \\ U_{2I} \\ U_{3I} \end{bmatrix} \otimes \begin{bmatrix} \frac{\partial N_I}{\partial X_1} \\ \frac{\partial N_I}{\partial X_2} \\ \frac{\partial N_I}{\partial X_3} \end{bmatrix} = \underset{\sim}{\mathbf{I}} + [\underset{\sim}{\mathbf{U}}^{(e)}][\underset{\sim}{\mathbf{B}}^{(e)}]^{\mathrm{T}} \quad . \tag{F.11}$$

The derivative of the updated microrotation tensor based on Eq. (4.58) with respect to the reference configuration using Eq. (4.57) can be expressed as

$$\begin{aligned} \frac{\partial \underset{\sim}{\mathbf{R}}^{(i+1)}}{\partial X_k} &= (\nabla_{X_k} \Delta \underset{\sim}{\mathbf{R}}) \underset{\sim}{\mathbf{R}}^{(i)} + \Delta \underset{\sim}{\mathbf{R}} (\nabla_{X_k} \underset{\sim}{\mathbf{R}}^{(i)}) \\ &= (\nabla_{X_k} N_I^{\phi}(\underline{\mathbf{X}}) \exp(\mathrm{Spn}(\Delta \underline{\boldsymbol{\phi}}_I))) \underset{\sim}{\mathbf{R}}^{(i)} + \Delta \underset{\sim}{\mathbf{R}} (\nabla_{X_k} N_I^{\phi}(\underline{\mathbf{X}}) \exp(\mathrm{Spn}(\underline{\boldsymbol{\phi}}_I^{(i)}))) \\ &= (\nabla_{X_k} N_I^{\phi}(\underline{\mathbf{X}}) \Delta \underset{\sim}{\mathbf{R}}_I) \underset{\sim}{\mathbf{R}}^{(i)} + \Delta \underset{\sim}{\mathbf{R}} (\nabla_{X_k} N_I^{\phi}(\underline{\mathbf{X}}) \underset{\sim}{\mathbf{R}}_I^{(i)}) \quad , \end{aligned} \tag{F.12}$$

with $k = 1, 2, 3$ for all three dimensions.

Table F.1: Gaussian integration point coordinates and corresponding weights.

Full integration with number of integration points $n_{\text{int}} = 8$.

p	$\sqrt{3}\xi_p$	$\sqrt{3}\eta_p$	$\sqrt{3}\zeta_p$	w_p
1	-1	-1	-1	1
2	$+1$	-1	-1	1
3	$+1$	$+1$	-1	1
4	-1	$+1$	-1	1
5	-1	-1	$+1$	1
6	$+1$	-1	$+1$	1
7	$+1$	$+1$	$+1$	1
8	-1	$+1$	$+1$	1

F.2 Linear element in 3D

For the linear element in 3D, the same FEM parameters are used as for the nonlinear element. For the sake of completeness, the differential operator matrix with respect to LSD strain and stress measures is given as

$$
[\underline{\mathbf{d}}] = \begin{bmatrix}
\frac{\partial}{\partial X_1} & 0 & 0 & 0 & 0 & \frac{\partial}{\partial X_2} & 0 & \frac{\partial}{\partial X_3} & 0 & 0 & 0 & 0 & 0 & 0 & 0 & 0 & 0 & 0 \\
0 & \frac{\partial}{\partial X_2} & 0 & \frac{\partial}{\partial X_1} & 0 & 0 & 0 & 0 & \frac{\partial}{\partial X_3} & 0 & 0 & 0 & 0 & 0 & 0 & 0 & 0 & 0 \\
0 & 0 & \frac{\partial}{\partial X_3} & 0 & \frac{\partial}{\partial X_1} & 0 & \frac{\partial}{\partial X_2} & 0 & 0 & 0 & 0 & 0 & 0 & 0 & 0 & 0 & 0 & 0 \\
0 & 0 & 0 & 0 & 0 & 0 & -1 & 0 & 1 & \frac{\partial}{\partial X_1} & 0 & 0 & 0 & 0 & \frac{\partial}{\partial X_2} & 0 & \frac{\partial}{\partial X_3} & 0 \\
0 & 0 & 0 & 0 & 1 & 0 & 0 & -1 & 0 & 0 & \frac{\partial}{\partial X_2} & 0 & \frac{\partial}{\partial X_1} & 0 & 0 & 0 & 0 & \frac{\partial}{\partial X_3} \\
0 & 0 & 0 & -1 & 0 & 1 & 0 & 0 & 0 & 0 & 0 & \frac{\partial}{\partial X_3} & 0 & \frac{\partial}{\partial X_1} & 0 & \frac{\partial}{\partial X_2} & 0 & 0
\end{bmatrix}^{\mathrm{T}} , \tag{F.13}
$$

where the derivatives are defined with respect to the reference configuration. Note that the arrangement of components is different to the one defined in Eq. (2.62) and is given as

$$
(\cdot)_{ij} \quad \text{with} \quad ij = \{11, 22, 33, 12, 13, 21, 23, 31, 32\} \quad . \tag{F.14}
$$

F.3 Linear element in 2D

The shape functions for the quadrilateral element (e) in the element parent space are given as

$$
\begin{aligned}
N_1^{(e)} &= \frac{1}{4}(1-\xi)(1-\eta) \quad , \quad N_2^{(e)} = \frac{1}{4}(1+\xi)(1-\eta) \quad , \\
N_3^{(e)} &= \frac{1}{4}(1+\xi)(1+\eta) \quad , \quad N_4^{(e)} = \frac{1}{4}(1-\xi)(1+\eta) \quad .
\end{aligned} \tag{F.15}
$$

The nodal displacements and rotations of an element (e) are stored in a generalized vector of nodal displacements and microrotations in the form

$$
[\underline{\mathbf{y}}^{(e)}] = [\ldots, U_{1I}^{(e)}, U_{2I}^{(e)}, \phi_{3I}^{(e)}, \ldots]^{\mathrm{T}} \quad , \tag{F.16}
$$

Table F.2: Gaussian integration point coordinates and corresponding weights.

Full integration with number of integration points $n_{\text{int}} = 4$.

p	$\sqrt{3}\xi_p$	$\sqrt{3}\eta_p$	w_p
1	-1	-1	1.0
2	$+1$	-1	1.0
3	$+1$	$+1$	1.0
4	-1	$+1$	1.0

Reduced integration with number of integration points $n_{\text{int}} = 1$.

p	ξ_p	η_p	w_p
1	0	0	4.0

where I denotes nodes $1-4$. The corresponding matrix of shape functions is

$$[\underset{\sim}{\mathbf{N}}^{(e)}] = \begin{bmatrix} \dots & N_I & 0 & 0 & \dots \\ \dots & 0 & N_I & 0 & \dots \\ \dots & 0 & 0 & N_I & \dots \end{bmatrix} \quad . \tag{F.17}$$

F.4 Post-processing of user elements

ABAQUS does not directly support post-processing of user elements and provides only rudimentary information in the user manual on how to achieve this. A brief description of a workaround is outlined, which makes post-processing possible by using an element overlay, see, e.g., [68].

For this purpose, an element from the ABAQUS element library is necessary, which is similar to the user element, i.e., shows the same interpolation functions, such as `C3D8` and `C3D8MP`. This element is further called *dummy element*. Both elements need to share the same nodes. Furthermore, it is important that the dummy elements should not influence the overall mechanical response. For this purpose, the dummy element must show a very compliant response compared to the user element, e.g., an isotropic material with a very low Young‘s modulus. This allows to visualize the DOFs of the user elements in the ABAQUS viewer. For the user element `C3D8MP`, this also applies to the rotational DOFs, even though these DOFs do not exist for the element `C3D8`.

If integration point values of the user element are also to be visualized, such as stresses and strains, the dummy element needs to be used in combination with an ABAQUS user material (UMAT). The UMAT of the dummy element must be implemented in the same environment as the user element so that the SDVs of the user element can be passed to the SDVs of the UMAT of the corresponding dummy element via a commonly shared `module`. Note that the integration point numbering for the `C3D8` is different from the user element `C3D8MP` given in Table F.1, which must be considered accordingly. In particular, $p = 3$ and $p = 4$ as well as $p = 7$ and $p = 8$ are interchanged. A constant offset in the element numbering between user and dummy elements is required to ensure that information is passed between the correct pairs of elements, cf. Appendix F.5. All further details can be found in the Fortran files of the implementation of the individual user elements.

F.5 User element usage

In the following, the usage of the user elements is outlined based on the user element C3D8MP. The type of element is specified by

```
*USER ELEMENT, TYPE=Ui, NODES=8, COORDINATES=3, VAR=360, PROPERTIES=j, UNSYMM
1,2,3,4,5,6
```

in the input file, where i denotes an input variable passed to the UEL subroutine, which is associated with a type of element defined by the user in the subroutine. For C3D8MP, i denotes the material subroutine and takes the values $i = 10$ for isotropic materials, $i = 11$ for PO lattices, and $i = 11$ for BCC lattices. The PROPERTIES flag must set to $j = 6$ for the isotropic materials and 21 for the lattices, respectively. The NODES flag defines the number of nodes, the COORDINATES flag specifies the spatial dimension, and the VAR sets the number of SDVs, i.e., for each integration point the stress measures, strain measures, and the microrotation tensors are stored, which is $n_{\text{int}} \cdot 45 = 360$ for the C3D8MP. The entries in the line below indicate the active DOFs of the element, where 1, 2, 3 are associated with displacement DOFs and 4, 5, 6 are associated with rotation DOFs. Next, the element is defined by using

```
*ELEMENT, TYPE=Ui, ELSET=ELALL
1,1,2,3,4,5,6,7,8
```

The first entry is the element label, the following entries are the node labels defining the element. The number of entries must coincide with the number specified in the NODES flag in the first expression. For isotropic material behavior, i.e., $i = 10$, the following expression is to be specified

```
*UEL PROPERTY, ELSET=ELALL
λ, μ, ν, α, β, γ
```

where the material moduli correspond to Eq. (2.68). For the lattices, i.e., $i = 11$ for PO and $i = 12$ for BCC type, the following expression needs to be specified

```
*UEL PROPERTY, ELSET=ELALL
E, ν, l1, l2, l3, A1, A2, A3, Im1,
Im2, Im3, In1, In2, In3, , It1, It2, It3, pnorm,
p1, p2, p3
```

where the input parameters correspond to the individual lattices, cf. Section 3.3. The last four entries, namely, p_{norm}, p_1, p_2, and p_3, denote an axial vector about which the elasticity tensors are to be rotated with respect to their principal material axes by using Eq. (2.76).

If dummy elements of type C3D8 are used for visualization of the C3D8MP including stress and strain measures, cf. Appendix F.4, the following expression needs to be added in the input file

```
ELEMENT, TYPE=C3D8, ELSET=ELALL_DUMMY
100001,1,2,3,4,5,6,7,8
*SOLID SECTION, ELSET=ELALL_DUMMY, MATERIAL=DUMMY_MATERIAL
1.0
*Material, name=DUMMY_MATERIAL
*Depvar
45,
```

```
1, stress11
2, stress12
...
*User Material, constants=0
BLANK,
```

The dummy element is defined by the same nodes as the user element and shows an offset of 100000 in the element label from the user element. Furthermore, a UMAT is defined using 45 SDVs indicated by the entry in the first line after `*Depvar`. The following lines specify all SDVs, where the first entry denotes the variable's number and the second entry defines its identifier for the ABAQUS viewer. For the total Lagrangian description, cf. Figure 4.1, the SDVs are the components $(\cdot)_{ij}$ of $\breve{\underset{\sim}{\mathbf{T}}}$, ${}^{\kappa}\breve{\underset{\sim}{\mathbf{T}}}$, $\underset{\sim}{\mathbf{E}}$, $\underset{\sim}{\boldsymbol{\mathscr{K}}}$, and $\underset{\sim}{\mathbf{R}}$ each given in the following sequence

$$(\cdot)_{ij} \quad \text{with} \quad ij = \{11, 12, 13, 21, 22, 23, 31, 32, 33\} \quad . \tag{F.18}$$

This is exemplified in the second line, where the first entry specifies the SDV, i.e., the stress component $\breve{T}_{11}$, while the second entry is the name of the SDV displayed in the ABAQUS viewer, i.e., "stress11". The third line follows as $\breve{T}_{12}$ displayed as "stress12" in the ABAQUS viewer. Additional lines are added until the last SDV is reached, namely, R_{33}. For the UMAT, no value is specified, i.e., is left blank, as this value is specified in the UMAT subroutine of the dummy element.

Bibliography

[1] NGS-Py Finite Element Tool. URL `https://docu.ngsolve.org/v6.2.2302/index.html`.

[2] H. Altenbach. *Kontinuumsmechanik: Einführung in die materialunabhängigen und materialabhängigen Gleichungen*. Springer Berlin Heidelberg, Berlin, Heidelberg, 2018.

[3] S. Arabnejad and D. Pasini. Mechanical properties of lattice materials via asymptotic homogenization and comparison with alternative homogenization methods. *International Journal of Mechanical Sciences*, 77:249–262, 2013.

[4] J. Argyris. An excursion into large rotations. *Computer Methods in Applied Mechanics and Engineering*, 32(1-3):85–155, 1982.

[5] M. Ashby. The properties of foams and lattices. *Philosophical Transactions of the Royal Society A: Mathematical, Physical and Engineering Sciences*, 364(1838):15–30, 2006.

[6] A. Askar and A. Cakmak. A structural model of a micropolar continuum. *International Journal of Engineering Science*, 6(10):583–589, 1968.

[7] K. J. Bathe. *Finite element procedures*. Watertown, MA, 2nd edition, 2014.

[8] S. Bauer, M. Schäfer, P. Grammenoudis, and C. Tsakmakis. Three-dimensional finite elements for large deformation micropolar elasticity. *Computer Methods in Applied Mechanics and Engineering*, 199 (41-44):2643–2654, 2010.

[9] S. Bauer, W. G. Dettmer, D. Perić, and M. Schäfer. Micropolar hyperelasticity: constitutive model, consistent linearization and simulation of 3D scale effects. *Computational Mechanics*, 50(4):383–396, 2012.

[10] Z. Bažant and M. Christensen. Analogy between micropolar continuum and grid frameworks under initial stress. *International Journal of Solids and Structures*, 8(3):327–346, 1972.

[11] K. Bertoldi, P. M. Reis, S. Willshaw, and T. Mullin. Negative Poisson's Ratio Behavior Induced by an Elastic Instability. *Advanced Materials*, 22(3):361–366, 2010.

[12] M. Bici, S. Brischetto, F. Campana, C. G. Ferro, C. Seclì, S. Varetti, P. Maggiore, and A. Mazza. Development of a multifunctional panel for aerospace use through SLM additive manufacturing. *Procedia CIRP*, 67:215–220, 2018.

[13] R. Biswas, L. Poh, and A. Shedbale. A micromorphic computational homogenization framework for auxetic tetra-chiral structures. *Journal of the Mechanics and Physics of Solids*, 135:103801, 2020.

[14] P. Boggs, A. Althsuler, A. Larzelere, E. Walsh, R. Clay, and M. Hardwick. DART system analysis. Technical Report SAND2005-4647, 876325, Sandia National Laboratories, 2005. URL `https://www.osti.gov/servlets/purl/876325/`.

[15] J. Chen. Fracture analysis of cellular materials: A strain gradient model. *Journal of the Mechanics and Physics of Solids*, 46(5):789–828, 1998.

[16] Z. Chi, J. Liu, and A. K. Soh. Micropolar modeling of a typical bending-dominant lattice comprising zigzag beams. *Mechanics of Materials*, 160:103922, 2021.

[17] E. Cosserat and F. Cosserat. *Théorie des corps déformables*. Hermann et fils, Paris, 1909.

[18] Z. Cui, Z. Yuan, and J. Ju. Mechanical Couplings of 3D Lattice Materials Discovered by Micropolar Elasticity and Geometric Symmetry. *Journal of Applied Mechanics*, 90(4):041001, 2023.

[19] F. dell'Isola, I. Giorgio, M. Pawlikowski, and N. L. Rizzi. Large deformations of planar extensible beams and pantographic lattices: heuristic homogenization, experimental and numerical examples of equilibrium. *Proceedings of the Royal Society A: Mathematical, Physical and Engineering Sciences*, 472 (2185):20150790, 2016.

[20] V. Deshpande, M. Ashby, and N. Fleck. Foam topology: bending versus stretching dominated architectures. *Acta Materialia*, 49(6):1035–1040, 2001.

[21] A. Desmoulins and D. Kochmann. Local and nonlocal continuum modeling of inelastic periodic networks applied to stretching-dominated trusses. *Computer Methods in Applied Mechanics and Engineering*, 313: 85–105, 2017.

[22] F. Dos Reis and J. Ganghoffer. Construction of micropolar continua from the asymptotic homogenization of beam lattices. *Computers & Structures*, 112-113:354–363, 2012.

[23] S. Duan, W. Wen, and D. Fang. A predictive micropolar continuum model for a novel three-dimensional chiral lattice with size effect and tension-twist coupling behavior. *Journal of the Mechanics and Physics of Solids*, 121:23–46, 2018.

[24] K. El Nady, I. Goda, and J.-F. Ganghoffer. Computation of the effective nonlinear mechanical response of lattice materials considering geometrical nonlinearities. *Computational Mechanics*, 58(6):957–979, 2016.

[25] K. El Nady, F. Dos Reis, and J. Ganghoffer. Computation of the homogenized nonlinear elastic response of 2D and 3D auxetic structures based on micropolar continuum models. *Composite Structures*, 170: 271–290, 2017.

[26] S. G. Erdelj, G. Jelenić, and A. Ibrahimbegović. Geometrically non-linear 3D finite-element analysis of micropolar continuum. *International Journal of Solids and Structures*, 202:745–764, 2020.

[27] V. A. Eremeyev and W. Pietraszkiewicz. Material symmetry group of the non-linear polar-elastic continuum. *International Journal of Solids and Structures*, 49(14):1993–2005, 2012.

[28] V. A. Eremeyev, L. P. Lebedev, and H. Altenbach. *Foundations of Micropolar Mechanics*. SpringerBriefs in Applied Sciences and Technology. Springer Berlin Heidelberg, Berlin, Heidelberg, 2013.

[29] A. Eringen and D. Edelen. On nonlocal elasticity. *International Journal of Engineering Science*, 10(3): 233–248, 1972.

[30] A. C. Eringen. *Microcontinuum field theories I. Foundations and Solids*. Springer, New York, 1st edition, 1999.

[31] N. A. Fleck, V. S. Deshpande, and M. F. Ashby. Micro-architectured materials: past, present and future. *Proceedings of the Royal Society A: Mathematical, Physical and Engineering Sciences*, 466(2121):2495–2516, 2010.

[32] S. Forest. Micromorphic Media. In F. Pfeiffer, F. G. Rammerstorfer, J. Salençon, B. Schrefler, P. Serafini, H. Altenbach, and V. A. Eremeyev, editors, *Generalized Continua from the Theory to Engineering Applications*, volume 541, pages 249–300. Springer Vienna, Vienna, 2013.

[33] S. Forest and R. Sievert. Nonlinear microstrain theories. *International Journal of Solids and Structures*, 43(24):7224–7245, 2006.

[34] J. Freund, A. Karakoç, and J. Sjölund. Computational homogenization of regular cellular material according to classical elasticity. *Mechanics of Materials*, 78:56–65, 2014.

[35] F. Fujii and E. Ramm. Computational bifurcation theory: path-tracing, pinpointing and path-switching. *Engineering Structures*, 19(5):385–392, 1997.

[36] A. Gad, X.-L. Gao, and K. Li. A strain energy-based homogenization method for 2-D and 3-D cellular materials using the micropolar elasticity theory. *Composite Structures*, 265:113594, 2021.

[37] M. Gaćeša. *Fixed-Pole Concept in 3D Beam Finite Elements Relationship to Standard Approaches and Analysis of Different Interpolations*. PhD thesis, University of Rijeka, Rijeka, 2015.

[38] L. J. Gibson and M. F. Ashby. *Cellular Solids: Structure and Properties*. Cambridge University Press, 2nd edition, 1997.

[39] I. Giorgio, A. Della Corte, F. dell'Isola, and D. J. Steigmann. Buckling modes in pantographic lattices. *Comptes Rendus Mécanique*, 344(7):487–501, 2016.

[40] R. N. Glaesener, C. Lestringant, B. Telgen, and D. M. Kochmann. Continuum models for stretching- and bending-dominated periodic trusses undergoing finite deformations. *International Journal of Solids and Structures*, 171:117–134, 2019.

[41] R. N. Glaesener, E. A. Träff, B. Telgen, R. M. Canonica, and D. M. Kochmann. Continuum representation of nonlinear three-dimensional periodic truss networks by on-the-fly homogenization. *International Journal of Solids and Structures*, 206:101–113, 2020.

[42] I. Goda, M. Assidi, S. Belouettar, and J. Ganghoffer. A micropolar anisotropic constitutive model of cancellous bone from discrete homogenization. *Journal of the Mechanical Behavior of Biomedical Materials*, 16:87–108, 2012.

[43] P. Grammenoudis and C. Tsakmakis. Finite element implementation of large deformation micropolar plasticity exhibiting isotropic and kinematic hardening effects. *International Journal for Numerical Methods in Engineering*, 62(12):1691–1720, 2005.

[44] S. Grbcic. *Linked interpolation and strain invariance in finite-element modelling of micropolar continuum*. PhD thesis, Université de Technologie de Compiègne; University of Rijeka, Rijeka, 2018.

[45] B. Hanks, J. Berthel, M. Frecker, and T. W. Simpson. Mechanical properties of additively manufactured metal lattice structures: Data review and design interface. *Additive Manufacturing*, 35:101301, 2020.

[46] A. D. Hasanyan and A. M. Waas. Micropolar Constitutive Relations for Cellular Solids. *Journal of Applied Mechanics*, 83(4):041001, 2016.

[47] S. Hassanpour and G. R. Heppler. Micropolar elasticity theory: a survey of linear isotropic equations, representative notations, and experimental investigations. *Mathematics and Mechanics of Solids*, 22(2): 224–242, 2017.

[48] G. A. Holzapfel. *Nonlinear solid mechanics: a continuum approach for engineering*. Wiley, Chichester, 2000.

[49] J. Huang and T.-L. Wang. Buckling analysis of large and complex structures by using substructuring techniques. *Computers & Structures*, 46(5):845–850, 1993.

[50] C. J. Hunt, F. Morabito, C. Grace, Y. Zhao, and B. K. Woods. A review of composite lattice structures. *Composite Structures*, 284:115120, 2022.

[51] M. Jalalpour, T. Igusa, and J. K. Guest. Optimal design of trusses with geometric imperfections: Accounting for global instability. *International Journal of Solids and Structures*, 48(21):3011–3019, 2011.

[52] D. M. Kochmann and K. Bertoldi. Exploiting Microstructural Instabilities in Solids and Structures: From Metamaterials to Structural Transitions. *Applied Mechanics Reviews*, 69(5):050801, 2017.

[53] R. S. Kumar and D. L. McDowell. Generalized continuum modeling of 2-D periodic cellular solids. *International Journal of Solids and Structures*, 41(26):7399–7422, 2004.

[54] R. Lakes. Experimental microelasticity of two porous solids. *International Journal of Solids and Structures*, 22(1):55–63, 1986.

[55] R. Lakes. Physical meaning of elastic constants in Cosserat, void, and microstretch elasticity. *Journal of Mechanics of Materials and Structures*, 11(3):217–229, 2016.

[56] G. Lin, J. Li, P. Chen, W. Sun, S. A. Chizhik, A. A. Makhaniok, G. B. Melnikova, and T. A. Kuznetsova. Buckling of lattice columns made from three-dimensional chiral mechanical metamaterials. *International Journal of Mechanical Sciences*, 194:106208, 2021.

[57] L. Liu, P. Kamm, F. García-Moreno, J. Banhart, and D. Pasini. Elastic and failure response of imperfect three-dimensional metallic lattices: the role of geometric defects induced by Selective Laser Melting. *Journal of the Mechanics and Physics of Solids*, 107:160–184, 2017.

[58] X. Liu, G. Huang, and G. Hu. Chiral effect in plane isotropic micropolar elasticity and its application to chiral lattices. *Journal of the Mechanics and Physics of Solids*, 60(11):1907–1921, 2012.

[59] M. H. Luxner, J. Stampfl, and H. E. Pettermann. Nonlinear simulations on the interaction of disorder and defects in open cell structures. *Computational Materials Science*, 47(2):418–428, 2009.

[60] T. Maconachie, M. Leary, B. Lozanovski, X. Zhang, M. Qian, O. Faruque, and M. Brandt. SLM lattice structures: Properties, performance, applications and challenges. *Materials & Design*, 183:108137, 2019.

[61] G. A. Maugin. Internal Variables and Dissipative Structures. *Journal of Non-Equilibrium Thermodynamics*, 15(2), 1990.

[62] G. A. Maugin. *Non-Classical Continuum Mechanics: A Dictionary*, volume 51 of *Advanced Structured Materials*. Springer Singapore, Singapore, 2017.

[63] D. McCallen and K. Romstad. A continuum model for the nonlinear analysis of beam-like lattice structures. *Computers & Structures*, 29(2):177–197, 1988.

[64] D. McCallen and K. Romstad. A continuum model for lattice structures with geometric and material nonlinearities. *Computers & Structures*, 37(5):795–822, 1990.

[65] R. Mindlin. Second gradient of strain and surface-tension in linear elasticity. *International Journal of Solids and Structures*, 1(4):417–438, 1965.

[66] R. D. Mindlin and H. F. Tiersten. Effects of couple-stresses in linear elasticity. *Archive for Rational Mechanics and Analysis*, 11(1):415–448, 1962.

[67] P. Moongkhamklang, D. M. Elzey, and H. N. Wadley. Titanium matrix composite lattice structures. *Composites Part A: Applied Science and Manufacturing*, 39(2):176–187, 2008.

[68] M. A. Msekh, J. M. Sargado, M. Jamshidian, P. M. Areias, and T. Rabczuk. Abaqus implementation of phase-field model for brittle fracture. *Computational Materials Science*, 96:472–484, 2015.

[69] I. Münch. *Ein geometrisch und materiell nichtlineares Cosserat-Modell: Theorie, Numerik und Anwendungsmöglichkeiten.* Nummer 13 in Berichte des Instituts für Baustatik, Universität Fridericiana Karlsruhe (TH). Institut für Baustatik, Karlsruhe, 2007.

[70] A. Nazir, K. M. Abate, A. Kumar, and J.-Y. Jeng. A state-of-the-art review on types, design, optimization, and additive manufacturing of cellular structures. *The International Journal of Advanced Manufacturing Technology*, 104(9-12):3489–3510, 2019.

[71] P. Neff, I.-D. Ghiba, A. Madeo, L. Placidi, and G. Rosi. A unifying perspective: the relaxed linear micromorphic continuum. *Continuum Mechanics and Thermodynamics*, 26(5):639–681, 2014.

[72] B. Niu and J. Yan. A new micromechanical approach of micropolar continuum modeling for 2-D periodic cellular material. *Acta Mechanica Sinica*, 32(3):456–468, 2016.

[73] A. K. Noor. Continuum modeling for repetitive lattice structures. *Applied Mechanics Reviews*, 41(7): 285–296, 1988.

[74] K. Nübel and W. Huang. A study of localized deformation pattern in granular media. *Computer Methods in Applied Mechanics and Engineering*, 193(27-29):2719–2743, 2004.

[75] L. Obrezkov, M. K. Matikainen, and R. Kouhia. Micropolar beam-like structures under large deformation. *International Journal of Solids and Structures*, 254-255:111899, 2022.

[76] R. K. Pal, M. Ruzzene, and J. J. Rimoli. A continuum model for nonlinear lattices under large deformations. *International Journal of Solids and Structures*, 96:300–319, 2016.

[77] S. D. Papka and S. Kyriakides. In-plane compressive response and crushing of honeycomb. *Journal of the Mechanics and Physics of Solids*, 42(10):1499–1532, 1994.

[78] G. P. Phlipot and D. M. Kochmann. A quasicontinuum theory for the nonlinear mechanical response of general periodic truss lattices. *Journal of the Mechanics and Physics of Solids*, 124:758–780, 2019.

[79] W. Pietraszkiewicz and V. Eremeyev. On natural strain measures of the non-linear micropolar continuum. *International Journal of Solids and Structures*, 46(3-4):774–787, 2009.

[80] W. Pietraszkiewicz and V. Eremeyev. On vectorially parameterized natural strain measures of the non-linear Cosserat continuum. *International Journal of Solids and Structures*, 46(11-12):2477–2480, 2009.

[81] M. Rashed, M. Ashraf, R. Mines, and P. J. Hazell. Metallic microlattice materials: A current state of the art on manufacturing, mechanical properties and applications. *Materials & Design*, 95:518–533, 2016.

[82] M. M. Schasching and M. Todt. Linear continuum modeling of lattice materials by means of the Finite Element Method. Technical Report 312, Institute of Lightweight Design and Structural Biomechanics, Vienna, 2021. URL `https://publik.tuwien.ac.at/files/publik_299386.pdf`.

[83] J. Schoeberl. C++ 11 implementation of finite elements in NGSolve. Technical report, Institute for analysis and scientific computing, Vienna University of Technology, 2014.

[84] D. Shidid, M. Leary, P. Choong, and M. Brandt. Just-in-time design and additive manufacture of patient-specific medical Implants. *Physics Procedia*, 83:4–14, 2016.

[85] J. Somnic and B. W. Jo. Status and Challenges in Homogenization Methods for Lattice Materials. *Materials*, 15(2):605, 2022.

[86] A. Spadoni and M. Ruzzene. Elasto-static micropolar behavior of a chiral auxetic lattice. *Journal of the Mechanics and Physics of Solids*, 60(1):156–171, 2012.

[87] T. Tancogne-Dejean, A. B. Spierings, and D. Mohr. Additively-manufactured metallic micro-lattice materials for high specific energy absorption under static and dynamic loading. *Acta Materialia*, 116: 14–28, 2016.

[88] P. Trovalusci and R. Masiani. Material symmetries of micropolar continua equivalent to lattices. *International Journal of Solids and Structures*, 36(14):2091–2108, 1999.

[89] C. A. Truesdell and W. Noll. *The non-linear field theories of mechanics*. Springer-Verlag, Berlin New York Paris [etc.], 2nd ed edition, 1992.

[90] S. van Bree, O. Rokoš, R. Peerlings, M. Doškář, and M. Geers. A Newton solver for micromorphic computational homogenization enabling multiscale buckling analysis of pattern-transforming metamaterials. *Computer Methods in Applied Mechanics and Engineering*, 372:113333, 2020.

[91] Z. Vangelatos, K. Komvopoulos, and C. Grigoropoulos. Regulating the mechanical behavior of metamaterial microlattices by tactical structure modification. *Journal of the Mechanics and Physics of Solids*, 144:104112, 2020.

[92] A. Vigliotti and D. Pasini. Linear multiscale analysis and finite element validation of stretching and bending dominated lattice materials. *Mechanics of Materials*, 46:57–68, 2012.

[93] A. Vigliotti, V. S. Deshpande, and D. Pasini. Non linear constitutive models for lattice materials. *Journal of the Mechanics and Physics of Solids*, 64:44–60, 2014.

[94] A. Vyatskikh, S. Delalande, A. Kudo, X. Zhang, C. M. Portela, and J. R. Greer. Additive manufacturing of 3D nano-architected metals. *Nature Communications*, 9(1):593, 2018.

[95] C. Völlmecke, M. Todt, and S. Yiatros. Buckling and postbuckling of architectured materials: A review of methods for lattice structures and metal foams. *Composites and Advanced Materials*, 30: 263498332110039, 2021.

[96] X. L. Wang and W. J. Stronge. Micropolar theory for two–dimensional stresses in elastic honeycomb. *Proceedings of the Royal Society of London. Series A: Mathematical, Physical and Engineering Sciences*, 455(1986):2091–2116, 1999.

[97] M. Yoder, L. Thompson, and J. Summers. Size effects in lattice structures and a comparison to micropolar elasticity. *International Journal of Solids and Structures*, 143:245–261, 2018.

[98] Q.-S. Zheng and A. Spencer. On the canonical representations for Kronecker powers of orthogonal tensors with application to material symmetry problems. *International Journal of Engineering Science*, 31(4):617–635, 1993.

[99] O. Červinek, H. Pettermann, M. Todt, D. Koutný, and O. Vaverka. Non-linear dynamic finite element analysis of micro-strut lattice structures made by laser powder bed fusion. *Journal of Materials Research and Technology*, 18:3684–3699, 2022.